UNIVERSITÀ DEGLI STUDI DI VERONA

DEPARTMENT OF

DIAGNOSTICS AND PUBLIC HEALTH

GRADUATE SCHOOL OF

LIFE AND HEALTH SCIENCES

DOCTORAL PROGRAM IN

NEUROSCIENCE, PSYCHOLOGICAL AND PSYCHIATRIC SCIENCES,

AND MOVEMENT SCIENCES

Cycle / year: XXXV/2019

TITLE OF THE DOCTORAL THESIS

DEVELOPMENT OF MURINE BRAIN ORGANOIDS AND THEIR APPLICATION FOR DISEASE MODELING

S.S.D. BIO/14

Coordinator: Prof. Michela Rimondini

Tutor: Prof. Ilaria Decimo

Co-tutor: Dr. Francesca Ciarpella

Doctoral Student: Dr. Raluca Georgiana Zamfir

SOMMARIO

Gli organoidi cerebrali sono strutture neurali derivanti da cellule staminali pluripotenti (PSC) che si auto-organizzano *in vitr*o nelle tre dimensionali (3D). Tutti i protocolli presenti in letteratura si basano sulla crescita degli organoidi cerebrali a partire da cellule staminali embrionali umane (hESC) o PSC indotte (hiPSC), mentre non sono riportati metodi per la generazione di strutture cerebrali 3D a partire da cellule di roditori. Sebbene l'utilizzo di cellule di derivazione umana detenga il maggior potenziale traslazionale, gli organoidi cerebrali derivati da roditori rappresentano uno strumento utile in termini di ottimizzazione dei protocolli, dato il minor tempo richiesto per la loro messa a punto rispetto a quelli di derivazione umana.

In aggiunta al breve tempo richiesto per la loro generazione, gli organoidi murini hanno un ridotto costo di produzione, permettendo dunque di studiare i meccanismi cerebrali disfunzionali e di vagliare diversi composti farmacologici su larga scala prima della loro validazione nei modelli umani. In questo modo gli organoidi prodotti a partire da fonti animali contribuiscono anche alla riduzione del numero di animali coinvolti nella ricerca, abbattendo i limiti etici che ne derivano. Complessivamente, gli organoidi generati da PSCs di derivazione animale sono dunque da considerarsi modelli complementari agli organoidi umani.

L'obiettivo generale di questa tesi di dottorato consisteva nella messa a punto di un protocollo riproducibile per lo sviluppo di organoidi cerebrali murini, nella caratterizzazione del loro sviluppo neuronale ed infine nella loro applicazione per modeling disease and drug testing. Nell'ottica di sviluppare un protocollo di coltura cellulare 3D murino, mi sono inizialmente focalizzata sulla scelta e tempo di utilizzo di fattori di crescita e differenziazione neuronale capaci di indurre nel tempo una progressiva maturazione. In particolare, il protocollo messo a punto prevedeva l'utilizzo di cellule staminali neurali derivate dalla subgranular zone (SGZ), isolate da embrioni E14.5 come fonte cellulare primaria ed il loro mantenimento in una cultura a tre fasi (i.e. espansione, induzione e differenziamento).

La chiave per sviluppare un protocollo solido e riproducibile è stata l'utilizzo di una precisa combinazione e concentrazione di bFGF ed EGF come fattori di crescita e BDNF come fattore di differenziazione per ogni fase del protocollo. Il metodo stabilito ha permesso di ottenere, in un mese, organoidi murini caratterizzati dalla coesistenza di diversi tipi cellulari e da una progressiva maturazione, anche dal punto di vista funzionale. Con l'obiettivo di valutare lo sviluppo e la maturazione neurale del modello murino cerebrale 3D, la sua riproducibilità, l'eterogeneità cellulare, le regioni cerebrali rappresentate e la funzionalità, il modello è stato ampiamente caratterizzato combinando diverse tecniche, dalla valutazione dell'espressione proteica, all'analisi del profilo genico, alle caratteristiche metaboliche e funzionali.

Nella seconda parte del lavoro, gli organoidi cerebrali murini sono stati utilizzati come strumento per studiare *in vitro* la Sindrome di Allan-Herndon Dudley (AHDS) e i difetti del neurosviluppo da questa causati.

L'AHDS è dovuta a mutazioni loss-of-function nel gene che codifica per il trasportatore dell'ormone tiroideo triiodotironina (T3). Ciò determina una mancanza di T3 nel sistema nervoso centrale, determinando un grave ritardo dello sviluppo neurologico nei neonati. Utilizzando gli organoidi murini come modello della malattia, ho indagato le conseguenze a livello dello sviluppo neuronale dovute alla patologia e ho fornito una prova di come gli organoidi murini possono essere impiegati per testare approcci terapeutici.

Per riprodurre lo scenario patologico, il protocollo di generazione degli organoidi è stato modificato andando a rimuovere il T3 dai terreni di coltura. In questo modo, pur non impiegando un modello genetico, siamo riusciti a mimare la mancanza dell'ormone tiroideo conseguente al difetto *in vivo* del suo trasportatore. Il modello patologico è stato poi caratterizzato dal punto di vista morfologico (microscopia in campo chiaro), della composizione cellulare e del fenotipo (immunofluorescenza), del profilo metabolico (analisi di immunoblot) e dell'espressione genica (sequenziamento dell'RNA). Come risultato, è emerso un difetto nello sviluppo degli organoidi AHDS. Abbiamo registrato infatti un tasso di proliferazione più

elevato (cellule $Ki67^+$) rispetto ai controlli, un fenotipo staminale più marcato (cellule $vimentina^+$) e la mancanza dell'organizzazione radiale delle cellule neuronali (cellule DCX^+ e $TUBB3^+$), tipiche del fisiologico sviluppo neuronale.

Sorprendentemente, la mancanza di T3 ha avuto un forte impatto sulla differenziazione delle NSCs, determinando un maggiore indirizzamento verso il fenotipo gliale piuttosto che neuronale. Gli astrociti sono infatti emersi come la popolazione cellulare più rappresentativa, a spese dei neuroni, con uno squilibrio tra la componente neuronale e gliale per un rapporto di 1 a 3. Le analisi metaboliche hanno evidenziato una ridotta fosforilazione ossidativa nei modelli 3D che riproducono la malattia insieme ad un'alterazione del metabolismo degli acidi grassi. Questi dati indicano che gli organoidi che mimano la AHDS presentano un difetto nello sviluppo metabolico. Considerato che il metabolismo mitocondriale è essenziale per la differenziazione e la maturazione neuronale, abbiamo influenzato il metabolismo degli organoidi AHDS per valutare se in tal modo i difetti dello sviluppo neurologico vengano ripristinati. A tal fine abbiamo utilizzato la Nicotinamide Riboside (NR), un precursore del NAD+ ed un farmaco già disponibile in commercio. Pertanto, abbiamo somministrato la NR agli organoidi AHDS, con l'obiettivo di verificare se aumentando il metabolismo ossidativo si possano migliorare i difetti dello sviluppo neurologico tipico della sindrome. Il trattamento con NR ha dimostrato di avere impatto sugli organoidi AHDS, riducendo la proliferazione cellulare e la popolazione staminale rispetto agli organoidi non trattati. Inoltre, i sistemi 3D coltivati in presenza di NR mostrano una migrazione radiale verso lo strato esterno degli organoidi durante la maturazione, sia per i progenitori neuronali che per i neuroni immaturi. Sorprendentemente, lo squilibrio rilevato tra astrociti e cellule neuronali è migliorato dopo l'aggiunta del NR nel mezzo di coltura. Questi risultati suggeriscono il trattamento con NR come nuova strategia per promuovere la piena maturazione neuronale, moderando il metabolismo mitocondriale.

In conclusione, i risultati prodotti durante il mio progetto di dottorato hanno mostrato la possibilità di ottenere organoidi cerebrali murini funzionali, che risultano una piattaforma stimolante per modeling disease e drug screening per nuovi farmaci candidati. Questi risultati dimostrano che gli organoidi murini svolgono un ruolo importante nella comunità di ricerca scientifica come strumenti complementari ai sistemi 3D di origine umana.

ABSTRACT

Brain organoids are *in vitro* three-dimensional (3D) self-organized neural structures, generated from pluripotent stem cells (PSCs). All the published protocols rely on the cerebral organoids' growth starting from human embryonic stem cells (hESCs) or induced PSCs (hiPSCs), whereas no methods are reported for the generation of rodent cerebral 3D structures. Although the human cells hold the greatest translational potential, rodent-derived brain organoids are useful for protocols' optimization, given the shorter amount of time requested for their set-up. Organoids produced from rodent sources are time- and cost-efficient, given the possibility to study dysfunctional brain mechanisms and to screen several compounds before their validation on human-derived models. Altogether, rodent derived 3D systems are to be considered complementary to the human derived organoids.

The overall aim of my thesis was the setting up of a reliable murine brain organoid model, its neurodevelopmental characterization and its application for modeling disease and drug testing. In the first part of the work, I focused on the fine-tuned generation of a murine 3D culture protocol, analyzing the timing and choice of efficient neuronal differentiating factors. We set up a three-phase protocol using SGZ-derived NSCs, isolated from E14.5 embryos as primary cell source. The established protocol allowed to obtain, in 1 month, a standardized method for the growth of murine SGZ-derived organoids, showing dorsal forebrain identity including different cell phenotypes. We extensively characterized the generated model, spacing from protein expression evaluation, whole transcriptome signature, metabolic features and functionality studies with the goal to evaluate the 3D brain murine model's neural development and maturation, reproducibility, cellular heterogeneity, brain region identity and functionality.

In the second part of the work, I exploited the murine cerebral organoid model to study *in vitro* the neurodevelopment defects of Allan-Herndon Dudley Syndrome (AHDS). AHDS is caused by loss-of-function mutations of the gene encoding for the transporter of the thyroid hormone triiodothyronine T3. This determines a lack

of T3 into the CNS, leading to a severe neurodevelopmental delay in infants. By using murine organoids, I investigated the neurological impairment established during the pathology and provided a proof-of-concept of therapeutical approaches, gaining additional insight on the use of murine organoids for drug testing.

To obtain the AHDS-like organoids, we slightly modified the three-step previously established protocol: by removing the T3 from the culture media we aimed to mimic the AHDS pathological scenario. Specifically, we investigated the morphology, cellular composition and phenotype, metabolic profile and gene expression of such model, revealing developmental defects in AHDS-like organoids. They display a higher proliferation rate ($Ki67^+$ cells) compared to the controls, a prolonged stem phenotype (vimentin expressing cells) and the lack of the radial organization of the neuronal cells (DCX^+ and $TUBB3^+$ cells), typical of physiological neuronal development.

Remarkably, the lack of T3 had a strong impact on the NSCs differentiation, determining a major commitment toward the glial lineage rather than the neuronal one. Thus, AHDS-like structures showed an abnormal balance between the neuronal and glial component, with astrocytes emerging as the most representative cell population into AHDS-like organoids, at the expense of neurons. The metabolic investigation highlighted a decreased expression of OXPHOS complexes in AHDS-like organoids and impaired fatty acid metabolism, suggesting that they also showed defect in metabolic development. Given the metabolic impairment found during AHDS-like organoid development, we decided to target mitochondrial metabolism to revert AHDS organoid neurodevelopmental defects. Mitochondrial metabolism it is well known to be essential for neuronal differentiation and maturation and the Nicotinamide Riboside (NR), a NAD+ precursor, is an already available drug to target oxidative phosphorylation. Therefore, we administered NR to the AHDS-like organoids in order to increase the oxidative metabolism and correct the AHDS neurodevelopmental defects. NR treatment reversed the abnormal phenotype, resulting in a reduced cellular proliferation, as well as in a minor stem phenotype of the AHDS-like organoids. Furthermore, NR-supplied 3D systems acquired the ability to perform a radial migration towards the organoids' external layer during maturation both for neuronal progenitors and immature

neurons. Strikingly, the imbalance between astrocytes and neuronal cells was ameliorated after NR supplementation. Those results suggested that NR treatment could represent a new strategy to promote full neuronal maturation in our 3D system, possibly targeting mitochondrial metabolism.

In conclusion, the results produced during my PhD project showed the possibility to obtain functional mouse cerebral organoids, that could be exploited as modeling disease tool as well as high-throughput screening platform for novel candidate drugs. These findings illustrate murine organoids play an important role in the research community as tools, complementary to the human-derived 3D systems.

CONTENTS

1. INTRODUCTION 14

1.1 Organoids 14
1.1.1 Principles of the organoids' formation 16
1.1.2 Cell sources for organoids generation 20

1.2 Brain Organoids 23
1.2.1 Human versus murine brain organoids 24
1.2.2 Protocols for the generation of brain organoids 27
1.2.3 Applications of brain organoids 29
1.2.4 Limits and future perspectives of brain organoids 36

1.3 Allan-Herndon-Dudley Syndrome (AHDS) 39
1.3.1 Models of AHDS 40
1.3.2 AHDS available treatments 43
1.3.3 The role of T3 in neurodevelopment 45

2. AIMS 48

3. MATERIALS AND METHODS 52

3.1 Animals 52
3.2 Neural stem cells extraction from subgranular zone (SGZ) murine tissue 52
3.3 Murine brain organoids generation 53
3.4 Murine Allan Herndon Dudley Syndrome (AHDS) organoid generation protocol 54
3.5 Nicotinamide Riboside (NR) administration in murine AHDS-like organoids 56
3.6 Organoid maximum diameter measurements 56
3.7 Optical Projection Tomography (OPT) and volume measurement in organoids 57
3.8 Viability assay on whole mount organoids 57
3.9 Organoids immunofluorescence assay 58
3.9.1 Immunofluorescence assay on sliced organoids 58
3.9.2 Immunofluorescence assay on whole mount organoids 58
3.10 Tissue immunofluorescence assay 59
3.11 Antibodies 59
3.12 Immunofluorescence image acquisition, analysis and quantification 61
3.13 Fluorescence intensity quantification 62
3.14 RNA sequencing analysis in murine cerebral organoids 62
3.15 RNA sequencing of AHDS-like T3- and control T3+ organoids 66

3.16 DNA extraction and mitochondrial DNA quantification of murine cerebral organoids 67
3.17 Immunoblot assay in murine cerebral organoids 68
3.17.1 Primary antibodies used for immunoblot assay 69
3.17.2 Immunoblot image acquisition, analysis and quantification 69
3.18 Bioenergetic assessment in murine cerebral organoids 69
3.19 Live metabolic assessment in whole mount murine cerebral organoids via seahorse technology 70
3.19.1 Preparation of substrates', inhibitors and uncouplers stocks 70
3.19.2. Three days before the assay 71
3.19.3 The day before the assay 72
3.19.4 The day of the assay 73
3.19.5 Running the assay 74
3.19.6 Normalization of seahorse data via DNA quantification (RNase-treatment) 76
3.20 Intracellular calcium imaging on whole mount organoids 77
3.21 Rabies virus and adenovirus 78
3.22 Quantitative RT-PCR analysis for SGZ-NSCs characterization 79
3.23 Quantification and statistical analysis 80
4. RESULTS **81**
4.1 Development of a standardized and reproducible protocol for murine brain organoids model 81
4.1.1 Generation of the protocol to grow murine brain organoids 81
4.1.2 Murine brain organoids show homogeneous morphology according to the developmental phase 83
4.1.3 Murine brain organoids show reproducible features 85
4.2 Characterization of brain organoid development and brain region identity specification 88
4.2.1 Organoids present neural differentiation and radial migration during the maturation 88
4.2.2 Organoids' neuronal maturation is sustained by the metabolic switch from a glycolytic to an oxidative process 101
4.2.3 Murine brain organoids display neuronal maturation and cellular functionality 109
4.2.4 Murine brain organoids showed dorsal forebrain identity 122
4.3 Murine brain organoids as a model to study Allan Herndon Dudley Syndrome (AHDS) and to identify new drug target 125
4.3.1 Generation of AHDS-like cerebral organoids 126
4.3.2 AHDS-like organoids show a delay in neuronal maturation 129

4.3.3 AHDS-like organoids show an imbalance between glial and neuronal populations 134

4.3.4 AHDS-like organoids show low expression of OXPHOS complexes, impaired fatty acid metabolism and altered mitochondrial dynamics 138

4.3.5 Pharmacological intervention promotes neural maturation in AHDS-like organoids 143

5. DISCUSSION 151

6. REFERENCES 162

INDEX OF FIGURES

Figure 1: Types of cell culture commonly used 15

Figure 2: Self-organization of stem cells 16

Figure 3: Image representing the principles of self-organization. 18

Figure 4: Cell sources for the generation of organoids 20

Figure 5: Human iPSCs applications 22

Figure 6: Applications of brain organoids 32

Figure 7:Assembloids 38

Figure 8: Processes of THs arrival, up-take and metabolism in the brain 46

Figure 9: Representation of mitochondrial development along differentiation of NSC to neurons. 47

Figure 10: V28 24-well Seahorse microplate 72

Figure 11: 24-well sensor cartridge. 73

Figure 12:Organoids' generation protocol 82

Figure 13:Percentage of successful organoids generation, disintegration or no aggregation 83

Figure 14:Morphology and viability of murine brain organoids. 84

Figure 15: Principal components analysis of RNAseq data performed on organoids and on murine cerebral tissues 86

Figure 16: Gene ontology analysis for upregulated genes in mature (32 days) versus early (7 days) organoids. 87

Figure 17: Box plots of GSVA RNAseq data analysis generated based on specific gene list for neural stem cells, neuronal progenitors and mature neurons. 87

Figure 18: Characterization of the starting cells. 89
Figure 19: Organoids' proliferation at different time-points. 90
Figure 20: Stem phenotype characterization of organoids...... 92
Figure 21: Heat map of RNAseq data from organoid samples, generated based on mature neurons gene list dataset. 95
Figure 22: Heatmap of RNAseq data from organoid samples, generated based on astrocytes gene list dataset 97
Figure 23: Characterization of neuronal and glial phenotype. 98
Figure 24: Fluorescence intensity analysis illustrating the expression of markers from the center to the edge of brain organoids. 99
Figure 25: Different cell populations over the total cellular populations' number, expressed in percentage in part-to-whole graphs 100
Figure 26: Organoids' mitochondrial assessment via immunoblot..... 103
Figure 27: Organoids' mitochondrial assessment via seahorse 105
Figure 28: ETC evaluation via seahorse 106
Figure 29: Non mitochondrial respiration in organoids at various time-points .. 107
Figure 30: ECAR evaluation in organoids. 109
Figure 31: Evaluation of neuronal phenotype in organoids. 110
Figure 32: Organoids form synapses..... 111
Figure 33: Organoids form inhibitory and excitatory synapses 113
Figure 34: Heat maps of RNAseq, generated based on inhibitory synapses gene lists 114
Figure 35: Heat maps of RNAseq, generated based on excitatory synapses gene lists 115
Figure 36: Inhibitory/excitatory neurons and glia contribution to synapses' formation. 117
Figure 37: Calcium analysis in organoids along the developmental stages..... 119
Figure 38: Synaptic RABV tracing in mature organoids. 121
Figure 39: Regional signature of brain organoids via transcriptomic analysis... 123
Figure 40: Regional signature of brain organoids via immunofluorescence 124
Figure 41: Organoids do not show ganglionic eminences presence 125

Figure 42: Scheme of the three-phases protocol for the generation of Allan-Herndon-Dudley Syndrome (AHDS) murine organoids. 128
Figure 43: Proliferative and stem signature in AHDS-like and T3+ organoids.. 131
Figure 44: Neuronal progenitors' distribution in AHDS-like and T3+ organoids 133
Figure 45: Neuronal and glial phenotypes in AHDS-like and T3+ organoids….137
Figure 46: Metabolic assessment of AHDS-like and T3+ samples…..……..139
Figure 47: Transcriptomic analysis of T3+ and T3- organoids at 7 days 141
Figure 48: Transcriptomic analysis of T3+ and T3- organoids at 14 days 142
Figure 49: Summary of gene ontology regarding mitochondrial related processes, downregulated and upregulated in T3+ and T3- organoids during the development. 143
Figure 50: Protocol for NR administration in AHDS-like and T3+ organoids... 145
Figure 51: Proliferative and stem signature in AHDS-like and T3+ organoids after NR treatment.. 147
Figure 52: Neuronal and glia phenotypes in AHDS-like and T3+ organoids after NR treatment 149

INDEX OF TABLES

Table 1: Details of the protocol used to generate murine cerebral organoids from SGZ-derived NSCs. 54
Table 2: Reagents contained into the T3+ home-made B27 supplement. 55
Table 3: Details of the protocols applied to grow AHDS-like (T3-) and T3+ murine cerebral organoids. 56
Table 4: Genes related to phenotypes of neural stem cells, neuronal progenitors and mature neurons 64
Table 5: Genes related to phenotypes of astrocytes, excitatory and inhibitory synapses. 65
Table 6: Mito stress assay media composition 70
Table 7: Glycolytic stress assay media composition 71
Table 8: Dilutions/Concentrations of inhibitors and uncoupler for the mitochondrial stress test. 74

Table 9: Dilutions/Concentrations of substrate and inhibitors for the glycolysis stress test 74
Table 10: Organoids' setting for the mitochondrial stress test..... 75
Table 11: Organoids' setting for the glycolysis stress test..... 75
Table 12: Solutions necessary for the DNA-quantification (RNAase-treatment) of organoids after seahorse..... 77
Table 13: List of primers used for SGZ-derived mNSCs' characterization..... 79
Table 14: Upregulated genes related to neuronal differentiation in mature (32 days) versus early (7 days) organoids,..... 94
Table 15: Upregulated genes related to astrocytes specification and maturation in mature (32 days) versus early (7 days) organoids..... 96
Table 16: Upregulated genes related to excitatory and inhibitory synaptic components in mature (32 days) versus early (7 days) organoids..... 116

1. INTRODUCTION

1.1 Organoids

Organoids' technology has developed in the past decades, representing the right compromise between animal -*in vivo*- and two-dimensional (2D) cell -*in vitro*- models. An organoid is defined as a three-dimensional (3D) cell culture system in which the stem cells, cultured in suspension, aggregate and grow in all dimensions, with an organized spatial distribution, mirroring the cytoarchitecture and functions of the *in vivo* organ of interest (Benito-Kwiecinski and Lancaster, 2020).

For decades, biomedical research relied on animal models and 2D cell cultures to shed light on countless basic physiological and pathological mechanisms (Kim et al., 2020; Corrò et al., 2020). Despite being classical models used in research, highly standardized and exploited to unveil many notions regarding development and diseases, there are some limitations that make them not fully reproducible of the human body features. Indeed, extrapolating results from animal models to humans is a major drawback, considering the species-specific gap, making it difficult to address question that are peculiar to the human physiology and disease, mainly when it comes to therapeutic approaches (Eichmuller and Knoblich, 2022). Indeed, specific biological process occurring in humans cannot be replicated in other animal models, for instance brain development, metabolism and the testing of drugs efficacy (Kim et al., 2020). Likewise, 2D cultures, consisting in cells growing in adhesion as a monolayer, are limited by the absence of the tissue cells' heterogeny (Schutgenes and Clevers, 2020) as well as the spatial organization and polarity found *in vivo*. 2D models lack cell-extracellular environment interactions (***Figure 1***) (Edmondson et al., 2014), thus the responsiveness of stimuli is altered as well as cell differentiation and proliferation (Kapalczynska et al., 2018) often owing an homogeneous developmental stage, oppositely to the *in vivo* situation (Pampaloni et al., 2007, Kim et al., 2020).

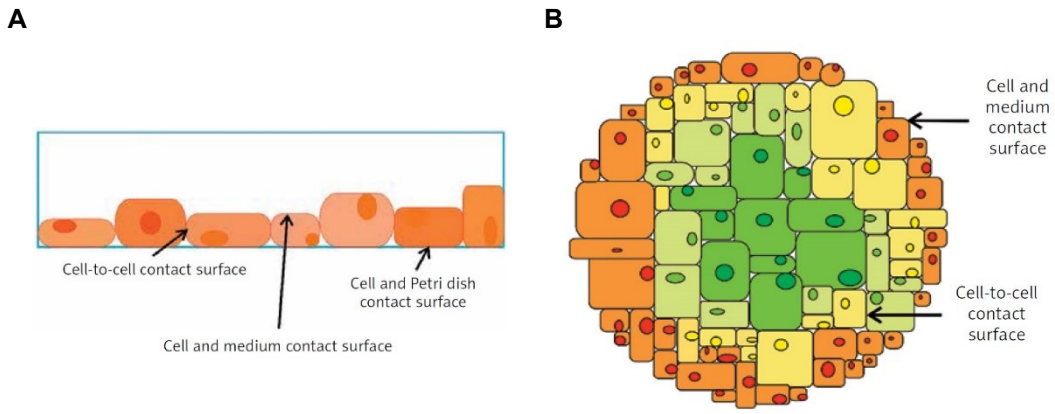

Figure 1: *Types of cell culture commonly used (A) 2D cells grown in a monolayer, adhering to the bottom of the culture dish and (B) a group of cells suspended in the culture medium: the cells are in contact with neighboring cells in all dimensions and with the culture medium. Green, yellow and orange cells represent stem, immature, and mature cells, respectively (B). From Kapałczyńska et al., 2018.*

These issues can be overcome with the advent of organoids. Stem cells inside organoids are coaxed to aggregate and grow in all dimensions, reflecting *in vitro* the tissue or the organ of interest. Three-dimensional structures have a heterogeneous phenotype, since they contain a multitude of organ-specific cells, that self-organize through spatially restricted lineage commitment (Clevers, 2016). Due to the ability of stem cells to self-renew and self-organize, 3D systems resemble the tissue's developmental process and functionality occurring *in vivo* (Simian and Bissell, 2017).

Organoids represent a prominent technological breakthrough, being an important compromise between the animal *in vivo* and 2D cell *in vitro* applications and having the ability to closely acquire a specific cellular organization but in a totally controlled and finely customizable environment.

Aside from being an innovative paradigm in describing and synthetizing the pathophysiologic processes that usually occur in humans, organoids are increasingly employed as a promising regenerative tool within animal transplants, besides representing a valid model for high-throughput drug screens and toxicity predictions (Fatehullah et al., 2016).

1.1.1 Principles of the organoids' formation

As mentioned before, the organoids form due to the stem cells' self-organization capacity, a pivotal aspect for the generation of highly 3D multicellular structures containing different cell types, as seen in human tissues. The "self-organization" capacity is the cardinal concept determining organoids' biology and it depends on three different elements: i) the control of the relative cell position, named "self-assembly"; this feature allows dissociated cells to subsequently reorganize into tissue-like structures ii) the spatiotemporal control of the cell stage, defined as "self-patterning"; and iii) the capacity to promote growth, and remodeling, which is termed "self-morphogenesis". This intrinsic ability of organization strongly depends on the physical and morphological properties of cells, the autologous and exogenous signals that they receive and the mechanical features of the microenvironment. Thus the interaction with the other stem cells and with the extracellular matrix (ECM) is essential in defining the destiny of the stem cells (Silva et al., 2019) (***Figure 2***).

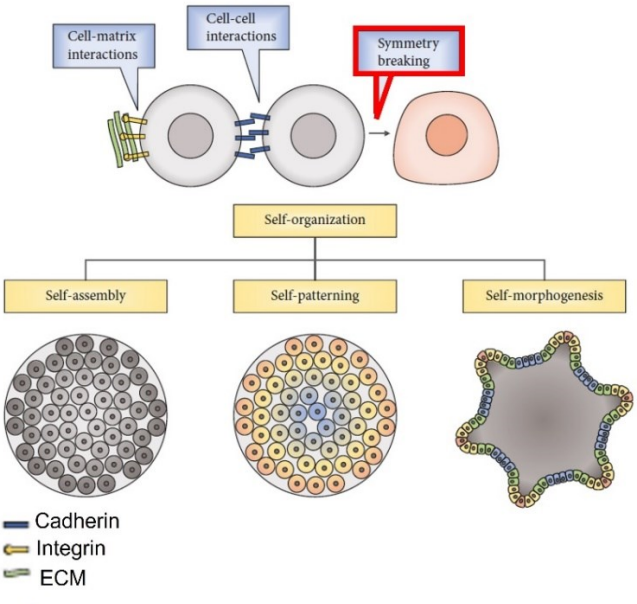

Figure 2: Self-organization of stem cells. *In tissue morphogenesis, the self-organization capacity of stem cells is achieved by a multicellular process involving cell-cell and cell-matrix interactions, as well as symmetry breaking, highlighted by the red box. The self-organization includes a combination of factors, such as self-assembly, self-patterning and self-morphogenesis, which involves the control of the cell position, spatiotemporal control of cell stage and control of tissue mechanics. Adapted from Silva et al., 2019.*

The main goal in the organoids' field is to accurately resemble *in vitro* the biological features belonging to the human tissue, above all the multicellular heterogeneity, high level of organization and overall maturity and functionality. This level of complexity is obtained by strictly controlling the time scale of the protocol used to grow the 3D structures, as well as the media composition and factors administered, crucial to set proper environmental differentiation conditions (Zakrzewski et al., 2019). Strikingly, the organoids' techniques are not transferable across systems, so that the timing and cocktail factors must be specific for each type of organoid, e.g. liver and brain organoids require different culturing condition (Lou and Leung, 2018).

Stem cells strongly depend on their surrounding environment for determining their identity (Fauchs et al., 2004). Indeed, stem cells maintain an undifferentiated state when they are physically anchored to the ECM. Once the stem cell is displaced and loses contact with the ECM is committed to exit the niche and to differentiate, breaking the symmetry division required for maintaining a stem phenotype. Concurrently, this requires a replenishment of the niche via self-renewal.

The niche homeostasis is maintained by sophisticated mechanisms that control the survival, self-renewal and differentiation of stem cells through local and systemic signals arriving to the niches (He et al., 2009).

Indeed, the stem cell population is a dynamic system, receiving both biochemical and biophysical stimuli from the microenvironment. Biochemical information can include autocrine signals (secreted and received by the same cell that produced them) or/and juxtacrine and paracrine signals, received from adjacent or neighbouring cells. Biophysical signals are mediated by cell–cell contact and by interactions with the ECM (Zakrzewski et al., 2019). Systemic information is represented by long-range signals, such as circulating hormones, cytokines, and/or neural activity, that regulate stem cell activity according to physiological demands (He et al., 2009).

As already stated, self-assembly is a critical initial step for the generation of many organoids. While several types of stem/progenitor cells have demonstrated an

intrinsic capacity to "self-organize" into 3D tissue-specific organoids (Takebe et al., 2012; Takebe et al., 2015), current approaches have little knowledge, thus poor control, over the factors determining the aggregation process (e.g., aggregate size, shape, formation's kinetics). This represents a limit for the optimization of stem cell expansion/differentiation processes and makes it difficult to identify the necessary conditions for organoids' formation (Xie et al., 2017).

Indeed, the technology behind organoids' methods is based on many studies trying to understand tissue patterning during development, in which tissues were dissociated and reaggregated to examine the movements of cells *in vitro*. The results show that cells can segregate in a process called "cell sorting out", to form structures resembling the *in vivo* ones. Moreover, spatially restricted cell-fate decisions also contribute to the process (***Figure 3***): stem cells give rise to progenitors, that, because of spatial constraints and/or division orientation, are forced into a more superficial position that promotes their differentiation. So, it seems that the basis of self-assembly resides in the segregation of cells with similar adhesive properties and in spatially restricted progenitor fate decision (Lancaster and Knoblich, 2014).

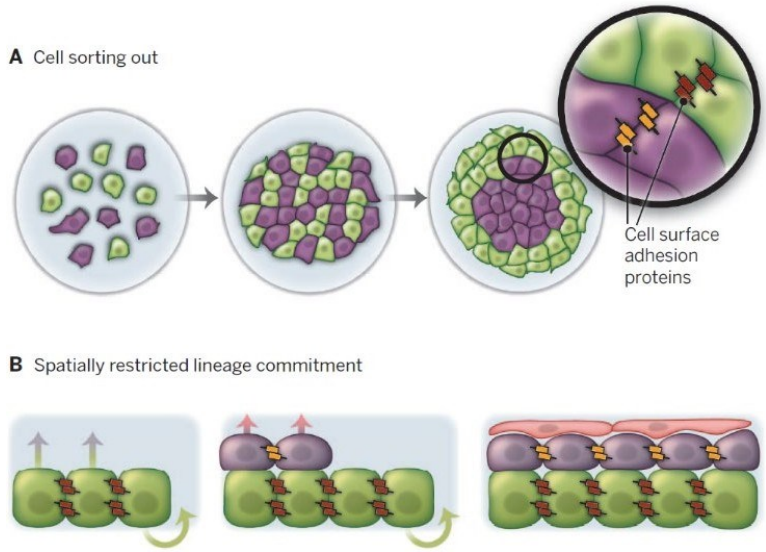

Figure 3: *Image representing the principles of self-organization. (A) "Cell sorting out" describes the movement of cells into different domains. Different cell types (purple or green) sort themselves based on different adhesive properties conferred by their differential expression of distinct cell adhesion molecules (brown or orange bars in the magnified image). (B) Spatially restricted cell-fate decisions determine differentiation, linked to a more superficial position of the cells:*

progenitors (green) originate progeny (purple), which differentiate, due to spatial constraints of the niche. These cells can generate more differentiated progeny (pink), further displaced from the contact with the ECM. From Lancaster and Knoblich, 2014.

Self-organization in organoids is a spontaneous process, that can result in variability in the morphology between various areas of the tissue and between different batches. The variability is also due to the lack of the typical axes formation that guides regional development. Importantly, self-organization may originate abnormal tissue architecture. Such issue may be tackled using extracellular matrices or biomaterials. As shown by the pioneer work by Sato et al. in 2009 and later by Lancaster's group (Lancaster et al., 2014), providing an ECM-like component during the organoids' generation can precisely guide them to a desired cellular architecture, to resemble more accurately the *in vivo* conditions.

Another decisive mechanism that allows organoids to mimic the *in vivo* scenario is the symmetry breaking (see ***Figure 2,*** red box). This phenomenon is essential during the animal development phase that precedes pattern formation, allowing a higher morphological and functional specialization. *In vivo*, symmetry is broken at the single cell level, where the cellular cytoskeleton and membrane-associated proteins are redistributed to create apicobasal polarity.
Symmetry breaking can be achieved by an initially homogeneous morphogen distribution, which can turn into a concentration gradient due to reaction-diffusion. In a reaction-diffusion model, the self-organization capacity of cells leads to symmetry breaking, activated by a stochastic disturbance of the system without a requirement of a dominant "master factor" (Wennekamp et al., 2013). Therefore, cell characteristics, including gene expression, cell polarity and local interactions between cells, can by themselves be responsible for lineage establishment. Reported studies already demonstrated that an uniform aggregate of stem cells is capable to originate a high level of organization, comparable to what is observed in native tissues. Some organoid models with minimal but sufficient complexity are able to undergo spontaneous symmetry breaking in the absence of spatial cues; in this case, a specific pattern is created including for example rostral-caudal

polarization in cortical serum-free floating culture of embryoid body–like aggregates with quick reaggregation (SFEBq) (Takata et al., 2017).
Therefore, symmetry breaking events can be attained *in vitro* by the addition of a single morphogen, through a diffusion-reaction mechanism, or by using more sophisticated bioengineering approaches to create symmetry breaking based on local morphogen delivery.

1.1.2 Cell sources for organoids generation

The establishment of organoids starts mainly from two major distinct cell sources: pluripotent stem cells (PSCs), including embryonic stem cells (ESCs) and induced PSCs (iPSCs) and tissue-specific adult stem cells (ASCs) (***Figure 4)***. Choosing an appropriate starting cell population is the key for the organoid's generation, since every cell line follows different self-patterning and developmental pathways (Azar et al., 2021; Rauth et al., 2021).

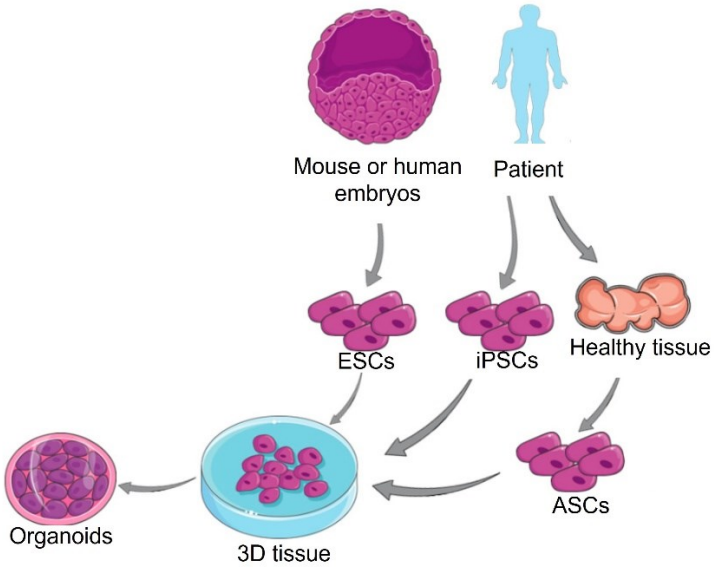

Figure 4: *Cell sources for the generation of organoids. Adapted from Azar et al., 2021.*

ESC-derived organoids are complex and might include mesenchymal, epithelial and, in certain instances, endothelial constituents. ESCs are briefly present in the early human or mouse embryo, a few days after fertilization. These ESCs have two

crucial characteristics: indefinite renewal and pluripotency, meaning they can be grown indefinitely and give rise to all cell types. Murine ESCs (mESCs) were isolated for the first time in 1981 from the inner cell mass (ICM) of a mouse blastocyst (Romito et al., 2016; Smith, 2001). However, in 1998, the first human ESCs were isolated from *in vitro* fertilization blastocysts (Thomson et al., 1998), marking a new era in the field of regenerative medicine. hESCs are collected from early-stage human blastocysts (Liu et al., 2020). Human ESCs-derived organoids include retinoblastoma (Liu et al., 2020) and retinal organoids (Wang et al., 2022), while organoids derived from mESCs include gastric organoids (Noguchi and Kurisaki, 2017) and heart organoids (Lee et al., 2020).

Considering PSCs are obtained from human and animal embryos at the blastocyst stage, organoids derived from this cell source consist in differentiating cells towards lineage-specific progenitors that will give rise to the tissue-specific organoid, when cultured in conditions that mimic the *in vivo* developmental processes. PSCs undergo unlimited self-renewal, while maintaining the pluripotency (McCauley and Wells, 2017). Human PSCs represent a great steppingstone for investigating physiological and pathological mechanisms, since they derive from human embryos. However, the destruction of the embryo raised strong ethical concerns, that hindered human PSCs employment for research purposes (Vazin and Freed, 2010; Azar et al., 2021).

The debate around human PSCs was largely circumvented in 2007, by the advent of the human induced PSCs (iPSCs) technology (Takahashi et al., 2007). The derivation of iPSCs sparked widespread enthusiasm for the development of new organoids' models of human development and disease, opening new perspectives for regenerative medicine and generating tools for preclinical studies (Lehmann et al., 2019). iPSCs are obtained by reprogramming an adult somatic cell inducing a pluripotent status by forcing the expression of a specific set of transcription factors (i.e. SOX2, c-Myc, KLF4, OCT3/4), typically expressed during the pluripotent stage. Once reprogrammed, adult cells can be differentiated into the desired specific cell types. iPSC technology set the basis for disease modeling and personalized

medicine, allowing the generation of patient-specific stem cells, exploited to produce 3D structures (Kim et al., 2020) (***Figure 5***).

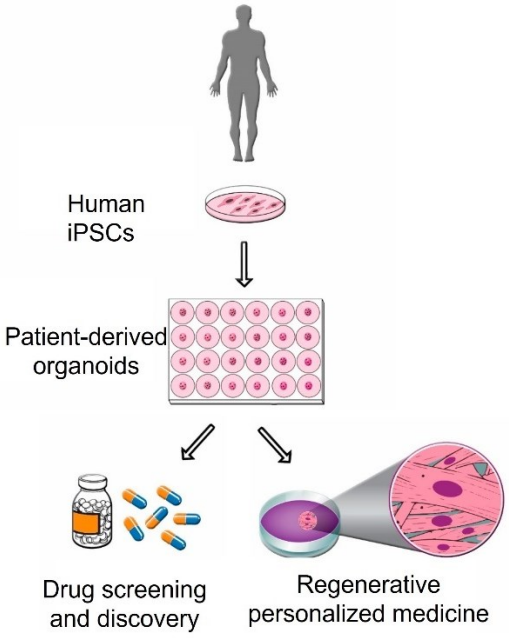

Figure 5: *Human iPSCs applications. Schematic use of human iPSCs-derived organoids for various biomedical and clinical applications including drug screening and discovery and regenerative medicine among many others. Adapted from Azar et al., 2021.*

The last source to consider is ASCs, that are undifferentiated cells among differentiated cells in a tissue or organ. ASCs have a limited differentiation potential and their primary roles are to maintain tissue homeostasis and, to some extent, to replace cells dead due to injury or disease (Ferraro et al., 2010). Equally, ASCs can be cultured in the presence of niche factors that maintain the stem cells in an undifferentiated state while allowing stem cell differentiation. ASCs can be isolated from biopsies of the organ of interest, from healthy people or patients. As a result, the cultured stem cells can generate ASCs-derived organoids. The main drawbacks of establishing ASCs-derived organoids are represented by the limited access to the tissue and the knowledge of the specific niche requirements for their culture. The iPSC line, instead, once established from a patient, can be used to repeatedly generate different tissue models without any time limit. Conversely to ASCs-derived organoids, iPSCs 3D structures resemble the fetal tissue stage, specifically

the embryo's early post-implantation, hardly mirroring the adult tissue stage. This aspect makes iPSCs-derived organoids an excellent system for studying organogenesis and developmental events (Rauth et al., 2021).
As far as ASCs organoids are regarded, the first milestone was represented by the development of small intestinal organoid, starting from murine small intestine cells and crypts (Sato *et al., 2009)*. Based on this method, organoids from human ASCs have been established from colon, stomach, liver, pancreas, lung, prostate, mammary gland, salivary gland, fallopian tube, taste buds and esophagus (Clevers, 2016) as well as from primary tumor tissue (Watanabe et al., 2017).

PSCs exposed to specific combinations and concentrations of growth factors and signals allow to obtain *in vitro* 3D organoids, similar to organs of all three germ layers. Some pathways are crucial during embryogenesis, specifically Wingless/Integrated (Wnt), Fibroblast Growth Factor (FGF), retinoic acid and Bone Morphogenetic Protein (BMP), since they define the patterning of the specific organ. The timing, dose and combination of these factors can have very different outcomes, mirroring various organs, such as the brain, eyes (Nakano et al., 2012), kidney (Takasato et al., 2014), lung (Dye et al., 2015), stomach (McCracken et al., 2014) and intestine (Spence et al., 2011).

1.2 Brain Organoids

Among the several organs that could be reproduced *in vitro* by organoids technology, the capability to resemble the *in vivo* cerebral tissue hold great interest since it allows the study of the intricate mechanisms of brain development, the reproduction of different neuronal disorders and the screening of drugs in a preclinical model. These brain-like structures should include fetal brain-like traits as cerebral folding (Li et al., 2017), cell heterogeny, omics expression profiles (Amiri et al., 2018, Camp et al., 2015) as well as neuronal function. Nonetheless, important brain-proper features, including the establishment of distinct cortical layers or layer-specific dendritic morphology and axonal projection patterns, are far to be correctly described with this technology.

The study of PSCs as source for the production and differentiation of neuronal cells started about 15 years ago. Earlier *in vitro* embryonic stem cell-derived neuronal populations were able to capture several aspects of the developing brain, including the organization of cells into rosettes with an inner lumen reminiscent of the neural tube, a preserved apical-basal polarity, production of layer-specific neurons and some degree of progenitor cell diversity (Elkabetz et al., 2008, Chambers et al., 2009, Shi et al., 2012). These neuronal models, albeit pioneering, had no spatial architecture resembling complex organ structure and shape like brain.

The problem was tackled with the introduction of brain organoids: preserving the features of neural rosettes, their complex 3D organization includes a broad variety of cell populations i.e. neuronal progenitors, mature neurons, astrocytes and interneurons. Eiraku and colleagues' works are considered milestones in the study of neuronal 3D cell structures: breaking away from the conventional 2D culture systems, in 2008 they showed that ESCs could be steered to differentiate into neuroepithelial tissues when cultured as floating aggregates in a serum-free medium (serum-free floating culture of embryoid body–like aggregates with quick reaggregation, hereafter termed SFEBq culture) (Eiraku et al., 2008).

Starting from this pioneering study, nowadays a broad range of cerebral organoids can be produced, either resembling macro brain identities or specific brain regions, useful for modelling different aspects of human brain complexity, development and functionality, though they are still not totally free from constraints: postnatal traits, shape, dimensions and reproducibility have to be improved.

1.2.1 Human versus murine brain organoids

The majority of literature data describe the growth of organoids starting from human cell sources. Surely, they are likely to be the best model to understand human biology. Specifically, the technology of iPSCs holds the greatest translational potential, being derived from healthy or diseased tissue of patients, paving the way to precision medicine and clinical studies. Nevertheless, organoids generated from murine sources are not to be overlooked, since they are complementary to the human 3D systems.

Brain organoids have rapidly gained popularity in exploring brain development and disease, but it must be considered that the 3D technology is at an early stage. The current human-derived protocols used to grow brain organoids are not optimal, lacking reproducibility, indeed the overall efficiency and consistency of differentiation can vary considerably between batches of organoids (Qian et al., 2019). Therefore, there is a continuing need for new and improved protocols that will consistently produce high quality organoids that closely resemble embryonic brain.

Early protocols for growing brain organoids were mainly pioneered initially using mouse embryonic stem cells (ESCs) (Eiraku et al., 2008; Nasu et al., 2012; Watanabe et al., 2005) and methods for the generation of brain organoids from human stem cells soon followed (Kadoshima et al., 2013; Lancaster et al., 2013; Paşca et al., 2015; Qian et al., 2016; Quadrato et al., 2017).

Murine derived organoids are well suited to improve protocols for the production of both cerebral organoids as well as region-specific organoids. Indeed, the protocol applied to originate thalamus-like organoids from human iPSCs (Xiang et al. 2019) was closely based on one originally designed using mouse ESCs (Shiraishi et al., 2017).

Another advantage in employing murine organoids is that they do not require expensive reagents necessary for the human PSCs, thus murine stem cells represent an excellent starting source to set up protocols before translating them to human-derived stem cells (Marshall and Mason, 2019). Indeed, improving protocols can often represent a huge challenge, considering all the variables that needs to be optimized. To grow organoids, many factors are needed, such as signaling molecules and each of them must be added at the right time and concentration, for the correct duration. Setting all these aspects using human cells is both time-consuming and expensive, so exploiting mouse stem cells in the first instance is results time and cost-efficient. It is possible that the precise timings and duration of exposure to signaling molecules and other factors will vary between mouse and human (O'Leary et al., 2007; Paridaen and Huttner, 2014; Rash and Grove, 2006; Tan and Shi, 2013; Taverna et al., 2014). However, a robust protocol developed in mouse is likely to provide a valuable starting point for designing a human protocol.

Additionally, mice brain holds stem cells niches that can be exploited for organoids' growth. Indeed, the most well-known stem cells are found in the subventricular zone of the lateral ventricles and the subgranular zone of the hippocampus, found in the embryos but also persisting in the postnatal and adult brain (Pino et al, 2017, Yang et al., 2011; Encinas, 2008; Lazutkin et al., 2019) Recently a new stem cell niche has been identified, residing into the meninges (Bifari et al., 2017; Decimo et al., 2012; Pino et al., 2017; Decimo et al., 2021). These sources are extremely accessible, thus facilitating the research when it comes to organoid production.

Considering organoids retain their species-specific developmental timescales, mouse brain organoids can be grown in a much shorter period than human ones. In fact, accordingly to human development timeline (Budday et al., 2015), hiPSC-derived brain organoids require long time (months) and high production cost for their *in vitro* generation that may hinder their potential application in large-scale studies (Ciarpella, Zamfir et al., 2021).

Another advantage of murine organoids, not to be neglected, is the huge amount of available data generated on murine brain development. Furthermore, lots of mutant *in vivo* phenotypes are described in detail, as well as their consequence on the brain. This aspect makes the generation of murine organoids reliable, since 3D structures can be compared to the *in vivo* evidence, both in healthy and disease conditions. Specifically, organoids presenting mutant genes can reliably present the same regulatory mechanisms found in mutant mice (Marshall and Mason, 2019). One experiment was performed comparing the effects of the same mutation in mouse organoids to those in the equivalent mutant mouse model, investigating the role of the transcription factor Foxg1 (Mall et al., 2017). Murine organoids were applied also to the study and validation of CRISPR/Cas9 technology, efficiently inactivating several genes involved in brain development (Acosta et al., 2018).

Notably, rodent 3D systems can significantly reduce the number of animals used in neurodevelopmental research. As mentioned before, one of the main benefits in using organoids is their accessibility, compared to the employment of intact embryos. Indeed, especially at the earliest stages of brain development, murine

embryos are particularly inaccessible and human ESCs employment raises ethical concerns (Guasch and Fuchs, 2005; Azar et al., 2021). In this context, murine organoids emerge as useful tools to study the normal neurodevelopment, allowing to investigate the behavior of the individual cells composing the 3D structure. For instance, nuclear migration was tracked in mouse ESCs-derived organoids (Nasu et al., 2012) and the rate of neurogenesis had been evaluated in brain organoids grown from murine cortical progenitor cells expressing a reporter transgene (Kosodo et al., 2017). Gene function can be studied using chimaeric murine organoids, formed by both mutant and control ESCs. This method was used to unveil the mechanisms determining the gradients of sonic hedgehog (Shh), involved in the development of the nervous system (Guo and Roelink, 2019).

Mouse brain organoids have also been employed to study the establishment of the antero-posterior pattern in the early neuroectoderm (Takata et al., 2017). A better understanding of how the antero-posterior axis is achieved *in vivo* can led to the generation of region-specific brain organoids.

To sum up, an initial optimization of protocols for brain organoid's growth using murine-derived stem cells can result very promising before the translation to human cells. This is particularly significant for the brain, considering its higher complexity compared to other organs in the human body.

Additionally, murine-derived organoids can be very precious tools not only in physiological research, but also in regenerative medicine, modeling disease and therapeutical approaches development (Azar et al., 2021)

1.2.2 Protocols for the generation of brain organoids

How far can human brain development be recapitulated *in vitro*? Answering to this challenging question, paired to a deep understanding of the principles guiding self-organization of these brain-like structures as well as the molecular cues involved in specific brain regions development and commitment will help us to exploit their potential in toto and to provide key insights for tackling their actual constraints.

Accordingly, protocols for human brain organoids generation have been inspired from *in vivo* patterning processes to recapitulate neurodevelopment in a dish.

Brain organoids generation approaches can be distinguished in two major categories: patterned and self-patterning protocols.

Self-patterned protocols rely on the intrinsic PSCs ability to aggregate and differentiate autonomously, without the guidance of external patterning factors for a specific stem cell lineage commitment. In particular, unguided organoids methods utilize basic fibroblast growth factor (bFGF) and retinoic acid during hPSCs reaggregation, with the establishment of self-patterning morphogens gradients that drive neuroectodermal identity, followed by the generation of whole-brain organoids exhibiting a variety of identities ranging from forebrain, midbrain and hindbrain, to retina and choroid plexus as well as different glial cell types and small populations of non-ectodermal cells (Lancaster et al., 2013). However, the propensity and efficiency of different hPSC lines to differentiate into ectoderm and resulting cortical cell types can vary, with downstream issue in creating comparable organoids derived from different PSC lines. The stochastic nature of cellular diversity in self-patterned organoids makes this approach not well suited for disease modelling and drug screening applications.

A higher regional accuracy and cellular reproducibility can be achieved with patterned protocols. In these guided organoids' generation methods, both applications of growth factors and morphogens are used during the differentiation process, coaxing PSCs to form cells and tissues resembling certain brain regions. A shared trait among most patterned protocols is an initial inhibition of the SMAD pathway, principal promoter of the generation of epidermis over neural ectoderm. Once recreated *in vitro*, early ectoderm is prone to generate dorsal forebrain fates (Espuny-Camacho et al., 2013); leveraging these process, different protocols for cortical organoids were established (Pasca et al., 2015, Qian et al., 2016, Bagley et al., 2017, Kadoshima et al., 2013, Velasco et al., 2019).

Cortical organoids, starting from the formation of neural-tube-like neuroepithelial structures, present diverse cortical cell types as observed in the *in vivo* human forebrain: inner and outer radial glia, intermediate progenitors, cortical neurons, astrocytes, and oligodendrocytes. Other patterned protocols had been establishes

for the differentiation of PSCs into various brain regions such as thalamus (Xiang et al., 2019), hippocampus (Sakaguchi et al., 2015), spinal cord (Winanto et al., 2019) and choroid plexus (Pellegrini et al., 2020).

Generally, these directed differentiation approaches do not recapitulate multiple brain regions or the long-range connectivity between them, which are required for refinement and specification of cells within a developing brain. Moreover, when a bath of morphogens is used to direct PSCs toward a neuroectodermal fate, non-ectodermal lineage cells are omitted, like microglia and endothelial cells, these last forming the vascular system. Non-ectodermal cell types play a critical role in brain development and their absence impacts negatively the human brain organoid development (Del Dosso et al., 2020).

1.2.3 Applications of brain organoids

Neurodevelopmental studies

Since their birth, brain organoids have been extensively studied as *in vitro* models of brain development (***Figure 6***), due to their ability to mimic the cellular architecture as well as the spatiotemporal formation of heterogeneous neural cell types found in the *in vivo* counterpart. Particularly, brain organoids contain multiple ventricular zone (VZ)-like rosettes regions, characterized by stem cells expressing radial glial markers genes; when neurogenesis occurs early, deep-layer neurons are generated followed by lateral generation of upper-layer neurons, but also astrocytes, oligodendrocytes and interneurons precursors are observed (Liour and Yu, 2003).

Several studies obtained good but still restricted spatial layering of neuronal cells (Lancaster et al., 2013, Lancaster and Knoblich, 2014, Qian et al., 2016, Pasca et al., 2015, Shi et al., 2020); furthermore, gene expression analyses were performed in various works using microarrays (Pasca et al., 2015), RNA-seq (Mariani et al., 2015, Qian et al., 2016, Luo et al., 2016) and single-cell RNA-seq (Camp et al., 2015, Quadrato et al., 2017, Pollen et al., 2019), showing that organoids developed from different protocols replicate a fetal brain environment, generating cells that share transcriptomics profiles restricted to the early fetal neocortex.

Recently, Gordon and colleagues sustained human cortical organoids (hCOs) in culture for a very-long period, more than 400 days and analyzed their gene expression and epigenetic profiles at different time points; after 250-300 days *in vitro*, many transcripts were correlated to early mammal postnatal stages. Although moving to more than 400 days a higher maturation level was achieved, a continual time-dependent aging in hCOs was registered and the variability of the organoids' differentiation was increased. For the first time, all these data indicate that brain organoids could be used to model different aspect of aging, especially those related to the onset of neurodegenerative events (Gordon et al., 2021).

Organoids aim to revolutionize the technical approach used so far in the study of organisms' development. Human organogenesis studies require the assessment of tissues that simply cannot be accessed experimentally, and thus their development, functionality and disease remain underexplored. Moreover, the rare available embryonic tissue biopsies give only a snapshot of the extended developmental processes, especially regarding central nervous system (CNS) (Arlotta and Pasca, 2019). The usage of 3D cell culture systems were exploited to mimic and highlight cellular behaviors in tissue development like brain (Lancaster et al., 2013) and retina (Eiraku and Sasai, 2011).

Modeling disease

Brain organoids permit modeling of neurological disorders, often studied with some constraints due to the lack of human brain tissue for research, the heterogeneity of disease traits among individuals and the inability of current model systems to recapitulate properly human diseases phenotypes (Amin and Pasca, 2018).

With the advent of patient iPSC-derived cerebral organoids, the phenotypes and mechanisms underlying neurodevelopmental and neuropsychiatric disorders started to be accurately reproduced *in vitro* (***Figure 6)***. Among the first, Lancaster group in 2013 modeled microcephaly patient-derived cerebral organoids, characterized by smaller size, reduced progenitor zones, decreased neurogenesis and an abnormal neuronal activity, compared to controls. Contrariwise, organoids derived from

PTEN-knockout hESCs exhibit increased surface area, proliferation and volume, all features clinically closed to macrocephaly (Li et al., 2017).

Mutations and molecular mechanisms related to schizophrenia were investigated using brain organoids: DISC1-mutated patient-derived cerebral organoids exhibited a delay in cell cycle progression (Li et al., 2017) and lacked ventricular-like structures with a decreased progenitor proliferation (Srikanth et al., 2018).

Studies conducted by Wang enabled to get many insights about Autism Spectrum Disorders (ASD) genetic background: cerebral organoids derived from iPSCs with heterozygous knockout of CHD8, a major risk factor for ASD, showed dysregulation in genes that play a critical role in GABAergic interneurons differentiation (Wang et al., 2017); COs were also exploited to replicate *in vitro* a calcium channel mutation found in Timothy Syndrome (characterized by ASD), accompanied by calcium signals defects and delayed GABAergic interneuron migration (Birey et al., 2017).

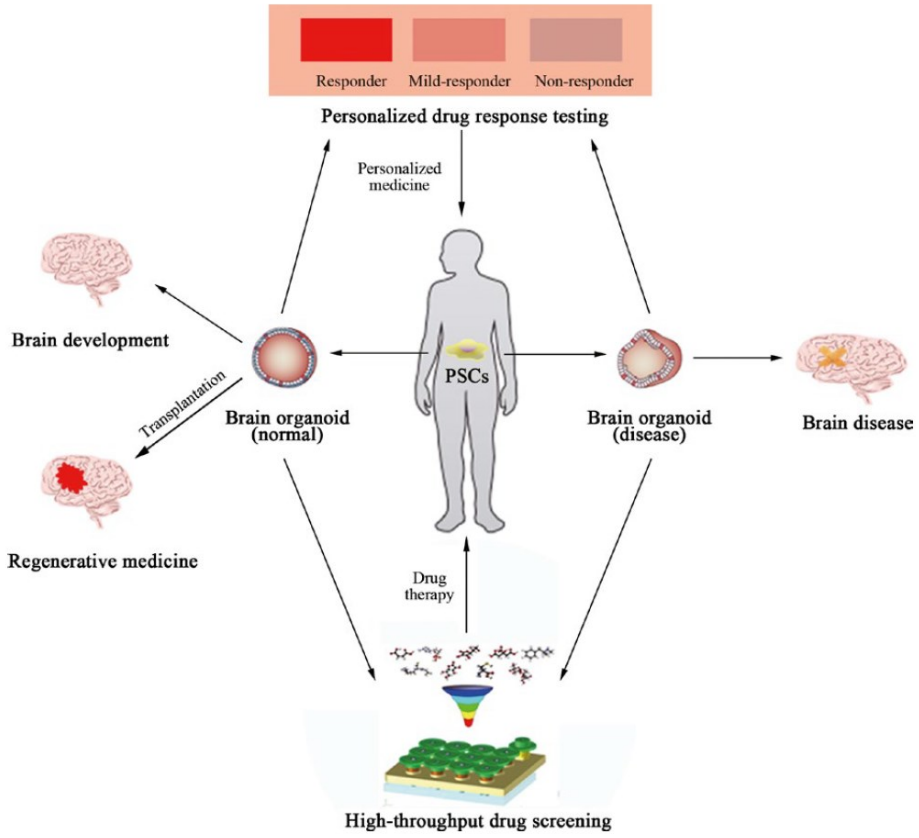

Figure 6: *Applications of brain organoids. Pluripotent stem cell (PSC)-derived brain organoids can be applied to study brain development and transplant into brain injury site to repair injured tissues as a regenerative medicine therapy. Disease models of brain organoids can be used to study brain diseases. Both normal and diseased brain organoids have a great potential application in personalized medicine through personalized drug response testing and contribute to drug discovery and therapy through high-throughput screening to test drug efficacy and toxicity. From Wang et al., 2017.*

In literature, an increasing number of manuscripts attest the reliability of 3D cerebral culture systems in reproducing neurodegenerative disorders, hitherto massively investigated with approaches ranging from animal models to 2D neuronal cultures, all of them far to be free from compromises. Alzheimer's disease patient-derived brain organoids harboring amyloid precursor protein (APP) duplication or presenilin (PSEN) mutations were able to develop age-dependent extracellular β-amyloid aggregations, hyperphosphorylated tau protein and endosome abnormalities (Raja et al., 2016); treatment with β- and γ-secretase inhibitors reduced amyloid and tau pathology. Proper Parkinson's disease' α-

synuclein aggregation (Kim et al., 2019) and decreased dopaminergic neuronal population (Smits et al., 2019) were showed in midbrain organoids generated from mutated iPSCs.

Adding pathogens in the culture medium, infectious diseases can be studied with brain organoids. Zika virus (ZIKV) infection of neuronal progenitor cells and astrocytes was registered in exposed brain organoids cultures, with subsequent cell death, failed cortical layering and reduced proliferative zones, confirming the microcephalic phenotype observed in affected infants (Qian et al., 2017, Watanabe et al., 2017).

Recently, many research groups exploited different region-specific brain organoid protocols to investigate the Sars-Cov-2 virus neurotropism. Epithelial cells of choroid plexus were determined as crucial in leading a productive viral infection, followed by cell death, increased inflammation and decreased cerebrospinal fluid (CSF) production (Jacob et al., 2020). This tropism was also confirmed by Lancaster, using CSF-producing choroid organoids (Pellegrini et al., 2020).

Organoids as disease modeling tools are widely appreciated for the study of different genetic disorders and several organoids model have been established to investigate these pathological states, including retinitis pigmentosa with retinal organoids (Sharma et al., 2017), lissencephaly, Rett syndrome, Timothy syndrome and ASD represented by cerebral organoids (Bershteyn et al., 2017, Gomes et al., 2020, Birey et al., 2017, Mariani et al., 2015). Patient-derived iPSCs allow the generation of specific cell lines, useful for recreating accurate 3D structures models holding the mutated genetic profile of the disease as well as the emblematic tissue or organ-like phenotypic impairment.

Regenerative medicine

Such *in vitro* brain-like structures in the future could play an essential role as committed and structured cell source for human neuroregenerative purposes, like transplants (***Figure 6***). Human cerebral organoids have already been grafted in animal hosts, like mouse, rat and monkey, with striking results. In 2018, for the first time, Mansour and colleagues transplanted human brain organoids in mice: they

noted progressive neuronal differentiation and maturation, gliogenesis, integration of microglia and grow of axons to multiple regions of the host brains; functional neuronal networks and blood vessels in the grafted organoids were observed as well (Mansour et al., 2018). Similar results were obtained also by Zou et al., which verified a higher survival rate of organoid grafts compared to neural progenitor cell (NPC) ones, with a robust multilineage neuron differentiation and the establishment of host vascular system inside transplants (Daviaud et al., 2018).

Starting from Pham's work (Pham et al., 2018), Wang group provided a vascularized brain organoid model (vOrganoid), using human umbilical vein endothelial cells (HUVECs) to form an empty but complex vessel system. After the grafting of vOrganoids in mice, the researchers surprisingly detected host blood streaming in HUVECs derived blood vessels, supposing a perfect functional integration between graft and host blood systems (Shi et al., 2020). Finally, extensive axonal projections along the corticospinal tracts from transplanted human cerebral organoids in mice and monkeys were recently showed by Takahashi (Kitahara et al., 2020). All these enthusiastic results will contribute to the development of a cell-replacement therapy for brain injury and stroke in human, far from being feasible for the time being.

High-throughput drug screening

Brain organoids modeling pathological conditions have been increasingly used as high-throughput screening platforms for novel candidate drugs (***Figure 6***). Organoids are breaking the rules in the pharmacology and toxicology environment: their easy manipulability and scalability are ideal traits for high throughput drug screening. The usage of animal models in preclinical studies may be limited in the next years: the *in vitro* human organ-like representation offered by organoids could improve the predictability of drugs efficacy or side effects.

For instance, Park and colleagues used more than 1300 iPSC-derived cerebral organoids from 11 AD-affected participants to build a high-content screening (HCS) system and test blood-brain barrier-permeable FDA-approved drugs, providing a strategy for precision medicine (Park et al., 2021). Cortical organoids

mimicking an epileptic phenotype were massively tested in a 3D high-throughput screening (HTS) platform, matching drug treatments with calcium imaging assays; a multiparametric analysis, focusing on calcium oscillation frequency and peak irregularities, was used to rank the compound's rescue effect (Negraes et al., 2021).

Drug candidates for treating ZIKV infection were successfully tested in human brain organoids and prostate cancer organoids, generated from castration-resistant Nkx3.1-expressing cells, have also been tested in modeling of a drug response (Chua et al., 2014).

In cancer research various therapeutic approaches are benchmarked using organoids, like hyperthermia therapy (Ubink et al., 2019) and immunotherapy (Gronholm et al., 2021). Tumor organoids, due to their organ-resembling nature, are a more reliable model than 2D cell cultures: the different cell surface receptors' organization, matched with *in vivo*-like cell density, proliferation rate and physiological conditions usually lead to a lower but much more *in vivo*-closed treatments success rate; these aspects give to scientists and clinicians novel insights for the study of increasingly innovative and effective therapies.

Viral and bacterial infections are well modelled with 3D cell cultures. Cerebral organoids are being used to elucidate the causes of Zika virus-associated microcephaly (Qian et al., 2017) as well as the neurotrophic effect of Sars-Cov-2 virus on different neuronal cell populations (Pellegrini et al., 2020). Human airway organoids are suitable models for the study of respiratory viruses. A valid example is the generation of human bronchial organoids for SARS-CoV-2 virus research (Fang et al., 2021); noroviruses and rotaviruses are studied by using human intestinal organoids (Saxena et al., 2016).

Genetic engineering

Reproducing all these diversified and currently with no treatments diseases is essential: the major part of these being rare pathologies, condensing them in an *in vitro* and totally controlled model is the turning point for developing cutting edge therapeutic technologies.

In this context genome editing has been playing an essential role. Combining organoid systems with CRISPR–Cas9 genome editing broadens the applications of the organoid system in many ways. For example, this system has been used to model monogenic disorders such as cystic fibrosis. Human gut organoids with F508del, causing misfolded Cistic Fibrosis Transmembrane Regulator (CFTR) channel protein that leads to rapid degradation, were precisely corrected into the normal sequence by CRISPR–Cas9; engineered organoids restored channel activity of CFTR *in vitro*, showing the causal relationship between the mutation and disease phenotype, as well as the possibility of using a similar strategy to generate autologous organoids for transplantation (Schwank et al., 2013).

These developments in genetic engineering, combined with human PSCs and human organoid technologies, have opened new opportunities for studies of human genetics, as it is possible to perform genetic experiments in small human organ models that closely reflect human physiology (Kim et al., 2020).

1.2.4 Limits and future perspectives of brain organoids

Although organoid technology has caught on in several research field, many limitation-filled aspects are still present. An organoid roughly summarizes various organ properties, but it is not a faithful replica of it in terms of shape, dimensions, cell heterogeny and molecular content.

Actual available organoid protocols drive cells to a specific tissue commitment, but how they can spatially organize is simply related to their self-assembly capacity; accordingly, a possible failure of *in vivo*-like cell compartmentalization and tissue structure could occur, with evident issue regarding large scale reproducibility of the system, which is essential for a massive employment of 3D cell cultures in drug screening tests (Sato et al., 2009).

Engineering strategies, such as increasing the degree of automation, the use of defined media and matrices and exact live assessments, need to be further explored to reduce variability in organoid development.

An important drawback of organoid systems is the limited time span for which they can be maintained in culture. This culture time restriction is even more problematic for reproducing the timing of *in vivo* organogenesis, especially in human systems.

As a consequence, these organoids generally fail to mature beyond a fetal phenotype (Fatehullah et al., 2016). Accordingly, brain organoids, for instance, mimic a fetal brain phenotype and further efforts reinforcing maturation are required to obtain a faithful model of the adult brain (Camp et al., 2015).

The limited lifespan of organoids is often a direct consequence of their culture condition. As organoids grow in size, diffusion-dependent nutrient supply and waste removal become less efficient. In human brain organoids, which can grow to several millimeters in size, nutrient inaccessibility leads to necrosis of the inner core, which can only partly be resolved by shaking cultures (Hofer and Lutolf, 2021).

Adding supplementary types of cell or molecular signals in organoids growing-medium could be crucial to increase some cell populations usually under-represented with standardized protocols, increasing the *in vivo*-like complexity, physiology and cell survival. Co-cultures of endothelial stem cells with organoids provide them a vascular-like system able to supply nutrients, oxygen and molecular cues, thus reducing the necrotic center. Once transplanted, a vascularized organoid can grow and fuse its vascular system with that of the host, extending the graft survival rate as well as a leading to graft-host cell integration (Shi et al., 2020).

As mentioned before, most of the spatial identities in organoids appear in an uncontrolled manner. The development of fused organoids, also known as assembloids (Pasca, 2019), enables the investigation of interregional dynamics in the embryonic brain (Chen et al., 2020). This technology has already been applied to study interneurons migration (Bagley et al., 2017, Birey et al., 2017, Xiang et al., 2017), brain circuits (Xiang et al., 2019, Andersen et al., 2020, Miura et al., 2020), oligodendrogenesis (Kim et al., 2019) and to establish the dorsoventral and anteroposterior axes within forebrain organoids (Cederquist et al., 2019) (**Figure 7**).

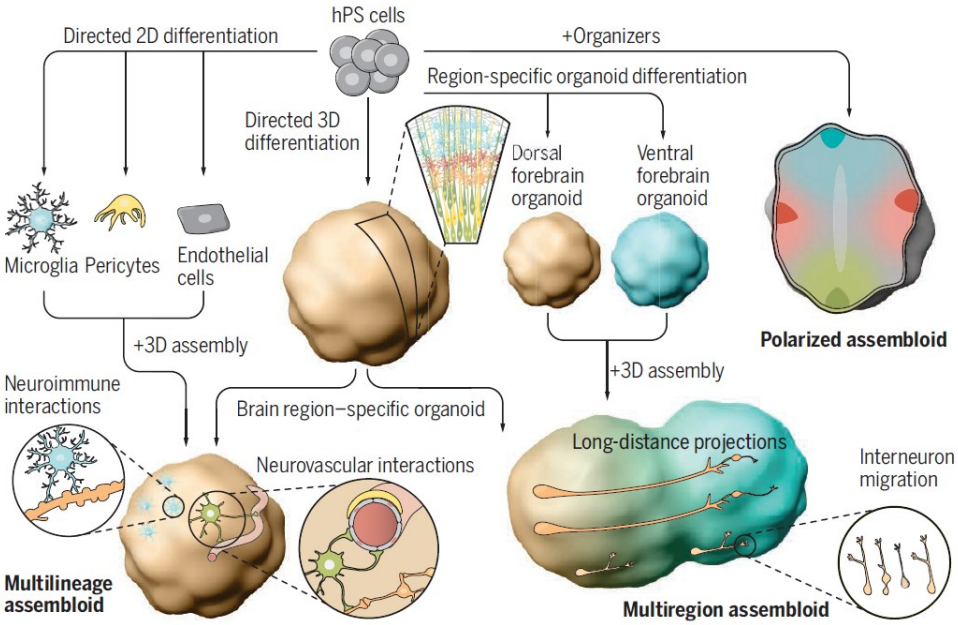

Figure 7: *Assembloids. Brain region–specific organoids are generated from human pluripotent stem (hPS) cells and can be assembled with other cell types (multilineage assembloids), with other organoids (multiregion assembloids), or with morphogens or organizer-like cells (polarized assembloids). Brain organoids and assembloids can be used to model complex cell-cell interactions and neural circuit formation in the human nervous system. From Pasca et al., 2019.*

Combining independently patterned organoids into a single tissue, Bagley and colleagues recreated *in vitro* the dorsal-ventral forebrain axis, with a downstream focus in neuronal migration study. Therefore, migrating cells within fused organoids exhibited migratory characteristic resembling those of migratory cortical interneurons, an *in vitro* cell behavior never investigated before (Bagley et al., 2017).

Further, Xiang's group generated human medial ganglion eminence (MGE) organoids (hMGEOs) and fused them with human cortical organoids (hCOs). Their experiments showed migration of interneurons progenitors within the assembloid was approximately close to the *in vivo* counterparts (Xiang et al., 2017).

Long distance-projections play essential roles in brain functions. Xiang et al. fused human thalamic organoids (hThOs) with human cortical organoids (hCOs). Their results demonstrated that hThOs projected thalamic axons to hCOs, in an *in vivo* similar manner (Xiang et al., 2019).

Recently, Andersen presented a 3D culture system from iPSCs resembling cerebral cortex, hidbrain/spinal cord and skeletal muscle, able to form neural circuits that can be manipulated to mode cortical control of muscle contraction *in vitro*; to achieve this purpose they fused intact human cortical spheroids (hCSs) with human spheroids resembling spinal cord (hSpS) and 3D human skeletal myoblasts (hSkMs). Next, an optogenetic approach was exploited to validate cortical activation of muscular part within the assembloid (Andersen et al., 2020).
Similar technical approaches were invested by Miura and colleagues. They generated cortico-striatal assembloids, in which cortical neurons sent axonal projections into striatal organoids, forming synaptic connections. Moreover, they derived cortico-striatal assembloids from patients with a neurodevelopmental disorder caused by a deletion on chromosome 22q13.3 and captured disease-associated defects in calcium activity (Miura et al., 2020).

1.3 Allan-Herndon-Dudley Syndrome (AHDS)

Among the pathologies affecting the central nervous system, the Allan-Herndon Dudley syndrome (AHDS) is an X-linked rare disorder characterized at the clinical level by potentially severe neurologic complications including mental retardation and movement disorders. AHDS is caused by loss-of-function mutations in the SLC16A2 gene encoding for monocarboxylate transporter 8 (MCT8), a specific transporter for thyroid hormone (TH) Triiodothyronine (T3). Patients affected by AHDS exhibit abnormal thyroid function tests that include normal Thyroid Stimulating Hormone, (TSH) levels with a low free Thyroxine (T4) and high levels of circulating T3. It is very likely that the neuronal disorder is secondary to the inability of T3 to gain access to neurons during development. This was shown in a recent study involving the analysis of human brains from a fetus and a child with AHDS. Both brains had anatomic and structural changes consistent with severe abnormalities of development concurrent with greatly diminished cerebral T3 levels (López-Espíndola et al., 2014). Also, the relationship of AHDS to a deficiency of T3 transport has been solidified by studies showing that human fetal and neonatal

brain from patients with AHDS look remarkably similar to brain from humans with severe hypothyroidism (Kim et al., 2015).

THs have showed to be fundamental during brain development having crucial roles for cell proliferation, neuronal differentiation and dendritic elaboration (Thompson and Cline, 2016); obviously, the prolonged deficiency of thyroid hormones provokes irreversible damages in the CNS, the consequences of which depend on the specific timing of onset and duration of thyroid hormone lack. Particularly, the early brain development is in part "protected" by the maternal TH supply, through an enzyme-mediated conversion of maternal T4. Therefore, the cerebral areas mostly affected will be those developed later, involved in processes such as spatial and associative memory, language, auditory processing, but also attention and executive processing (Prezioso et al., 2018). The earlier stages of progenitor migration, differentiation and maturation seem particularly impaired in TH-deprived rat models. Specifically, maternal induced hypothyroidism or hypothyroxinemia in rats led to critical damages in the rat brain architecture, such as aberrant neuronal migration and structural gray matter organization in the somatosensory cortex and the hippocampus (Ausó et al., 2004). Additional studies on thyroid hormone receptor α1 (TRα1) knock-in and knock-out rats have reported impairment of dendrites and axonal development of GABAergic interneurons, pivotal for early neuronal circuit organization (Sawano et al., 2013). These experiments on rats appear to be strongly representative of what occurs in human with fetal TH deficiency: whether the fetus carries genetic mutations, or maternal hypothyroidism occurs, the child's psychomotor abilities and neurological outcomes will be affected.

1.3.1 Models of AHDS

The development of targeted therapies for rare diseases mainly depends on the presence of good *in vitro* and *in vivo* models, that favor the investigation of the pathogenesis of the disease and allow preclinical studies to evaluate therapeutic strategies.

The study of the AHDS first saw the generation and the extensive study of an Mct8 knock-out (Mct8KO) mouse model. These mice models displayed only low levels

of T3 in different brain areas and a thyroid hormone's profile in serum levels similar to the one of the disease. Remarkably, MCT8-deficient mice manifest thyroid alterations but lack neurological signs. It is believed that Mct8 deficiency in mice is compensated by another transporter of T4, called Slco1c1-encoded organic anion transporter polypeptide 1c1 (Oatp1c1). This allows T4 to enter the brain and to be converted in T3, generating sufficient local T3 to prevent hypothyroidism (Morte et al., 2021). The compensating role of Oatp1c1, by preserving T4 transport, has been demonstrated, showing that double SLC16A2 /Slco1c1 KO mice have profound brain hypothyroidism (Mayerl et al., 2014). Intriguingly, two Mct8 knockout (KO) mouse strains closely recapitulate the thyroid phenotype, but they fail to display neurological or behavioral abnormalities (Dumitrescu et al., 2006; Trajkovic et al., 2007). When hypothyroidism was induced in AHDS mice at the neonatal stage, the exogenous supplementation of T4, but not T3, was able to rescue a mild phenotype in the cerebellum (Ceballos et al., 2009). This suggests that T4, but not T3, may cross the mouse blood-brain barrier (BBB) even in MCT8-deficiency condition, through the presence of a mouse-specific T4 transporter that is absent in human (Vatine et al., 2017). Several transgenic models were subsequently generated to identify the mouse-specific TH transporter. These included KO models of Mct10 (Slc16a10) (Müller et al., 2014), L-type amino acid transporter (Lat2 and Slc7a8) (Núñez et al., 2014), Organic anion-transporting polypeptide 1c1 (Oatp1c1) and SlcO1c1), either as independent KO or with MCT8 (Mayerl et al., 2012, 2014). While most of these models did not exhibit the desired neurological phenotype, the Mct8/Oatp1c1 double KO displayed a severe form of CNS-specific hypothyroidism, including decreased myelination and abnormal neuronal differentiation (Mayerl et al., 2014). Interestingly, Oatp1c1 is highly expressed in endothelial cells of the rodent BBB (Roberts et al., 2008), but not the human BBB (Uchida et al., 2011), suggesting a crucial differential regulation of TH transporters among species.

MCT8-deficient patient fibroblasts and human cell lines expressing wild-type or mutant MCT8 have been used to analyze TH transport (Visser et al., 2009) and gene expression (Visser et al., 2010). While these cell models showed some features of MCT8 deficiency, they do not harbor the characteristics of affected neural or

endothelial cells that are required for a relevant human cell-based disease model of AHDS. iPSCs technology (Takahashi and Yamanaka, 2006; Yu et al., 2007), provide an unprecedented platform for studying human genetic disorders (Ebert et al., 2009; Mattis et al., 2015). Indeed, Vatine and collegues generated iPSCs from patients carrying MCT8 mutations, along with CRISPR/Cas9 engineered system (Li et al., 2013). The obtained cells showed diminished TH uptake, however, they still displayed normal T3 dependent neuronal maturation. Additionally, BBB was considered since it controls TH entry into the brain. In the same study, BBB characterized by MCT8-deficiency was modeled from iPSC-derived brain microvascular endothelial cells. A minor T3 concentration was observed in MCT8-deficient brains, showing that T3 transport across the BBB is dependent on MCT8, likely driving the decreased registered.

The blood brain barrier consists in a highly specialized arrangement of the vasculature that has the function of regulating the entry of molecules into the brain and to provide protection from potentially harmful pathogens arriving from the bloodstream. However, the BBB does permit the passage of nutrients and other molecules necessary for CNS function, thus it is permeable to some molecules. The BBB is formed mainly of brain endothelial cells held closely together by tight junctions and additional cell types with which the endothelial cells interact (including pericytes, microglial, neuron and astrocytic end-feet) (Akhtar, 2015; Aksoy et al., 2015).When co-cultured under low adherence conditions, human primary brain endothelial cells, astrocytes and pericytes assemble three-dimensional spheroidal structures comprised of astrocytes in the core with brain endothelial cells and pericytes being on the exterior surface (Alafuzoff et al., 1983; Alexianu et al., 2001; Bergmann et al., 2019). Thus, these multicellular BBB organoids can be established as a reliable and predictive *in vitro* platform to analyse and screen for brain-penetrating compounds (Logan et al., 2019).

In this context, organoids may result extremely powerful platforms for reproducing the AHDS, allowing also to study the role of BBB tight junction and the ability of compounds to enter the brain, in order to target specific clues that determine AHDS.

1.3.2 AHDS available treatments

To date, the therapeutic approaches used for the treatment of Allan-Herndon-Dudley syndrome aim to increase the supply of thyroid hormones to the central nervous system to recover and improve neuronal function as well as to decrease the peripheral hyperthyroidism. The main therapeutical interventions consist in the administration of several molecules, among which levothyroxine (LT4), propylthiouracil (PTU), acide 3,3',5-triiodothyroacetique (TRIAC) and (DITPA). **Levothyroxine** is a synthetic version of the thyroxine hormone and it is recommended as replacement therapy for thyroid hormone deficiency (Azizi et al., 2020). It is usually administered together with **PTU**, an inhibitor of type 1 deiodinase, normally used to treat hypothyroidism. PTU/LT4 is probably the most accessible combination of medication. The treatment is aimed to increase the serum T4 concentration and decrease that of T3, by reducing the conversion of T4 to T3 in peripheral tissue. PTU does not inhibit type 2 deiodinase, thus T4 (entering CNS) can generate T3 in the brain. High circulating levels of T3 cause the inability to gain weight, malnutrition and organs' toxicity. PTU administration reduces the formation of T3 in the body and consequently decreases the burning of calories. Considering its mechanism of action, PTU administration will not further reduce the already compromised supply of T3 to the brain (MCT8-AHDS Foundation, https://mct8.info/treatment).

A male subject affected from AHDS, hospitalized at the age of 14 for malnutrition (body weight = 25 kg), was treated with propylthiouracil (PTU), first alone and subsequently in combination with levothyroxine (LT4). After PTU (200mg/d) administration alone, serum free T4 was undetectable and serum free T3 was reduced, with high TSH levels. While PTU prescription was continued, high LT4 doses (100mg/d) were needed to normalize serum TSH levels. Consequently, serum free T4 was normal, serum free T3 was slightly high and weight gain was 3 kg in 1 year (before treatment, oral overfeeding (1600 kcal/d) was unsuccessful, leading to a weight gain of 200g in one year) (Wémeau et al., 2008).

TRIAC is a thyroid hormone analogue and it is also physiologically present in low concentrations in the normal organism. TRIAC treatment could result in normalization of the abnormal serum TH values in AHDS patients. It shares similar structure to and works in the same way as the thyroid hormone T3. However, unlike T3, it can enter developing nerve cells without the MCT8 transporter protein and thus enter CNS in AHDS patients, thereby allowing the nerves to develop properly and relieving symptoms of the disease (MCT8-AHDS Foundation, https://mct8.info/treatment).

TRIAC has been tested for a maximum of one year in an international multicentric study of 46 individuals affected by AHDS. The main objective was the normalization of the free T_3 blood level and TRIAC resulted effective in pursuing it. Other favorable findings were increased body weight, decreased heart rate, systolic blood pressure and hypertension. An improved development in seven children, two of whom had started TRIAC treatment before the age of four, was registered, in fact they achieved independent sitting and full head control after 12 months of treatment (Sarret et al., 2020).

Lastly, **DITPA** is a thyroid hormone-like compound which does not require MCT8 to enter tissues. DITPA effect was evaluated in four children affected by AHDS, treated for 26-40 months. Treatment was initiated at ages between 8.5-25 months and an increased dose was administered according to the weight. DITPA normalized the elevated serum T3 and TSH when the dose reached 1 mg/kg · d and T4 and T3 lowered to the normal circulating range. Additionally, there was no weight loss and weight gain occurred in two subjects. None of the treated children developed seizures and no adverse effects were observed. DITPA (1-2 mg/kg · d) almost completely normalizes thyroid tests and reduces the hypermetabolism and the tendency for weight loss. The effects of earlier commencement and long-term therapy remain to be determined (Verge et al., 2012).

The FDA has approved a protocol to use DITPA to treat pregnant women carrying a male fetus affected by AHDS. The gender will be determined from the mother's blood and further investigation to detect MCT8 mutations will be carried out. If the baby carries an MCT8-deficiency related mutation, then treatment will start immediately (DITPA will be taken by mouth) and the protocol applies to pregnancies for no more than 8 weeks along. This compound can reach the brain of the child without the need of the MCT8 transporter. By reaching the brain early during development, the hope is that DITPA can prevent some if not all the neurological deficits seen in children with MCT8 mutations (MCT8-AHDS Foundation, https://mct8.info/treatment).

1.3.3 The role of T3 in neurodevelopment

Thyroid hormones T4 (L-thyronine) and T3 (triiodo-L-thyronine/thyroxine) are protein-bound moieties essential for growth and development in humans. Their synthesis and secretion are modulated by the hypothalamic-pituitary-thyroid (HPT) axis, which, in response to a series of environmental stimuli, secretes the thyroid stimulating hormone (TSH), that will eventually stimulate the production of thyroid hormones from the thyroid.

Once synthesized, T3 and T4 are transported to target cells through membrane carriers: (i) monocarboxylate transporters (MCTs) 8 and 10, (ii) the L-type amino acid transporters (LATs), (iii) the organic anion transporters (OATPs). The main circulating form of THs is T4 while T3 has been considered its bioactive form since most of it is directly obtained within the target tissue by undergoing the deiodination process (stereospecific removal of iodine), performed by enzymes called deiodinases (DIOs). Their cell-specific expression determines the amount of T3 available within a specific organ/tissue. T4 is the main TH that crosses the blood-brain barrier (BBB) using MCT8 in humans and MCT8, OATP1C1 and LAT in mice, as carriers ***(Figure 8)***.

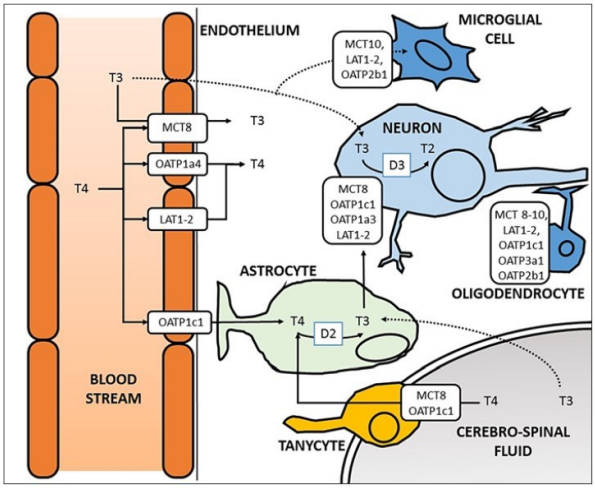

***Figure 8**: Processes of THs arrival, up-take and metabolism in the brain. Adapted from Prezioso et al., 2018.*

Among the most critical actions of thyroid hormone in humans there are those exerted during brain development, both during gestation and after birth (Bernal, 2022; Schiera et al., 2021). Severe TH deficiency in fetal and neonatal periods results in various CNS pathologies, such as cretinism (Schroeder et al., 2014), and Allan-Herndon-Dudley Syndrome (AHDS, OMIM #300523).

It has been showed that THs are able to regulate neural stem cell fate (Gothié et al., 2020). Particularly, THs regulate neurogenesis, neural cell differentiation and neural cell migration (Bernal, 2022; Navarro et al., 2014; Fauquier et al., 2014; Del Río et al., 1997) and development (Trentin Gonçalves et al., 2003).

THs have several implications in mitochondrial biogenesis, dynamics and metabolism. T3 increases mitochondrial energy production in astrocytes and this plays a role in neuroprotection, since they are essential in supporting neuronal function and enhancing neuronal resistance to oxidative stress (Morita et al., 2019). Indeed, it has been demonstrated that T3-stimulated, FAO-dependent ATP production protects against damaged induced by cerebral ischemia (Sayre et al., 2017). Neurogenesis requires a metabolic switch from glycolysis to oxidative phosphorylation (OXPHOS). Most proliferating stem cells exhibit a glycolytic metabolic program to support the synthesis of cellular building blocks for sustaining cell growth; on the other hand, during differentiation, the metabolism switches to OXPHOS to generate ATP more efficiently (Richiardone et al., 2022) (***Figure 9***).

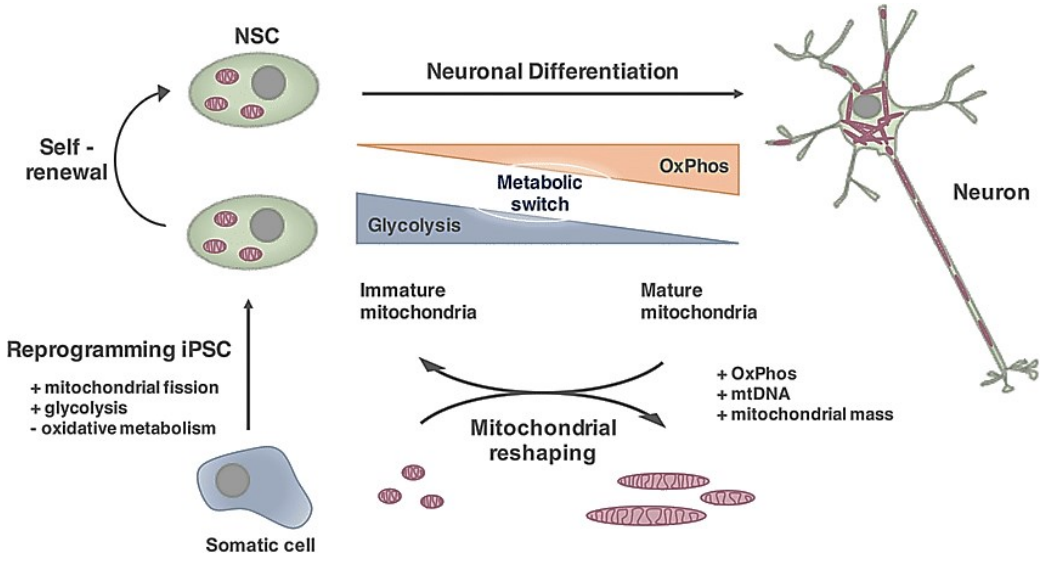

Figure 9: Representation of mitochondrial development along differentiation of NSC to neurons. Mitochondria in stem cells are smaller and functionally less mature compared with differentiated neurons, which are characterized by larger mitochondrial biomass and mtDNA as well as elongated mitochondria. The main source of energy in neurons depends on oxidative metabolism from mitochondria (OxPhos), while stem cells are characterized by a high activity of glycolytic enzymes, accompanied by a low mitochondrial biomass and DNA content. This metabolic switch between proliferative and differentiated states is also observed in iPSC reprogrammed from somatic cells. From Arrázola et al. 2019.

2. AIMS

Brain organoids are complex self-organized neural structures grown from pluripotent stem cells (PSCs) that mirror *in vitro* the architecture, heterogeneity and function of the *in vivo* counterpart tissue (Lancaster and Knoblich, 2014). During the past decades, organoids have drastically changed the *in vitro* models' concept, rapidly becoming promising three-dimensional (3D) tools for unraveling neurodevelopment and neurological disorders. Currently, brain organoids are mainly obtained from human PSCs, as these represent the closest model to the human being. Nevertheless, murine derived brain organoids are not to be excluded from the scientific panorama, instead they need to be considered complementary to the human 3D systems. Mouse stem cells-derived organoids result pivotal for setting up protocols to develop cerebral or brain region-specific organoids in a minor amount of time compared to human organoids. Remarkably, murine 3D systems can reduce the number of animals used for research purposes. The variety and robustness of existing data on mouse models and the presence of mutant phenotypes offer strong points of comparison to validate organoids as tools to study the genetics of brain development (Marshall and Mason, 2019).

In this context, the overall aims of my thesis project consisted into the development and characterization of a highly reproducible and standardized cerebral organoid model, derived from murine neural stem cells (NSCs), and its application for modeling disease and therapies testing. Specifically, the established brain murine 3D tool was extensively characterized at a cellular, molecular and functional level and further exploited for modeling the Allan Herndon Dudley Syndrome (AHDS) and to test pharmacological intervention.

AIM 1: Development of a standardized and reproducible protocol for murine brain organoids' model

As first aim, I exploited the subgranular zone (SGZ) derived neural stem cells (NSCs), one of the most well-known cerebral regions holding neurogenic potential (Pino et al., 2017; Decimo et al., 2020), to define the more suitable culture

conditions allowing the generation of cerebral organoids. By adapting the well-established method published by Lancaster and Knoblich (Lancaster and Knoblich, 2014), we defined the best media composition and time window for an effective protocol leading to murine brain organoids growth and differentiation. Morphological and RNA sequencing analysis were used to support the reproducibility of the method.

AIM 2: Characterization of brain organoid development and brain region identity specification

The settings performed in AIM 1 led to the definition of an optimized protocol, characterized by three specific phases, allowing to growth standardized murine brain organoids derived from NSCs extracted from the SGZ of E14.5 post fertilization days embryos. In the second aim, the generated murine brain organoids were extensively characterized at morphological, cellular, metabolic and functional level during the culture steps providing a picture of the developmental processes occurring during organoid maturation.

The progressive brain organoids' cell differentiation and distribution were evaluated by looking at the expression and localization of NSCs, neural progenitors, neurons, and glial cells throughout the brain organoid developmental stages by immunofluorescence analysis. Considering the metabolic changes occurring *in vivo* during neuronal maturation, we evaluated the metabolic profile of organoids at different developmental stages by western blotting and seahorse live measurements techniques.

Neuronal differentiation and maturation were investigated by combining immunofluorescence analysis and RNA sequencing data. Calcium imaging (Fluo4-AM dye) acquisitions and adenoviral (modified rabies virus) monosynaptic tracing were exploited to deepen organoids neuronal connections. Lastly, considering we used an unguided approach for generating the murine 3D samples, we deepen their cerebral regional identity via immunofluorescence and RNA sequencing data.

AIM 3: Murine brain organoids as a model to study Allan Herndon Dudley Syndrome (AHDS) and to identify new drug target

The results obtained in AIM 2 illustrated the possibility to grow reproducible murine brain organoids which resemble the *in vivo* neurodevelopment (Ciarpella, Zamfir et al., 2021). Based on this, the aim 3 was focused on exploiting the murine brain organoids for modeling disease. To this end, the organoids' protocol was modified to reproduce an *in vitro* model for the Allan Herndon Dudley Syndrome (AHDS), a neurodevelopmental disorder caused by loss-of-function mutation in the gene encoding for the T3 transporter into the CNS (Saret et al., 1993).

To establish the AHDS disease 3D model, we adapted our in-house protocol for the generation of murine cerebral organoids following a three-phase protocol lasting up to 21 days and consisting in culture media depleted of T3. The lack of T3 from the culture medium should in part resemble the AHDS hypothyroidism condition while control organoids were generated by standard culture with T3-supplented media.
To study the neurological effects dictated by T3 deficiency in the organoid model, we used immunofluorescence analysis to evaluate the presence and different abundance of proliferative, stem and neuronal progenitor cells. The neuronal commitment and maturation were followed along the culture protocol by investigating the presence of immature neurons and astrocytes and their relative abundance in control and AHDS-like organoids.
During CNS maturation, the activation of mitochondrial metabolism is fundamental to fulfill the high energetic costs required by differentiating neural progenitor cells and a metabolic switch was already highlighted in murine brain organoid (aim 2). Due to the importance of T3 in regulating the mitochondrial activity, we investigated whether AHDS-like organoids showed alteration in mitochondrial processes by RNA sequencing analysis and immunoblot.

Considering the role of T3 in the modulation of mitochondrial metabolism and the relevance of mitochondrial metabolism during neuronal development, we lastly aimed to test the therapeutical potential of the nicotinamide riboside (NR), a NAD^+ precursor and activator of mitochondrial biogenesis and metabolism. By targeting

mitochondrial metabolism, we thus attempted to overcome mitochondrial and neuronal impairment observed in absence of T3. AHDS-like organoids treated with NR were characterized at a morphological and cellular level by brightfield and immunofluorescence analysis. With this aim, we attempted to provide a proof-of-concept of pharmacological interventions targeting mitochondrial metabolism to rescue neurological impairment and we gave evidence of the feasibility of the use of murine organoids as drug screening platform.

3. MATERIALS AND METHODS

3.1 Animals

Animal housing and all experimental procedures were approved by the Istituto Superiore della Sanità (I.S.S., National Institute of Health; protocol n. C46F4.N.N4E, Italy), Italy and the Animal Ethics Committee (C.I.R.S.A.L., Centro Interdipartimentale di Servizio alla Ricerca Sperimentale) of the University of Verona (Italy). Wild-type (WT) C57Bl/6J E14.5 mice were obtained from Charles River Laboratories (Wilmington, MA).

3.2 Neural stem cells extraction from subgranular zone (SGZ) murine tissue

Pregnant C57Bl/6J female mice were sacrificed by cervical dislocation. Murine NSCs were extracted from E14.5 embryos' brains using fine tweezers under stereo microscope and collected into ice-cold HBSS solution (sterile water, HBSS 10X (GIBCO, Cat#14180-046), HEPES 0.3 M, 1% Pen/Strep (GIBCO, Cat#15140-122)). After centrifugation at 300g per 1 minute, HBSS was substituted with PBS 1X and then the sample underwent one more centrifugation at 300g for 1 minute. The pellet was suspended in a solution containing DNase (Sigma Aldrich) and Trypsin 1X (GIBCO Cat#25200-056) diluted 1:5. The first round of dissociation was performed using the gentleMACS™ Dissociator (Miltenyi Biotec) programme BRAIN_01.01. Following 10 minutes of incubation at 37°C, other two rounds of dissociation were done with the gentleMACS™ Dissociator's programmes BRAIN_02.01 and BRAIN_03.01. Then PBS 1X was added to dilute the enzymes and the sample was filtered with a cell strainer (40 μm diameter) to remove cellular debris. After a 10 minutes final centrifugation at 300g, the sample was suspended in DMEM-F12 GlutaMAX^{TM} (GIBCO, Cat#31331-028) containing 2% B27 (GIBCO, Cat#17504-044), 1% N2 (GIBCO, Cat#17502-048), 1% Pen/Strep (GIBCO, Cat#15140-122), enriched with 20 ng/ml basic fibroblast growth factor (bFGF, Peprotech, Cat#100-18B) and epidermal growth factor (EGF, Peprotech, Cat#AF-100-15). Cells were stained with Trypan blue 0,4% (GIBCO, Cat#15250-061), counted and cultured as neurospheres in suspension in T75 flasks (Falcon,

Cat#156499) up to the second passage at 37°C in a humidified atmosphere of 5% CO_2 in air. After 7–10 days, neurospheres were collected, centrifuged, mechanically dissociated to a single-cell suspension (Dolci et al., 2017) and further used for organoid generation.

3.3 Murine brain organoids generation

Brain organoids were generated starting from mouse SGZ-derived NSCs. The protocol was adapted from the one published by Lancaster (Lancaster and Knoblich, 2014). We generated a three-phase protocol (see ***Table 1***) to obtain reproducible murine 3D systems. Briefly, 20.000 cells/well were seeded into 24-well plates (Thermofisher) in 500 µl of neurosphere culture medium (DMEM/F-12 GlutaMAX, (GIBCO, Cat#31331-028), 2% B27 supplement (GIBCO, Cat#17504-044), 1% N2 supplement (GIBCO, Cat#17502-048), 1% Pen/Strep (GIBCO) supplied with a high concentration (20 ng/ml) of epidermal growth factor (EGF) (Peprotech, Cat#AF-100-15) and basic fibroblast growth factor (bFGF) (Peprotech, Cat#100-18B). This first phase refers to the *Expansion phase***,** lasting from the seeding day till day 4. During the induction phase, from day 5 to 14, the concentration of bFGF and EGF was gradually scaled down: at day 5, both growth factors were decreased to 10 ng/ml while at day 7, bFGF concentration was reduced to 5 ng/ml and EGF was removed. During the differentiation phase, starting at day 15, the organoids were supplied with 50 ng/ml of brain-derived neurotrophic factor (BDNF) (Peprotech, Cat#450-02). During all the culture time (until day 32), plates were kept in continuous agitation (65rpm) using the ORBi-SHAKER CO_2 (Benchmark Scientific) at 37°C in a humidified atmosphere of 5% CO_2 in air. Seven different batches of SGZ-NSCs belonging to seven different embryos extraction were used to generate organoids.

EXPANSION PHASE	INDUCTION PHASE		DIFFERENTIATION PHASE
Day 0-4 DMEM/F12-Glutamax bFGF/EGF (20 ng/ml) Pen-Strep 1% N2 1% B27 2%	**Day 5-6** DMEM/F12-Glutamax bFGF/EGF (10 ng/ml) Pen-Strep 1% N2 1% B27 2%	**Day 7-14** DMEM/F12-Glutamax bFGF (5 ng/ml) Pen-Strep 1% N2 1% B27 2%	**Day 15-32** Neurobasal medium Pen-Strep 1% B27 2% L-glut 0.25% BDNF (50 ng/ml)

Table 1: *Details of the protocol used to generate murine cerebral organoids from SGZ-derived NSCs.Each phase consists in a distinct medium, supplied with specific factors at a determined concentration. Also, the time-window is strictly defined.*

3.4 Murine Allan Herndon Dudley Syndrome (AHDS) organoid generation protocol

AHDS mouse organoids were obtained starting from E14.5 murine SGZ-derived NSCs, like murine cerebral organoids described in the Paragraph 4.3. AHDS-like organoids were cultured until day 21 and produced removing the T3 hormone, contained into the B27 supplement, from the culture media.

B27 supplement without the hormone (T3-) was prepared in our laboratory. The reagents indicated in ***Table 2*** were assembled to obtain T3 devoid home-made B27 supplement, following the Hanna Lab Protocol – Weizmann Institute of Science (Version 2 of 17/02/2016). Once the B27 devoid of T3 supplement was done, T3 was added to obtain the T3+ home-made B27 supplement.

Compound	Code
Catalase	Sigma C40
Glutathione reduced	Sigma G6013
Human insulin	Sigma 91077C
Superoxide dismutase	Sigma S5395
Human Holo-Transferrin	Sigma T0665
T3+	Sigma T6397
L-carnitine	Sigma C0283
Ethanolamine	Sigma E9508
D+ - galactose	Sigma G0625
Putrescine dihydrochloride	Sigma P5780
Sodium selenite	Sigma S9133
Corticosterone	Sigma C2505
Linoleic acid	Sigma L1012
Linolenic acid	Sigma L2376
Progesterone	Sigma P8783
Retinol acetate	Sigma R7882
DL-alpha tocopherol (vit E)	Sigma T3251
DL-alpha tocopherol acetate	Sigma T3001
Biotin	Sigma B4639
BSA Fraction V IgG Free Fatty acid poor	Invitrogen 30036578

Table 2: *Reagents contained into the T3+ home-made B27 supplement.*

The protocols used to produce AHDS-like (T3 less), and T3+ murine organoids are illustrated in the following table (***Table 3***). T3+ organoids were used as control counterpart.

	T3- organoids (AHDS-like)	T3+ organoids (control)
Expansion phase	**Day 0-4** DMEM/F12-Glutamax FGF/EGF (20ng/ml) Pen-strep 1% N2 1% B27 2%, T3 less	**Day 0-4** DMEM/F12-Glutamax FGF/EGF (20ng/ml) Pen-strep 1% N2 1% B27 2%, T3 supplied
Induction phase	**Day 5-6** DMEM/F12-Glutamax FGF/EGF (10ng/ml) Pen-strep 1% N2 1% B27 2%, T3 less	**Day 5-6** DMEM/F12-Glutamax FGF/EGF (10ng/ml) Pen-strep 1% N2 1% B27 2%, T3 supplied
	Day 7-14 DMEM/F12-Glutamax FGF (5ng/ml) Pen-strep 1% N2 1% B27 2%, T3 less	**Day 7-14** DMEM/F12-Glutamax FGF (5ng/ml) Pen-strep 1% N2 1% B27 2%, T3 supplied
Differentiation phase	**Day 15-21** Neurobasal medium Pen-strep 1% B27 2%, T3 less L-glut 0,25% BDNF 50ng/ml	**Day 15-21** Neurobasal medium Pen-strep 1% B27 2%, T3 supplied L-glut 0.25% BDNF 50ng/ml

Table 3: *Details of the protocols applied to grow AHDS-like (T3-) and T3+ murine cerebral organoids. Both T3+ and T3- B27 supplements were home-made.*

3.5 Nicotinamide Riboside (NR) administration in murine AHDS-like organoids

NR (Selleck Chemicals LLC, Cat#S2935) was added fresh in culture media of both T3+ and T3- (AHDS-like) organoids three times a week, starting from day 7 until the end of the protocol *(day 21)* at a final concentration of 0.5 mM..

3.6 Organoid maximum diameter measurements

To determine the organoids' maximum diameter, bright field images were acquired during the various stages of the protocol. For AIM1, organoids were measured every day up until day 40, n>30 for each time point. For the optimized protocol, measures were taken at 2, 5, 7, 9, 11, 14, 21, 28 and 32 days, n>30 for each time

point, using the Axiovert 200M (Carl Zeiss, Munch, Germany) microscope. The maximum diameter was measured using the "straight line" tool of ImageJ software (U.S. National Institutes of Health). The pixel obtained value was then converted in mm.

3.7 Optical Projection Tomography (OPT) and volume measurement in organoids

In-house-built 3D imaging system for Optical Projection Tomography (OPT) (Belay et al., 2021) was used to image and characterize the 3D structures of the organoids. Brightfield OPT was used to capture the 360-degree structure of the organoids. White LED source (LTCL23; Opto Engineering, Mantova, Italy) with a 0.65 μm voxel size (1 px = 0.65 μm) illuminated the samples in 0.9° intervals while a 10× objective captured a total of 400 projection images simultaneously rotating the sample. The projection images were then used to reconstruct the 3D tomographic image of the sample using a filtered back-projection algorithm (Matlab; MathWorks, Natick, MA, USA) (Figueiras et al., 2014) and further edited using Fiji (ImageJ) and Avizo (ThermoFisher Scientific). All 3D images were manually segmented using Avizo, and organoid volumes, images, and rotating videos were calculated and processed based on the 360-degree reconstructions using Avizo.

3.8 Viability assay on whole mount organoids

Organoid viability was assessed using a fluorescence staining solution containing propidium iodide (50%), fluorescein diacetate (50%) and Hoechst (1:1200), freshly prepared the day of the experiment and protected from light. The propidium iodide is an intercalating red fluorescent dye labeling dead cells, fluorescein diacetate is hydrolized to fluorescent fluoresceine in live cells, whereas Hoechst is used for total nuclei staining. Whole mount organoids (n = 3 samples/time point) were washed in PBS 1X and incubated for 5 minutes in the staining solution. Three PBS 1X washes were performed, then the samples were fixed in a 4% PFA and 4% sucrose solution for 10 minutes, before being acquired at Zeiss LSM710 confocal microscope (Carl

Zeiss, Munich, Germany). Quantification of the propidium iodide positive cells was done by counting positive cells on total nuclei. Then, the number of viable cells was obtained. The quantification was performed using a specific plugin of ImageJ software (U.S. National Institutes of Health) and a semi-automated cell count.

3.9 Organoids immunofluorescence assay

Murine brain organoids were selected at different time points (7, 14, 21 and/or 32 days for standard, if not otherwise stated) after seeding and fixed for 15 minutes in 4% PFA / 4% sucrose, then rinsed and stored in PBS 1X at 4°C until immunostaining was performed.

3.9.1 Immunofluorescence assay on sliced organoids

For cryosectioning, each organoid was embedded in Cryobloc (Diapath, Cat#070130) and cut at 30 µm. Immunostaining was performed after 1 hour incubation in blocking solution (PBS 1X with 0.25% Triton X-100, 2% bovine serum albumin for cytosolic antigens and PBS 1X with 0.5% Triton X-100, 2% bovine serum albumin for nuclear antigens) (Formaggio et al., 2010). Sections were then incubated with primary antibodies in blocking solution at 4°C for 2 hours. After rinsing 3 times for 10 minutes in blocking solution, appropriate secondary antibodies were applied for 1.5 hours at room temperature. After final washing steps in blocking solution and then in PBS 1X, nuclear staining with TOPRO™-3 (TO-PRO-3, Molecular Probes-Thermo Fisher Scientific) or DAPI (1:2000, Invitrogen Thermo Fisher Scientific) was performed, and slides were mounted using 1,4-Diazabicyclo [2.2.2] octane (DABCO) (Sigma).

3.9.2 Immunofluorescence assay on whole mount organoids

For immunofluorescence staining, whole mount organoids were incubated in blocking solution (PBS 1X with 0.5% Triton X-100, 2% bovine serum albumin) for 1 hour (Sigma-Aldrich, Protocol Guide: Immunofluorescent Staining of Whole-Mount Organoids using Antibodies); then, they were incubated with primary

antibodies in blocking solution and kept on a shaker overnight at 4°C. After rinsing 3 times for 10 minutes in PBS 1X, secondary antibodies were applied for 6 hours at room temperature. Following final washing steps in PBS 1X, nuclear staining with TOPRO™-3 or DAPI was performed. To preserve the 3D structure of the organoid at the end of the staining, an in-house method was set up, fixing a parafilm chamber on a glass slide; the whole mount organoid was inserted in the chamber and mounted using DABCO.

3.10 Tissue immunofluorescence assay

Intact adult mice brain tissues were extracted after animal perfusion in 4% PFA then rinsed in PBS 1X and stored in sucrose 30% at 4°C. Medio-lateral sagittal or coronal sections were cryosectioned at 35 µm throughout the entire samples. Slides were stored at -20°C until immunostaining was performed. Immunostaining on cryosections was done after 30 minutes incubation in blocking solution (PBS 1X with 0.25% Triton X-100, 2% bovine serum albumin). Samples were then incubated with primary antibodies in blocking solution overnight at 4°C. After rinsing 6 times for 5 minutes in blocking solution, appropriate secondary antibodies were applied for 4 hours at room temperature. After final washing steps in blocking solution and then in PBS 1X, nuclear staining with TOPRO™-3 was performed and slides were mounted using DABCO.

3.11 Antibodies

The following primary antibodies were used: anti-SOX2 (goat, 1:200, R&D System, Cat#AF2018), anti-Vimentin (chicken 1:400, Millipore, Cat#AB5733), anti-Ki67 (rabbit, 1:200, Abcam, Cat#ab16667), anti-DCX (rabbit, 1:400, Cell Signaling Technology, Cat#4604), anti-β3Tubulin (mouse, 1:400, Promega, Cat#G7121), anti-MAP2 (mouse, 1:200, Sigma-Aldrich, Cat#M1406), anti-ZBTB20 (rabbit, 1:200, Genetex, Cat#GTX121616), anti-KA1 (rabbit, 1:200, Abcam, Cat#ab67404), anti PROX1 (rabbit, 1:400, Abcam, Cat#ab101851), anti-NeuN (rabbit, 1:200, Genetex, Cat#GTX121616), anti-GAD65/67 (mouse, 1:400, Santa Cruz Biotechnology, Cat#sc-365180), anti-NMDA (mouse, 1:400, Santa

Cruz Biotechnology, Cat#sc-365597), anti-GlnSyn (mouse, 1:400, Santa Cruz Biotechnology, Cat#sc-74430), anti-GFAP (goat, 1:200, Abcam, Cat#ab53554), anti-synaptophysin (guinea pig, 1:200, Synaptic System, Cat#101004), anti-PSD95 (mouse, 1:200, Millipore, Cat#MAB1596), anti-gephyrin (mouse, 1:200, Synaptic Systems, Cat#147011), anti-VGAT (guinea pig, 1:400, Synaptic Systems, Cat#131004), anti-VGLUT (rabbit, 1:400, Synaptic Systems, Cat#135303), anti-Total OXPHOS Rodent WB Antibody Cocktail (mouse, 1:200, Abcam, ab110413), anti-VDAC1 (rabbit, 1:200, Cat#ab15895), anti-Lamin B (rabbit, 1:200, Abcam, Cat#ab16048), anti-GSX2 (rabbit, 1:200, Genetex, Cat#GTX129390), anti-FOXG1 (rabbit, 1:200, Abcam, Cat#18259), anti-NKX2.1 (mouse, 1:200, Genetex, Cat#GTX34907), anti-PreAlbumin (chicken, 1:200, Genetex, Cat#GTX85112), anti-Frizzled9 (rabbit, 1:200, Genetex, Cat#GTX71581), anti-Musashi 2 (rabbit, 1:200, Genetex, Cat#GTX117808), anti-OCT3/4 (mouse, 1:200, Santa Cruz Biotechnology, Cat#sc-5279), anti-OCT6 (rabbit, 1:200, Abcam, Cat#ab272925), anti-E-Cadherin,(rabbit, 1:200, Genetex, Cat#GTX100443), anti-NANOG (mouse, 1:200, Genetex, Cat#GTX627421), anti-SOX1 (goat, 1:200, R&D Systems, Cat#967237), anti-Nestin (mouse, 1:200, R&D Systems, Cat#MAB2736).

Appropriate secondary antibodies were used: donkey anti-rabbit Alexa Fluor 488 (donkey, 1:1000, Thermo Fisher Scientific, Cat#A21206), donkey anti-mouse Alexa Fluor 488 (donkey, 1:1000, Thermo Fisher Scientific, Cat#A21202), donkey anti-guinea pig CY3 (donkey, 1:1000, Jackson ImmunoResarch, Cat#AB2340460), goat anti-mouse CY3 (goat, 1:1000, Amersham, Cat#PA43002), donkey anti-goat Alexa Fluor 546 (donkey, 1:1000, Invitrogen by Thermo Fisher Scientific, Cat#A-11056), goat anti-rabbit CY3 (goat, 1:1000, Amersham, Cat#PA43004), donkey anti-rabbit Alexa Fluor 546 (donkey, 1:1000, Thermo Fisher Scientific, Cat#A10040), goat anti-chicken Alexa Fluor 546 (goat, 1:1000, Thermo Fisher Scientific, Cat#A11040). TO-PRO™-3 (1:3000, Molecular Probes-Thermo Fisher Scientific) or DAPI (1:2000, Invitrogen Thermo Fisher Scientific) were used to visualize the cell nuclei.

3.12 Immunofluorescence image acquisition, analysis and quantification

Immunofluorescence imaging of sliced and whole-mount organoids was performed using a Zeiss LSM710 confocal microscope (Carl Zeiss, Munich, Germany). Both reconstruction of 3D images and quantification were performed using a specific plugin of ImageJ software (U.S. National Institutes of Health) and a semi-automated cell count. In AIM1 the quantification of positive-immunoreactive cells for SOX2, DCX, anti-β3Tubulin, MAP2, ZBTB20 and nestin was done by counting positive cells over the total number of nuclei (TOPRO™-3) per field. In AIM2 the quantification of the fluorescence signal was performed using a specific plugin of ImageJ software (U.S. National Institutes of Health) and the positive-immunoreactive expression for Vimentin, SOX2, Ki67, DCX, TUBB3, MAP2 and GFAP was expressed as positive fluorescent-related marker area over the total fluorescent area of the sliced organoids, including the positivity for the nuclear marker (TOPRO™-3). Synaptic density was expressed as synaptophysin-positive area against the $MAP2^+$ neuronal cells area per field. The number of excitatory synaptic puncta was measured by evaluating the co-localization of the expression of the presynaptic marker vGLUT and the postsynaptic marker PSD95; the presence of inhibitory GABAergic synapses was quantified by analyzing the co-localization of the presynaptic marker vGAT and the postsynaptic marker gephyrin. The co-localization analysis was performed in blind using a custom-designed macro in Image J. In AHDS organoids, the quantification of the fluorescent signal for non-synaptic markers was performed using a specific plugin of ImageJ software (U.S. National Institutes of Health) and was expressed as positive fluorescent-related marker area over the total area of the sliced organoids, including the positivity for the nuclear marker ($TOPRO^{TM}$-3).

The quantification of marker expression was performed on at least 3 slices for each organoid sample, from $n \geq 3$ different organoids. For whole-mount staining, at least 10 plane sections were acquired and analyzed for each organoid. Statistical differences between marker expression at different time points were calculated by ordinary one-way ANOVA followed by Tukey's post-hoc test or by t-test. $p < 0.05$ was considered statistically significant.

3.13 Fluorescence intensity quantification

Fluorescence intensity in cryosections was obtained using the Plot Profile command in ImageJ (Fiji). Fluorescence intensity graphs for each marker was obtained by further using the Fit Function (8th Degree Polynomial) in ImageJ.

3.14 RNA sequencing analysis in murine cerebral organoids

Total RNA was extracted from 14 samples (7 days organoids: n = 3 pools, each pool containing 3 organoids, 14 days organoids: n = 3 pools, each pool containing 3 organoids, 30 days organoids: n = 3 pools, each pool containing 3 organoids, adult (3 months) cerebral tissue: n = 3, P0 cerebral tissue: n = 2) using the RNeasy Plus Micro Kit (Qiagen, Cat#74034) according to the manufacturer's protocol and RNA integrity was evaluated using the Fragment Analyzer (Agilent Technologies). RNAseq library preparation was performed starting from 100 ng high-quality total RNA using the “TruSeq Stranded mRNA library prep kit” (Illumina, San Diego, USA). Briefly, the mRNA fraction was purified from total RNA by polyA capture, fragmented and subjected to cDNA synthesis. Barcoded DNA adapters were ligated to both ends of the double-stranded cDNA and subjected to PCR amplification. The library products were evaluated using Fragment Analyzer (Agilent Technologies), then sequenced on an Illumina NextSeq500 sequencer using 75bp single-end reads, generating ∼17 million reads per sample. Quality control was conducted using the software Scythe (v0.991) and Sickle (v1.33). Transcript expression levels were then quantified in each sample by running the computer software Salmon v.1.0.0 against the reference sequence of the mouse transcriptome (Gencode M23-GRCm38).

Differential expression analysis on sequence count data was performed using negative binomial distribution models as implemented in the library DESeq2 of R software (https://www.r-project.org/), using the Benjamini-Hochberg method to adjust the p-values for multiple comparisons. Transcript expression fold-changes were estimated for each expressed transcript in every comparison. The most relevant up-regulated genes were then summarized into biological processes and molecular functions by an enrichment analysis based on gene ontologies as

implemented in the library dnet of R. Gene Set Variation Analysis was performed using the package GSVA (ver 1.38.2) of R to identify functionally enriched gene sets.

Selected gene lists were adapted from literature: (i) neural stem cell dataset, neuronal progenitors (Bifari et al., 2020); (ii) mature neurons (Cahoy et al., 2008); (iii) astrocytes (Boisvert et al., 2018; Zhang et al., 2014); (iv) inhibitory synapses and excitatory (Hayamizu et al., 2014) synapses (***Tables 4 and 5***). The possible contribution from Hippocampus (H) and Cortex (C) cells in the organoid, based on gene expression was estimated by investigating different proportions of H and C cells into the organoid tissue according to gene expression profiles of selected genes (cortical signature: *Stard8, Sytl2, Tnnc1, Myl4, Drd2, Calb2, Reln, Lhx1, Lhx5, Ebf3, Cux1, Satb2, Dok5, Ctp2, Emx1, Tiam2, Tbr1, Foxg1, Pvrl3*; hippocampal signature: *Zbtb20, Sipa1l3, Gpr161, Crlf1, Glis3, Dcx, Nrp2, Tgf2b, Gria1, Tnip2, Slc39a6, Prox1, Slc26a10, Trpc6, Neurod1, C1ql2, Gqrik4, Elavl2, Elavl4, Dkk3, Nectin3, Scip, Spock1*) defining either hippocampal or cortical phenotype. For each gene lists and different amounts of H and C cells, the sum of the difference of gene expression levels was calculated (log-TMP transformed values) with the organoid sample (7 days organoids: n = 3 pools of 3 organoids each, 14 days organoids: n = 3 pools of 3 organoids each, 30 days organoids: n = 3 pools of 3 organoids each) under investigation. The difference between samples was estimated as the normalized values of the squared differences between samples (C+H and organoid tissues). Lower overall values of differences suggested a higher confidence of the suggested proportion H and C cells in the organoid. To validate the selected gene list, we performed the above analysis by including adult murine hippocampal and cortical tissue (adult (3 months) cortical tissue: n = 3, adult (3 months) hippocampal tissue: n = 3). A low value of differences was obtained by both hippocampal and cortical samples, thus suggesting reliability of the analysis performed. The percentage of similarity to hippocampus or cortex was evaluated based on the H/C proportion showing the higher confidence.

Neural Stem Cells			Neuronal Progenitors	Mature Neurons
Abcg2	*Acot1*	*Slc4a1*	*Tbr2/Eomes*	*Neun*
Bmi-1	*Lxn*	*Gm12222*	*Mash1/Ascl1*	*Snap25*
Chd2	*Mut*	*Asrgl1*	*Neurog2*	*Syt1*
Cxcr4	*Tpbg*	*Etv4*	*Neurog1*	*Scn2a*
Ctnnb1	*Decr1*	*Abcd3*	*Tacc2*	*Vamp1*
Fabp7	*Cldn12*	*Slc15a2*	*Blbp*	*Cdkl5*
Fzd-1	*Slc9a3r1*	*Mfge8*	*Grm5*	*Rab3a*
Fzd-2	*Slitrk2*	*Acadl*	*Ly6h*	*Basp1*
Hes5	*Cpne2*	*Gas1*	*Lrp8*	*Runx1t1*
Msi 1	*Polr3h*	*Grm3*	*Prox1*	*Hpcal1*
Msi 2	*Luzp2*	*Lrrc16a*	*Nes*	*Pkm*
Nes	*Paqr7*	*Cnih2*	*Vim*	*Acot7*
Notch1	*Bcl2*	*Ctnnd2*	*Neurod1*	*Trim67*
Nr2f1	*Prom1*	*Trim9*	*Sox11*	*Bcat1*
Neurod4	*Ccdc80*	*Traf3*	*Foxg1*	*Sdc2*
Pax6	*Sardh*	*Adgrb1*	*Dcx*	*Sarm1*
Pax3	*Cdc42ep1*	*Sorbs1*	*Tbr1*	*Lancl2*
Prom1	*Tspan12*	*Ezr*	*Aplp1*	*Gdap1*
Rest	*Lfng*	*Fabp7*	*Stathmin 1*	*Smpd3*
Slc1a3	*Fam181b*	*Ptprz1*	*Ncam*	*Crmp1*
Smad1/2	*Sall3*	*Trib2*	*Tubb4a*	*Stmn2*
Sox2	*Nr2e1*	*Kcnj10*	*Tubb3*	*Srrm3*
Sox11	*Rlbp1*	*Ttyh1*	*Map6*	*Mllt11*
Vim	*Fjx1*	*Rgma*	*Dbn1*	*Cttn*
Sox8	*Gramd4*	*Cspg5*	*Tagln3*	*Kctd13*
Sox9	*Car2*	*Slc1a2*		*Map1b*
Tst	*Mt3*	*Atp1a2*		*Nsg2*
Creb5	*Tmem98*	*Plpp3*		
Cbr3	*Eepd1*	*Fbln2*		
Bcar3	*Hes5*	*Ednrb*		
Rgcc	*Abcb9*	*Lrig1*		
Palld	*Thbs4*	*Bcan*		
	Trim47	*Ddah1*		
		Aldh1l1		
		Nsg1		

Table 4: *Genes related to phenotypes of neural stem cells, neuronal progenitors and mature neurons, used for GSVA* ***(related to Table 14 and Figures 17 and 21)***

Astrocytes	Excitatory synapses	Inhibitory synapses
Aldh1l1	Ap3d1	Calb1
Aqp4	Apba1	Camk4
Bmp6	Apbb1	Gabbr1
Bmpr1b	Arf1	Gabbr2
Cbs	Arf4	Gabra1
Ccdc80	Arf6	Gabra2
Cth	Chrm1	Gabra3
Fgfr3	Chrm3	Gabra4
Gfap	Chrm4	Gabra5
Grm3	Clta	Gabra6
Hes5	Cnih2	Gabrb1
Hgf	Cnih3	Gabrb2
Itga7	Cplx1	Gabrb3
Itih3	Cplx2	Gabrd
Mlc1	Gria1	Gabrg2
Nog	Gria2	Gabrg3
Paqr6	Gria3	Gabrr1
Pla2g3	Gria4	Gabrr2
S100b	Grid1	Gad1
Slc1a2	Grid2	Gad2
Slc1a3	Grik1	Glra1
Slc4a4	Grik2	Glra3
Slc6a11	Grik3	Glrb
Thbs1	Grik4	Gphn
	Grik5	Nlgn2
	Grin1	Nlgn3
	Grin2a	Nr3c2
	Grin2b	Nrxn1
	Grin2c	Plcb1
	Grin2d	Ptpro
	Grin3a	Rims1
	Grip1	Rims2
	Grip1	Slc6a1
	Grip2	Slc6a11
	Gripap1	Slc32a1
	Grm1	Syt7
	Grm3	Syt11
	Grm4	
	Grm5	
	Grm7	
	Grm8	
	Kcna1	
	Kcna3	
	Kcna4	

	Kcnc3	
	Kcnc4	
	Kcnd2	
	Nlgn1	
	Nlgn3	
	Rims1	
	Rims2	
	Rims3	
	Rims4	
	Slc1a2	
	Slc1a6	
	Slc1a7	
	Syn2	
	Syn3	
	Syp	
	Syt1	
	Syt4	
	Syt6	
	Syt7	
	Vamp1	

Table 5: *Genes related to phenotypes of astrocytes, excitatory and inhibitory synapses, used for GSVA (related to Table 15 and Figure 22 for astrocytes investigation; related to Table 16 and Figures 34 and 35 for inhibitory and excitatory synapses respectively).*

3.15 RNA sequencing of AHDS-like T3- and control T3+ organoids

Total RNA was extracted from 16 samples (7 days T3+ control organoids: n=4 pools of 3 organoids each, 7 days AHDS-like organoids: n=4 pools of 3 organoids each, 14 days T3+ control organoids: n= 4 pools of 3 organoids each, 14 days AHDS-like organoids: n= 4 pools of 3 organoids each) using the RNeasy Plus Micro Kit (Qiagen, Cat #74034) according to the manufacturer's instructions, and RNA integrity was evaluated using the Fragment Analyzer (Agilent Technologies). RNAseq library preparation was performed starting from 100ng high-quality total RNA using the "TruSeq Stranded mRNA library prep kit" (Illumina, San Diego, USA). Briefly, the mRNA fraction was purified from total RNA by polyA capture, fragmented and subjected to cDNA synthesis. Barcoded DNA adapters were ligated to both ends of the double stranded cDNA and subjected to PCR amplification. The library products were evaluated using Fragment Analyzer (Agilent Technologies), then sequenced on an Illumina NextSeq500 sequencer using 75bp single-end reads,

generating ~17 million reads per sample. Quality control was conducted using the software Scythe (v0.991) and Sickle (v1.33). Transcript expression levels were then quantified in each sample by running the computer software Salmon v.1.0.0 against the reference sequence of the mouse transcriptome (Gencode M23-GRCm38). Differential expression analysis on sequence count data was performed using negative binomial distribution models as implemented in the library DESeq2 of R software (https://www.r-project.org/), using the Benjamini-Hochberg method to adjust the p-values for multiple comparisons. Transcript expression fold-changes were estimated for each expressed transcript in every comparison.

The most significantly up-regulated and down-regulated genes in i) AHDS-like (T3-) vs T3+ control organoids at day 7, ii) AHDS-like (T3-) vs T3+ control organoids at day 14, iii) AHDS-like (T3-) organoids from day 7 to day 14 (evolution analysis) and iiii) T3+ control organoids from day 7 to day 14 (evolution analysis) were then clustered into biological processes, cellular components and molecular functions by an enrichment analysis based on gene ontologies as implemented in the library dnet of R. Gene Set Variation Analysis was performed using the package GSVA (ver 1.38.2) of R to identify functionally enriched gene sets.

3.16 DNA extraction and mitochondrial DNA quantification of murine cerebral organoids

Total DNA was extracted from organoids (n = 9-11 for each time point) with proteinase K-based protocol. Briefly, each organoid was incubated in Lysis Buffer (Tris-HCl pH 8.5 100 mM, EDTA 5 mM, SDS 0.2% and NaCl 200 mM) supplemented with 10 µg/ml of proteinase K at 55°C for 2 hours. After centrifugation to remove cell debris, the supernatant was collected and DNA was precipitated with isopropyl alcohol, washed with 70% v/v ethanol, suspended in TE buffer and quantified with NanoDrop™ One/OneC Microvolume UV-Vis Spectrophotometer (ThermoFisher Scientific). Mitochondrial DNA was quantified by Sybr Green-based real time PCR (QuantStudio™ 3 Real-Time PCR System, Applied Biosystem) according to the ΔΔCt method (Quiros et al., 2017). The mitochondrial gene MT-ND1 and the nuclear gene Hexokinase 2 (HK2) were amplified from approximately 20 ng of total DNA. Triplicate experiments were

carried out for each biological replicates. For each time point, n = 9 organoids were evaluated. Statistical analysis was performed by one-way ANOVA followed by Tukey's comparison test. $p < 0.05$ was considered statistically significant. The same method was applied also for AHDS-like and T3+ organoids DNA extraction and mitochondrial DNA quantification.

3.17 Immunoblot assay in murine cerebral organoids

Immunoblot analysis was performed as previously described. Murine NSCs-derived organoids were pooled (n = 2 organoids/pool at 7 and 14 days, n = 5 organoids/pool at 21 and 32 days, frozen very dry at -80°C until use). Organoids were analysed at 7, 14, 21 and/or 32 days of culture. Samples were homogenized in modified radioimmunoprecipitation assay (RIPA) buffer [100 mM NaCl, 50 mM Tris-HCl pH 7.4, 1% NP-40, 1% sodium deoxycholate, 0.1% sodium dodecyl sulfate (SDS), DTT 5 mM, $MgCl_2$ 5 mM, Glycerol 3%, Phenylmethylsulfonyl fluoride (PMSF) 5 mM, and Benzonase 2 unit/µl] in the presence of protease and phosphatase inhibitors. Samples were incubated on ice for 30 minutes and centrifuged at 10.000g for 15 minutes at 4°C (AHDS organoids were sonicated with the ultrasonic bath (Branson 1800-E) for 1 min before the 30 minutes incubation on ice). Protein concentration was determined with the Bicinchoninic Acid (BCA) protein assay Kit (Thermo Scientific, Cat#A53225). Aliquots (20 µg each) were run through a 4–15% SDS–polyacrylamide gel electrophoresis (PAGE), electroblotted onto a PVDF membrane. Amido Black staining solution (Sigma, Cat#A8181-1EA) was used to detect total protein. After blocking, the membranes were probed by the primary antibodies (see paragraph 1.13) overnight at 4°C and subsequently incubated with horseradish peroxidase-conjugated secondary antibodies (anti-mouse, 1:5000, Promega, Cat#W402B; anti-rabbit, 1:5000, Promega, Cat#W4018) for 2 hours at room temperature. Chemiluminescence-based immunostaining (Clarity Western ECL Substrate, Biorad, Cat#170-5060) was performed. The quantification was performed using Image Lab software, version 6.0.1 for Mac (Bio-Rad Laboratories). The same method was applied also for AHDS-like and T3+ organoids immunoblot assay.

3.17.1 Primary antibodies used for immunoblot assay

The following primary antibodies were used: total oxidative phosphorylation (OXPHOS) rodent antibody cocktail (mouse, 1:1000, Abcam, Cat#ms604-300), VDAC-1 (rabbit, 1:5000, Abcam, Cat#ab15895), Lamin B (rabbit, 1:1000, Abcam Cat#ab16048).

3.17.2 Immunoblot image acquisition, analysis and quantification

Images were acquired with the ImageQuant LAS 4000 apparatus (GE Healthcare). The quantification was performed using Image Lab™ software, version 6.0.1 for Windows (Bio-Rad Laboratories). For each time point $n > 3$ organoid pools were evaluated. Statistical differences in graphs were calculated by ordinary one-way ANOVA. $p < 0.05$ was considered statistically significant.

3.18 Bioenergetic assessment in murine cerebral organoids

Organoids were kept at 37°C in a humidified atmosphere of 5% CO_2 in air, on an orbital shaker, with culture medium supplemented either with glucose or galactose as carbon source. Total ATP content was evaluated in samples at different time points. The glucose media consisted of DMEM supplemented with 17 mM glucose, 1 mM sodium pyruvate, 1% Pen/Strep, 2% B27 plus 1% N2 and 5 ng/ml bFGF or 50 ng/ml BDNF for organoids at 7 or 14 and 32 days, respectively. Galactose media consisted of DMEM supplemented with 5 mM galactose, 1 mM sodium pyruvate, 1% Pen/Strep, 2% B27 plus 1% N2 and 5 ng/ml bFGF or 50 ng/ml BDNF for organoids at 7 or 14 and 32 days, respectively. After 60 hours, the cellular ATP content was evaluated by CellTiter-Glo 3D Cell Viability Assay (Promega, Cat#G9681) in $n = 8$ (7 days), $n = 8$ (14 days), $n = 10$ (32 days) organoids for each condition, following manufacturer's instructions. To exclude any differences in cell proliferation/viability, a subset of organoids treated as above (7 days: $n = 4$, 14 days: $n = 4$ and 32 days: $n = 6$ for each media condition) was used for data normalization by evaluating the DNA content with CyQUANT Cell Proliferation Assay Kit (Promega, Cat#G9681), following manufacturer's instructions. Results were then expressed as A.U. relative to glucose and presented as mean ± SEM. Statistical

differences were evaluated by two-tailed unpaired t-test for two datasets (glucose versus galactose) at each time point. $P < 0.05$ was considered significantly different.

3.19 Live metabolic assessment in whole mount murine cerebral organoids via seahorse technology

3.19.1 Preparation of substrates', inhibitors and uncouplers stocks

Oligomycin (cat #04876; 50 mg/ml), FCCP (cat #C2920; 19.60-20.40 mg/mL), Rotenone/Antimycin A (cat #R8875/A8674; 0.5mg/ml Rot and 50mg/ml Ant A), 2-Deoxy-D- Glucose (cat #D8375; 50mg/ml dissolved in water), glucose (cat #G8270; 1g of glucose dissolved in 1.1 ml of water at 25 °C) were purchased from Sigma Aldrich. Stock concentrations were prepared by resuspending compounds in DMSO to obtain a final concentration of 1mM. Aliquots were stored at -20°C.

Mitochondrial stress test assay medium: as shown in ***Table 6***, the assay medium was prepared by resuspending 10 mM glucose, 4 mM glutamine and 1 mM sodium pyruvate in XF Agilent Base Medium DMEM (cat #102353-100). Then assay medium pH was checked and adjusted to 7.4, filtered and aliquots were made depending on the volume required for the assay. Short storage was done at 4°C, while long storage at -20°C.

Compound	Stock	Final concentration in port	Dilution
Glucose	1M	10Mm	1:100
Glutamine	200mM	4mM	1:50
Sodium Pyruvate	100mM	1mM	1:100

Table 6: *Mito stress assay media composition and final concentration in the sensor Cartridge port.*

Glycolytic stress test assay medium: as shown in ***Table 7***, the medium was prepared by resuspending only 4 mM glutamine in XF Agilent Base Medium DMEM (cat #102353-100). As for the mitochondrial stress medium assay, pH was checked and adjusted to 7.4, then filtered and aliquots were made depending on the volume required for the assay. Short storage was done at 4°C, while long storage at -20°C.

Note: both assay media can also be prepared the day of the assay. In any case, media must be kept at 37°C before use.

Compound	Stock	Final concentration in port	Dilution
Glutamine	200mM	4mM	1:50

Table 7: *Glycolytic stress assay media composition and final concentration in the sensor Cartridge port.*

3.19.2. Three days before the assay

3.19.2.1 Coating of seahorse V28 24-well microplate

To perform seahorse analysis on intact organoids, specific V28 24-well microplates were used. Organoids needed to be firmly attached to the bottom of the microplate, to obtain reliable results from the Seahorse assays. To this aim, a Poly-D-lysine coating was performed, preparing a sterile PBS 1X solution, at a final Poly-D-lysine (SIGMA Cat#P6407) working concentration of 100 µg/ml. For each well of the V28 plate, 150 µl of coating solution was added, and the plate was kept at 37°C in a humidified atmosphere of 5% CO_2 in air for 30 minutes. Afterwards, the coating solution was removed under sterile conditions and three washes with sterile distilled water were performed to remove Poly-D-lysine residues. Plates were kept open until dry, under the sterile hood.

3.19.2.2 Organoids' plating on the coated V28 24-well microplate

Organoids at different developmental stages (7 days, 14 days, 21 days, 30 days) were plated in the V28 24-well coated microplate (n = 5 replicates for each time point). Organoids were moved from their culture plate to the coated V28 microplate and placed exactly at the center of the well, taking care not to disrupt their integrity. Then organoids were resuspended (***Figure 10***) in a small volume (200 µl) of the specific culture media (according to the time-point) and statically incubated with 5% CO_2 at 37°C for 3 days before performing the assay, so they could stick to the bottom of the microplate. Wells A1, B4, C3 and D6 were left as blanks, containing only the respective medium but no samples.

Figure 10: *V28 24-well Seahorse microplate. Black signs indicate the blank wells (no samples). The other wells contain the organoids at various stages: line A: 7 days organoids; line B: 14 days organoids; line C: 21 days organoids and line D: 28 days organoids. On the right, detail of the V28 24-well Seahorse microplate. The black box indicates a magnification of the bottom of a V28 well (upper panel) containing an organoid (indicated by the black arrow) and a schematic rendition of the bottom of a V28 well (lower panel). The grey circle represents a schematic organoid, while the three white circles represent the sensors placed on the well's bottom.*

3.19.3 The day before the assay

3.19.3.1 Sensor cartridge hydration and seahorse instrument heating

The day before running the assay, the Seahorse instrument was set at 37°C and a sensor cartridge (***Figure 21***) was hydrated. This step was crucial, since each probe tip of the sensor cartridge contains sensors material that requires hydration for correct functioning, i.e detecting changes in O_2 concentration and pH.

To perform the hydration, the sensor cartridge (in green in ***Figure 11***) was removed from the utility plate (transparent plate in ***Figure 11***). The latter was filled with 1 ml of XF Calibrant (Agilent Technologies, Cat#102353-100) into each well. Subsequently, the sensor cartridge was placed back on the utility plate, with the hydro booster (in pink in ***Figure 11***) in between, such that the probe tips of the sensor cartridge were submerged in the XF Calibrant without touching the bottom of the utility plate. The sensor cartridge was placed in a non-CO_2 humidified incubator overnight.

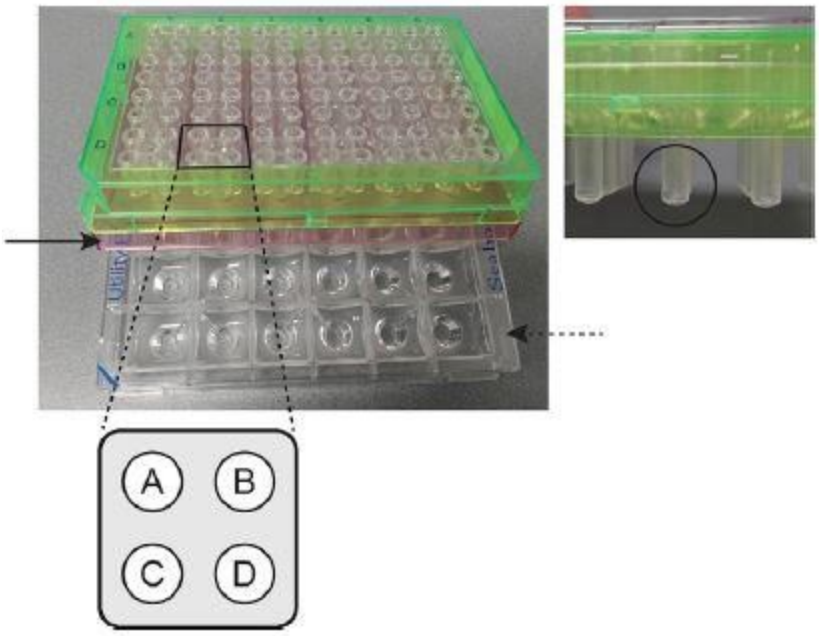

Figure 11: *24-well sensor cartridge (in green). Each 24-well has 4 ports, called respectively A, B, C and D (black square magnified in the schematic rendition), where different drugs can be pipetted. The dashed arrow indicates the transparent utility plate containing the XF Calibrant, while the black arrow shows the hydro booster (in pink). The magnified image on the right highlights the sensors of the cartridge (black circle showing a sensor in detail).*

3.19.4 The day of the assay

3.19.4.1 Preparation of the organoids plated in the V28 microplate for the assay

The Seahorse V28 cell culture microplate was removed from the 37°C, 5% CO_2 incubatorand organoids were examined under the microscope to ensure they are still attached to the bottom of the well. The culture medium was removed from the V28 microplate and the organoids were washed once with about 200-300 µl warmed assay medium (type of assay media depending on the test performed). V28 wells, including the blanks, were then filled up with 525 µl assay medium (mitochondrial stress test) or with 500 µl (glycolytic stress test) and placed in a non-CO_2 humidified incubator for 1h.

3.19.4.2 Preparation of the compounds to be loaded in the sensor Cartridge

The aliquots of inhibitors were prepared starting from the stock in assay media. Preliminary experiments were performed to test different concentrations of Oligomycin and FCCP, to achieve the appropriate but minimal concentration of drug required to

perform its function. After a series of titrations, the concentrations presented in ***Tables 8 and 9*** resulted to be ideal for the organoids' mitochondrial stress and glycolysis assays respectively.

Port	Compound in port	Final conc.	Conc. in port	Volume in port	Dilution in Assay medium
A	Oligomycin	3 µM	24 µM (8x)	75 µl	48 µl of Stock in 2 ml
B	FCCP	5 µM	40 µM (9x)	75 µl	90 µl of Stock in 2 ml
C	Rotenone/ Antimycin A	7 µM	70 µM (10x)	75 µl	140 µl each of Stock in 2 ml

Table 8: *Dilutions/Concentrations of inhibitors and uncoupler for the mitochondrial stress test.*

Port	Compound in port	Final conc.	Conc. in port	Volume in port	Dilution in Assay medium
A	Glucose	10 µM	100 mM (10x)	56 µl	0.15 ml of Stock in 1.5 ml
B	Oligomycin	3 µM	30 µM (10x)	62 µl	60 µl of Stock in 2 ml
C	2-DG*	50 µM	304.5 mM (6x)	123.6 µl	160 mg/3.2 ml

Table 9: *Dilutions/Concentrations of substrate and inhibitors for the glycolysis stress test*

*. *Note: the maximum solubility of 2-DG in aqueous solution is 50 mg/ml = 304.5 mM*

3.19.5 Running the assay

The assay was performed using the wave application, exploiting a template set up to run the specific type of assay. The first step was the calibration ("equilibration" in ***Tables 10 and 11***) of the hydrated sensor Cartridge. The Cartridge lid and the pink hydro booster must be removed before loading the Cartridge into the instrument. To note, the sensor Cartridge needs to have a specific orientation when positioned into the Seahorse instrument. Once calibration was completed, the utility plate was ejected by the instrument and the V28 microplate containing the brain

organoids in the assay medium was placed (with a specific orientation) into the Seahorse instrument and the assay started.

The template settings for the tests required to correctly measure the metabolism of brain organoids are reported in ***Tables 10 and 11***. The number of cycles for the drug administration were set up and extended, compared to the default settings, with the aim of allowing the compounds to better penetrate in the organoid and reach the inner mitochondrial membrane, considering the morphology and complex architecture of the 3D structures.

Settings			Default	Brain-derived organoids
Equilibration (recommended)				
Baseline	8 cycles	Mix	3 min	2 min
		Wait	2 min	1 min
		Measure	3 min	2 min
Injection 1 port A : Oligomycin	12 cycles	Mix	3 min	2 min
		Wait	2 min	1 min
		Measure	3 min	2 min
Injection 2 port B : FCCP	6cycles	Mix	3 min	2 min
		Wait	2 min	1 min
		Measure	3 min	2 min
Injection 3 port C : Rot/Ant A	8 cycles	Mix	3 min	2 min
		Wait	2 min	1 min
		Measure	3 min	2 min

Table 10: *Organoids' setting for the mitochondrial stress test.*

Settings			Default	Brain-derived organoids
Equilibration (recommended)				
Baseline	8 cycles	Mix	3 min	2 min
		Wait	2 min	1 min
		Measure	3 min	2 min
Injection 1 port A : Glucose	12 cycles	Mix	3 min	2 min
		Wait	2 min	1 min
		Measure	3 min	2 min
Injection 2 port B : Oligomycin	6cycles	Mix	3 min	2 min
		Wait	2 min	1 min
		Measure	3 min	2 min
Injection 3 port C : 2-DG	8 cycles	Mix	3 min	2 min
		Wait	2 min	1 min
		Measure	3 min	2 min

Table 11: *Organoids' setting for the glycolysis stress test.*

After the assay was finished, the organoids were washed once with PBS 1X to remove the residues of the assay medium. Afterwards, they were stored very dry at -80°C, for at least one night, before normalization.

3.19.6 Normalization of seahorse data via DNA quantification (RNase-treatment)

Quantifying bioenergetic parameters requires normalization to correct differences in numbers of cells, organoids, or the amount of biological material. Normalization of organoids was technically challenging due to the different number of cells inside the organoids at the various stages: early organoids are bigger, decreasing in size as the maturation proceeds. These features made it impossible to normalize the organoids' Seahorse data through the comparation of the cell number. Thus, a reliable alternative for the normalization of OCR and ECAR measurements was to take into account only the organoids' DNA content (Ludikhuize et al., 2021), but not the RNA. The latter was eliminated by pre-treating organoids with DNase-free RNase (Thermo Fisher, Cat#EN0531).

The CyQUANT Cell proliferation Assay Kit (Invitrogen, Cat#C7026) was used to perform the normalization. The kit includes 2 main components: cell lysis buffer and CyQUANT^{TM} GR dye, consisting in a green, fluorescent dye, that exhibits a stronger fluorescence as the binding to cellular nucleic acids enhances. Additionally, there is a prepared solution for the preparation of the standard curve (λ DNA standard). To create a DNA standard curve, a series of serial dilutions were made with 200 µl samples of bacteriophage λ DNA using CyQUANT^{TM} GR/cell-lysis buffer (already prepared reagent) to obtain concentrations ranging from 0-1000 ng/l. A control well was included which lacked DNA. Fluorescence was measured at an excitation wavelength of 480 nm and emission of 520 nm. Once the standard curve was ready, the organoids could be normalized.

After staying overnight at -80°C, as mentioned before, organoids were thawed in a 37°C non-CO_2 humidified incubator for 15 minutes then placed back at -80°C for

15 minutes. This passage was done three times to enhance the cells' lysis via thermal shock. At this point, DNA was isolated from 3D structures. To this aim, two working solutions (1 and 2) were necessary (***Table 12***). Note: the working solutions, specifically the probe contained in the working solution 2, are sensitive to light. Prepare each working solution right before use.

Working solution 1 (50 µl /well)	**Working solution 2 (50 µL /well)**
• 180 mM NaCl	• Lysis Buffer 1X
• 1 mM EDTA	• Probe 1:200
• 1X Lysis buffer (stock 20x)	• Bring to volume with distilled H_2O
• 1.35 kU/ml RNase (1000 kU/ml → 1KU/µL)	
• Bring to volume with distilled H_2O	

Table 12: *Solutions necessary for the DNA-quantification (RNAase-treatment) of organoids after seahorse.*

Initially, 50 µl of working solution 1 was added to each well, pipetted to break the organoids avoiding bubbles and then incubated at room temperature (RT) for 1 hour, protected from light. Subsequently, 50 µl of working solution 2 was added to wells, pipetted and the content of each V28 well was transferred into glass bottom 96-well cell imaging plate and incubated at room temperature for 2-5 minutes protected from light. Fluorescence measurements were made with the spectrophotometer Victor instrument, which reads the 96-well plates (Eppendorf #0030741030) at an excitation wavelength of 480 nm and emission of 520 nm.

3.20 Intracellular calcium imaging on whole mount organoids

To test spontaneous calcium activity, whole mount organoids at various developmental stages (7 days: n = 4; 14 days: n = 3; 21 days: n = 3; 32 days: n = 3)

were assessed with Fluo-4 Direct Calcium Assay Kit (Invitrogen). For calcium dye loading, the organoids were first incubated 10 minutes with HEPES pH 7.3 (Sigma, H3375-250G), rinsed and then incubated with equal parts of physiological salt solution (PSS) pH 7.4 (140 mM NaCl, 5 mM KCl, 1.2 mM Na_2PO_4, 1.4 mM $MgCl_2$, 1.8 mM $CaCl_2$, 11.5 mM glucose, 10 mM HEPES) and Fluo-4 acetoxymethyl ester solutions for 3 hours at 37°C. Excess dye was removed by washing with culture medium, and a 30 minutes incubation in culture medium was done at 37°C in order to allow the complete de-esterification of the dye and avoid artifacts such as continuous increase in fluorescence intensity during the experiment. Imaging was carried out at 37°C and 5% CO_2 using epifluorescence microscopy optics (Eclipse Ti Nikon Microscope), while the organoids were placed in glass bottom 96-well cell imaging plate (Eppendorf #0030741030) maintained in the appropriate culture medium according to their differentiation state.

Time-lapse imaging was performed at 1 frame/100 ms for 3 minutes and then processed using ImageJ software. For calcium imaging analysis the intensity signal of the calcium indicator of different cells of interest (n=10/organoid) within the organoids over the entire time of acquisition was measured using the "Plot Z-axis profile" plugin of ImageJ. The fluorescence change over time was defined as $\Delta F/F=(F-F_{basal})/F_{basal}$, where F is the fluorescence of a ROI at a specific time point and F_{basal} is the corresponding fluorescence of a background area. Cells were considered active when at least a change in the fluorescence intensity (peak) was detected. For each ROI corresponding to a selected cell within an organoid, the number of intensity fluorescence peaks were counted and expressed as mean of peaks per minute.

3.21 Rabies virus and adenovirus

To assess the synaptic connections between neuronal cells, organoids at 18 days (n = 6) were transfected with adenoviral vector *pAAV-Syn-H2B-GFP-TVA-oG-WPRE3* (MOI = 50) and kept at 37°C in a humidified atmosphere of 5% CO_2 in air, on an orbital shaker for the first 30 minutes, to promote the transfection and then in static culture for about 20 hours. Fresh medium was supplied the day after

transfection and the AVV cellular transfection was evaluated with a fluorescence microscope (Nikon Ti Eclipse). 48 hours later, *BRVenVA-1 G-deleted Rabies mcherry* (Osakada et al., 2011) virus (MOI = 0.25) was added to the culture media. The green, red, and yellow spots were evaluated in the following days by confocal microscope (LSM510 confocal microscope).

3.22 Quantitative RT-PCR analysis for SGZ-NSCs characterization

Total RNA was extracted from 4 different SGZ-NSCs samples (50.0000 cells/sample) and from 6 different mature (32 days) organoids sample (3 organoids: n = 3 pools of 6–8 organoids each) using the RNeasy Plus Micro Kit (Qiagen, Cat#74034) according to the manufacturer's protocol and RNA abundance was evaluated using the NanoDrop™ One/OneC Microvolume UV-Vis Spectrophotometer (ThermoFisher Scientific). Reverse transcription was carried out using Superscript VILO Master Mix (Invitrogen, Thermo-Fisher Scientific, Cat #11755050, Waltham, USA). Expression level of specific hippocampal or embryonic and neural stem cells genes was quantified by Sybr Green-based real-time quantitative RT-PCR (7900HT Real-time PCR System, Applied Biosystems) according to the ΔΔCt method and by using Tbp and Gapdh as reference genes for data normalization. The list of primers used for S*GZ*-derived mNSC characterization are illustrated in ***Table 13.***

Gene	**Forward**	**Reverse**
m*Sox5*	TACAAGGCTGGGTCCAGTGA	TGGGCCTAAGCCTGGTGTT
m*Sox1*	GCCGAGTGGAAGGTCATGTC	TGTAATCCGGGTGTTCCTTCA
m*Slc1a3*	ACCCCTGGGTTTTCATTGGA	GGGTAGGGTGGCAGAACTTG
m*Dach1*	CCATGGCAATGAGTCAGATGA	TCGGGAACACGCTCCTTAAT
m*Stat3*	GGGCACGAACACAAAAGTGA	CTCCCTAAGGGTCAGGTGCTT
m*Cdh1*	TCCTGGGCAGAGTGAGATTTG	TCTGTCGCCACTTTGAATCG
m*Klf4*	CTATGCAGGCTGTGGCAAAA	GGTTTCTCGCCTGTGTGAGTTC
m*Oct3/4*	CTGGGCGTTCTCTTTGGAAA	TGTTCTTAAGGCTGAGCTGCAA

m*Nanog*	AAGCGGTGGCAGAAAAACC	GTGCTGAGCCCTTCTGAATCA
m*Musashi*	GTTTGAGAGCGAGGACATCGT	CTTGCATTCCACCATTTTGTT
m*Nes*	TGTCCCTTAGTCTGGAAGTGG	GGTGTCTGCAAGCGAGAGTT
m*Dcx*	TTGGACATTTTGACGAACGA	CCCTTCTTCCAGTTCATCCA
m*Sox2*	GCACATGAACGGCTGGAGCAACG	TGCTGCGAGTAGGACATGCTGTAGG
m*Vim*	AGGAGGCCGAGGAATGGT	CATCGTTGTTCCGGTTGG
m*Pax6*	CAGCCCACCACACCTGTCT	ATGGGTGGCAAAGCACTGTAC

Table 13: *List of primers used for SGZ-derived mNSCs' characterization.*

3.23 Quantification and statistical analysis

Unless otherwise stated, n ≥ 3 samples or replicates were used for statistical analysis. Data on graphs are expressed as mean ± SEM. Statistical differences were calculated by two-tailed unpaired t-test for two datasets and ordinary one-way or two-way analysis of variance (ANOVA) test for multiple datasets using Prism (GraphPad Inc., La Jolla, CA). $p < 0.05$ was considered statistically significant. ∗∗∗∗$p < 0.0001$; ∗∗∗$p < 0.001$; ∗∗$p < 0.01$; ∗$p < 0.05$; *ns* not statistically significant.

4. RESULTS

4.1 Development of a standardized and reproducible protocol for murine brain organoids model

4.1.1 Generation of the protocol to grow murine brain organoids

To develop the new protocol, we took a cue from the already well-established protocol available for human-derived pluripotent stem cells published by Lancaster's group (Lancaster at al. 2014). We choose as primary cell source for the murine brain organoids' growth the neural stem cells (NSCs) isolated from the subgranular zone (SGZ), a well-known stem cells niche (Pino et al., 2017; Decimo et al., 2021), of mouse brain embryos (E14.5). The protocol consisted of three phases, in which time-windows and media supplements were strictly defined to determine the best NSCs proliferation and maturation (***Figure 12A***). During the first phase of the protocol, referred to as expansion phase (days 0–4), the SGZ-derived NSCs were seeded at a specific cell density (20000 cells/well) (Lancaster and Knoblich, 2014) in each well of a 24-well plate (day 0) and kept in dynamic culture in growth media supplemented with 20 ng/mL of epidermal growth factor (EGF) and 20 ng/mL of basic fibroblast growth factor (bFGF). At this stage, cells started to self-assemble into neurospheres (Figure 30B). To reduce cell proliferation and trigger cell differentiation, we subsequently lowered the growth factors concentration to 10 ng/mL EGF and bFGF (day 5) and then 5 ng/mL bFGF (day 7) (induction phase, days 5–14). By day 7, we observed organoids with smooth edges, a bright and optically translucent surface, and a darker center (***Figure 12B***).

To specifically induce neuronal differentiation and maturation, following the induction phase, we added the brain-derived neurotrophic factor (BDNF) 50 ng/mL to the culture media (differentiation phase, days 15–32) (***Figure 12A***). The BDNF belongs to the neurotrophin family, is a key molecule in neural development and function, and is required to increase the neurite number, length and complexity, as well as dendritic spine density in primary 2D NSC-derived neuronal cultures (Silva et al., 2009). During this phase, the organoids showed a thinner translucent surface with a darker core (***Figure 12B***).

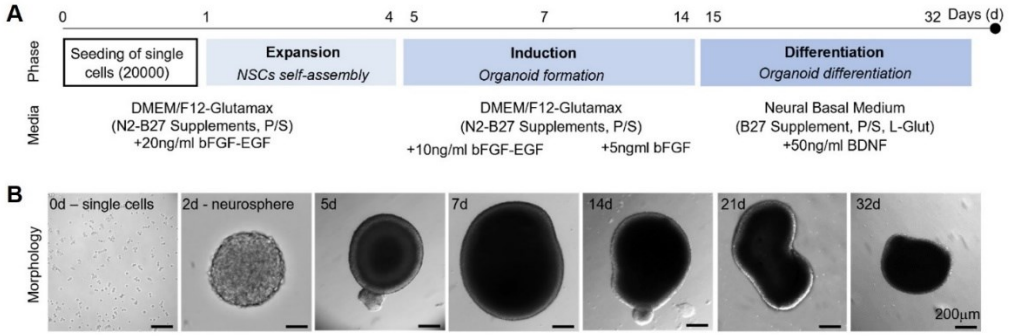

Figure 12: *Organoids' generation protocol.* ***(A)*** *Scheme of the three-phases mouse brain organoid generation protocol. After single cells (20.000 cells/well) seeding on a 24 well plate (day 0), the protocol started with the initial Expansion Phase that lasted up to day 4: mouse NSCs proliferated to form neurospheres in a culture medium enriched with bFGF and EGF (20ng/ml). Induction Phase from day 5 to day 14: early organoid formed in a medium supplemented with gradual decrease of bFGF and EGF (day 5 to day 6: 10 ng/ml bFGF and EGF; day 7 to day 14: 5 ng/ml bFGF). Differentiation Phase from day 15 to day 32: organoids matured in differentiation medium supplied with BDNF (50 ng/ml) up to day 32. During all the three phases, the organoids were maintained on an orbital shaker (dynamic culture). Adapted from Ciarpella, Zamfir et al., 2021.* ***(B)*** *Representative brightfield images of single NSCs (day 0), a neurosphere (day 2) and murine brain organoids at different time points (5 days, 7 days, 14 days, 21 days and 32 days). Scale bars: 200µm.*

To assess the overall success rate of organoids' formation by using this protocol, we quantified the number of formed organoids across different murine SGZ-derived NSCs batches (n = 7). A minimum of 54 organoids for each batch were produced, for a total of 732 generated 3D structures. Organoids successfully formed and maintained their structure along the 32 days *in vitro* culture in 95% of the cases, whereas the rate of organoids' disintegration after 14 days or no aggregation within the first 2 days was 5% (***Figure 13***) This data highlighted the achievement of an effective method to obtain murine brain organoids.

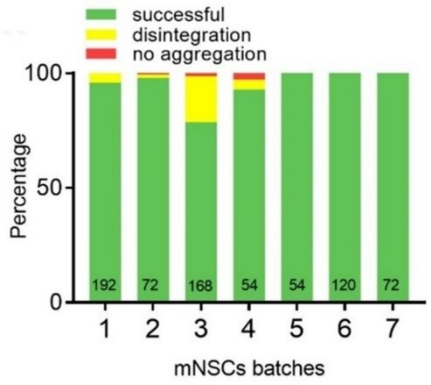

***Figure 13**: Percentage of successful (green) organoids generation**,** disintegration (yellow) or no aggregation (red) up to 32 days in vitro, for 7 different mNSCs batches (n = 732, number inside each bar indicates the number of organoids evaluated for each mNSCs batch).*

4.1.2 Murine brain organoids show homogeneous morphology according to the developmental phase

The precise initial cell seeding density allowed us to obtain, in each well, one organoid with defined size and low variability in organoids dimension (mm) was observed during all the culture stages. Morphological analysis revealed an increasing dimension of the organoids till the beginning of the induction phase with samples owning at day 4 a maximum diameter of 0.82±0.01 mm that reached their maximum size at day 9 (1.7±0.02 mm, n = 89). A stationary maximum diameter was then achieved starting from day 28 (0.79±0.01 mm, n = 59) (***Figure 14A***).

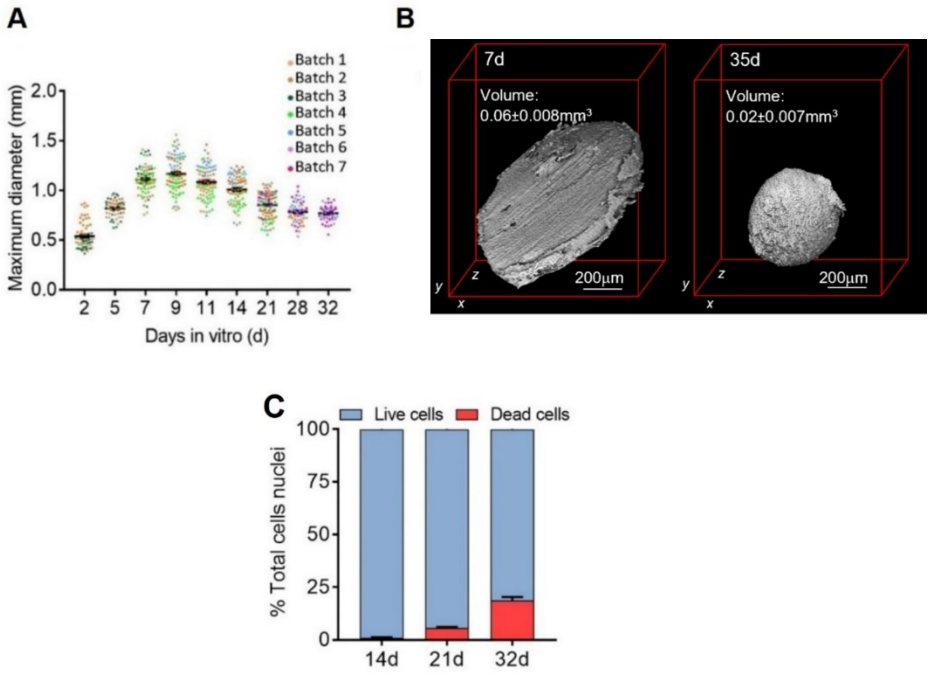

Figure 14: *Morphology and viability of murine brain organoids.* ***(A)*** *Graph representing the growth curve (diameter, mm) of murine brain organoids from day 2 to day 32. Data are expressed as mean ± SEM of the maximum diameter (n ≥ 30/time point). Organoids from different SGZ-NSCs batches were represented in distinct colors* ***(B)*** *Optical projection tomography (OPT) reconstruction of representative organoids at day 7 (beginning of the protocol) and day 35 (end of the protocol), showing the 3D structure of the in vitro generated organoids. The reported organoids volume was measured for n = 2 samples at day 7 and n = 3 samples at day 35, based on the 360-degree OPT reconstructions using Avizo. Data are expressed as mean ± SEM. The red boxes highlight the three-dimensional nature of the organoids, indicating the x, y and z axes. Scale bars: 200 µm.* ***(C)*** *Graph showing the number of live (blue bars) and dead (red bars) cells, expressed in % of total cells number. The analysis was performed on n = 3 organoids/time point (14, 21 and 32 days). Propidium iodide positive cells were dead cells, while the number of live cells was calculated by subtracting the number of dead cells from the total nuclei.*

The morphological assessment was then implemented by looking at the organoids' volume. 3D optical projection tomography (OPT) reconstruction (Belay et al., 2021) was performed in collaboration with Professor Jari Hittinen, BioMediTech, Faculty of Medicine and Health Technology, Tampere University, Finland. This analysis highlighted that during the induction phase, organoids at 7 days displayed a higher volume ($0.063 \pm 0.008\ mm^3$), associated with a considerable flat

appearance, compared to the differentiation stage ($0.023 \pm 0.007\ mm^3$), when organoids cultured for 35 days achieved a spherical shape (***Figure 14B***). These data are in line with the maximum diameter measures showed previously. The different shapes and volumes observed in the mature organoid compared with the early organoid may be correlated to a progressive changing in the cellular spatial organization during the *in vitro* organoid maturation.

Interestingly, in line with the relatively small dimension of organoids, we detected a high cell viability at all time points considered (98.97 ± 0.36% vs 94.17 ± 0.48% vs 81.21 ± 1.72% of live cells detected inside the organoids at 14, 21 and 32 days respectively; n = 3 organoids/time point) indicating that the even in mature organoids there is sufficient nutrient and oxygen diffusion that does not substantially impact the cell survival within the 3D structure (***Figure 14C).*** These data indicated the conditions we established for our protocol phases are suitable for maintaining organoids' vitality.

Overall, these results illustrated the effectiveness of the established method for murine organoids, which allow to obtain 3D structures with high vitality and a homogeneous growth in line with the three-phase protocol.

4.1.3 Murine brain organoids show reproducible features

To assess brain organoid features reproducibility and signature profile across their development, we performed global transcriptomic analysis (RNA sequencing – RNAseq), in collaboration with Professor Giovanni Malerba, Department of Neurosciences, Biomedicine and Movement Sciences at the University of Verona. Specifically, organoids at (i) early (end of expansion phase – day 7), (ii) intermediate (end of induction phase - day 14) and (iii) mature stages (differentiation phase - day 32) were analysed and compared to mouse cerebral tissues at neonatal (P0) and adult (3 months) stages. The various samples clustered in five groups following Principal Component Analysis (PCA) of the gene expression: (i) organoids at 7 days; (ii) organoids at 14 days; (iii) organoids at 32 days; (iv) P0 murine cerebral tissue and (v) adult mouse cerebral tissue (***Figure 15***).

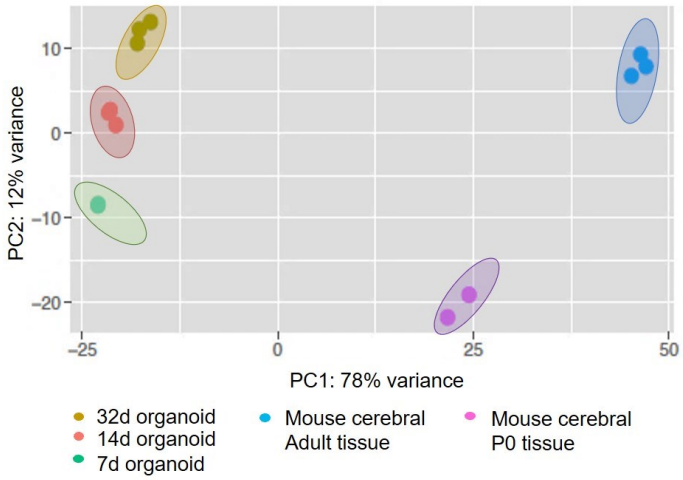

***Figure 15**: Principal components analysis (PCA) of RNAseq data performed on organoids and on murine cerebral tissues. Organoids were evaluated at different steps of the protocol (7 days: n = 3; 14 days: n = 3; 32 days: n = 3). Tissues were analysed at P0 (n = 2) and at adult (n = 3) stages. PCA illustrates organoids, as well as tissues, cluster according to their different maturation phase, as indicated in the graph's legend.*

These results confirmed that organoids at the same developmental stage present a similar gene expression signature, further reinforcing the reproducibility and robustness of the protocol. A progressive organoids' maturation can be observed during the various phases of the protocol, as shown by the clusters generated through the PCA. As expected, the samples' nature (organoid or tissue) accounted for the predominant source of PCA variation (Principal Component 1: 78%). Indeed, being *in vitro* generated samples, the organoids do not accurately mirror the *in vivo* development (Qian et al., 2019), an aspect that could explain the differences seen at the transcriptional level between the 3D structures and the murine tissue. Strictly, organoids belonging to the same developmental stage clustered together, determining the 12% of variation of the Principal Component 2 (PC2) (***Figure 15***).

Through gene ontology analysis we also found out that the most significant categories of up-regulated genes in mature organoids compared to immature ones resulted to be related to (i) ion channels, including voltage gated ion channels, calcium ion transport and development of calcium ion homeostasis; (ii) neuronal differentiation, including the formation of dendritic spines and the regulation of

neuron projection and (iii) synapse structures, vesicular trafficking and glutamate- and GABA-specific receptors (***Figure 16***).

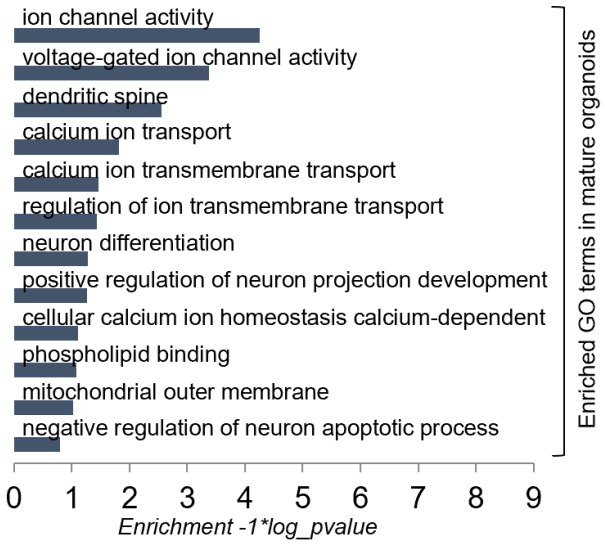

Figure 16*: Gene ontology (GO) analysis for upregulated genes in mature (32 days) versus early (7 days) organoids. GO terms enriched in the upregulated genes in mature compared to early organoids were classified according to their cellular components, molecular function and biological processes.*

Additionally, gene set variation analysis (GSVA) illustrated that genes related to NSCs identity (e.g., *Nes, Pax6, Sox2, Sox9 and Vim*) are highly expressed in the early and intermediate organoids, whereas genes related to mature neurons (e.g., *Map1b, NeuN, Snap25, Vamp1, and Syt1*) are mainly expressed in 32 days organoids (***Figure 17***). Major information about the selected gene list can be found in the Material and Methods section, ***Table 4***.

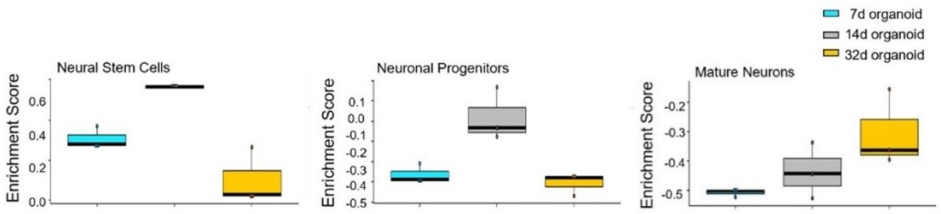

Figure 17*: Box plots of GSVA RNAseq data analysis generated based on specific gene list for three distinct categories: neural stem cells, neuronal progenitors and mature neurons. Analysis was performed on 7 days, 14 days and 32 days organoids, showing genes related to neuronal maturation*

are upregulated in late organoids. The Enrichment Score indicates the amount of over-representation of the genes in the specific gene list.

Overall, these data showed the development of a protocol for murine cerebral organoid generation that allow to obtain 3D structure sharing common features and progressively mature in culture with low variability among samples belonging to same developmental stage.

4.2 Characterization of brain organoid development and brain region identity specification

4.2.1 Organoids present neural differentiation and radial migration during the maturation

To better investigate the cellular composition of murine brain organoids and how cells spatial rearrange within the 3D structure during development, we combined immunofluorescence and RT-PCR analysis.

As a first step, we characterized the SGZ-derived murine NSCs used as source to generate the organoids via RT-PCR technique. As expected, we found that embryonic (E14.5) SGZ-derived neurospheres expressed the bona fide NSCs hallmark genes (Sox5, Pax6, Sox1, Vimentin, Dcx), the specific SGZ hippocampal derived NSC genes (Sox2, Musashi, Slc1a3, Nestin, Dach1), and ESC genes (Nanog, Oct3/4, Klf4, Stat3, Cdh1) (Abranches et al., 2009; Kuegler et al., 2010; Palmqvist et al., 2005) (***Figure 18A***).

The expression of SGZ hippocampal derived NSC (SOX2, Musashi, Nestin) and bona fide NSC (SOX1, Vimentin) markers (***Figure 18B***) was also confirmed by protein expression. No expression of the ESC markers (Oct3/4, Nanog, E-cad) was observed at protein level (***Figure 18C***).

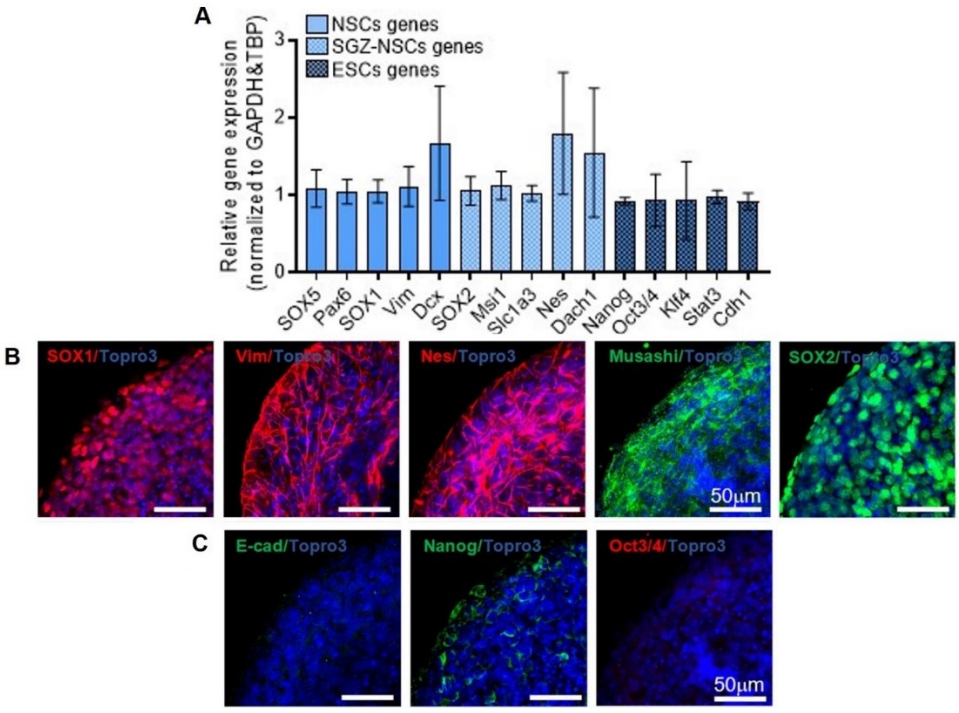

Figure 18: *Characterization of the starting cells.* ***(A)*** *Graph showing the Relative gene expression (normalized to GAPDH and TBP) levels of genes related to bona fide NSCs (SOX5, Pax6, SOX1, Vim, Dcx), SGZ-derived NSCs (SOX2, Msi1, Slc1a3, Nes, Dach1) and ESCs (Nanog, Oct ¾, Klf4, Stat3, Cdh1) evaluated in n = 4 different SGZ-derived murine NSCs batches. Data are expressed as mean ± SEM.* ***(B-C)*** *Representative confocal immunofluorescence images of SGZ-derived NSCs neurospheres at 3 days in culture, stained for specific NSCs, SGZ-derived NSCs and ESCs markers.* ***(B)*** *NSCs markers SOX1 and Vimentin (Vim) as well as SGZ-NSCs markers Nestin (Nes), Musashi and SOX2.* ***(C)*** *Specific ESCs analysed markers were E-Chaderin (E-Cad), Nanog and Oct3/4). Little or no expression of the ESCs markers were detected, confirming the starting cells used for the murine organoids' production were NSCs. All the pictures shown are maximum intensity projection of Z stack images and nuclei are stained in blue (TOPRO3). Scale bars: 50 µm.*

We subsequently focused on studying cell proliferation, thus we quantified the cells expressing the cell cycle G1/S-G2/M marker Ki67 (***Figure 19A and B***).

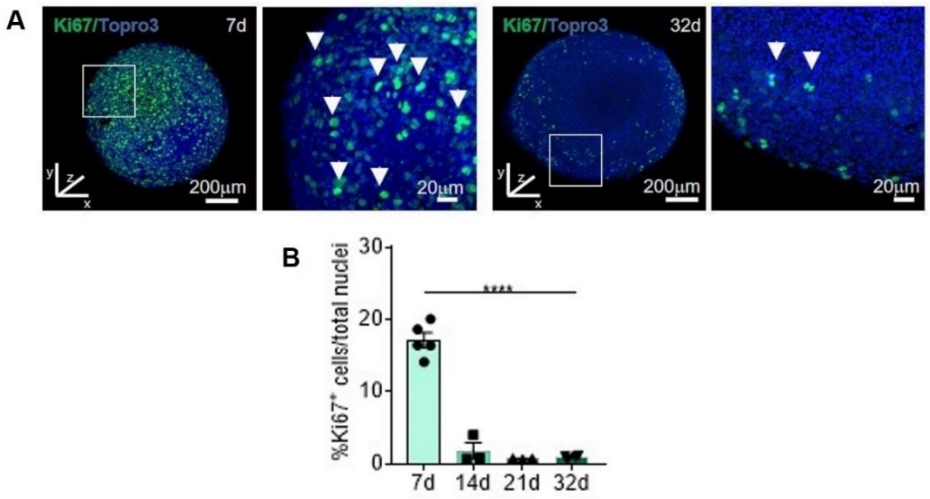

Figure 19: *Organoids' proliferation at different time-points.* ***(A)*** *Representative confocal immunofluorescence maximum intensity projections of Z stack images of whole mount murine brain organoids at 7 days (first panel on the left) and 32 days (third panel from the left), showing the Ki67 proliferative marker (in green). Total nuclei are marked in blue (TOPRO3). Scale bars for the whole mount: 200 µm. White boxes indicate a magnification of the whole mount organoids (second panel for 7 days and fourth panel for 32 days organoids, from the left, respectively). White arrows indicate Ki67$^+$ cells. Scale bar for the magnification regions: 20 µm.* ***(B)*** *Graph representing the % of Ki67$^+$ cells over total nuclei at different time points (7, 14, 21 and 32 days in vitro). Data are expressed as mean ± SEM. Analysis was performed on n = 3 different organoids and at least on 3 entire sections for each organoid. $p < 0.05$ was considered statistically significant. Statistical differences between marker expression at various stages were calculated by ordinary one-way ANOVA followed by Tukey's multiple comparison test. ****$p < 0.0001$.*

During the expansion phase, organoids showed a high proliferation rate, which drastically diminished from the end of the induction phase (Ki67$^+$ cells over total cell nuclei: 17.18±1.03% at 7d vs 1.9±1.08% at 14d; $p<0.0001$) to the differentiation phase (0.76±0.04% and 0.98±0.12% at 21d and 32d, respectively; $p<0.0001$) These data were in line with the morphological results, showing a decreased proliferation starting from the second stage of the established protocol, suggesting cellular maturation during the induction phase.

We thus evaluated the progressive cerebral organoid cellular differentiation. Specifically, we looked for the presence and localization of NSCs (SOX2$^+$ cells) as

well as neural progenitors (DCX^+ cells), immature ($TUBB3^+$) and mature ($MAP2^+$) neurons and glia ($GFAP^+$ cells).

Immunofluorescence analysis performed at the end of the expansion phase (day 7) showed a high number of stem cells expressing Vimentin (15.45±0.5% among the total cell nuclei) and sex determining region Y-box 2 (SOX2: 79.1±2.95% among the total cell nuclei), progressively decreasing during the differentiation (8.79±1.02% and 7.88±1.15% $Vimentin^+$ cells at 21 and 32 days, respectively, $p = 0.01$ and $p = 0.02$ respect to 7 days; 9.95±2.42% and 10.79±0.51% $SOX2^+$ cells at 21 and 32 days, respectively, $p<0.0001$ compared to day 7) (***Figures 20A, B, C and D***).

Qualitative analysis of cellular spatial distribution on sliced organoids showed that $Vimentin^+$ and $SOX2^+$ NSCs have an intersperse localization at day 7, which is maintained in the inner and the external layer until the later mature stage (Figure 38A-B). This scattering distribution was shown also in whole mount organoids immunostained at day 7 both for Vimentin (***Figure 20F***) and SOX2 (***Figure 20G***)

We also detected the presence of neural progenitors, expressing doublecortin (DCX) during the first stages of organoid formation (10.97±1.60% and 17.1±2.83% at 7 days and 14 days, respectively). The DCX^+ cells significantly diminished their number during later time points (day 21: 5.77±1.07%; day 32: 5.73±0.9%, $p = 0.01$ and $p = 0.009$ compared to day 14 respectively) suggesting that the maturation process towards the neuronal lineage (***Figure 20B and E***), in fact the increment in mature neurons ($MAP2^+$ cells) detected at 21 and 32 days (see Figure 23D) counteract the DCX decrease. Interestingly, both sliced (***Figure 20B***) and whole mount (***Figure 20H***) early organoids showed, at day 7, a widespread distribution of DCX^+ neural progenitors, whereas they spatially rearranged starting from day 14 (induction phase), clustering in the organoid's external region (***Figure 20B***).

Overall, as the cerebral organoid maturation proceeds, we observed a progressive statistically significant decrease in the number of stem cells and neuronal progenitors, occurring mainly at 21 and 32 days.

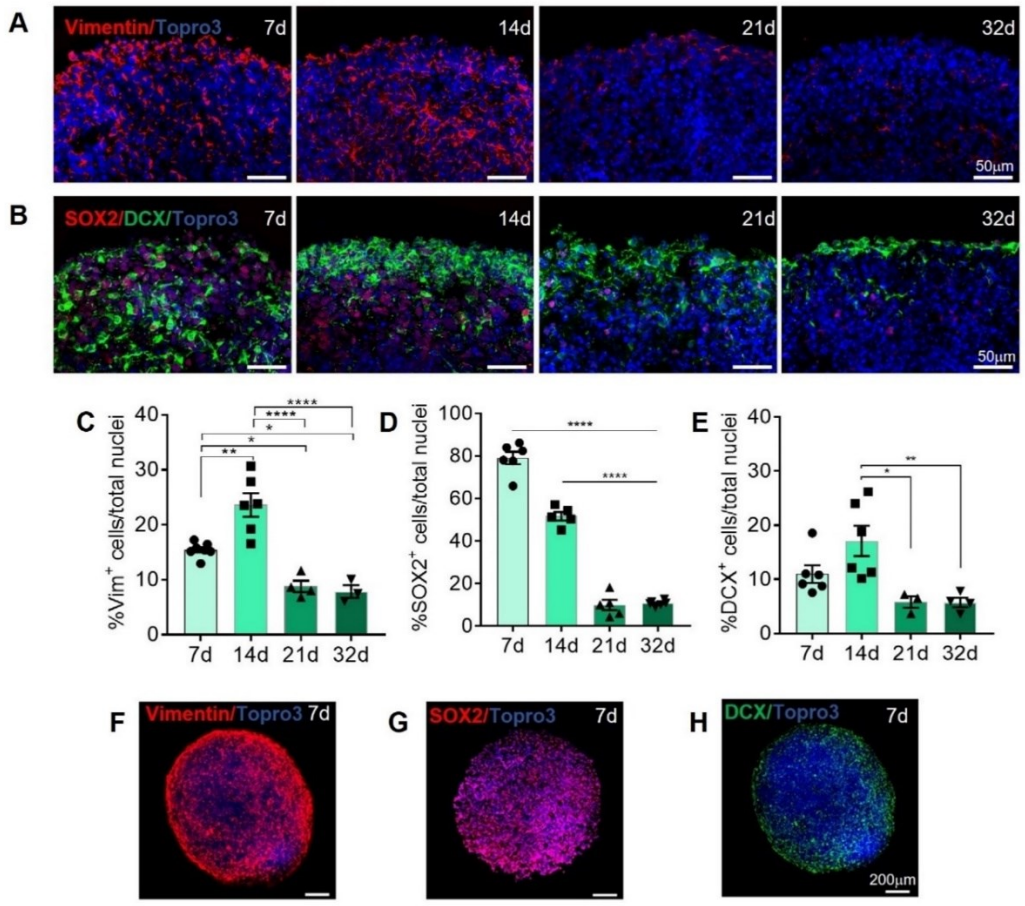

Figure 20: *Stem phenotype characterization of organoids.* ***(A-B)*** *Representative confocal immunofluorescence images of sliced organoids, showing the stemness Vimentin (A) and SOX2 (B) and the neuronal progenitors DCX (B) markers at different protocol stages. Total nuclei are stained in blue (TOPRO3). Scale bars: 50 µm. At day 7 and day 14, Vimentin$^+$ cells do not show an evident organization, with a widespread distribution inside the organoid. At later stages of maturation (days 21 and 32), few Vimentin$^+$ cells were still detected. Similarly, at day 7, SOX2$^+$ and DCX$^+$ cells inside the organoid lacked spatial organization. From day 14 (beginning of the differentiation phase), the immature neuronal cells spatially rearranged, clustering on the external layer of the organoid. The middle organoid's region remained mainly staminal (Vimentin$^+$ and SOX2$^+$ cells). At later time points (days 21 and 32), few SOX2$^+$ cells were present and DCX$^+$ cells were still localized on the organoid's edge. All the pictures in (a) and (B) are maximum intensity projection of Z stack images. Scale bars: 50 µm* ***(C-E)*** *Graphs representing the percentage of Vimentin (C), SOX2 (D) and DCX (E), positive cells over total cell nuclei at 7, 14, 21 and 32 days. Data in all graphs are expressed as mean ± SEM. Analysis was performed on n ≥ 3 different organoids and at least on 3*

*entire sections for each organoid. $p < 0.05$ was considered statistically significant. Statistical differences between marker expression at different time-points were calculated by ordinary one-way ANOVA followed by Tukey's multiple comparison test. ****$p < 0.0001$; **$p < 0.01$; *$p < 0.05$.* ***(F-H)*** *Representative confocal immunofluorescence Z stack-projection image of whole mount early (7 days) NSCs-derived organoid showing the presence and widespread distribution of Vimentin (F), SOX2 (G), and DCX (H) positive cells. Total nuclei are stained in blue (TOPRO3). Scale bars: 50 µm.*

Along with the decrease of the stem cells and neuronal progenitors, we observed a progressive neuronal maturation, confirmed by the increased number of neuronal cells overtime. Specifically, the immature neurons were highlighted by the expression of the Tubulin Beta 3 Class III (TUBB3) (17.55±2.35% and 7.63±1.56% at 32 days and 7 days, respectively; $p = 0.0014$) ***(Figure 23A and C)*** while mature neurons expressed the Microtubule-Associated Protein 2 (MAP2) (24.4±2.08% and 7.38±1.43% at 32 days and 7 days, respectively; $p < 0.0001$) ***(Figure 23B and D)*** As seen for the neuronal DCX^+ progenitors, both $TUBB3^+$ and $MAP2^+$ neurons were detected on the organoid's edge starting from day 14 and more consistently during the differentiation stage ***(Figure 23A and B)***. The immature as well as the mature neuronal external layer increased in thickness from the induction to the differentiation phase ($TUBB3^+$ cells layer: 18.69±0.55µm at 14 days and 30.96±3.99µm at 32 days; $MAP2^+$ cells layer: 17.89±1.13µm and 30.76±2.19µm at 14 and 32 days, respectively; $p = 0.0009$). These data are in line with the increment of the total neurons and with their rearrangement overtime, suggesting that SGZ-derived NSCs into the organoid undergo a progressive differentiation into neurons, mainly localized at the edge organoid's zone, forming a neuronal network ***(Figure 23F and G)***.

The maturation of neuronal cells observed via immunofluorescence was also confirmed via RNAseq analysis, performed in collaboration with Professor Giovanni Malerba, Department of Neurosciences, Biomedicine and Movement Sciences and Dr. Monica Castellucci, Centro Piattaforme Tecnologiche (CPT), University of Verona, Italy. Results underlined that mature organoids have an higher expression of genes encoding specific mature neuron proteins (*Vamp1, Map1b*) (Cahoy et al., 2008; Bifari et al., 2020; Zhang et al., 2014) and of genes

related to synaptic formation and plasticity (*Cttn, Nsg2, Syt1, Snap25*) and signal transduction (*Srrm3, Stmn2, Trim67*) compared to early organoids (***Table 14***). Major information about the selected gene list can be found in the Material and Methods section, ***Table 4***.

Gene	Padj	log2FoldChange
Cttn	5,49E-05	0,604238035
Nsg2	7,35E-49	1,727314216
Syt1	7,61E-13	2,227795404
Snap25	3,64E-16	2,029859858
Srrm3	4,64E-09	2,730721037
Stmn2	3,77E-09	5,992616238
Trim67	3,04E-24	1,812663846
Vamp1	0,000220385	1,924336274
Map1b	2,15E-07	0,794654091
Nsg1	0,297850458	0,209721151
Sdc2	4,11E-52	1,808401762
Mllt11	0,195099757	0,202658043
Rab3a	0,638534197	0,112657704
Gdap1	1,42E-09	1,1904085
Scn2a	0,000377824	0,873899441

Table 14: *upregulated genes related to neuronal differentiation in mature (32 days) versus early (7 days) organoids obtained by RNAseq analysis. Padj: adjusted p-values for multiple comparisons using Benjamini-Hochberg method; log2FoldChange: transcript expression fold-changes estimated for each expressed transcript comparing early and mature organoids (related to figure 21).*

The above-mentioned data were supported also by RNA-seq investigation in organoids at various developmental stages, considering the expression of mature neurons gene list dataset. Specifically, samples at 7, 14 and 32 days were compared. As the maturation proceeded, an increased expression of gene correlated to synaptic functionality, neurotransmission's regulation, metabolism and axonal growth were registered, as illustrated in the Heat map below (***Figure 21***).

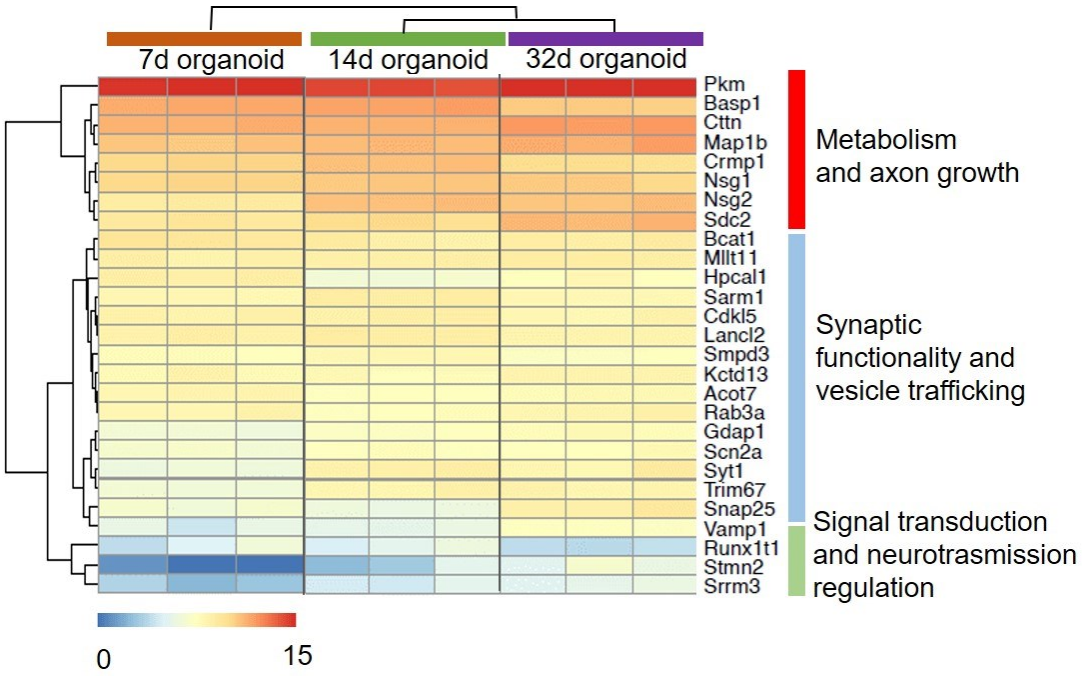

Figure 21: *Heat map of RNAseq data from organoid samples, analysed at different differentiation stages (7 days: n = 3; 14 days: n = 3; 32 days: n = 3) generated based on mature neurons gene list dataset. Analysis showed an increased expression of genes related to neurotransmission and synaptic functionality.*

It is well known that neural stem cells can originate both neuronal and glial cells, primarily. Additionally, we wanted to evaluate the cell heterogeneity of murine 3D model, thus we looked for the presence of glial fibrillary acidic protein $(GFAP)^+$ astrocytes as well as neural/glial antigen 2 ($NG2^+$) oligodendrocytes, ionized calcium-binding adapter molecule 1 ($Iba1^+$) microglia cells and cluster of differentiation 31 ($CD31^+$) endothelial cells via immunofluorescence staining. As expected, no oligodendrocytes, microglia, nor endothelial cells were detected at any

time point, while a stable number of ~10% of astrocytes was found in close association with neural cells both in sliced ***(Figure 23B and E)*** and whole mount samples ***(Figure 23G).*** RNA sequencing analysis further corroborated the presence of glia: the obtained data highlighted the expression of genes related to astrocyte maturation such as *Slc1a2* (encoding for a transporter protein that clears the glutamate from the extracellular synaptic space), *Aqp4, Gfap*, *Slc1a3* and *Slc4a4* (Boisvert et al., 2018; Cahoy et al., 2008) (***Table 15***). Major information about the selected gene list can be found in the Material and Methods section, ***Table 5***.

Gene	Padj	log2FoldChange
Slc1a2	4,94E-05	0,658058139
Aqp4	1,71E-159	4,837930849
Gfap	3,21E-90	8,579001665
Slc1a3	0,423719767	0,105205933
Slc4a4	0,076303712	0,23595097
Bmp6	2,44E-25	5,425047152
Paqr6	0,000495747	6,123786905
Ccdc80	1,94E-26	3,708314486
Itih3	1,13E-31	4,280860113
S100b	6,30E-93	3,332617766
Fgfr3	0,37888097	0,095574269
Bmpr1b	1,94E-07	0,723439631
Mlc1	8,69E-49	1,804347648

Table 15: *upregulated genes related to astrocytes specification and maturation in mature (32 days) versus early (7 days) organoids obtained by RNAseq analysis. Padj: adjusted p-values for multiple comparisons using Benjamini-Hochberg method; log2foldchange: transcript expression fold-changes estimated for each expressed transcript, comparing early and mature organoids (related to figure 22).*

RNA-seq analysis based on astrocytes gene list dataset was performed in murine organoids at various time-points, e.g. 7, 14 and 32 days. The Heatmap below illustrates that the genes specifically expressed in mature astrocytes increased in late organoids, regulating processes linked to ions' transport, metabolic development and regulation of cell differentiation and proliferation (***Figure 22***).

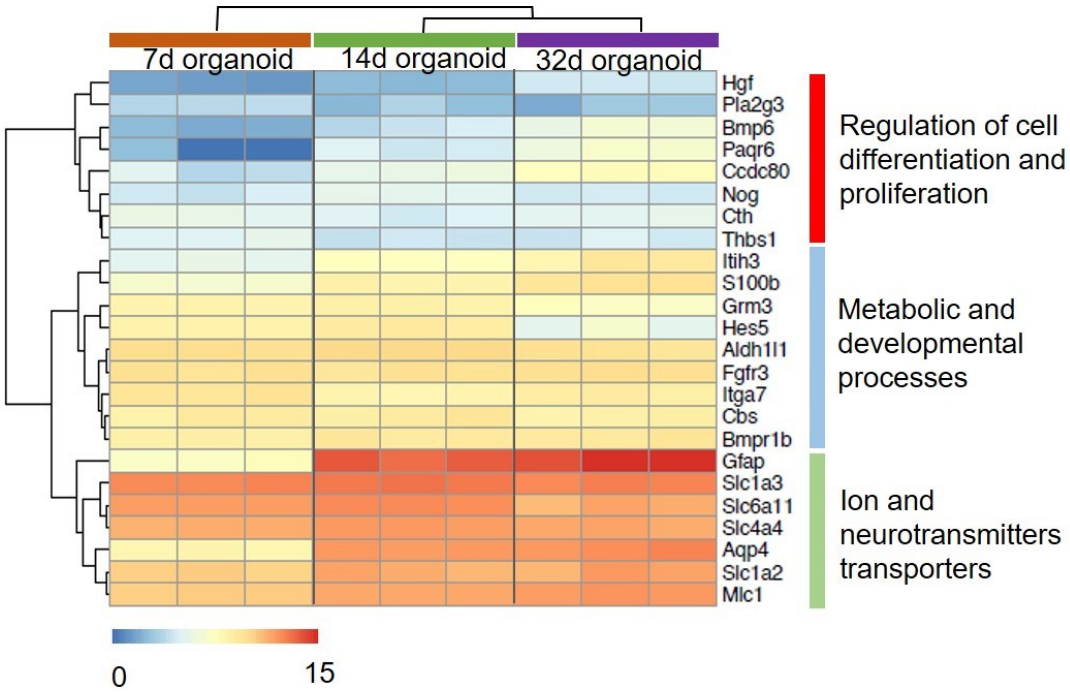

Figure 22: *Heatmap of RNAseq data from organoid samples at different stages of differentiation (7 days: n=3; 14 days: n=3; 32 days: n=3) generated based on astrocytes gene list dataset. Analysis illustrated an astrocyte's involvement in the metabolic and neuronal differentiation.*

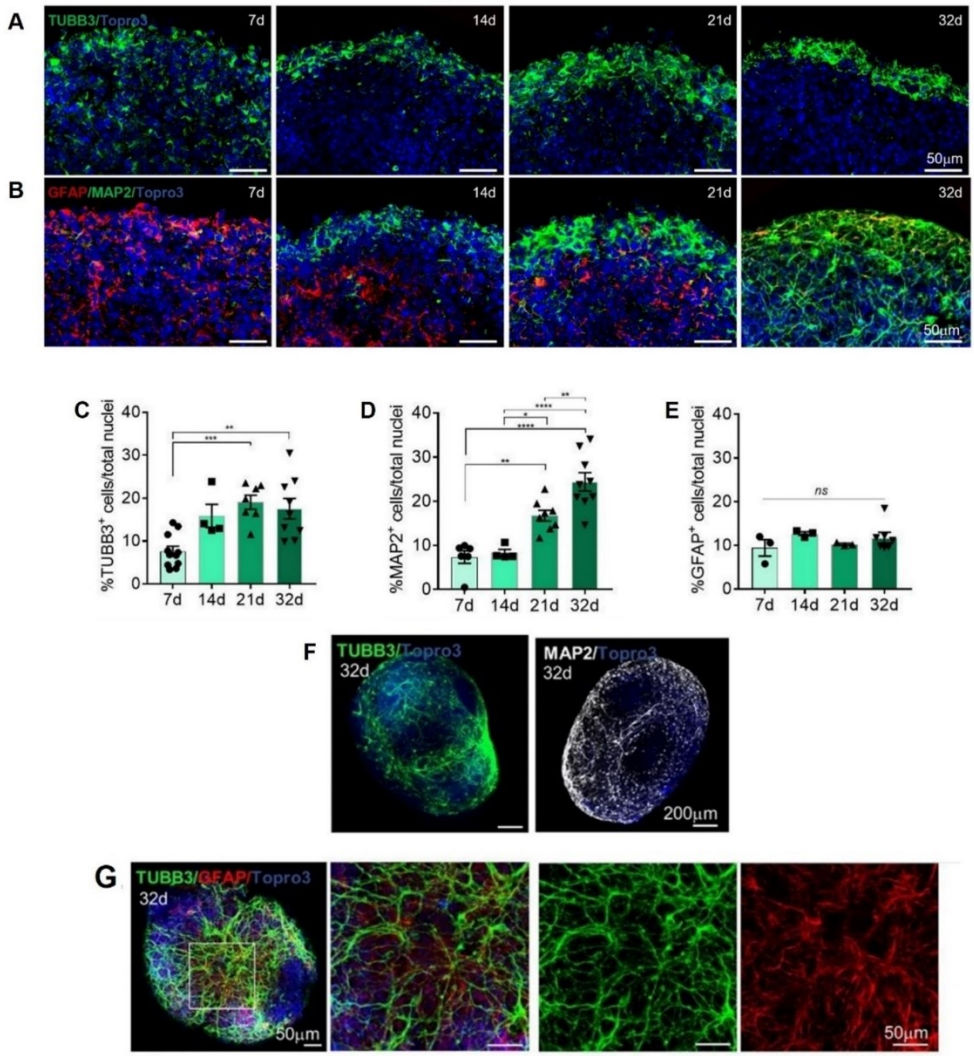

Figure 23: *Characterization of neuronal and glial phenotype.* ***(A-B)*** *Representative confocal immunofluorescence images of sliced murine brain organoids at different time points, illustrating the immature neurons (TUBB3$^+$ cells, in green), the mature neurons (MAP2$^+$ cells, in green) and the astrocytes (GFAP$^+$ cells, in red). At day 7, the organoid structure presented few scattered immature neurons, which progressively organized on the edge of the organoid starting from day 14 and along the late maturation stages (21 and 32 days). At 21 days, the TUBB3$^+$ edge is thicker compared to 14 days, with a minor thickening at 32 days, since at this time-point mature neurons are over-represented. During the protocol steps, the MAP2$^+$ cells increased in number, being in close association with the astrocytes and the neuronal maturation takes place on the organoid's external layer. A progressive thickening of the mature neuronal cell layer is observed overtime, along with the formation of a neuronal network at later stages (21 and 32 days). All the pictures in this figure are maximum intensity projection of Z stack images. Scale bars: 50 µm.* ***(C-E)*** *Graphs representing the percentage of TUBB3 (C) MAP2 (D) and GFAP (E) positive cells over total cell nuclei at different time points. Data in all graphs are expressed as mean ± SEM. Analysis was*

*performed on n ≥ 3 different organoids and at least on 3 entire sections for each organoid. Statistical differences between marker expression at different time-points were calculated by ordinary one-way ANOVA followed by Tukey's multiple comparison Test. p < 0.05 was considered statistically significant. ****p < 0.0001; ***p<0.001; **p < 0.01; *p < 0.05; ns not statistically significant.* ***(F)*** *Representative confocal immunofluorescence Z stack-projection images of whole mount mature (32 days) NSCs-derived organoid showing the distribution and neuronal network formed by TUBB3$^+$ (green) and MAP2$^+$ (white) positive cells. Nuclei are shown in blue (TOPRO3). Scale bars: 200 µI* ***(G)*** *Representative confocal immunofluorescence Z stack-projection image of whole mount mature (32 days) NSCs-derived organoid showing the presence of TUBB3$^+$ neuronal cells (in green) connected with GFAP$^+$ astrocytes (in red). Total nuclei are stained in blue (TOPRO3). The white box highlights a magnified zone, reported also in the green and red split channels. Scale bars: 50 µm.*

Overall, the different cellular populations identified inside the organoids rearranged during the development stages, defining a 3D structure that presents a radial distribution of the neuronal cells starting from the differentiation phase. Indeed, neuronal progenitors and immature and mature neurons cluster on the organoid's surface, while the stem cells preserved a widespread distribution inside the organoid at all time points (***Figure 24***).

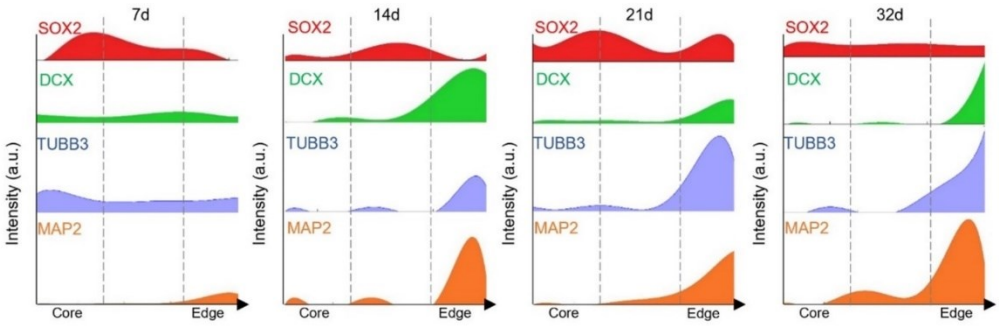

Figure 24: *Fluorescence intensity analysis illustrating the expression of SOX2 (red), DCX (green), TUBB3 (blue) and MAP2 (orange) plotted versus the distance from the center (left side of the graph) to the edge (right side of the graph) of brain organoids at 7, 14, 21 and 32 days. Upright black dashed lines define the various zones of the organoid's slice, from the core to the edge. Mature organoids showed a progressive accumulation of neuronal cells on the edge zone. The plots were obtained using the Plot Profile command in ImageJ (Fiji) followed by the Fit Function (8th Degree Polynomial) in ImageJ.*

Considering all the cells detected inside the generated organoids, early 3D structures (7 days in culture) showed mainly the presence of NSCs and neuronal progenitors (~80%). Consistently with the organoid's maturational steps, intermediate stage organoids (14 days) showed an increased number of immature neurons and neural progenitors (~32%) and at later stages (21 and 32 days) ~ 60% of the total cellular population was represented by immature and mature neurons (***Figure 24).*** As previously stated, astrocytes were detected during all the developmental stages of the protocol, maintaining a constant number (~10%)

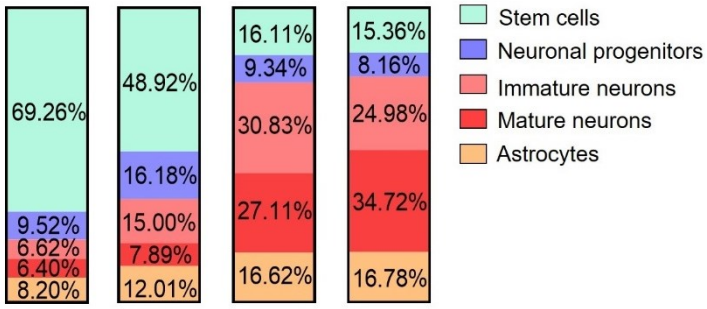

Figure 25: *Different cell populations over the total cellular populations' number, expressed in percentage in part-to-whole graphs. SOX2 marker is expressed in stem cells, DCX positive cells indicates neuronal progenitors whereas TUBB3 and MAP2 positive cells are immature and mature neurons respectively. GFAP positive cells identify astrocytes.*

Overall, these data indicated that the organoid showed a progressive maturation during the protocol's phases, decreasing the proliferation as well as the stem and neuronal progenitor populations overtime, phenomena balanced by an increment of the neuronal cells. Additionally, starting from day 14, during the induction phase, organoids are characterized by an organized distribution of neural cell types, not registered at previous time-points. Indeed, early-stage organoids were characterized by the spread proliferative and stemness markers expression, which lacked a specific structural organization. In keeping with the differentiation, organoids displayed a radial distribution of neurons which, during the mature stage, increased in number and outer layer thickness.

4.2.2 Organoids' neuronal maturation is sustained by the metabolic switch from a glycolytic to an oxidative process

Neuronal differentiation does not imply only changes in morphology and cellular distribution, but also in the metabolism. In fact, full neuronal differentiation requires a high amount of ATP, that is provided by the oxidative phosphorylation (OXPHOS) mechanism rather than glycolysis. The switch from glycolysis towards OXPHOS occurring in mitochondria is crucial for the differentiation of immature neuronal precursors into neurons (Bifari et al., 2020). So far, the bioenergetics of cerebral organoids has not been studied in depth and only few recent papers indicated a metabolic characterization of in vitro 3D systems (Ludikhuize et al., 2021; O'Brien t al., 2015; Menacho and Pigione, 2020).

We analysed the metabolic profile of developing organoids by evaluating the mitochondrial proteins expression as well as by live mitochondrial function analysis. First, we assessed the mitochondrial mass of the organoids throughout the different maturation stages of the protocol. An index of the mitochondrial mass is the mitochondrial DNA (mtDNA) copy number. This parameter progressively and significantly increased over time (438±36.47 mtDNA molecules/cell at day 7 against 809.7±59.82 mtDNA molecules/cell at day 32; $p < 0.001$), as shown in ***Figure 26A***. These data indicated an enhancement of the mitochondrial amount during the maturation of the organoid.

Subsequently, we performed immunoblot analysis on total cellular extracts to evaluate the mitochondrial proteins and OXPHOS system quantity. The mitochondrial markers were expressed as fold-change of the nuclear marker Lamin B, rather than as total protein content *per* lane. Indeed, considering the cell composition heterogeneity inside the brain organoids (see Figure 25) as well as their variation in size (Figure 14A) across the developmental stages, equal amounts of protein/organoid pool at different maturation phases may not correctly reflect the cell number. The voltage-dependent anion-selective channel 1 (VDAC 1) protein, a mitochondrial channel located into the outer mitochondrial membrane widely used as an indicator of mitochondrial mass (Bugiardini et al., 2020), underwent a

significant increment in the organoids during the protocol phases (from 1 ± 0.59 at 7 days to 19.99 ± 1.52 at 32 days; $p < 0.0001$) (***Figure 26H***). Beside, the amounts of specific complex subunits belonging to the mitochondrial respiratory chain complexes I-V increased as well (***Figure 26B***). Specifically, ATP5A, UQCRC2, MTCO1, SDHB, and NDUFB8 proteins, that are structural subunits of complexes V, III, IV, II, and I, respectively, significantly increased along the organoid's maturation process (**ATP5A**: 1.041±0.04 at 7 days vs 9.676±2.267 at 32 days; **UQCRC2**: 1±1.454 at 7 days vs 20.450±1.567 at 32 days; **MTCO1**: 1±0.671 at 7 days vs 19.130±0.429 at 32 days; **SDHB**: 1.262±0.262 at 7 days vs 9.619±1.277; **NDUFB8**: 1±0.798 at 7 days vs 26.240±1.244 at 32 days) (***Figures 26C-G*** respectively). Overall, these data confirms that organoids' mitochondrial mass as well as the electron transport through the inner mitochondrial membrane increased during their neuronal maturation.

To deeply characterize the metabolic shift of the organoids toward OXPHOS taking place during the neuronal maturation, we replaced glucose with galactose in the organoids' culture medium at different time points. Galactose is a highly oxidative substrate and the aim of this experiment was to force the organoids to use OXPHOS for the ATP production. The organoids' ability to produce ATP was evaluated by measuring the ATP content through the CellTiter 3D cell viability assay. When switching the carbon source to a fully oxidative substrate, early organoids (7 days) significantly decreased their ATP content in response to the galactose, illustrating they could not obtain energy by exploiting only the OXPHOS (7 days: glucose 1±0.07 vs galactose 0.47±0.03). Remarkably, we observed a 2-fold increase in cellular ATP content in intermediate organoids (14 days) cultured in galactose medium (14 days: glucose 1±0.06 vs galactose 2.21±036). Strikingly, this data suggested that organoids at this stage can switch to mitochondrial metabolism, if required. Total ATP content in mature organoids (32 days) was even higher (32 days: glucose 1±0.08 vs galactose 2.43±0.24) (***Figure 26I***), indicating the presence of complete differentiated mature neurons, capable to easily accommodate to oxidative substrates.

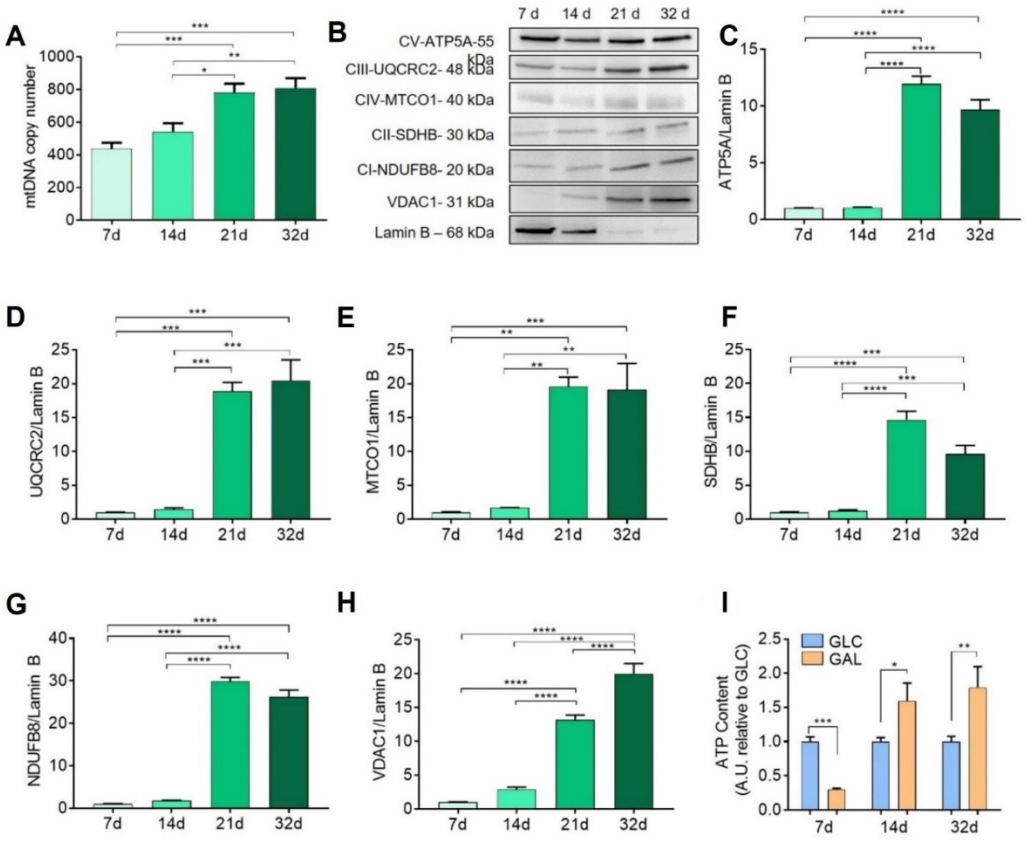

***Figure 26**: Organoids' mitochondrial assessment via immunoblot. **(A)** Mitochondrial mass, identified via mitochondrial DNA (mtDNA), progressively increased in organoids from day 7 to day 32. n = 9 organoids analysed for each time point. Data are reported as mean ± SEM. Statistical differences between time points were calculated by ordinary one-way ANOVA. $p < 0.05$ was considered statistically significant. ***$p < 0.001$; **$p < 0.01$; *$p < 0.05$. **(B)** Representative western blotting analysis, reported to the nuclear marker Laminin B, of organoids at various stages for OXPHOS complex subunits (ATP5A, UQCRC2, MTCO1, SDHD, NDUFB8) and VDAC1 protein, illustrating an increment of the electron passing through the electron transport chain and of the mitochondrial mass respectively. **(C-H)** Quantitative analysis of the western blot in (B). n>3 organoid/time point. Data are reported as mean ± SEM. Statistical differences between time points were calculated by ordinary one-way ANOVA. $p < 0.05$ was considered statistically significant. ****$p < 0.0001$; ***$p < 0,001$ **$p < 0.01$. Mature organoids (21 and 32 days) showed an increment in ATP5A (C), UQCRC2 (D), MTCO1 (E), SDHB (F), NDUFB8 (G) protein amount, when reported to the nuclear marker Laminin B, suggesting an increased electron transport chain activity in organoids' cells. **(I)** Graph indicating the total ATP content (expressed as A.U. relative to glucose) measured in organoids cultured in media containing different carbon sources (glucose – GLC, in blue and galactose – GAL, in orange). The analysis was done at different time points, considering $n \geq 8$ samples for each time point and normalized to cell number. Data are reported as mean ± SEM.*

*Statistical differences were calculated via two-tailed unpaired t test for two datasets (GLC vs GAL). $p < 0.05$ was considered statistically significant. ***$p < 0.001$; **$p < 0.01$; *$p < 0.05$.*

Mitochondrial respiration increases as the organoids' maturation proceeds

We also investigated mitochondrial respiration and electron transport chain (ETC) by Seahorse metabolic analyzer, which allows to assess, in live organoids, the mitochondrial function by real-time monitoring of the oxygen consumption rate (OCR), primary consumed by glucose metabolism via the citric acid cycle (Underwood et al., 2020). The mitochondrial respiration in organoids at different time points (i.e. 7, 14, 21 and 30 days in culture) was evaluated through the mitochondrial stress test implying the use of modulators to target the mitochondrial respiratory chain. The mitochondrial stress test allows the measurement of the basal respiration, maximal respiration, ATP-driven respiration, spare respiratory capacity, coupling efficiency and proton leak.

The basal OCR is defined by all the cellular processes consuming oxygen, including mitochondrial and non-mitochondrial respiration, thus, to obtain the basal OCR, the non-mitochondrial value is subtracted to define the mitochondrial oxygen utilization. The ATP-driven respiration indicates the quantity of ATP produced by the cell after the inhibition of the ATP synthase. The maximal respiration parameter is an index of the electron transport capacity of the cell, thus of the protons ability to flow into the inner mitochondrial membrane. The spare respiratory capacity indicates the cell's ability to increase the ATP production. This value is determined by the difference between the basal respiration and the maximal respiratory rate. The coupling efficiency indicates the reactions occurring into the ETC, thus the electron's transport into the inner mitochondrial membrane to produce ATP. Finally, the proton leak illustrates the permeability of the inner mitochondrial membrane to protons. The mitochondrial stress test illustrated a slight but significant decrease in organoids' mitochondrial basal respiration at the various analysed stages (***Figure 27A-D***).

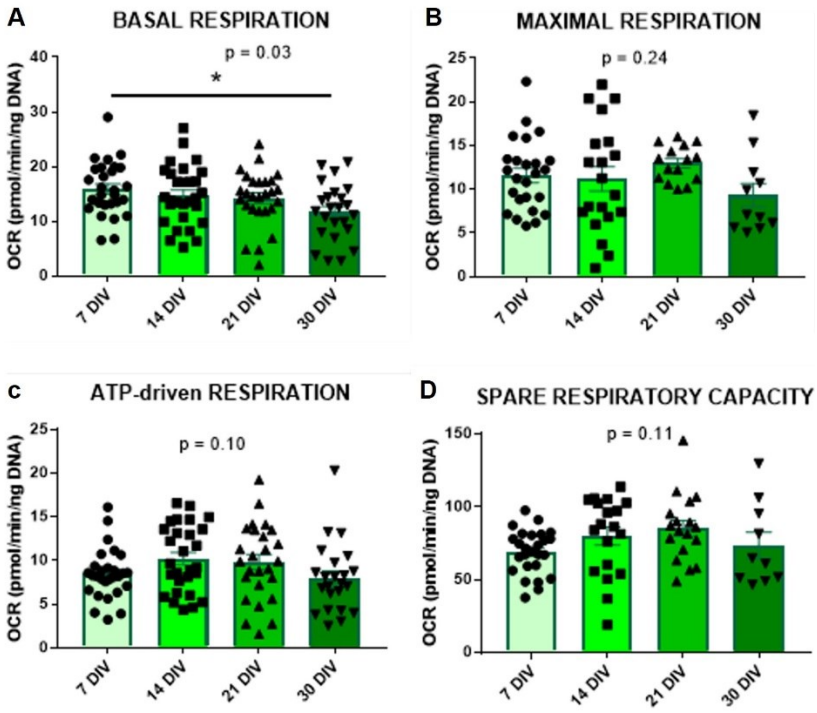

Figure 27: *Organoids' mitochondrial assessment via seahorse.* ***(A-D)*** *Basal respiration in 30 DIV organoids was lower compared to 7 days samples. Biological replicates: n = 6 independent experiments of different cultures and assay, performed on different days with 4-5 technical replicates for each biological measurement. Data are presented as mean ± SEM. Oxygen consumption rate (OCR) for mitochondrial respiratory parameters (i.e basal respiration, maximal respiration, ATP-driven respiration and spare respiratory capacity) expressed as pmol/min/ng DNA. Statistical differences between the various time points were determined by one-way ANOVA followed by H'lm-Sidak's multiple comparisons test. p < 0.05 was considered statistically significant. *p < 0.05. DIV: days in vitro*

Since these data alone are not sufficient to assess mitochondrial efficiency, we focused on ETC functioning by analysing the proton leak and the coupling efficiency of basal, maximal-ATP driven and spare capacity respiration, which are modular kinetics of OXPHOS (Brand and Nicholls, 2011). Both proton leak and coupling efficiency are parameters that describe the physiological state of the mitochondrial inner membrane and ETC, as well as the mitochondrial membrane potential. Thus, in order to assess the efficiency of the mitochondrial inner membrane and ETC based on the mitochondrial respiration analysis performed, I evaluated the mitochondrial coupling efficiency as a fraction between the OCR of

the basal respiration and the percentage of ATP produced ((OCR_{OLIGO} – $OCR_{ROT.ANT}$)/(OCR_{BASAL} – $OCR_{ROT.ANT}$)*100). Results showed that 7 days organoid had the lowest coupling efficiency, the latter increasing significantly across the maturational steps and reaching its maximum value in 30 days organoids (***Figure 28A***).

The proton leak across the mitochondrial membrane *in situ* was directly measured by evaluating the respiration rate in the presence of oligomycin. Oligomycin functions as an inhibitor of the complex V of the ATP synthase and it is injected during the Seahorse assay after the basal measurements. It has an impact on the electron flow through the ETC, resulting in a decreased OCR. The latter is linked to the ATP production. In line with the data obtained for the coupling efficiency, the proton leak was major in early organoids (7 days), while decreasing in the later developmental stages of the 3D structures (***Figure 28B***). Taken together, these results indicated that the mitochondria in the cerebral organoids acquired a more efficient coupling state during maturation.

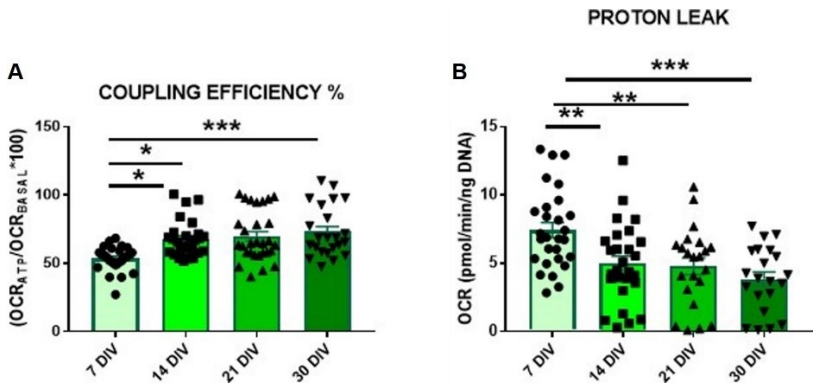

Figure 28: *ETC evaluation via seahorse.* ***(A)*** *Coupling efficiency reached its lowest value in 7 days organoids, increasing over time and reaching the highest value in 30 days organoids.* ***(B)*** *Proton leak decreased during the various developmental stages, with the lowest value registered in 30 days organoids. Both these parameters show an increased efficiency of the electron transport chain, indicating organoids, during their maturation, increased the use of OXPHOS for the ATP production. Biological replicates: n = 6 independentexperiments of different cultures and assay, performed on different days with 4-5 technical replicates for each biological measurement. Data are presented as mean ± SEM. Oxygen consumption rate (OCR) for mitochondrial respiratory parameters (i.e. coupling efficiency in percentage and proton leak), expressed in pmol/min/ng DNA.*

*Statistical differences between the different time points were calculated by one-way ANOVA. p < 0.05 was considered statistically significant. ***p<0.001; **p<0.01; *p<0.05. DIV: days in vitro*

Subsequently, we evaluated the non-mitochondrial respiration in the generated 3D model. This value is obtained after the inhibition of the complex I and III of the ATP synthase in the presence of rotenone (complex I inhibitor) and antimycin A (complex III inhibitor). The injection of such combination shuts down mitochondrial respiration and enables to obtain the non-mitochondrial respiration. Non-mitochondrial sources of ATP consumption results to be due to enzymes within the endoplasmic reticulum, peroxisomes or plasma membrane, for instance NADPH oxidases (Herst et al., 2004). After the rotenone/antimycin A injection, non-mitochondrial respiration significantly decreased between early (7 days) and mature (30 days) organoids (***Figure 29***). Overall, this parameter indicates that early organoids (7 days) do not activate OXPHOS process, mainly relying on non-mitochondrial respiration for their energy requirement. Strikingly, the opposite process occurs in late organoids (32 days), indicating they are able to perform oxidative phosphorylation.

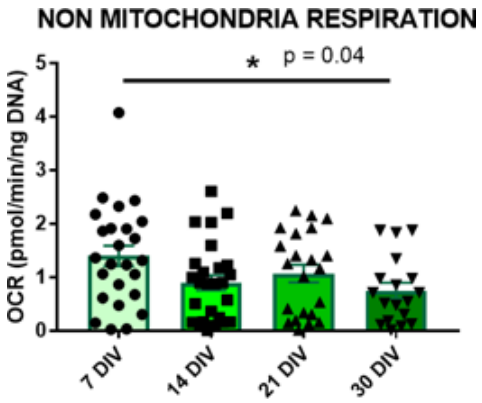

Figure 29: *Non mitochondrial respiration in organoids at various time-points. This data illustrates that in the presence of mitochondrial inhibitors, organoids at the earlier stages are not able to rely on OXPHOS mechanisms, exploiting the non-mitochondrial respiration. Mature organoids are able to reverse this aspect and lower their non mitochondrial respiration. Biologicalreplicates: n = 6 independent experiments of different cultures and assay, performed on different days with 4-5 technical replicates for each biological measurement. Data are presented as mean ± SEM. Oxygen consumption rate (OCR) for non-mitochondrial respiration expressed in pmol/min/ng DNA. Statistical differences between the various time points were obtained by one-way ANOVA, followed*

*by Tukey's multiple comparisons test. $p < 0.05$ was considered statistically significant. *$p<0.05$. DIV: days in vitro.*

Brain organoids showed lower glycolysis during the maturation process

Previously reported data suggested that early organoids rely preferentially on glycolysis for their energy production. To further assess the role of glycolytic pathway in brain organoids during their developmental steps, we performed a preliminary analysis by using the glycolysis stress test. ., We obtained the value of the extracellular acidification rate (ECAR), an estimation of glycolysis deriving from the lactate production. Specifically, we investigated the pivotal parameters of the glycolytic flux: basal glycolysis, the glycolytic capacity and the glycolytic reserve. Glycolysis is the metabolic process that converts glucose into pyruvate, an anaerobic reaction occurring in the cytosol (Kim et al., 2020). Such metabolic reaction generates ATP, NADH, water and protons. The following conversion of pyruvate to lactate produces the cofactor NAD+, that is extruded from the cytosol into the extracellular space, determining an increment of the ECAR. Through the inhibition of the mitochondrial ATP synthase, the metabolism is shifted to glycolysis and the subsequent increment in ECAR allows to define the cellular glycolytic capacity. The glycolytic reserve results from the difference between the glycolytic capacity and the glycolysis rate (see Material and Methods section for details). The obtained data illustrated a significant increase of the basal glycolysis from 7 to 14 days organoids and a significant decrease between 14 days and 30 days organoids (***Figure 30A***). A similar trend was seen for the glycolytic capacity (***Figure 30B***). No significant changes were observed for the glycolytic reserve between organoids at all time points (***Figure 30C***). Thus, considering this preliminary data and the results obtained from mitochondrial respiration experiments, it is possible to suppose a reduction of the glycolytic process during the maturation of the murine cerebral organoids.

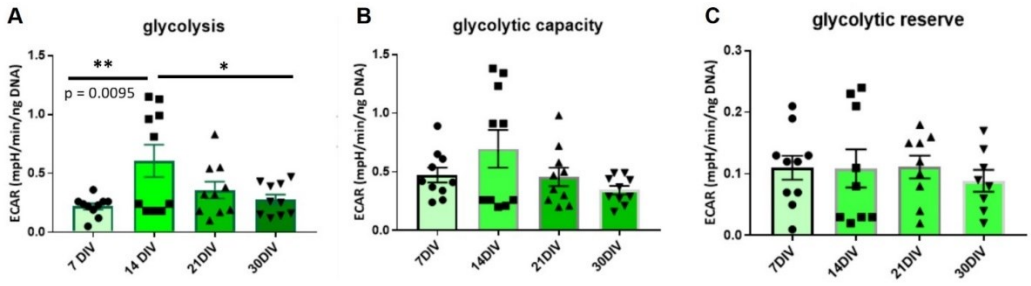

Figure 30: *ECAR evaluation in organoids.* ***(A)*** *ECAR increased from 7 day to 14 days organoids. Opposite results were obtained for organoids going from 14 to 30 days, meaning the glycolytic process diminishes as the maturation proceeds.* ***(B)*** *A similar trend was observed also for the glycolytic capacity, but no significant differences were detected.* ***(C)*** *No significant differences were registered for the glycolytic reserve. Biological replicates: n = 2 independent experiments of different cultures and assay, performed on different days with 5 technical replicates for each biological measurement. Data are presented as mean ± SEM. Extracellular Acidification rate (ECAR) for glycolytic parameters (i.e. glycolysis, glycolytic capacity and glycolytic reserve), expressed in mpH/min/ng DNA. Statistical differences between the various protocol's stages were calculated by one-way ANOVA. p < 0.05 was considered statistically significant. **p<0.01; *p<0.05. DIV: days in vitro.*

In conclusion, these results indicated that the progressive organoids maturation is paired to and sustained by changes of mitochondrial metabolism.

4.2.3 Murine brain organoids display neuronal maturation and cellular functionality

Mature murine brain organoids are characterized by a 3D neuronal network, forming inhibitory and excitatory synapses

To specifically analyze the neuronal maturation, we focused on the analysis of neuronal connection and expression of synaptic components combining sliced and whole mount immunostaining and 3D imaging reconstruction. As shown ***in Figure 31A and B***, mature $MAP2^+$ neuronal cells created an intricate neuronal network with cells localized on the entire organoid surface and elongating processes extending in the three dimensions across the organoid structure, suggesting that they may contact both adjacent and distal cells.

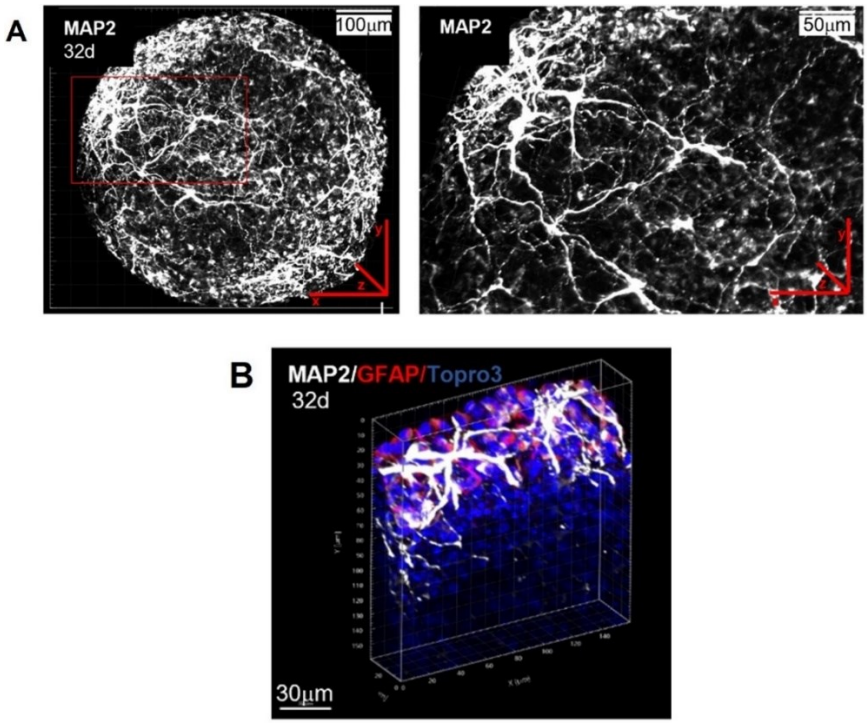

Figure 31: *Evaluation of neuronal phenotype in organoids.* ***(A)*** *Representative immunofluorescence maximum z projection confocal images of whole mount organoid at 32 days. The sample was stained for the MAP2 marker (in white), showing that mature neurons are characterized by the typical neuronal elongation processes. To note, the extensive network MAP2$^+$ cells form mainly on the organoid's external surface. The red box highlights a magnification region of the organoid, where neuronal processes can be better appreciated. Scale bar of whole mount organoid: 100 µm. Scale bar of the magnification: 50 µm.* ***(B)*** *Representative IMARIS 3D reconstruction of maximum z projection confocal image of a mature (32 days) organoid, immunostained for MAP2$^+$ cells (in white). Mature neuronal cells have a spatial distribution in all the three dimensions. Astrocytes (GFAP$^+$ cells), shown in red, localized close to the mature neurons. Nuclei are visible in blue (TOPRO3). Scale bar: 30 µm.*

To investigate whether the organoid has the potential to develop neuronal connections, we performed immunofluorescence analysis, evaluating the expression area of the presynaptic marker synaptophysin (Syn) in MAP2$^+$ neurons at different developmental stages. In line with the overall increment of MAP2$^+$ cells throughout organoid development (***Figure 32A and B***), illustrated also in ***Figure 23*** (MAP2*:* 24.4±2.08% and 7.38±1.43% at 32 days and 7 days, respectively; $p < 0.0001$), we observed the increased expression of Syn marker at day 32 (Syn

positive area over $MAP2^+$ area: 34.52±4.26 vs 0.62±0.25 at 32 and 7 days respectively, p< 0.001) (***Figure 32C***).

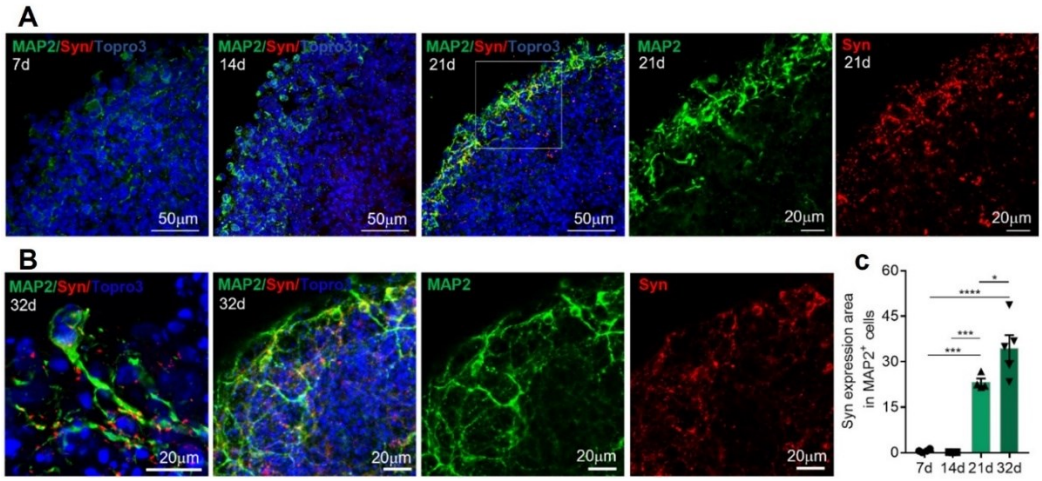

Figure 32*: Organoids form synapses.* ***(A)*** *Representative maximum Z projection of confocal images of sliced organoid*s stained *at 7, 14 and 21 days for the Synaptophysin (Syn, in red) and the MAP2 (green) markers. Early organoids (7 days and 14 days) showed no evident expression of Syn. Starting from day 21, organoids expressed Syn, which colocalized with the neuronal cells. White box in the third panel highlights the colocalization between Syn and MAP2 at 21 days, shown in the magnified separated channels. Scale bars: 50 µm. Scale bar for the magnified images: 20 µm.* ***(B)*** *Representative high magnification of maximum intensity z stack confocal projection of an image showing a mature (32 days) organoid (first panel). The sample was immunostained for $MAP2^+$ cells and for Synaptophysin (Syn) positive cells. The illustrated mature neuron had the characteristic elongation process and it colocalized with the Syn protein. Scale bar: 20 µm. Representative maximum intensity projection of Z stack confocal images of a 32 days whole-mount organoid (other panels). Immunostaining was performed for $MAP2^+$ (green) and Syn^+ (red) cells, showing neuronal cells and the synaptic marker colocalized. $MAP2^+$ cells and Syn^+ cells were also shown as separated images. Scale bar: 20 µm* ***(C)*** *Graph illustrating the synaptic density (% Syn^+ area in $MAP2^+$ cells area, in a 100 μm^2 field) during the steps of the organoids' development. Late organoids (21 days and 32 days) showed mature neurons having the capacity to generate synaptic contacts. Data are expressed as mean ± SEM. Statistical differences between the various time points were calculated by ordinary one-way ANOVA. p < 0.05 was considered statistically significant. ****p<0.0001; ***p < 0.001; *p < 0.05.*

To deeply analyse the synapses, we assessed the presence of inhibitory and excitatory synaptic puncta in mature organoids, specifically at 21 and 32 days. The presence of synapses was indicated by the co-localization of presynaptic and

postsynaptic puncta (Dzyubenko et al., 2016). In order to distinguish inhibitory (GABAergic) and excitatory (glutamatergic) synapses, I characterized the co-localization of specific pre-synaptic and post-synaptic marker proteins (Dzyubenko et al., 2016). Inhibitory synapses were marked by the vesicular GABA transporter vGAT and gephyrin, identifying respectively the pre- and post-synaptic terminals (***Figure 33A***), while the excitatory counterpart was indicated by the vesicular glutamate transporter VGlut and the scaffolding protein PSD95, localized at the pre- and post-synaptic terminals respectively ***(Figure 33B***). In keeping with what is observed during the physiological brain development (Levinson and El-Husseini, 2005; Cline, 2005), immunofluorescence analysis of vGLUT-PSD95 colocalization reached about 80% of the total synaptic puncta per 100 μm^2 in 21 days samples, revealing that excitatory synapses were mainly expressed in early mature organoids. In late mature organoids (32 days), the excitatory synapses were about 50% of the total amount of synaptic puncta. On the other hand, the analysis of the vGAT-gephyrin colocalization showed an increase of inhibitory synapses during organoid maturation (about 20% and 50% over the total synaptic puncta per 100μm^2 at 21 and 32 days, respectively). At the later mature stage (32 days) of organoid development, the relative amount of excitatory and inhibitory synaptic puncta reached an equal proportion (***Figure 33C***).

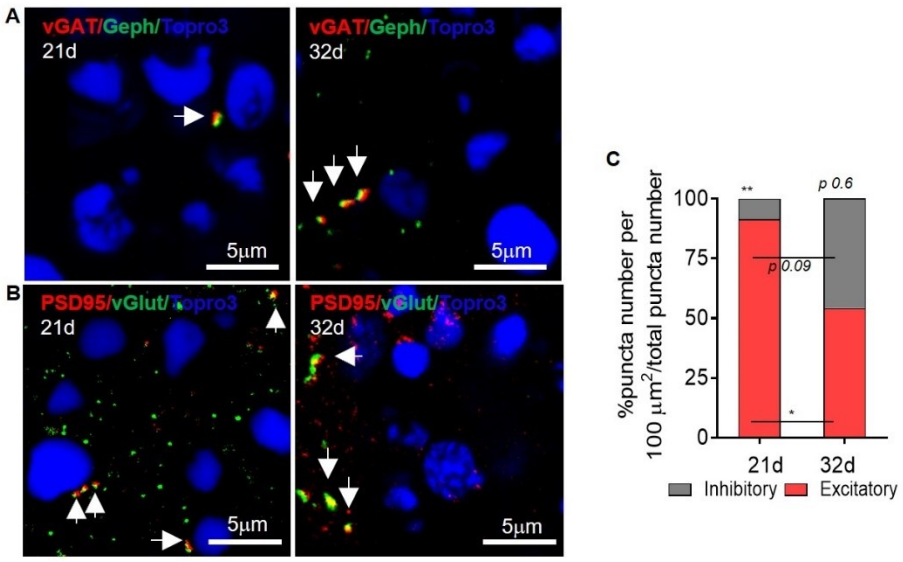

Figure 33: *Organoids form inhibitory and excitatory synapses.* ***(A-B)*** *Representative confocal immunofluorescence maximum intensity z stack projection images of sliced murine brain organoids. The analysis was performed on 21 days and 32 days samples, stained for synaptic markers. Specifically, organoids were tested for the presence of (A) inhibitory (vGat-Gephyrin) and (B) excitatory (PSD95-vGlut) synapses. The white arrows indicate the colocalization of vGat-Gephyrin and PSD95-vGlut in double-positive cells generating inhibitory and excitatory synaptic contacts, respectively. Nuclei are visible in blue (TOPRO3). Scale bars: 5 µm.* ***(C)*** *Graph displaying the percentage of inhibitory and excitatory synaptic puncta colocalization, in a field of 100 µm^2. Remarkably, while at 21 days the excitatory synapses (red bars) represented the majority of the total amount of synapses, at 32 days there was a decrement of the excitatory synapses paired to the increment of the inhibitory (grey bars) ones. The analysis was performed on n ≥ 3 different organoids and at least 3 entire sections for each organoid. Data in the graph are represented as mean ± SEM. p < 0.05 was considered statistically significant. Statistical differences between the different groups were measured by ordinary one-way ANOVA. **p < 0.01; *p < 0.05.*

In addition to the observed expression of synaptic proteins, we further evaluated the presence of inhibitory (***Figure 34***) and excitatory (***Figure 35***) synapses via transcriptomic analysis, performed in collaboration with Professor Giovanni Malerba, Department of Neurosciences, Biomedicine and Movement Sciences, University of Verona, using selected gene panels (Hayamizu et al., 2005). Heatmap profiles and DESeq2 analysis revealed that mature (32 days) rather than early (7 days) organoids showed an upregulation of genes related to NMDA and cholinergic receptors (i.e. *Chrm1, Chrm4*), glutamate receptors and reuptake (i.e. *Grin2b,*

Grin1, Grm4, Grik1) as well as GABA receptors and transporters (i.e. *Gabra4, Gabrb1, Camk4, Gabra1, Slc32a1, Gabra5, Gabrg2, GAD2*) (see ***Table 5*** in the Material and Methods section for major information about the selected gene list).

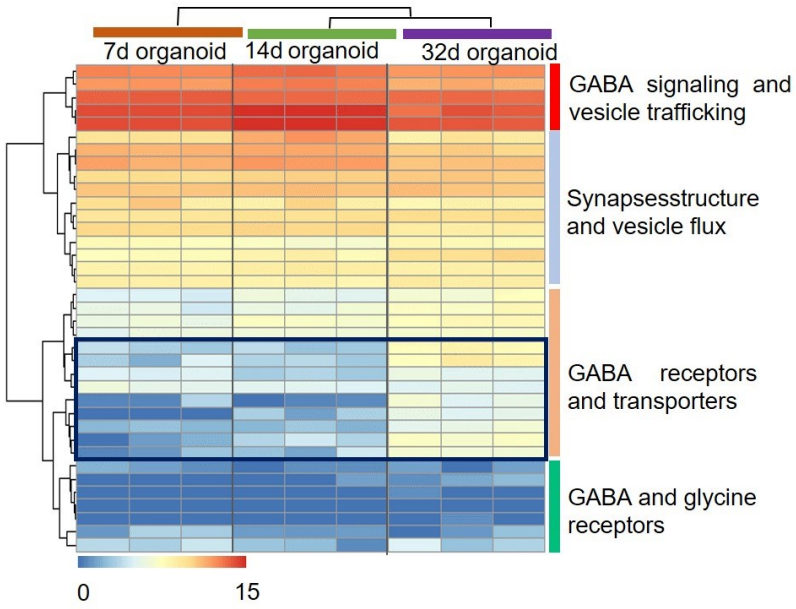

Figure 34*: Heat maps of RNAseq, generated based on inhibitory synapses gene lists. The analysis was performed on organoids at different developmental stages (7 days: n=3; 14 days: n=3; 32 days: n=3)s. Blue boxes highlight the most upregulated genes in mature organoids (32 days) compared to early organoid (7 days and 14 days). Specifically, the most up regulated inhibitory synaptic genes in 32 days organoids compared to early samples involve GABA receptors and transporters (i.e. Gabra4, Gabrb1, Gabrg3, Gabra1, Gabra5, Gabrg2, Camk4, Slc32a1, Gad2).*

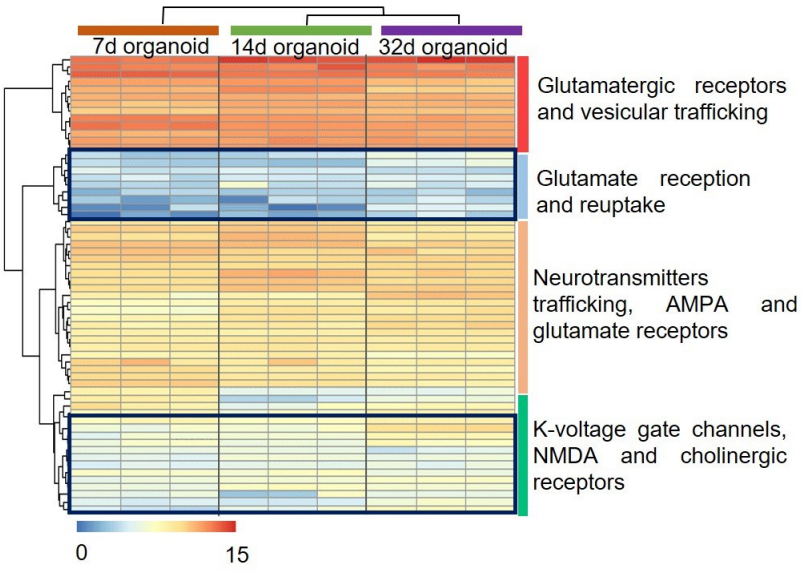

Figure 35: *Heat maps of RNAseq, generated based on excitatory synapses gene lists. The analysis was performed on organoids at different developmental stages (7 days: n=3; 14 days: n=3; 32 days: n=3)s. Blue boxes highlight the most upregulated genes in mature organoids (32 days) compared to early organoid (7 days and 14 days). Specifically, the most up regulated excitatory synaptic genes in mature organoids respect to early samples involve glutamate reception and reuptake (i.e., Grin2b, Grin1, Grin2a, Grm4, Grik1) and K-voltage gate channels, NMDA and cholinergic receptors(i.e., Kcnc4, Chrm1, Chrm4, Chrm3, Kcna3).*

Among all synaptic genes differentially expressed between early and mature organoids, RNAseq data illustrated that the gene expression of the *Kcc2,* the chloride extruding K^+-Cl^- cotransporter isoform 2, was upregulated in mature compared to early organoids (padj value <0.00001; log2FoldChange: 3.11) while the *Nkcc1,* the chloride-importing Na^+-K^+-Cl^- cotransporter isoform 1, was downregulated during organoid development (padj value <0.00001; log2FoldChange:−0.81) (see ***Table 16***). The change in the expression of *Nkcc1* and *Kcc2* during the organoid developmental stages might be an index of a shift of GABAergic-signaling from excitatory-to-inhibitory, an *in vivo* neuronal brain development feature (Ganguly et al., 2001; Rivera et al., 2005; Ben-Ari and Spitzer, 2004). Indeed, a low expression of NKCC1 and a high expression of KCC2 occurs in adult neurons (Liu et al., 2020).

Gene	Padj	log2FoldChange
Chrm1	0,136379601	0,617163002
Chrm4	0,217145943	0,563989234
Grin2b	NA	0,162510622
Grin1	0,087245674	0,58285698
Grm4	0,024267454	0,881524425
Grik1	5,42E-06	1,652355096
Gabra4	3,05E-22	5,054167025
Gabrb1	8,47E-15	5,002966532
Camk4	0,37045951	0,452115506
Gabra1	2,56E-06	5,404443403
Slc32a1	2,27E-09	8,089790215
Gabra5	9,04E-10	3,736376851
Gabrg2	3,89E-21	6,425753483
Gad2	1,49E-12	5,63162592
Kcc2	5,84E-13	3,108971239

Table 16: *Upregulated genes related to excitatory and inhibitory synaptic components in mature (32 days) versus early (7 days) organoids, obtained via RNAseq analysis. Padj: adjusted p-values for multiple comparisons using Benjamini-Hochberg method; log2FoldChange: transcript expression fold-changes estimated for each expressed transcript comparing early and mature organoids (related to Figures 34 and 35)*

In line with the data mentioned above, we identified inhibitory neurons, in murine organoids at 32 days, by the double staining of TUBB3 and glutamate decarboxylase 65-67 (GAD65-67) markers, while excitatory neurons were recognized, at 21 days, by double staining of N-methyl-D-aspartate (NMDA) and TUBB3 (***Figure 36A-B***).

It is well known that astrocytes are essential for the synaptogenesis occurring into the brain (Son et al, 2019). Considering the presence of those cells in our murine organoid model, we questioned whether they could contribute to boosting the synapses formation and specification at later time points of organoids' development. We immunostained 21 days organoids both for glutamine synthetase (Gln Syn) and GFAP and we found that astrocyte expressed Gln Syn, suggesting their possible contribution in the formation of the neuronal network (***Figure 36C***).

Overall, these data suggested that the 3D neuronal network formed by the mature brain organoids is coupled to inhibitory and excitatory synapses. Furthermore, the glial cells are integrated into the neuronal network, indicating synaptogenesis process is supported by mature astrocytes.

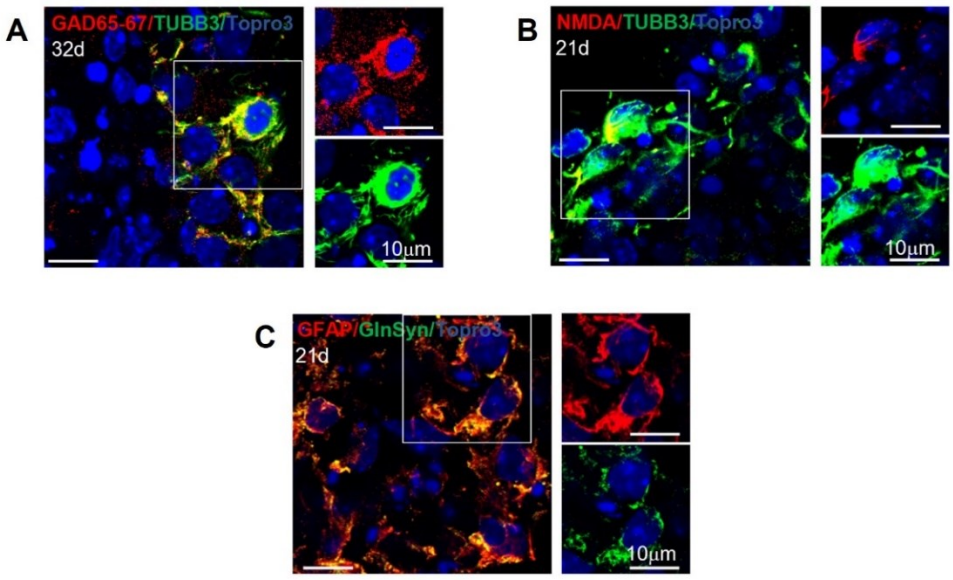

Figure 36: *Inhibitory/excitatory neurons and glia contribution to synapses' formation.* ***(A)*** *Representative confocal immunofluorescence maximum intensity z stack projection images of sliced organoids,immunostained at 32 days for the GAD65-67 (red) and TUBB3 (green) markers.* ***(B)*** *Representative confocal immunofluorescence maximum intensity z stack projection images of sliced organoid, immunostained at 21 days for the NMDA (red) and TUBB3 (green) markers.* ***(C)*** *Representative confocal immunofluorescence maximum intensity z stack projection images of sliced organoid, immunostained at 21 days for the GFAP (red) and Glutamine Synthetase (Gln Syn) (green) markers. The white boxes in (A-C) highlight the double positive cells shown also in the red and green split channels. Nuclei are visible in blue (TOPRO3). Scale bars: 10 µm.*

Developing organoids showed spontaneous cellular calcium oscillations

Together with the presence of synapses, we then questioned about functional neuronal activity. Spontaneous neuronal activity is an important step during neuronal development. The first spontaneous electrical activity in the immature brain is driven by intracellular calcium fluctuations (Rosenberg and Spitzer, 2011). We evaluated the overall intracellular spontaneous calcium fluctuations by time-course live calcium imaging in whole-mount cerebral organoid at different maturational stages, i. e. early (7 days) (***Figure 37A***), intermediate (14 days) (***Figure 37B***) and mature (21 days and 32 days, as shown in ***Figure 37C and D*** respectively) via the fluorescent calcium dye Fluo4-AM. The cellular spontaneous activity of the organoids was analyzed through 3 minutes of live-imaging acquisition and through the fluorescence intensity signal's evaluation of the calcium dye in different cells for each organoid (n = at least 10 cells/organoid, n = at least 3 organoids/time point). The Fluo4-AM dye presents a fluorescence's increment after binding Ca^{2+}, thus determining fluorescent signal, corresponding to intracellular calcium fluctuations.

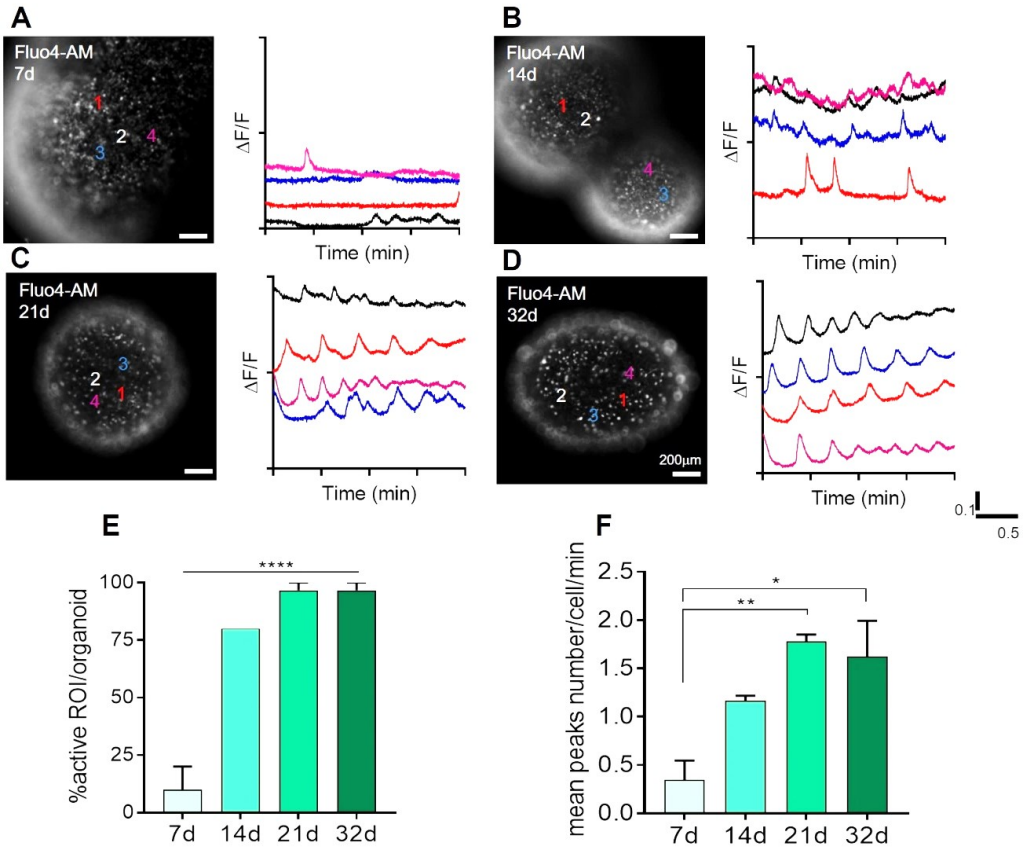

***Figure 37**: Calcium analysis in organoids along the developmental stages. **(A-D)** Representative fluorescence images of whole mount organoids during the time-lapse calcium FLUO4-AM dye assay. Organoids are shown in greyscale at various time-points (7 days in (A), 14 days in (B), 21 days in (C), 32 days in (D)). Each organoid is paired to the corresponding graph illustrating calcium oscillation of representative analysed cells (indicated with numbers from 1 to 4). Cellular activity, as well as peaks synchronization, increased overtime, reaching the maximum at 32 days. **(E)** Graph showing the percentage of active cells inside the organoid at 7, 14, 21 and 32 days (n = 3 organoid/time-point and n = 10 cells analysed/each organoid). **(F)** Graph illustrating the mean number of the peaks counted for each cell per minute at various time points (n = 3 organoid/time point and n = 10 cells analysed/each organoid). Data in both graphs are illustrated as mean ± SEM. $p < 0.05$ was considered statistically significant. Statistical differences between the different time points were measured by ordinary one-way ANOVA. ****$p < 0.001$; **$p < 0.01$; *$p < 0.5$.*

As shown in the graphs above (***Figure 55E and F***), early organoids present almost no peaks, indeed there were only 4 active cells out of 40 total evaluated cells. Starting from the differentiation phase of the protocol (day 14), an increment in the

Ca^{+2} spontaneous activity was observed, with 24 cells displaying calcium flux out of 30 total analyzed cells. The majority of the evaluated cells both at 21 and 32 days illustrated spontaneous Ca^{+2} fluctuations (29 active cells/30 analysed cells) along the acquisition time (***Figure 37E***). By evaluating the mean number of the detected peaks per minute of recording per organoids at different developmental stage, we observed a statistically significant higher number of calcium peaks in mature organoids (1.78±0.07 peaks/min, p = 0.006 and 1.62±0.37 peaks/min, p = 0.01 at 21 and 32 days respectively) compared to the peaks detected in early organoids (0.34±0.20 peaks/min at 7 days), as illustrated in ***Figure 37F***. These data indicated that the spontaneous calcium activity, as well as the peaks' synchronization, progressively increase during the organoids' differentiation steps.

Synaptic tracing showed functional synapses inside organoids

The presence of functional synaptic connections was further evaluated by exploiting the rabies virus (RABV)-based monosynaptic tracing technique (Wickersham et al., 2007). The expression of the EnvA receptor (TVA, e.g. RABV EnvA's receptor) under synaptophysin promoter was delivered into the organoids at 18 days in culture through the infection with a lentiviral vector encoding GFP- and EnvA-pseudotyped DG RABV (pAAV-Syn-H2B-GFP-TVA-oG-WPRE3). This initial procedure had the objective to confine primary RABV infection to the neuronal population expressing nuclear GFP, defined as "starter neurons" (***Figure 38***, left panel, white asterisk). After 48 hours, a second transduction was performed to infect the organoid with the rabies virus encoding for mCherry and the RABV glycoprotein (BRVenVA-1 G-deleted Rabies mCherry), considering that EnvA recognizes the TVA receptor on the starter cell. This step is crucial for the subsequent monosynaptic transfer to the starter cells' coupled neuron.

At this point, starter neurons were yellow (GFP^{+}/$mCherry^{+}$ double-positive) and were visible inside the organoid 24 hours after the second infection (***Figure 38***, middle panel, white asterisks and arrows). Inside the starter neurons the RABV was able to complete its structure by incorporating the G protein, necessary for the retrograde infection of neurons establishing synaptic contacts with a starter

neuron. Only the neurons activating a synaptic contact with a starter neuron ($GFP^+/mCherry^+$ double-positive) were able to be infected by the viral particle and they appeared red, since they expressed solely mCherry ($mCherry^+/GFP^-$), as illustrated in ***Figure 38*** (middle panel, white arrows). One week after the last transduction, clusters of $mCherry^+/GFP^-$ neurons were distributed on the external layer of the organoid (***Figure 56***, right panel, white arrows). These data indicated the creation of monosynaptic connections between $mCherry^+/GFP^-$ neurons and $GFP^+/mCherry^+$ double-positive starter neurons, suggesting that neurons of mature murine brain organoid established functional neuronal synaptic connections.

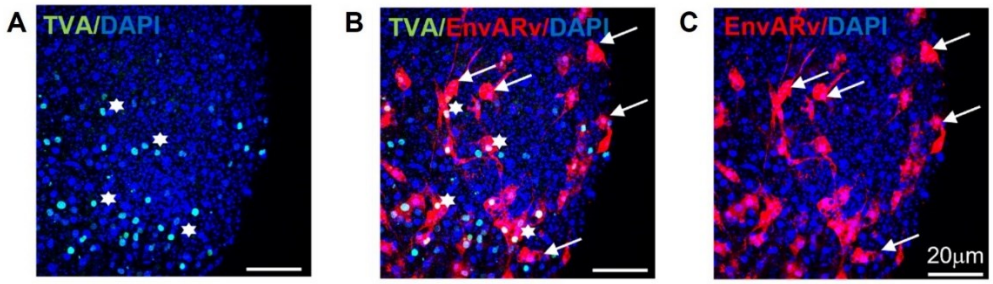

Figure 38: *Synaptic RABV tracing in mature organoids.* ***(A)*** *Representative maximum Z-projection of confocal images of Pseudotyped rabies virus (EnvARv)–based trans-synaptic tracing in neural cells of whole mount mouse hippocampal organoid at 32 days. Starter neurons are indicated by white asterisks.* ***(B)*** *Neurons inside mouse hippocampal organoids formed a complex active neuronal synaptic network, as confirmed by the presence of $GFP^+/mCherry^+$ neurons (white asterisks and arrows) and* ***(C)*** *$GFP^-/mCherry^+$ pre-synaptic input neurons (white arrows). Note the lack of GFP signal and the proper expression of mCherry reporter in (C). Scale bars in all panels: 20 µm. Nuclei are indicated in blue (TOPRO3) in all images.*

In conclusion, the analysis presented so far showed that mature brain organoids have the ability to establish 3D neuronal network and the presence of spontaneous cellular activity in mature organoids. Taken together, these elements pave the way for the generation of functional circuits throughout the 3D structure (Khazipov and Luhmann, 2006).

4.2.4 Murine brain organoids showed dorsal forebrain identity

The protocol for the generation of murine cerebral organoids described in this work does not imply the administration of any extrinsic patterning factor into the culture media. Thus, the organoids' development in not guided towards a specific brain region, but single SGZ-derived NSCs rely on spontaneous neuronal differentiation. Given the origin of NSCs cells, they might intrinsically be directed towards different cerebral regional patterning, such as dorsal or ventral. We deepen this aspect by characterizing the regional cerebral identity of the murine organoids at 7 days, 14 days and 32 days and compared it to murine adult cortical and hippocampal tissues. We reached this aim through RNAseq analysis, performed in collaboration with Professor Giovanni Malerba, Department of Neurosciences, Biomedicine and Movement Sciences, University of Verona, Italy.

We evaluated the percentage of similarity between the organoids and the murine tissue. As expected, *hippocampal and cortical tissue revealed 100% of similarity for hippocampal and cortical gene sets,* respectively, validating the reliability of the selected genes. Early organoids (7days and 14 days) do not acquire a defined regional identity considering the RNAseq analysis did not reveal any similarity between the gene set of adult murine cortex and hippocampus and organoids at these time-points. Remarkably, 32 days organoids had about 70% of gene similarity with hippocampal adult murine tissue and about 30% with cortical adult murine tissue (***Figure 39***). These data suggested mature organoids may spontaneously acquire a dorsal forebrain signature, with a major hippocampal component. However, this did not exclude the possible presence of other brain regional identities.

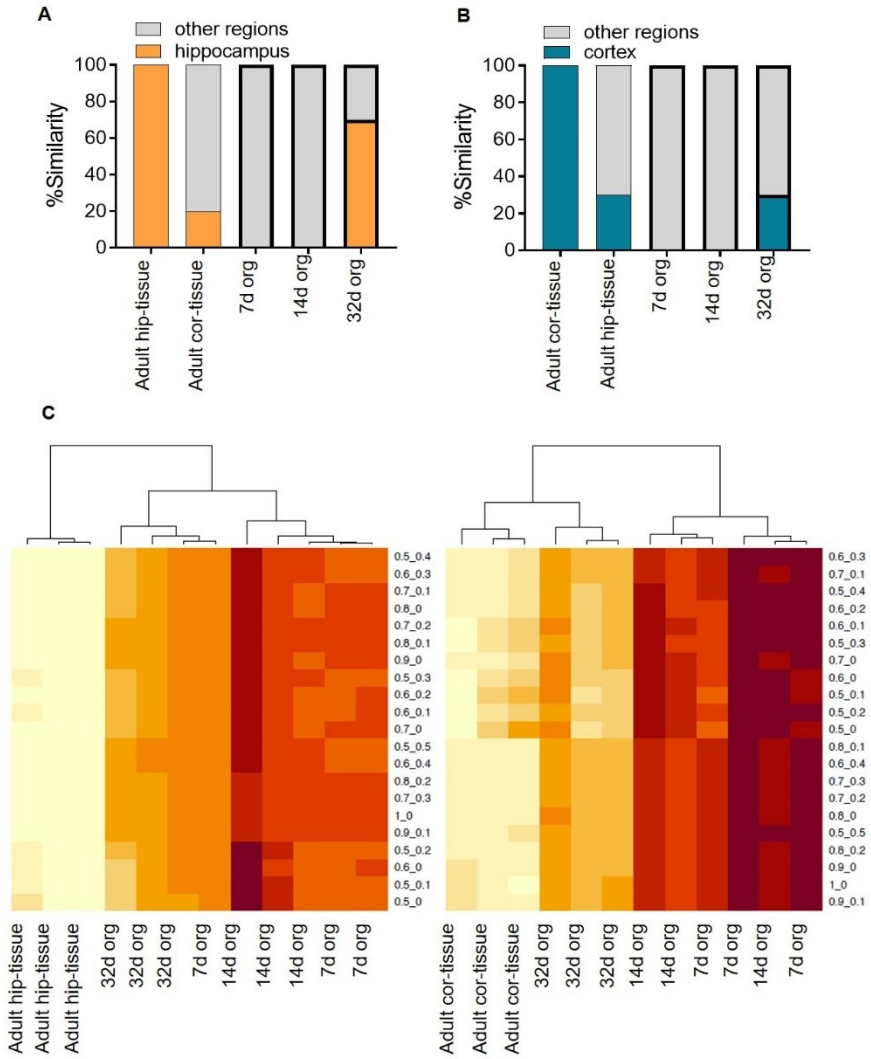

Figure 39: *Regional signature of brain organoids via transcriptomic analysis.*

(A-B) *Graphs illustrating the percentage of similarity between adult murine hippocampal tissue (Adult hip-tissue), adult murine cortical tissue (Adult cor-tissue) and organoids at 7 days (7d org), 14 days (14d org) and 32 days (32d org). Percentage of similarity of organoids to adult hippocampal tissue is shown in* ***A****, while percentage of similarity of organoids to adult cortical tissue is shown in* ***B****. © Heatmaps showing the degree of similarity between adult murine hippocampal tissue (Adult hip-tissue), adult murine cortical tissue (Adult cor-tissue) and organoids at 7 days (7d org), 14 days (14d org) and 32 days (32d org) considering various proportions of hippocampal and cortical components.*

As mentioned above, different brain regions, except from cortex and hippocampus, may be represented inside the murine brain organoids. To elucidate this aspect, we checked the presence of specific cortical FOXG1, hippocampal FZD9, choroid

plexus TTR and ganglionic NKX2.1 and GSX2 markers (Renner et al., 2017) by immunofluorescence. In support of RNAseq data, late organoids expressed both FOXG1 and FZD9 markers. Interestingly, they clustered mainly on the organoid's edge zone. In addition to the hippocampal and cortical identity, some TTR^+ cells were present inside the organoid, localizing at the centre of the structure. As expected, all these markers were found in the specific cerebral murine tissue, used as control for the staining (***Figure 40***).

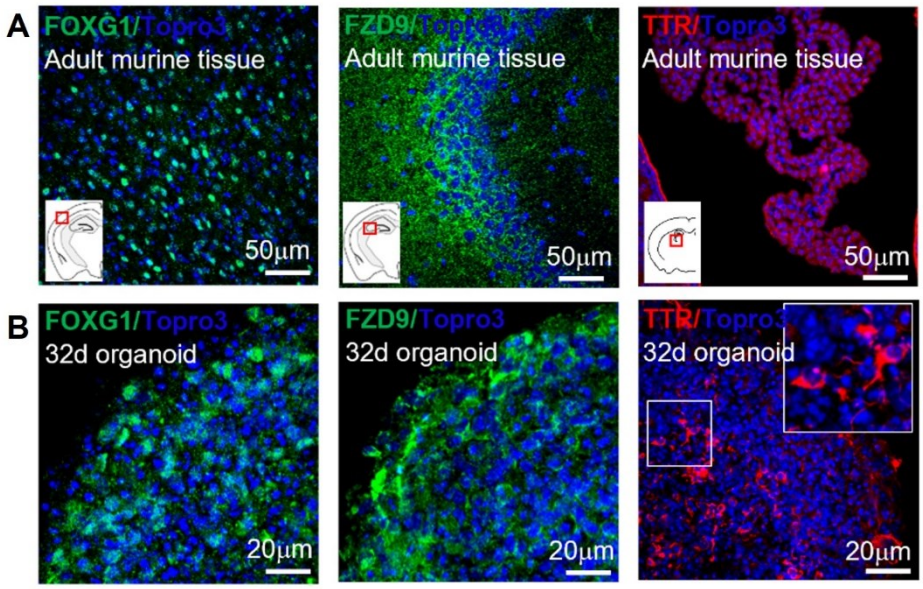

Figure 40: *Regional signature of brain organoids via immunofluorescence.* ***(A-B)*** *Representative immunofluorescence confocal maximum intensity z stack projection images of sliced adult murine cerebral tissue (A) and mature organoids (B). The expression of FOXG1 (cortex), FZD9 (hippocampus) and TTR (choroid plexus) markers is shown both in the murine tissue (A) and the 32 days organoids (B). White insets in the adult murine tissue panels (A) represent a coronal mouse brain section and the red boxes point out the brain region where the staining was performed. The white box in the TTR organoid panel (B, last panel) illustrates a magnification of TTR^+ cells. Nuclei are stained in blue (TOPRO3) in all reported panels. Scale bars in tissue's images: 50 µm. Scale bars in organoids' images: 20 µm.*

Ganglionic markers NKX2.1 and GSX2 were not present in the mature organoids (32 days) while they were expressed in ventral brain tissue (8 weeks) (***Figure 41***). Taken together, these data suggested that during their spontaneous development the murine brain organoids acquired features of dorsal forebrain tissue.

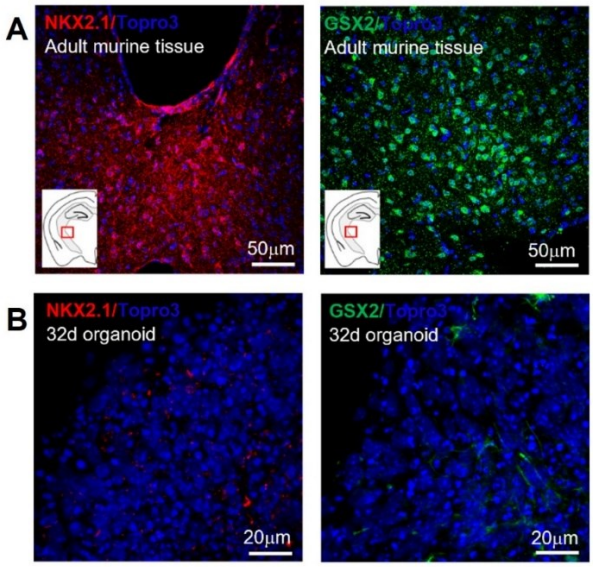

Figure 41: *Organoids do not show ganglionic eminences presence.* ***(A-B)*** *Representative immunofluorescence maximum intensity Z stack projections confocal images of sliced adult murine brain tissue (A) and mature murine brain organoids (B). No expression of NKX2.1 and GSX2 ganglionic eminences markers was detected in organoids. White inserts in the adult murine tissue panels (A) represent a coronal mouse brain section and the red boxes point out the brain region where the staining was performed. Nuclei are stained in blue (TOPRO3) in all reported panels. Scale bars in tissue's images: 50 μm. Scale bars in organoids' images: 20 μm*

Alltogheter these data suggested that murine brain organoids undergo neuronal maturation and structural organization over time, acquiring a dorsal forebrain identity during the development. Considering these features, the generated model results being valid and reproducible, thus a solid tool to investigate neurodevelopment. Importantly, the hereby developed murine brain organoid was exploited for modelling disease and drug testing.

4.3 Murine brain organoids as a model to study Allan Herndon Dudley Syndrome (AHDS) and to identify new drug target

The establishment of a reproducible and well characterized tool as the murine brain organoids previously described in aim 1 and aim 2, paved the way to exploite them

for modelling disease; specifically, we revised the developed protocol to obtain a 3D system mirroring the Allan-Herndon-Dudley Syndrome (AHDS).

4.3.1 Generation of AHDS-like cerebral organoids

To replicate AHDS brain development *in vitro*, the established protocol was modified by subtracting the T3 from the culture medium. We adopted this method since it ensures no TH can enter the neuronal cells. Indeed, the molecular mechanisms determining AHDS are different between humans and mice. Although in humans the disease depends solely on the mutation of the MCT8 transporter, in mice the presence of the OATP1C1 (Grijota-Martínez et al., 2020) and Lat1 (Núñez et al., 2014) transporters allows TH to still enter the brain, thus establishing a compensatory mechanism for T3 level. For this reason, both MCT8 transporter knock-out mice (Mct8KO mice) and MCT8/OATP1C1 (Mayerl et al., 2014) deficient mice do not properly reproduce AHDS.

As for the standard protocol, AHDS organoids were cultured following the three – expansion, induction and differentiation – phases, while removing the T3 hormone form the B27 supplement used in the media. Thus, to generate AHDS organoids, SGZ-derived NSCs were cultured in the absence (indicated as T3- or AHDS-like organoids) or presence (referred to as T3+ organoids, used as the counterpart control) of T3 during all the protocol's steps, that lasted from day 0 to day 21 (***Figure 42A***). See Material and Method section for details regarding the T3- and T3+ media composition.

To elucidate whether significant differences were present between T3+ and T3- organoids, we first monitored their morphology and growth overtime, via brightfield imaging and by measuring their maximum diameter (mm). In both cases, NSCs were able to self-assembly and generate organoids, indicating that the absence of T3 does not have an impact on the NSCs self-aggregation. Both samples presented the morphological features of the developing organoids, with a brightened translucent surface tissue during the first two stages of the protocol and a thinner translucent surface with a dark centre during the last stage (***Figure 42B***).

Remarkably, T3- organoids displayed a major diameter compared to the T3+ samples throughout all the protocol phases. At 5 days, T3- and T3+ organoids' maximum diameters (mm) were 0,665±0,011 (n = 80) and 0,620±0,012 (n = 70) respectively. At 7 days T3- organoids displayed a dimension of 0,747±0,011 (n = 97), while T3+ samples had a size of 0,670±0,012 (n = 91). The maximum diameter was 0,777±0,014 (n = 88) and 0,720±0,013 (n = 74) at 9 days for T3- and T3+ 3D structures respectively. At 11 days T3- organoids reached the dimension of 0,764±0,012 (n = 99) while for the T3+ counterpart the maximum diameter was 0,657±0,015 (n = 93). At the end of the induction phase, the dimensions were 0,730±0,014 (n = 90) vs 0,678±0,014 (n = 83), for T3- and T3+ samples respectively. At the end of the protocol (21 days), T3- samples reached 0,516±0,007 (n = 85) whereas T3+ had a size of 0,474±0,008 (n = 80) (***Figure 42C***). This might suggest that the T3 hormone lack into the T3- organoids make them maintain stronger proliferative features compared to their T3+ counterpart.

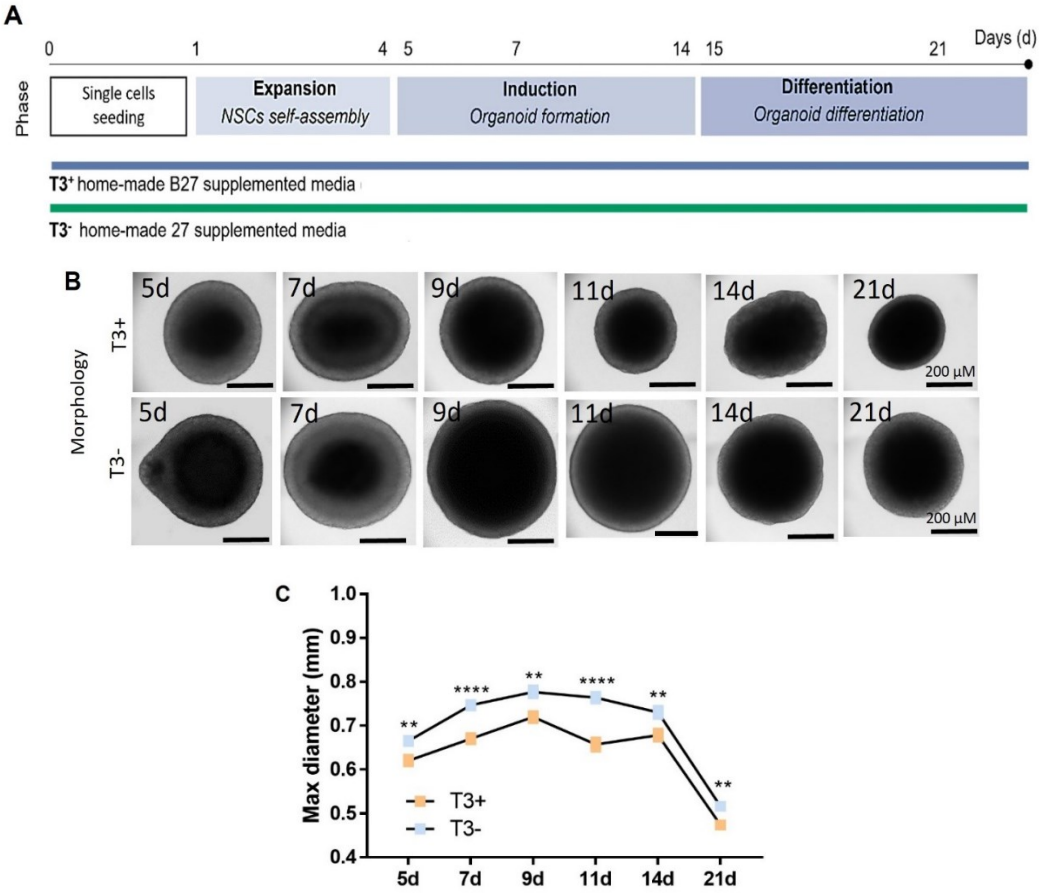

Figure 42*: (A) Scheme of the three-phases protocol for the generation of Allan-Herndon-Dudley Syndrome (AHDS) murine organoids.Single cells (20000 cells/well) were seeded on a 24 well plate (day 0) in the presence (blue squares) or absence (green squares) of the T3+ hormone, contained or not into the home-made B27 supplement medium respectively. These two conditions were maintained over time, up to the end of the protocol. The initial Expansion Phase (day 1 to day 4) consisted in the mouse NSCs proliferation and neurospheres' formation in a culture medium enriched with bFGF and EGF (20 ng/ml). The Induction Phase (day 5 to day 14) led to early organoid's formation in a medium supplemented with gradual decrease of bFGF and EGF (day 5 to day 6: 10 ng/ml bFGF and EGF; day 7 to day 14: 5 ng/ml bFGF). The Differentiation Phase (day 15 to day 21) determined the organoids' maturation via the addition of BDNF (50 ng/ml). During all the protocol's steps organoids were maintained on an orbital shaker (dynamic culture). Adapted from Ciarpella, Zamfir et al., 2021.* ***(B)*** *Representative brightfield images of T3+ and T3- organoids at various steps of maturation. In both cases, early formed organoids have a brightened translucent surface tissue, with a quite dark core. As the differentiation proceeds, the organoids develop a dark and compact structure, remodeling their architecture. Notably, T3- organoids are bigger compared to the T3+ counterpart. Scale bars: 200 µm.* ***(C)*** *Graph representing the growth curve (dimeter, mm) of AHDS T3+ (orange squares) and AHDS T3- (blue squares) murine organoids from day 5 to day 21. To note, T3+ organoids are smaller than T3- samples. Data were compared via multiple t*

*test- one per row and expressed as mean ± SEM of the maximum diameter in mm (n ≥ 30/time point). p < 0.05 was considered statistically significant. ****p < 0.0001; **p < 0.01.*

4.3.2 AHDS-like organoids show a delay in neuronal maturation

Considering the morphological difference seen between T3+ and T3- organoids, we then assessed AHDS samples cellular composition, investigating whether and how cells spatially rearrange inside the organoid at different developmental stages. Based on the results of organoid dimensions, we started by anlaysing cell's ability to proliferate, via the immunohistological quantification of Ki67 positive cells. Subsequently, we investigated the expression of NSCs ($SOX2^+$ and $Vimentin^+$ cells), as well as neuronal progenitors (DCX^+ cells), immature neurons (TUBB+ cells) and astrocytes ($GFAP^+$ cells). The immunofluorescence analysis and quantification were performed at 7, 14 and 21 days. The main objective of this analysis was to shed light on the differences in spatial localization and cellular distribution between T3+ and T3- organoids, verifying how the T3 influences neuronal development.

At 7 days, Ki67 was significantly more expressed in T3- organoids, rather than in the control T3+ counterpart (T3- organoids: 24.563±2.261, expressed as % of $Ki67^+$ area/organoid sliced area; T3+ organoids: 13.124±0,928, expressed as % of Ki67 area/organoid sliced area, $p<0.001$). As expected, at 14 days, T3+ organoids diminished their proliferative state (6.209±0.556 % of $Ki67^+$ area/organoid sliced area) while T3- organoids still expressed a high rate of Ki67 (16.747±4.773 % of $Ki67^+$ area/organoid sliced area). At 21 days in culture, few or no $Ki67^+$ cells were detected in both samples (T3+ organoids: 0.420±0.0348 % of $Ki67^+$ area/organoid sliced area; T3- organoids: 0.616±0.416 % of $Ki67^+$ area/organoid sliced area) (***Figure 43A and B***). These results were in line with the maximum diameter analysis, stressing a pivotal difference that exists between the two samples: organoids cultured in absence of T3 were more proliferative compared to the samples exposed to the hormone, suggesting that T3 hormone deprivation could lead to a sustained proliferation that may hinder AHDS-like organoid's maturation.

This latter aspect was sustained by a major expression of Vimentin in T3- organoids. Specifically, at 7 days, T3- samples presented more Vimentin (15.366±0.710 % of Vimentin$^+$ area/organoid sliced area) compared to the T3+ samples (11.445±0.365 % of Vimentin$^+$ area/organoid sliced area, $p<0.001$). At the end of the induction phase (14 days), T3+ organoids diminished the Vimentin expression (10.310±0.564% of Vimentin$^+$ area/organoid sliced area) while T3- samples still have high Vimentin presence (38.800±8.695 % of Vimentin$^+$ area/organoid sliced area, $p<0.05$), as seen for the Ki67 expression. At the end of the protocol (21 days), fewer cells positive for the Vimentin NSCs marker were detected in both samples (T3- showed 10.274±1.113 % of Vimentin$^+$ area/organoid sliced area; T3+ showed 10.100±1.737 % of Vimentin$^+$ area/ organoid sliced area) (see ***Figure 43A and C***). These data illustrate that T3- retain higher stem proprieties, further strengthening that the absence of the T3 hormone led to an impaired neuronal development and a major stemness signature.

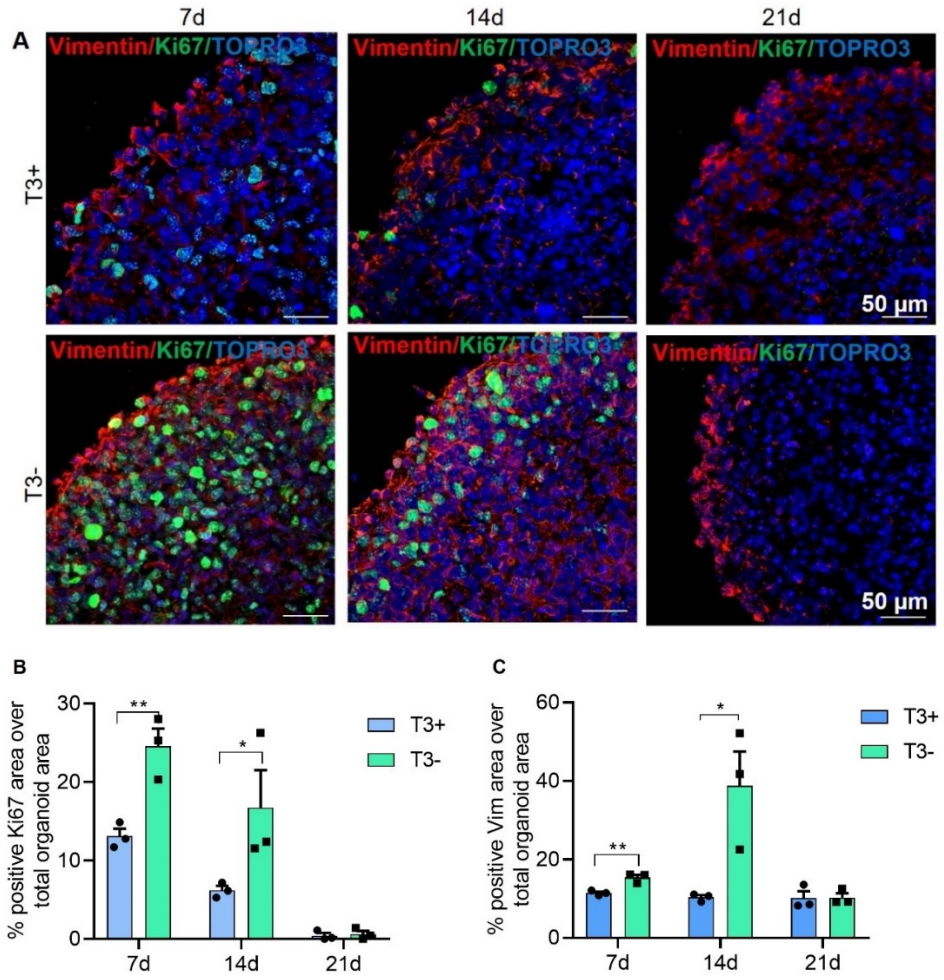

Figure 43: *Proliferative and stem signature in AHDS-like and T3+ organoids.* ***(A)*** *Representative immunofluorescence confocal maximum intensity Z stack projection images of sliced organoids at 7,14 and 21 days. The upper and lower panels illustrate the T3+ and T3- samples respectively, stained for Ki67^{+} and Vimentin^{+} cells. Remarkably, T3- organoids appeared to be more proliferative and to retain more stemness compared to the T3+ counterpart. Nuclei are stained in blue (TOPRO3). Scale bars: 50 µm.* ***(B)*** *Graph showing the percentage of Ki67^{+} area over the organoid sliced area in T3+ (blue bars) and T3- (green bars) organoids. At 7 and 14 days, organoids deprived of T3 showed a higher percentage of proliferation, compared to the samples supplied with the hormone.* ***(C)*** *Graph showing the percentage of Vimentin^{+} area over the organoid sliced area in T3+ (blue bars) and T3- (green bars) organoids. At 7 and 14 days, T3- organoids expressed more stem cells compared to theT3+ samples. In both graphs data are expressed as mean ± SEM. Statistical differences between the two groups were measured by t test, considering n=3 organoids/time point and at least 3 sliced/each organoid. P < 0.05 was considered statistically significant. **p < 0.01; *p < 0.05; ns: not significant*

We then checked for the expression of the stemness marker SOX2. However, at all analyzed time-points, no significant differences were registered between the two samples. Both T3- and T3+ organoids illustrated a decrease in the SOX2 expression (T3- organoids illustrated the following SOX2 expression: 63.947 ± 6.869 % of $SOX2^+$ area/ organoid sliced area at 7 days, 39.463±7.107 % of $SOX2^+$ area/organoid sliced area at 14 days and 15.067±2.074 % of $SOX2^+$ area/organoid sliced area at 21 days; T3+ organoids illustrated the following SOX2 expression: 72.148%±1.234 of $SOX2^+$ area/organoid sliced area at 7 days, 46.035±6.481 % of $SOX2^+$ area/organoid sliced area at 14 days and 32.730±6.562 % of $SOX2^+$ area/organoid sliced area, p = 0.06 at 21 days) (***Figure 44A-C***).

To verify the neuronal maturation, we investigated the presence of the neuronal progenitors (DCX expressing cells), as well as their spatial localization. In T3+ organoids, DCX^+ cells acquired an interspersed distribution during the induction phase, spatially rearranging into the external organoid's layer during the differentiation stage. The T3- organoids, instead, maintained a scattered distribution also at 21 days, not clustering on the organoid's edge. These data suggested T3 deprivation impacts the ability of the cells to correctly migrate during the development. During the induction phase, the DCX expression increased both in T3- and T3+ 3D structures, decreasing during the differentiation stage, with no significant differences between the two experimental groups (T3- organoids illustrated the following DCX expression: 22.394±7.531 % of total DCX^+ area/organoid sliced area at 7 days, 26.950±2.247 % of DCX^+ area/organoid sliced area at 14 days and 16.823±2.408 % of DCX^+ area/organoid sliced area at 21 days; T3+ organoids illustrated the following DCX expression: 16.379±6.490 % of DCX^+ area/organoid sliced area at 7 days, 23.987±1.935 % of total DCX^+ area/organoid sliced area at 14 days and 14.197±0.829 % of total DCX^+ area/organoid sliced area at 21 days) (see ***Figure 44A, B, and D***). Strikingly, even if no statistical difference was registered between T3- and T3+ organoids, T3- samples showed a higher DCX expression trend compared to the T3+ controls.

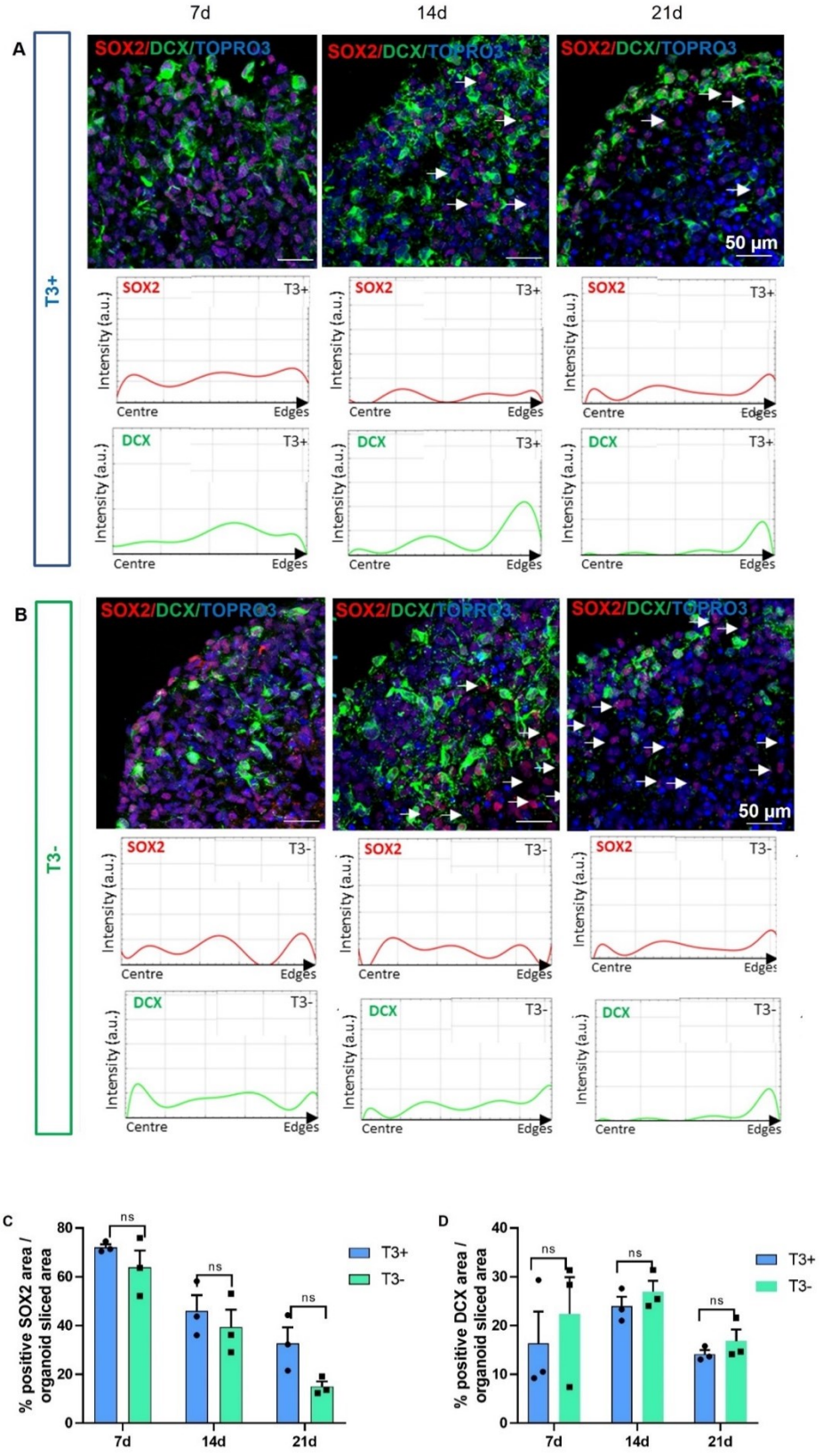

Figure 44: *Neuronal progenitors' distribution in AHDS-like and T3+ organoids.* ***(A-B)*** *Representative immunofluorescence confocal maximum intensity Z stack projection images of T3+*

(A) and T3- (B) sliced organoids at 7,14 and 21 days. The samples were stained for $SOX2^+$ and DCX^+ cells. White arrows illustrated $SOX2^+$ cells. Nuclei are stained in blue (TOPRO3). Scale bars: 50 μm. Fluorescence intensity analysis illustrating the expression of SOX2 (red) and DCX (green), plotted versus the distance from the center (left side of the graph) to the edge (right side of the graph) of T3+ (A) and T3- (B) brain organoids at 7, 14 and 21 days. Mature T3+ organoids showed a progressive accumulation of neuronal progenitors on the edge zone, while DCX^+ cells remained interspersed in T3- samples even at 21 days. Stem cells had an interspersed distribution both in T3+ and T3- samples at all time-points. The plots were obtained using the Plot Profile command in ImageJ (Fiji) followed by the Fit Function (8^{th} Degree Polynomial in ImageJ. ***(C)*** *Graph showing the percentage of $SOX2^+$ area over the organoid sliced area* ***(D)*** *Graph showing the percentage of DCX^+ area over the organoid sliced area. In both graphs data are expressed as mean ± SEM. Statistical differences between the two groups were measured by t test, considering n=3 organoids/time point and at least 3 sliced/each organoid. $p < 0.05$ was considered statistically significant. ns: not significant*

Overall, these results suggested that NSCs differentiate towards neuronal progenitors in both T3+ and T3- organoids. The minor levels of DCX at 21 days in the AHDS-like and control organoids may be due to different causes, considering the distribution of the neural progenitors inside the samples. The radial organization that DCX acquires in T3+ organoids may suggest the neuronal maturation proceeds toward more mature neuronal phenotype. Conversely, the scattered distribution of the progenitors in T3- organoids may be an index of a delayed maturation, that may occur later when NSCs grow in hypothyroidism conditions. Thus, we could hypothesize the lack of T3 can impact the ability of the cell to correctly migrate during development.

4.3.3 AHDS-like organoids show an imbalance between glial and neuronal populations

To deeply investigate the impact of T3 deprivation on organoids cellular phenotype and on neuronal development, we performed immunostaining looking for the presence of immature neurons, marked by the TUBB3 presence (***Figure 45***). Considering cell progenitors could generate not only the neuronal lineage, but also

glial cells, we also investigated the presence of astrocytes, marked by GFAP staining (***Figure 45***).

While T3+ samples were characterized by an increased TUBB3 expression overtime (6.601±1.630 % of $TUBB3^+$ area/organoid sliced area at 7 days, 10.317±1.267 % of $TUBB3^+$ area/organoid sliced area at 14 days and 14.623±0.862 % of positive $TUBB3^+$ area/organoid sliced area at 21 days), T3- organoids presented a TUBB3 increment till 14 days, whereas at later stage the TUBB3 content slightly decreased (8.253±2.321 % of TUBB3+ area/organoid sliced area at 7 days, 15.080±1.962 % of TUBB3+ area/organoid sliced area at 14 days and 10.627±3.552 % of TUBB3 area/organoid sliced area at 21 days) (***Figure 45A***). Qualitative distribution analysis of TUBB3+ cells showed that immature neurons remained interspersed inside the T3- organoid throughout all the analyzed time-points, showing no specific localization at early developmental stages (7 and 14 days) and little cells distribution on the organoid's external region at 21 days. Instead, at this stage, mature T3+ organoids presented a cluster of immature neurons that migrated to localize on the edge of the 3D structure (***Figure 45C and D***). These data suggested that neurons do not present a completely organized structure inside the T3- organoids, indicating a lack of cellular migration possibly reflecting impairment in neuronal differentiation.

Looking at the presence of astrocytes, we observed a low GFAP expression at 7 days in both samples (T3- organoids: 3.337±0.787 % of $GFAP^+$ area/organoid sliced area; T3+ organoids: 6.132±1.174 % of $GFAP^+$ area/organoid sliced area). Strikingly, statistically significant differences were found in the GFAP expression starting at day 14. Intermediate T3- organoids (14 days) presented a huge increment of the GFAP levels (35.847±7.824 % of $GFAP^+$ area/total organoid sliced area) compared to the T3+ counterpart (14.160±2.162 % of $GFAP^+$ area/organoid sliced area, $p=0.05$). The same results were observed at 21 days (T3- organoids: 30.254±2.010 % of $GFAP^+$ area/organoid sliced area; T3+ organoids: 19.267±0.480 % of $GFAP^+$ area/organoid sliced area; $p<0.01$) (***Figure 45B***). Moreover, different localization of $GFAP^+$ was observed in the two experimental groups in all analyzed

stages; $T3^+$ organoids were characterized by a scattered distribution overtime, while in $T3^-$ organoids astrocytes were mainly found at the core of the organoid (***Figure*** 45***C and D***). Importantly, starting from day 14, T3+ and T3- organoids differ considerably in the glial cells' content. To note, the ratio between neurons and astrocytes populations in $T3^+$ brain organoids was maintained at ~1:1 (14DIV: TUBB3 13%, GFAP 16%; 21DIV: TUBB3 19%, GFAP 25%) while in $T3^-$ brain organoids the ratio was ~ 1:3 (14 DIV: TUBB3 10%, GFAP 25%; 21DIV: TUBB3 16%, GFAP 45%).

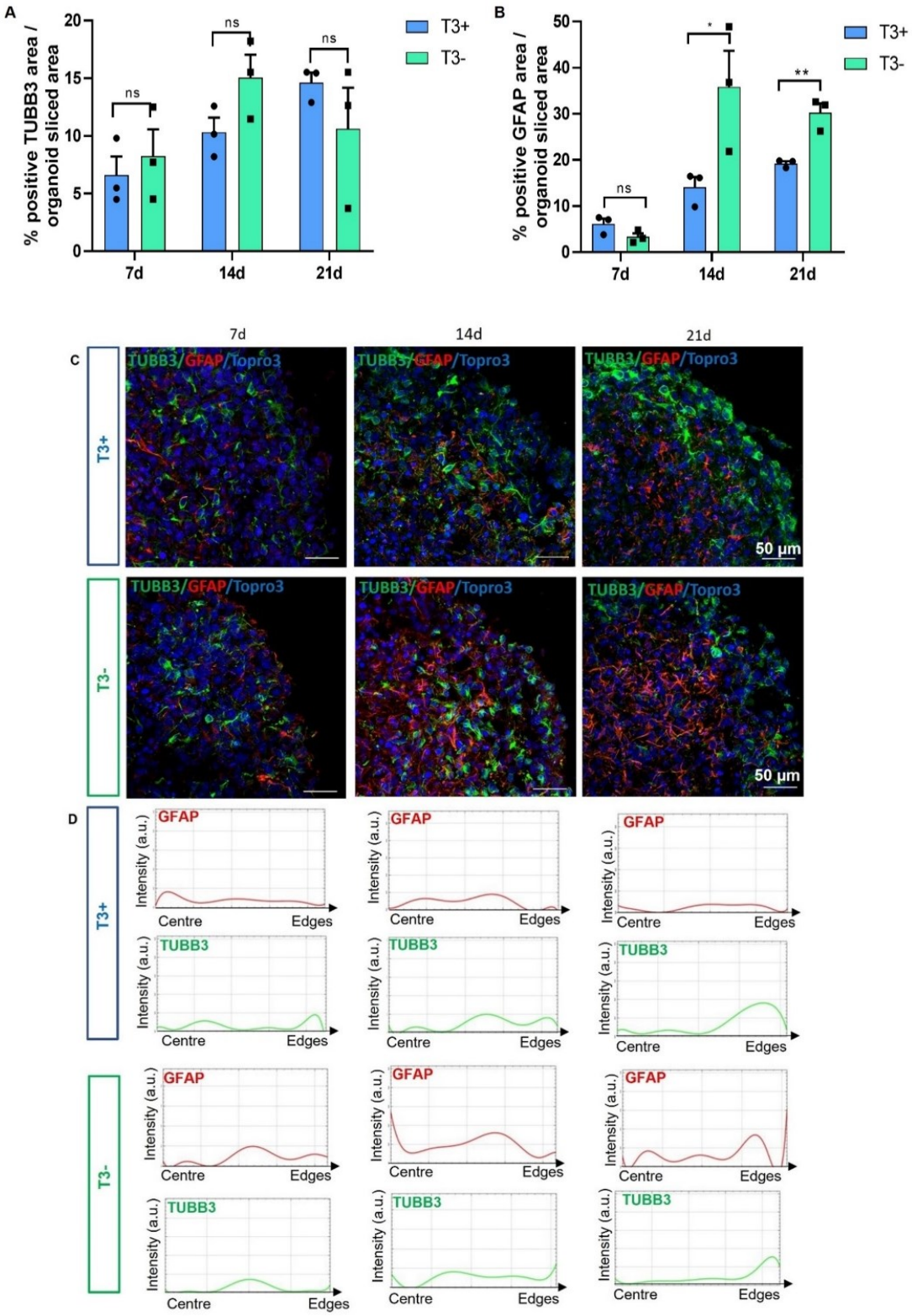

Figure 45: *Neuronal and glial phenotypes in AHDS-like and T3+ organoids.* ***(A)*** *Graph showing the percentage of TUBB3$^+$ area over the organoid sliced area in T3+ (blue bars) and T3- (green bars) samples* ***(B)*** *Graph showing the percentage of GFAP$^+$ area over the organoid sliced area (T3+ organoids: blue bars; T3- organoids: green bars). Note the major presence of astrocytes in T3-*

*organoids at 14 and 21 days compared to the T3+ counterpart. In both graphs data are expressed as mean ± SEM. Statistical differences between the two groups were measured by t test, considering n=3 organoids/time point and at least 3 sliced/each organoid. $p < 0.05$ was considered statistically significant. **$p < 0.01$; $p < 0.05$; ns: not significant.* ***(C)*** *Representative immunofluorescence confocal maximum intensity Z stack projection images of T3+ (upper panel) and T3- (lower panel) sliced organoids at 7,14 and 21 days. The samples were stained for $TUBB3^+$ and $GFAP^+$ cells. Nuclei are stained in blue (TOPRO3). Scale bars: 50 µm.* ***(D)*** *Fluorescence intensity analysis illustrating the expression of GFAP (red) and TUBB (green), plotted versus the distance from the center (left side of the graph) to the edge (right side of the graph) of T3+ (upper panels) and T3- (lower panels) brain organoids at 7, 14 and 21 days. Mature T3+ organoids showed a progressive accumulation of immature neurons on the edge, while T3- samples maintained a widespread distribution of TUBB3 at all time points. Additionally, more astrocytes were present in the T3- organoids. The plots were obtained using the Plot Profile command in ImageJ (Fiji) followed by the Fit Function (8^{th} Degree Polynomial in ImageJ.*

In conclusion, AHDS-like organoids showed a major proliferative and stem signature, paired with a minor neuronal maturation compared to control organoids. These developmental impairments might be due to different factors: the inability of neural cells to migrate and cluster on the organoid's edge and the asymmetry between the glial and neural populations inside T3 deprived organoids.

To further investigate the delayed neural maturation of T3- organoids, we checked their metabolic profile, considering metabolism strongly influences neurodevelopment.

4.3.4 AHDS-like organoids show low expression of OXPHOS complexes, impaired fatty acid metabolism and altered mitochondrial dynamics

A metabolic switch toward a more efficient oxidative phosphorylation (OXPHOS) and an increase of mitochondrial content has been already showed to occur during organoids' maturation (see AIM2, Paragraph 5.2.2. Metabolic assessment of murine brain organoids). To evaluate the metabolic profile of AHDS-like organoids, immunoblot analysis was performed to assess differences in the levels of mitochondrial markers between T3+ and T3- organoids. We focused on the voltage-

dependent anion-selective channel 1 (VDAC1) marker to evaluate the mitochondrial mass, and on mitochondrial OXPHOS complexes V (ATP5A), III (UQCRC2) and IV (MTCOI) to evaluate the ability of mitochondria to transport electrons (***Figure 46***).

ATP5A expression significantly increased in T3+ organoids over time and we observed a higher expression in T3+ vs T3- counterparts at day 21. Notably, UQCRC2 expression strongly increased in both organoid groups over time and 21 DIV T3+ organoids presented a higher complex III content than T3- organoids.

T3+ group had higher content of MTCO1 than T3- samples at both day 7 and day 21, while no differences were detected in VDAC1 expression. However, in both T3+ and T3- organoids VDAC1 content significantly increased over time. Taken together, these results highlighted a more pronounced expression of OXPHOS complexes in T3 supplied samples.

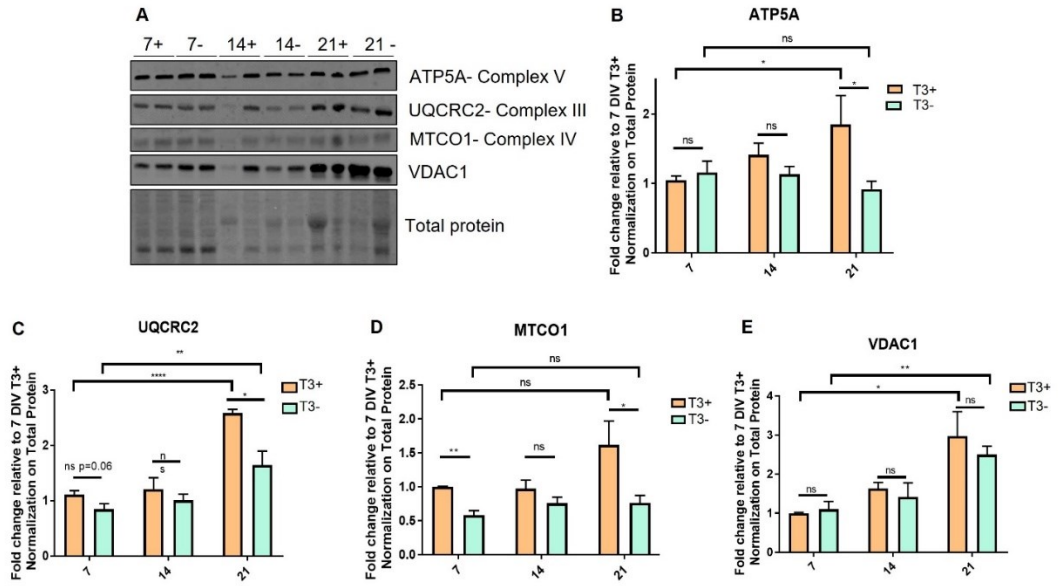

Figure 46: *Metabolic assessment of AHDS-like and T3+ samples.* ***(A)*** *Representative western blotting analysis, reported to the total protein of T3+ and T3- organoids at various stages for OXPHOS complex subunits (ATP5A, UQCRC2, MTCO1) and VDAC1 protein, illustrating an increment of the electron passing through the electron transport chain and of the mitochondrial mass overtime in T3+ organoids.* ***(B-E)*** *Quantitative analysis of the western blot in (A). For ATP5A: n≥5 organoid/time point; for UQCRC2: n≥4; for MTCO1 and VDAC1: n≥3. Data are reported as mean ± SEM. Statistical differences between time points were calculated by ordinary one-way ANOVA. $p < 0.05$ was considered statistically significant. ****$p < 0.0001$; **$p < 0.01$; *$p < 0.05$;*

ns: not significant. Mature T3+ organoids (21 days) showed an increment in ATP5A (B) and UQCRC2 (C) protein amount, when reported to the total protein, suggesting an increased electron transport chain activity in organoids' cells. The VDAC1 protein amount increment in T3+ organoids at 21 days suggests an increased mitochondrial mass.

RNA-Sequencing analysis were performed in collaboration with the team of Professor Giovanni Malerba, Department of Neuroscience, Biomedicine and Movement Sciences, University of Verona. We analyzed both T3+ and T3- organoids at 7 and 14 days ***(Figure 47 and 48 respectively)***. While T3+ organoids progressively upregulated the expression of genes involved in mitochondrial complex I and III assembly, this did not occur in T3- samples. The latter, instead, downregulated the processes of mtDNA replication, mitochondrial fission and fusion. Also, T3- organoids reduced the expression of genes involved in the fatty acid (FA) metabolism, i.e., biosynthesis and mitochondrial β-oxidation, including ctp1a, both at 7 and 14 days, compared to T3+ organoids.

Gene ontology analysis illustrated the main mitochondrial processes up and downregulated ***(Figure 49)*** in T3- and T3+ organoids overtime. AHDS-like organoids downregulated the mtDNA replication as well as mitochondrial fusion and fission. On the other hand, T3+ samples showed an incremented expression of genes related to mitochondrial respiratory chain and electron transport.

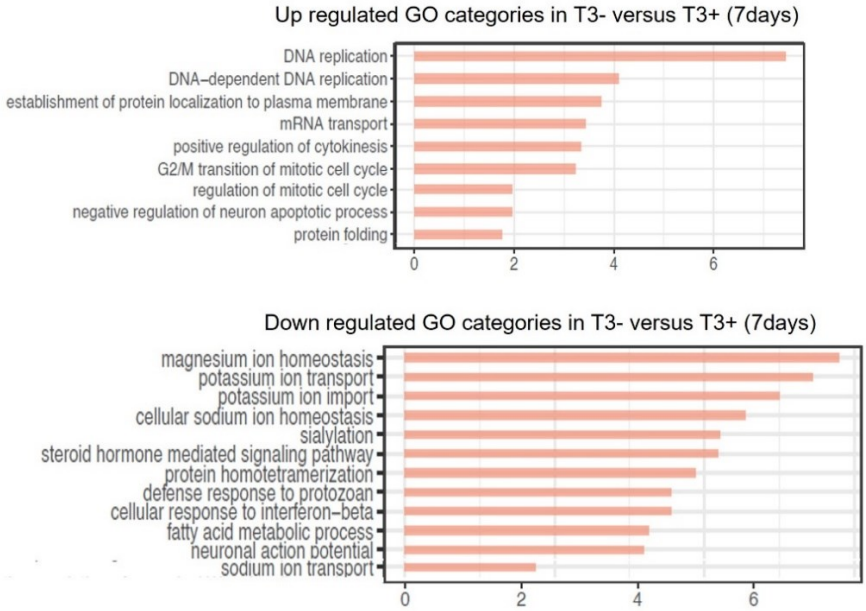

Figure 47*: Transcriptomic analysis of T3+ and T3- organoids at 7 days. Gene ontology (GO) analysis for upregulated (upper panel) and downregulated (lower panel) genes classified according to biological processes in T3- vs T3+ organoids.*

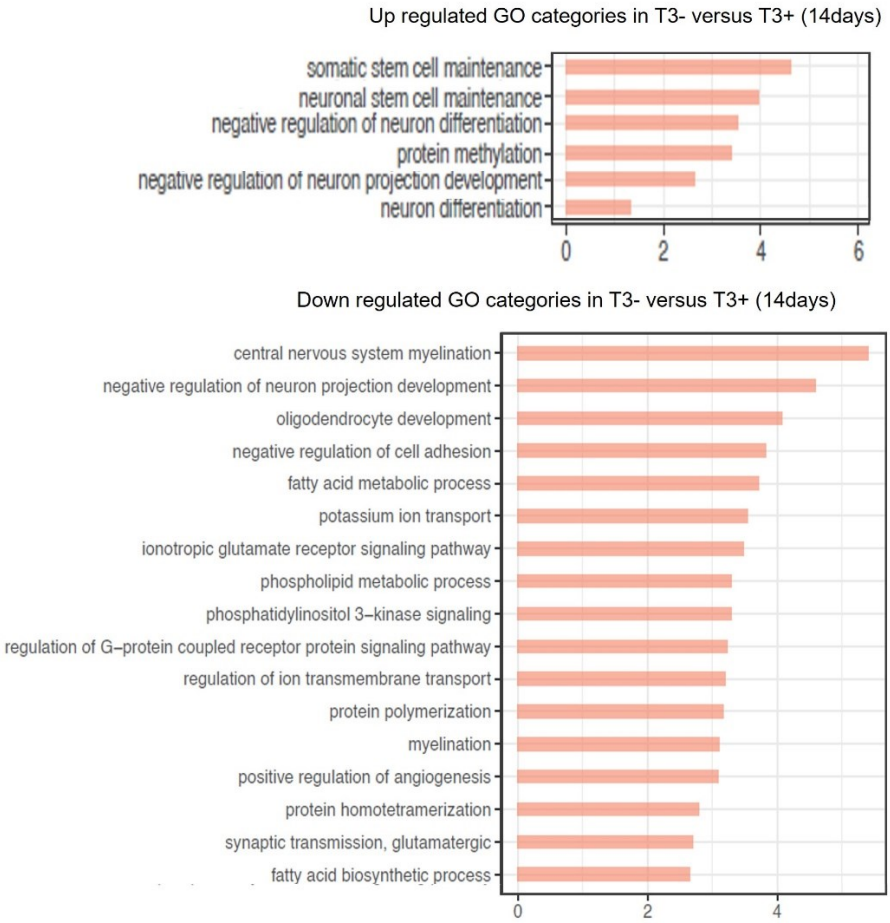

Figure 48: *Transcriptomic analysis of T3+ and T3- organoids at 14 days. Gene ontology (GO) analysis for upregulated (upper panel) and downregulated (lower panel) genes classified according to biological processes in T3- vs T3+ organoids.*

GO-term Down in T3- over time	p-value
mitochondrial DNA replication	0,011
mitochondrial fusion	0,049
mitochondrial fission	0,043
GO-term Up in T3+ over time	**p-value**
mitochondrial respiratory chain complex I assembly	1,70*E-2
mitochondrial respiratory chain complex III assembly	1,70*E-3
mit electron transport, NADH to ubiquinone	7,40*E-3
mit electron transport, ubiquinol to cytochrome c	7,40*E-3

Figure 49: *Summary of GO regarding mitochondrial related processes, downregulated (upper panel) and upregulated (lower panel)* in T3+ and T3- organoids during the developmental protocol phases.

The western blotting and RNA sequencing investigation in T3+ and T3- organoids suggested that T3 deprivation negatively impacts metabolism. This suggested T3 is necessary for a correct mitochondrial development, thus an activation of the OXPHOS-linked processes. The analysis of the cellular phenotype and the delay in neuronal maturation registered in AHDS-like organoids were in line with the metabolic assessment.

4.3.5 Pharmacological intervention promotes neural maturation in AHDS-like organoids

Literature data show evidence regarding the role of T3 hormone in the modulation of mitochondrial metabolism (Viscomi et al., 2015; Lanni et al., 2916; Weitzel et al., 2003). Additionally, it is well known that mitochondrial metabolism is relevant when it comes to neuronal development (Bifari et al., 2020). Our results showed that AHDS-like organoids have altered oxidative phosophorilation, thus, targeting mitochondrial metabolism may be a good therapeutic intervention to promote neuronal maturation in the absence of T3. With this aim, T3- organoids were treated with Nicotinamide Riboside (NR), a NAD^+ precursor and activator of the

mitochondrial biogenesis and metabolism as well as of the regenerative potential of stem cells (Zhang et al., 2016).

NR was supplied fresh to the organoids' culture media starting from day 7, three times a week, at a final concentration of 500 μM, until the end of the protocol (21 days), as illustrated in ***Figure 50A***. Firstly, the effects of NR were investigated by analysing the organoids' size and growth: brightfield images showed that NR administration determined a reduction of T3- organoids dimension, which become more similar to T3+ organoids (***Figure 50B***).

Notably, compared to T3- untreated organoids, maximum diameter (in mm) of T3- organoids diminished after two days of treatment with NR (9 days: T3- 0,777±0,014 (n = 88) vs T3-NR 0,685±0,009 (n = 79), and it was reduced at every time-point analysed (11 days: 0,764±0,012 (n = 99) vs 0,643±0,010 (n = 62); 14 days: 0,730±0,014 (n = 90) vs 0,630±0,012 (n = 58); 21 days: 0,516 ±0,007 (n = 85) vs 0,478±0,010 (n = 52)) (***Figure 50C***), resembling T3+ organoids size and growth (T3+ organoids: 0.712±0.092 at 9 days (n = 20); 0.639±0.131 at 11 days (n = 73); 0.663±0.123 at 14 days (n = 53); 0.452±0.059 at 21 days (n = 25). T3+ NR organoids: 0.642±0.069 at 9 days (n = 23); 0.566±0.065 at 11 days (n = 12); 0.598±0.097 at 14 days (n = 26); 0.479±0.037 at 21 days (n = 11)).

These data revealed that the NR treatment restored the growth of the T3- organoids, suggesting a modulation of the cell proliferation.

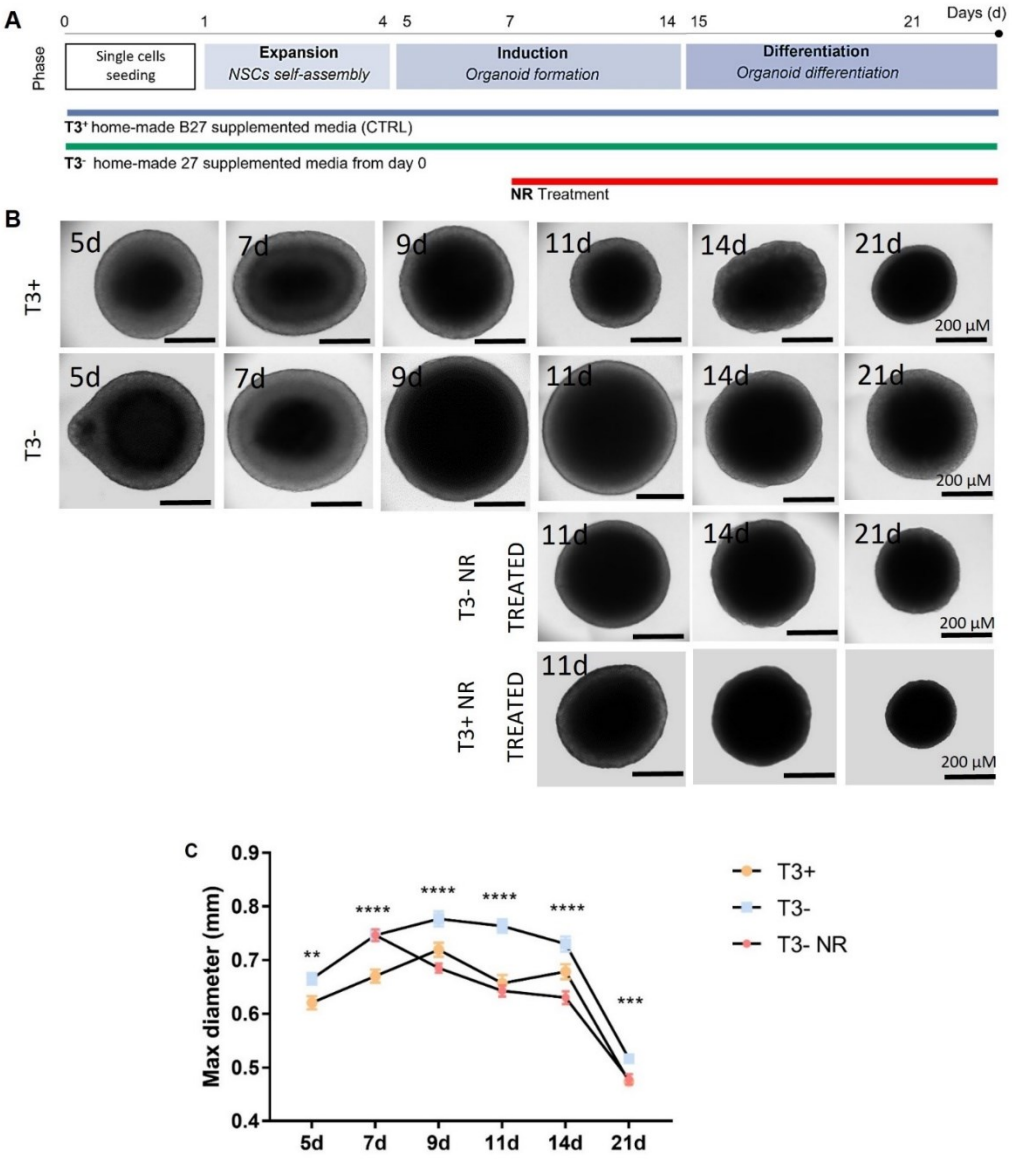

Figure 50: *Protocol for NR administration in AHDS-like and T3+ organoids.* ***(A)*** *Scheme of the three-phases protocol of Allan-Herndon-Dudley Syndrome (AHDS) murine organoids treated with Nicotinamide Riboside (NR) at 0.5 mM. Single cells (20.000 cells/well) were seeded on a 24 well plate (day 0) in the presence (blue squares) or absence (green squares) of the T3+ hormone. These two conditions were maintained until the end of the protocol. The initial Expansion Phase (day 1 to day 4) consisted in the mouse NSCs proliferation and neurospheres' formation in a culture medium enriched with bFGF and EGF (20 ng/ml). The Induction Phase (day 5 to day 14) led to early organoid's formation in a medium supplemented with gradual decrease of bFGF and EGF (day 5: 10 ng/ml bFGF and EGF; day 7: 5 ng/ml bFGF). At day 7, NR started to be administered, every other day, until the end of the protocol. The Differentiation Phase (day 15 to day 21) determined the organoids' maturation via the addition of BDNF (50 ng/ml). During all the protocol's steps organoids were maintained on an orbital shaker (dynamic culture). Adapted from Ciarpella, Zamfir*

et al., 2021. ***(B)*** *Representative brightfield images of T3+ and T3- organoids, as well as NR-treated T3- organoids and NR-treated T3+ organoids at various steps of maturation. T3- treated organoids were more similar to T3+ organoids. Scale bars: 200 µm.* ***(C)*** *Graph representing the growth curve (dimeter, mm) of AHDS T3+ (orange dots), T3- (blue dots) and NR-treated T3- (pink dots) murine organoids from day 5 to day 21. To note, T3+ organoids are smaller than T3- samples. NR-treated T3- organoids resemble T3+ organoids. Data were compared via multiple t test- one per row and expressed as mean ± SEM of the maximum diameter in mm ($n \geq 30$/time point). $p < 0.05$ was considered statistically significant. ****$p < 0.0001$; ***$p < 0.001$; **$p < 0.01$.*

We then questioned about the effect of NR on cellular composition. We investigated, by immunofluorescence analysis, the presence and different abundance of neuronal stem cells (Vimentin), proliferating cells (Ki67), astrocytes (GFAP) and neurons (TUBB3).

As shown in ***Figure 51A-C***, proliferation is highly impacted by the NR treatment at 14 days (intermediate organoids). Indeed, NR-treated T3- organoids showed a minor proliferative rate ($Ki67^+$ cells) compared to T3- structures (14 days, percentage of $Ki67^+$ cells: 3.23±0.53 vs 0.61±0.29 in T3- and T3-/NR organoids respectively). Similar results were obtained also for the Vimentin expressing cells, with a reduction of positive cells from 3.76±0.84 to 0.91±0.09 % in T3- and T3-/NR organoids respectively, at 14 days. At an early mature stage (21 days), the NR treatment results effective both in reducing the percentage of proliferative and stem cells (21 days, percentage of $Ki67^+$ cells: 0.52±0.52 vs 0.13±0.06 in T3- and T3-/NR organoids respectively; 21 days, percentage of Vim^+ cells: 1.02±0.11 vs 0.63±0.05 in T3- and T3-/NR organoids respectively). Taken together, these results suggested that NR is able to impact the T3- organoids' phenotype, reducing proliferation, thus confirming the morphological and maximum diameter analysis. Additionally, the NAD^+ precursor diminishes the stem cells percentage at 21 days.

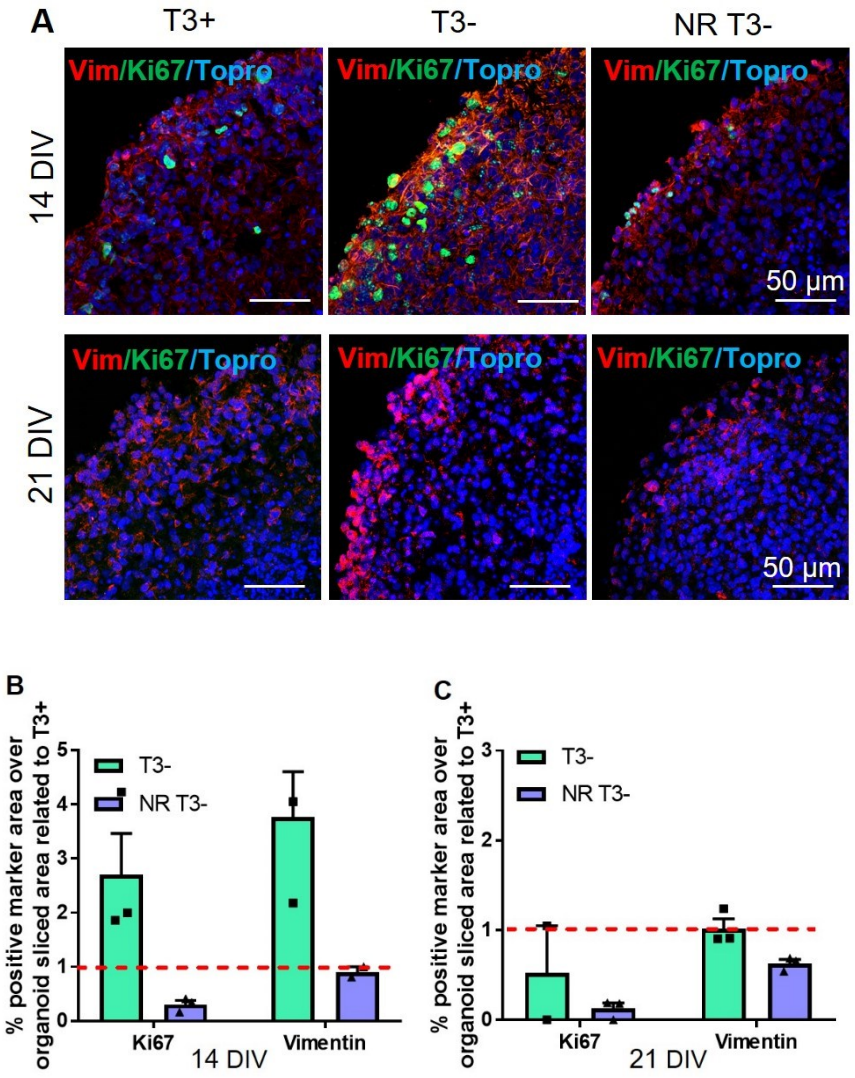

Figure 51: *Proliferative and stem signature in AHDS-like and T3+ organoids after NR treatment.* ***(A)*** *Representative immunofluorescence confocal maximum intensity Z stack projection images of sliced organoids at 14 (upper panels) and 21 (lower panels) days. The figure shows the T3+, T3- and NR-treated T3- (NR T3-) organoids, stained for Ki67^{+} (in green) and Vimentin^{+} (in red) cells. Remarkably, after the NR administration, T3- organoids appeared to be less proliferative compared to the T3- ones. Nuclei are stained in blue (TOPRO3). Scale bars: 50 µm.* ***(B-C)*** *Graphs showing the percentage of Ki67^{+} and Vimentin^{+} area at 14 (B) and 21 (C) days. The quantification is illustrated as fold change of positive markers area in T3- (green bars) and T3-/NR (blue bars) organoids over sliced organoids area compared to T3+ organoids (red dashed line, set to 1). Both at 14 and 21 days, treated organoids were less proliferative and contained less stem cells compared to T3- organoids. Data are expressed as mean ± SEM. Statistical differences between the two groups were measured by t test, considering n≥2 organoids/time point and at least 3 sliced/each organoid.*

To deeply unravel the organoids' cellular composition and the relative abundance of neurons and astrocytes following NR treatment, we performed immunostaining analysis for immature neurons and astrocytes (***Figure 52A***). Both at 14 and 21 days, the NR administration did not produce any statistically significant effect on the immature neurons' number (14 days, percentage of $TUBB3^+$ cells: 1.46±0.19 vs 1.52±0.20 in T3- and T3-/NR organoids respectively; 21 days, percentage of $TUBB3^+$ cells: 0.73±0.24 vs 0.79±0.03 in T3- and T3-/NR organoids respectively) (***Figure 52B***) but, remarkably, it impacted the ability of the cells to spatially rearrange. In fact, NR T3- organoids presented a cluster of neurons on the edge of the organoid, whereas T3- organoids showed a widespread localization of $TUBB3^+$ cell in intermediate organoids (***Figure 52D-E***). Interestingly, by looking at the presence of astrocytes, we noted a reduction of $GFAP^+$ cells following NR supplementation, compared to untreated T3- organoids, both at 14 and 21 days (14 days: percentage of $GFAP^+$ cells: 2.53±0.55 vs 1.49±0.11 in T3- and T3-/NR organoids respectively; 21 days: percentage of $GFAP^+$ cells: 1.57±0.10 vs 1.40±0.10 in T3- and T3-/NR organoids respectively) (***Figure 52C***), even if no statistically significant difference was observed. Strikingly, NR led to a distribution of astrocytes more similar to the T3+ group, both in the immature and mature organoids. (***Figure 52D-E***).

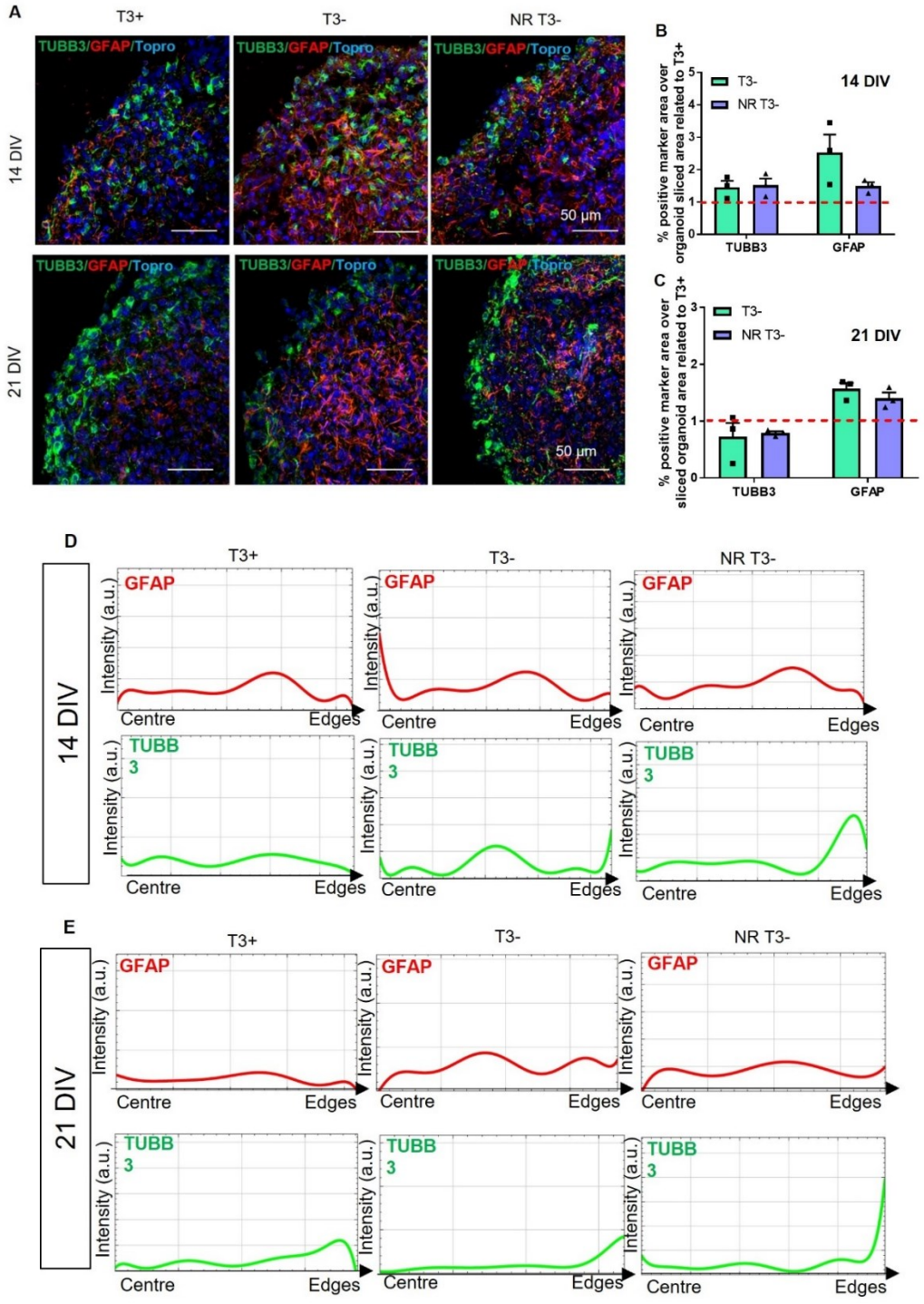

Figure 52: *Neuronal and glia phenotypes in AHDS-like and T3+ organoids after NR treatment.* ***(A)*** *Representative immunofluorescence confocal maximum intensity Z stack projection images of sliced organoids at 14 (upper panels) and 21 (lower panels) days. The figure shows the T3+, T3- and NR-treated T3- (NR T3-) organoids, stained for TUBB3$^+$ (in green) and GFAP$^+$ (in red) cells. Remarkably, after the NR administration, at 14 days, neuronal progenitors localize on the edge. Nuclei are stained in blue (TOPRO3). Scale bars: 50 µm.* ***(B-C)*** *Graphs showing the percentage of*

$TUBB3^+$ and $GFAP^+$ area at 14 (B) and 21 (C) days. The quantification is illustrated as fold change of positive markers area in T3- (green bars) and T3-/NR (blue bars) organoids over sliced organoids area compared to T3+ organoids (red dashed line, set to 1). Data are expressed as mean ± SEM. Statistical differences between the two groups were measured by t test, considering n≥2 organoids/time point and at least 3 sliced/each organoid. ***(D-E)*** *Fluorescence intensity analysis illustrating the expression of GFAP (red) and TUBB3 (green), plotted versus the distance from the center to the edge of T3+, T3- and NR T3- organoids at 14 and 21 days. The plots were obtained using the Plot Profile command in ImageJ (Fiji) followed by the Fit Function (8^{th} Degree Polynomial) in ImageJ.*

Overall, after the NR treatment, T3- organoids resulted to be less proliferative and to have a minor stemness phenotype. Additionally, they showed less glial cells content and a major presence of neurons during the developmental stages, suggesting that NR may have the ability to re-equilibrate the astrocyte/neurons content, acting on the NSCs lineage commitment.

In conclusion, the results produced during my PhD led to the establishment of murine organoids derived from the SGZ of E14.5 days post fertilization embryos and to their application for modeling disease and therapeutical approach. The presented 3D system underwent a maturation process similar to the one observed in vivo during neurodevelopment and resulted being standardized and reproducible. These features made them an excellent platform for modeling AHDS and analyzing the potential therapeutic effect of the NR administration.

By removing the T3 hormone from the initial standard protocol, I was able to generate AHDS-like organoids, with an aberrant proliferation and unbalanced ratio between glial and neurons. As a tool for study the disease, the murine organoids set the basis for trying to unveil the mechanisms determining AHDS, as well as attempting to reverse the pathological phenotype through NR treatment. Interestingly, the success of NR treatment, although it requires deeper investigation, indicated that the AHDS-like 3D tools may represent a good platform for testing different drugs and therapeutic intervention.

5. DISCUSSION

The work conducted during my thesis project led to the generation of a highly standardized protocol for the generation of brain organoids starting from murine embryonic neuronal stem cells gaining the potential to be used as innovative tool for modeling disease and drug testing. To date, many studies reported in literature describe the production of brain organoids (Lancaster et al., 2014; Yakoub and Sadek, 2018) or region-specific cerebral organoids (Trujillo et al., 2019; Urresti et al., 2021; Ballabio et al., 2020; Lee et al., 2022) starting from human iPSCs, however no data were available for organoid derived from rodents' stem cells.

Murine brain organoids can provide a useful model to improve and optimize protocols in a shorter time compared to iPSCs. Taking into account their fast growth rate, murine derived model could be used in a first step of validation before translating the method to the human organoids. Additionally, murine 3D models are worthy tools to investigate the genetics of brain development, considering the huge amount of data produced on mice, that serve as point of comparison. Remarkably, murine organoids can contribute to diminish the number of animals used in studies of brain development. Overall, murine three-dimensional tools are complementary to human organoids and the employment of one rather than the other depends on the aim of the study (Marshall and Mason, 2019).

Development of a standardized and reproducible protocol for murine brain organoid model

To set up the protocol for murine brain organoids, we revised and adapted the protocol introduced to obtain human brain organoids by Lancaster's group (Lancaster et al., 2014) and we explored the conditions suitable for the standardized generation of functional murine organoids. Generally, a multistage protocol is needed to extend and differentiate NSCs, and for each stage, a specific cocktail of growth factors is required (Azar et al, 2021). Specifically, our method consisted in three phases and the use of specific media that were fine tuned for each phase in

terms of growth factors' concentration and administration time was the key to develop a valid model. The seeding of a defined number of cells at the starting point of the protocol was also of extreme relevance for obtaining organoids with defined size and developmental stage. Thus, the generation of a robust murine brain organoids protocol and its extensive characterization was one of my primary goals.

We started from NSCs extracted from the SGZ of mice embryos. During the first step of the protocol, the *expansion phase*, a high (20 ng/ml) bFGF and EGF concentration was required, to start the cells' proliferation. Subsequently, during the induction stage, the growth factors' dose was gradually scaled down (days 5 and 6: 10 ng/ml of bFGF and EGF; day 7 to 14: 5 ng/ml bFGF), to trigger cell differentiation. Lastly, the differentiation phase was characterized by the complete removal of growth factors and the administration of the BDNF to drive neural differentiation and maturation. BDNF is a neurotrophin and a key molecule in neural development and function. Its effect on neuronal differentiation and neurite outgrowth in embryonic and adult NSCs has been well reported (Ahmed et al., 1995; Silva et al., 2009), whereas its application to developing primary hippocampal neurons resulted in a significant higher number of primary neurites as well as an increase in neurite complexity and length and dendritic spine density (Ji et al., 2005; Kwon and Sabatini, 2011; Kellner et al., 2014).

By extensively characterizing the generated model, we demonstrated that murine SGZ-derived NSCs can efficiently self-assembly and differentiate into brain tissue-like structure endowed with functional mature neurons by combining different techniques, spacing from protein expression evaluation, genetic profile, metabolic features and functionality. As already described (Abranches et al., 2009; Kuegler et al., 2010; Palmqvist et al., 2005), murine SGZ-derived from E14.5 embryos display neuronal commitment with the expression of markers that are specific for NSCs. This pointed out an important difference with the protocol used for human-derived organoids (Lancaster and Knoblich, 2014; Pasca et al., 2015; Sakaguchi et al., 2015; Andersen et al., 2020) that require neuroepithelial induction, not necessary for murine SGZ-derived NSCs brain organoid generation. In line with *in vivo* brain development (Seto and Eiraku, 2019) whole transcriptomic analysis showed the progressive maturation of the organoid highlighting the downregulation of gene

related to neural stem cells and the upregulation of gene related to neuron differentiation, synapse structures, calcium ion transport and homeostasis. We specifically observed increasing expression of genes related to NMDA and cholinergic receptors, glutamate receptor and reuptake as well as GABA receptors and transporters further supporting functional neuronal maturation.

During *in vivo* neuronal development, cellular migration occurs from the SVZ to the cortical plate (Lange et al., 2016; Bifari et al., 2017). In line with this evidence, murine organoids showed an initial high amount of stem cells and neuronal progenitors distributed through the entire organoid, with no specific organization. Along the protocol, starting from the differentiation phase, we observed neuronal cells mainly acquiring a radial-like organization: DCX^+, $TUBB3^+$ and $MAP2^+$ cells moved from the center to the edge of the organoid, replicating the *in vivo* migration.

Interestingly, the neuronal differentiation occurring inside the organoids was sustained also by the study of the metabolism, via different techniques, such as western blotting and seahorse live imaging. *In vivo* and *in vitro* experiments previously showed that neuronal precursors are highly glycolytic and switch toward oxidative metabolism during the migration and maturation to the upper cortical layer (Beckervordersandforth et al., 2017; Lange et al., 2016; Zheng et al., 2016). Likewise, our organoid model displayed a metabolic shift from glycolysis, typical of the more immature stages, to oxidative phosphorylation, mainly seen into the later stages of organoid's neuronal maturation.

The progressive organoid maturation led to the presence of neuronal cells with extended processes forming a 3D neuronal network with synaptic connections. A stringent balance between excitatory and inhibitory synapses formation is required for the proper brain development and function (Cline, 2005). *In vivo* synaptogenesis is characterized by an initial overproduction of excitatory synapses that subsequently undergoes a pruning process. The latter consists of an activity-dependent elimination of synapses until the synaptic density is almost stable (Neniskyte and Gross, 2017). Refining the amount of excitatory synapses is a typical feature of the maturational process, that ensures the right ratio between excitatory and inhibitory synapses. By evaluating the expression of specific

excitatory and inhibitory synaptic markers, we showed that the murine brain organoids were able to reach a balance between the number of excitatory and inhibitory synapses during neuronal maturation, suggesting the accomplishment of the pruning process.

The protocol proposed relied on an unguided approach, since no specific patterning molecules were used to precisely drive cellular phenotype. Indeed, we only prompt the neuronal differentiation by providing BDNF. The unguided protocol leads to a cerebral organoid characterized by the presence of different brain regional identities (Kim et al., 2021); in our case dorsal forebrain signature with no evident expression of ganglionic components was the one mainly manifested. Interestingly, a higher similarity to hippocampal rather than to cortical tissue was observed in mature SGZ-NSCs derived organoids, that could be attributable to the initial stem cell source.

Several studies showed that the synaptic development and pruning are controlled by glial cells (Neniskyte and Gross, 2017) and, in line with published data reporting the presence of astrocytes within human brain organoids (Pasca et al., 2015; Quadrato et al., 2017; Lancaster et al., 2013), we observed a stable amount of astrocytes in murine organoids, suggesting their role in promoting neuronal maturation, synapses formation and balance in the developed organoid (Allen and Eroglu, 2017). The establishment of functional connection among neurons belonging to the organoids was further supported by calcium signaling imaging, that revealed a developing cellular activity inside the organoids, going hand in hand with the maturation stages. To identify whether our organoid model presents an active neuronal connection, we exploited the rabies virus transneuronal tracing technology, which specifically propagates exclusively between connected neurons in a strictly unidirectional (retrograde) transneuronal transfer (Ugolini, 2011). Using this technique, we demonstrated that neurons composing the 3D murine brain organoids were connected by active synapses.

To gain a deeper insight about the functionality of the synaptic network detected inside our 3D model further studies are necessary. More information could arise from additional techniques such as patch clamp and 3D MEA, that may better

elucidate the features of the neuronal connectivity. A critical point about the complete evaluation of neuron activity within the organoid is represented by the 3D spheroid structure itself, that limits the use of current electrophysiological technologies, designed for 2D cultures. Indeed, acute MEA recordings were performed in few studies only (Fair et al., 2020; Trujillo et al., 2019; Renner et al., 2020; Park et al., 2021; Zafeiriou et al., 2020; Yao et al., 2020; Giandomenico et al., 2019) the majority of which described the functionality of organoid-derived cells outgrowing as a monolayer culture (Trujillo et al., 2019; Yao et al., 2020) or of organoid slices (Zafeiriou et al., 2020; Giandomenico et al., 2019). To avoid disrupting the organoid, the use of 3D MEAs (Huang et al., 2022) could be extremely relevant. The generation of assembloids could also give interesting outputs (Xiang et al., 2019).

Overall, our results showed for the first time that murine SGZ-derived NSCs can generate reliable and reproducible brain organoids undergoing progressive maturation and containing functional neurons that can generate synaptic contacts. Murine brain organoids require a short period of time (5 weeks) to reach the maturational state. Such aspect, paired to the accessibility of the stem cell source and the reproducibility, robustness and flexibility of the set-up organoids make them valuable supporting tools for human iPSCs-derived organoid protocol optimization, brain disease modeling (Birey et al., 2017; Lancaster et al., 2013; Qian et al., 2016) and for high throughput drug screening (Watanabe et al., 2017).

Modeling Allan Herndon Dudley Syndrome (AHDS) using murine brain organoids

Indeed, we exploited the generated murine brain organoids as a tool for modeling disease. Specifically, we generated 3D murine organoids to study the Allan-Herndon-Dudley syndrome (AHDS). AHDS is a rare X-linked neurodevelopmental disorder caused by loss-of-function mutations (i.e. missense, deletions) in the *SCL16A2* gene (Xq13.2). The latter encodes for the monocarboxylate transporter 8

(MCT8), necessary for the T3 uptake inside neurons into the CNS. The developing CNS is highly sensitive to the T3 presence and action (Schroeder and Privalsky, 2014; Prezioso et al., 2018), which is involved in mechanisms such as neurogenesis, migration, differentiation and establishment of synaptic connections (Bernal, 2002). Patients suffering from AHDS are clinically affected by intellectual disability, motor impairment and development delay (López-Espindola et al., 2014). By exploiting the use of murine brain organoids, we aimed to resemble the AHDS scenario and to deepen the pathological mechanisms leading to neurological defect clinical manifestation.

AHDS-like murine cerebral organoids were produced following the generated protocol, which was revised by removing the T3 hormone from the culture media, following the Hanna Lab Protocol – Weizmann Institute of Science (Version 2 of 17/02/2016). Bearing in mind mice and humans have different biological features regarding AHDS, we decided to deplete the media of T3, without inducing the MCT8 genetic mutation in the SGZ-derived NSCs. Indeed, the genetic murine models described in literature (Bárez-López et al., 2019; Mayerl et al., 2014) are weak and fail in completely resembling AHDS, due to mechanisms that compensate the absence of MCT8.

MCT8 transporter knock-out mice (Mct8KO mice) showed a patient-like thyroid profile and low levels of T3 in different brain areas, but only subtle defects and behavioural changes were found (Grijota-Martínez et al., 2020), suggesting that these animals present some compensatory mechanism that prevents neurological damage, i.e. the presence of the organic anion transporter OATP1C1 and the deiodinase type 2 (DIO2) enzyme. OATP1C1 transporter is expressed abundantly in rodent brain barriers, but to a much lesser extent in humans. The thyroid, subsequently to the activation of the hypothalamic-pituitary-thyroid (HPT) axis, produces the THs that are released into the blood. The main circulating form of THs is tyroxine (T4). The latter can undergo the stereospecific removal of iodine, called deiodination process, performed by deiodinases. Due to this process, T4 can be transformed in T3.

As mentioned before, T4 can also entry the murine brain through OATP1C1transporter. The subsequent action of deiodinase enzyme, specifically

deionidase 2 (DIO2), that transforms T4 in T3 provides enough T3 in the mouse brain, compensating for the lack of MCT8 (Grijota-Martínez et al., 2020).

To avoid this compensatory mechanisms, MCT8/DIO2 (Bárez-López et al., 2019) or MCT8/OATP1C1 (Mayerl et al., 2014) deficient mice have been generated and used to investigate AHDS. However, these genetic models do not reliable reproduce AHDS, since T3 and T4 could be still detected in mice brain homogenates (Mayerl et al., 2014). This residual THs presence is due to the activity of the L-type amino acid transporter LAT1, highly expressed in endothelial cells of the BBB, suggesting its compensatory role for the absence of both MCT8 and OATP1C1 transporters (Núñez et al., 2014).
Those literature data support our experimental strategy and the decision of removing T3 from the organoids' culture media is still a valuable evidence that, according to the desired application, the conditions applied to develop our murine organoids can be easily rearranged as needed. Thus, murine organoids are to be retained highly relevant for modeling disease: considering the short time scale for their generation, once established the protocol to resemble the physiological conditions, the method can be effortlessly adapted to create a pathological scenario.

We investigated AHDS-like brain organoid model via morphological analysis and protein expression, monitoring changing during developmental stages related to T3 deprivation. In line with high levels of cellular proliferation reported in chronic hypothyroidism conditions (Gothié et al., 2017), we noticed a sustained proliferative activity during development in absence of T3, with higher expression of $Ki67^{+}$ proliferative cells leading to bigger T3-deficient organoid's dimension compared to organoids grown in T3 accessibility. The high proliferative state of AHDS-like murine organoids was also associated to an immature signature, as indicated by the stem cells' marker Vimentin, which expression persisted for longer during the protocol, contrary to what was observed in T3-supplied organoids. Overall, these data indicated that the deprivation of T3 hormone interferes with organoid's proliferation capacity which, in turns, results into an immature profile

and thus that T3 deficiency could affect the developmental process of the cerebral organoids model.

An essential step in the genesis of the nervous system is neuronal migration and aberrant events in this process have been linked to cognitive deficits (Bernal, 2022). Literature data show that thyroid hormones deficiency can determine alterations of neuronal migration: in rodents, delayed migration of cerebellar granule neurons, positional alterations of Purkinje cells and ectopic location of neurons in the cortex had been detected (Alvarez-Dolado et al., 1999). T3-deprived organoids illustrated a scattered distribution of both neuronal precursors and immature neuronal cells, that did not show a radial migration toward the edge of the organoid as registered for the controls. These findings suggest a delayed and lower state of neural maturation in hypothyroidism conditions, according to the key role of T3 as a neurogenic factor (Gothié et al., 2017). According to the observed impaired migration, we also noted high values of neuronal precursors DCX positive cells both during the early and the last phase of the development while the expression level of immature $TUBB3^{+}$ neurons dropped at the later time point analyzed, further suggesting an impaired maturation process, with cells unable to undergo complete differentiation. However, a detailed assessment of the mature neurons' presence is still to be performed, together with the investigation of the ability to generate synapses. Further, functional neuronal network analysis may help to reveal important information about the T3 lack effect on murine organoids recapitulating the AHDS. Indeed, post-mortem examination of two cases with MCT8 mutation showed altered neuronal differentiation with lower expression of neurofilaments and reduced synaptogenesis with impaired synaptophysin expression (López-Espindola et al., 2014; Heuer, 2007).

Beside the characterization of neuronal population, we also found the increasing presence of the GFAP in AHDS-like organoids. Astrocytes are relevant in neuronal maturation (Clarke and Barres, 2013; Farhy-Tselnicker and Allen, 2018). Organoids cultivated in T3-supplied media showed a balance between astrocytes and neuronal population, ranking to a ratio of 1:1. Strikingly, the organoids grown in the absence of T3 were characterized by a greater amount of glia with a ratio of ~3 astrocytes for every single neuron. These data suggested that the T3 hormone

could impact the commitment of the neuronal progenitors, in favor of the glial lineage.

Literature data indicate an essential interplay between neurons and astrocytes for preserving T3 physiologic levels in the CNS (Schroeder and Privalsky, 2014). A higher expression of GFAP indicates an active inflammatory state of the astrocytes, that has been detected in disorders such as Alzheimer's disease, Huntington disease, ischemic stroke and epilepsy (Siracusa et al., 2019). The process of astrocytes' activation is referred to as reactive gliosis (Pekny and Nilsson, 2005), that can be caused by any insult to the CNS. Reactive gliosis is characterized by a morphological change and functional atrophy of the astrocytes themselves (Pekny and Pekna, 2015), reflected by the expression of many different genes (Sofroniew, 2009), among which Gfap, Vim, Nestin, Stat3, Sox9. Deeper investigation in AHDS-like murine organoids could elucidate to what extent reactive gliosis is present and the possible links with AHDS pathology and T3 deficiency.

Lastly, immunoblot analysis and RNA sequencing data on AHDS-like and control T3+ organoids highlighted a minor expression of genes related to mitochondrial biogenesis and maturation towards an oxidative metabolism in AHDS-like organoids compared to controls.

Nicotinamide Riboside (NR) treatment of AHDS-like murine organoids

Considering the commitment of NSCs populations depends on metabolic regulations (Bifari et al., 2020; Inak et al., 2021) and given the well-established role of T3 in the activation of PGC1a, a master gene regulator of mitochondrial biogenesis (Wulf et al., 2007), mitochondrial mass regulation (Lanni et al., 2016) and ultimately mitochondrial metabolism (Cioffi et al., 2022), a deeper metabolic investigation of the AHDS-like organoids could also be very informative. Indeed, already existing data illustrate how neuronal development is strictly dependent on mitochondrial metabolism (Bifari et al., 2020) and that the last-mentioned one is modulated by the T3 hormone (Lanni et al., 2016). Considering this, we attempted to restore neuronal impaired maturation observed in AHDS-like organoids by treating them with Nicotinamide Riboside (NR). NR is a compound similar to vitamin B3, functioning as a precursor to nicotinamide adenine dinucleotide

(NAD+) (Bogan et al., 2008). Recently, NR has gained much interest due to its ability to positively regulate physiological processes. Evidence shows that it improves stem cells' function and delays the senescence of NSCs (Zhang et al., 2016). NAD+ is fundamental in the energy metabolism since, by accepting H+, it become the main source of reducing compounds that are then taken to fuel the OXPHOS. Additionally, NAD+ and its coenzymes are substrates for many classes of enzymes like sirtuins (SIRT1), a group of deacetylases (Blander and Guarente, 2004). In presence of NR, SIRT1 activity is stimulated to deacetylate target proteins like PGC-1α which is then activated and promotes mitochondrial biogenesis and functions while reducing oxidative stress (Cantó et al., 2015).

By administering the NR to culture media of organoids grown in absence of T3, we obtained promising results in restoring the impaired development. Specifically, the most evident effect of the NR in T3 lack conditions was on the organoids' morphology and, consequently, on proliferation and stemness phenotype. AHDS-like murine organoids treated with NR showed a reduced dimension of the maximum diameter, a proliferative activity re-established to comparative level of control samples as well as a minor stem population. Indeed, literature data illustrate NAD+ acts on various signaling pathways, regulating cell cycle progression among others (Chiarugi et al., 2012). Furthermore, studies regarding NR administration as nutraceutical had shown multiple positive effects, for instance an improved regenerative potential of stem cells (Mehmel et al., 2020). These findings sustain our results and maybe AHDS affected patients may benefit from oral intake of NR.

Literature data report a diminished expression of $GFAP^+$ cells linked to a decreased inflammation in a mouse model of optic nerve crush treated with systemically administration of NR (Zhang et al., 2021). In line with this data, AHDS-like organoids, supplied with NR, were characterize by a reduction of $GFAP^+$ cells starting from the differentiation phase, contrary to untreated T3- organoids. By diminishing the presence of astrocytes, NR seems to restore an equilibrium between the glial and neuronal lineages thus suggesting a role in influencing the neuronal progenitors' commitment. Remarkably, after the NR treatment, TUBB3 expressing cells illustrated the ability to rearrange and localize on the organoid's external layer, while the untreated organoids maintained an interspersed neural distribution. The

mechanisms activated by NR deserved a deeper investigation, that may lead to unveiling new processes involved in AHDS.

Additionally, further investigations looking for the presence of mature $MAP2^+$ neurons would be necessary to fully elucidate the NR effect on cerebral hypothyroidism. The analysis of the synapses' presence as well as of neuronal functionality would help elucidating whether NR can strengthen a healthy phenotype in AHDS-like 3D systems. Additionally, the study of AHDS-like organoids and NR supplied samples from a metabolic point of view is of extreme importance to enlighten the relationship between the T3 hormone and neuronal progenitors' differentiation.

The positive effects induced by NR administration to the culture media of AHDS-like organoids proved that murine brain organoids are suitable for drug testing, validating the hereby proposed model for this application. Taking into account the short time scale for the production of murine organoids and the ease of the protocol modulation, other compounds may be tested for their ability to have a therapeutic efficacy in AHDS-like murine organoids.

In conclusion, the results obtained in my thesis' work showed for the first time the effective establishment of a reliable and reproducible murine organoids, that have been successfully exploited for modeling disease and drug administration, fields that could benefit from using murine brain organoids. Indeed, the fast production, low cost and the mirroring of *in vivo* development represent key aspect to successfully use the established 3D model for these purposes. Remarkably, as the NR treatment suggested, murine brain organoids could well fit for drug screening, allowing in an efficient time window to highlight the effectiveness or weakness of treatments.

6. REFERENCES

Abranches E, Silva M, Pradier L, Schulz H, Hummel O, Henrique D, Bekman E. Neural differentiation of embryonic stem cells in vitro: a road map to neurogenesis in the embryo. PLoS One. 2009 Jul 21;4(7):e6286. doi: 10.1371/journal.pone.0006286. PMID: 19621087; PMCID: PMC2709448.

Acosta S, Fiore L, Carota IA, Oliver G. Use of two gRNAs for CRISPR/Cas9 improves bi-allelic homologous recombination efficiency in mouse embryonic stem cells. Genesis. 2018 May;56(5):e23212. doi: 10.1002/dvg.23212. Epub 2018 May 11. PMID: 29676032; PMCID: PMC6098704.

Ahmed S, Reynolds BA, Weiss S. BDNF enhances the differentiation but not the survival of CNS stem cell-derived neuronal precursors. J Neurosci. 1995 Aug;15(8):5765-78. doi: 10.1523/JNEUROSCI.15-08-05765.1995. PMID: 7643217; PMCID: PMC6577638.

Akhtar A. The flaws and human harms of animal experimentation. Camb Q Healthc Ethics. 2015 Oct;24(4):407-19. doi: 10.1017/S0963180115000079. PMID: 26364776; PMCID: PMC4594046.

Aksoy I, Utami KH, Winata CL, Hillmer AM, Rouam SL, Briault S, Davila S, Stanton LW, Cacheux V. Personalized genome sequencing coupled with iPSC technology identifies GTDC1 as a gene involved in neurodevelopmental disorders. Hum Mol Genet. 2017 Jan 15;26(2):367-382. doi: 10.1093/hmg/ddw393. PMID: 28365779.

Alafuzoff I, Adolfsson R, Bucht G, Winblad B. Albumin and immunoglobulin in plasma and cerebrospinal fluid, and blood-cerebrospinal fluid barrier function in patients with dementia of Alzheimer type and multi-infarct dementia. J Neurol Sci. 1983 Aug-Sep;60(3):465-72. doi: 10.1016/0022-510x(83)90157-0. PMID: 6631444.

Alexianu ME, Kozovska M, Appel SH. Immune reactivity in a mouse model of familial ALS correlates with disease progression. Neurology. 2001 Oct 9;57(7):1282-9. doi: 10.1212/wnl.57.7.1282. PMID: 11591849.

Allen NJ, Eroglu C. Cell Biology of Astrocyte-Synapse Interactions. Neuron. 2017 Nov 1;96(3):697-708. doi: 10.1016/j.neuron.2017.09.056. PMID: 29096081; PMCID: PMC5687890.

Alvarez-Dolado M, Ruiz M, Del Río JA, Alcántara S, Burgaya F, Sheldon M, Nakajima K, Bernal J, Howell BW, Curran T, Soriano E, Muñoz A. Thyroid hormone regulates reelin and dab1 expression during brain development. J Neurosci. 1999 Aug 15;19(16):6979-93. doi: 10.1523/JNEUROSCI.19-16-06979.1999. PMID: 10436054; PMCID: PMC6782883.

Amin ND, Paşca SP. Building Models of Brain Disorders with Three-Dimensional Organoids. Neuron. 2018 Oct 24;100(2):389-405. doi: 10.1016/j.neuron.2018.10.007. PMID: 30359604.

Amiri A, Coppola G, Scuderi S, Wu F, Roychowdhury T, Liu F, Pochareddy S, Shin Y, Safi A, Song L, Zhu Y, Sousa AMM; PsychENCODE Consortium, Gerstein M, Crawford GE, Sestan N, Abyzov A, Vaccarino FM. Transcriptome and epigenome landscape of human cortical development modeled in organoids. Science. 2018 Dec 14;362(6420):eaat6720. doi: 10.1126/science.aat6720. PMID: 30545853; PMCID: PMC6426303.

Andersen J, Revah O, Miura Y, Thom N, Amin ND, Kelley KW, Singh M, Chen X, Thete MV, Walczak Araujo APB, Carpi-Santos R, Gomes FCA. The Role of Astrocytes in the Development of the Cerebellum. Cerebellum. 2019 Dec;18(6):1017-1035. doi: 10.1007/s12311-019-01046-0. PMID: 31218566.

Arlotta P, Paşca SP. Cell diversity in the human cerebral cortex: from the embryo to brain organoids. Curr Opin Neurobiol. 2019 Jun;56:194-198. doi: 10.1016/j.conb.2019.03.001. Epub 2019 Apr 30. PMID: 31051421.

Ausó E, Lavado-Autric R, Cuevas E, Del Rey FE, Morreale De Escobar G, Berbel P. A moderate and transient deficiency of maternal thyroid function at the beginning of fetal

neocorticogenesis alters neuronal migration. Endocrinology. 2004 Sep;145(9):4037-47. doi: 10.1210/en.2004-0274. Epub 2004 Apr 15. PMID: 15087434.

Azar J, Bahmad HF, Daher D, Moubarak MM, Hadadeh O, Monzer A, Al Bitar S, Jamal M, Al-Sayegh M, Abou-Kheir W. The Use of Stem Cell-Derived Organoids in Disease Modeling: An Update. Int J Mol Sci. 2021 Jul 17;22(14):7667. doi: 10.3390/ijms22147667. PMID: 34299287; PMCID: PMC8303386.

Azizi F, Amouzegar A, Mehran L, Abdi H. LT4 and Slow Release T3 Combination: Optimum Therapy for Hypothyroidism? Int J Endocrinol Metab. 2020 Apr 7;18(2):e100870. doi: 10.5812/ijem.100870. PMID: 32636887; PMCID: PMC7322563.

Bagley JA, Reumann D, Bian S, Lévi-Strauss J, Knoblich JA. Fused cerebral organoids model interactions between brain regions. Nat Methods. 2017 Jul;14(7):743-751. doi: 10.1038/nmeth.4304. Epub 2017 May 10. PMID: 28504681; PMCID: PMC5540177.

Bahat A, Gross A. Mitochondrial plasticity in cell fate regulation. J Biol Chem. 2019 Sep 20;294(38):13852-13863. doi: 10.1074/jbc.REV118.000828. Epub 2019 Aug 5. PMID: 31383739; PMCID: PMC6755789.

Ballabio C, Anderle M, Gianesello M, Lago C, Miele E, Cardano M, Aiello G, Piazza S, Caron D, Gianno F, Ciolfi A, Pedace L, Mastronuzzi A, Tartaglia M, Locatelli F, Ferretti E, Giangaspero F, Tiberi L. Modeling medulloblastoma in vivo and with human cerebellar organoids. Nat Commun. 2020 Jan 29;11(1):583. doi: 10.1038/s41467-019-13989-3. PMID: 31996670; PMCID: PMC6989674.

Bárez-López S, Grijota-Martínez C, Ausó E, Fernández-de Frutos M, Montero-Pedrazuela A, Guadaño-Ferraz A. Adult Mice Lacking Mct8 and Dio2 Proteins Present Alterations in Peripheral Thyroid Hormone Levels and Severe Brain and Motor Skill Impairments. Thyroid. 2019 Nov;29(11):1669-1682. doi: 10.1089/thy.2019.0068. Epub 2019 Sep 23. PMID: 31359845.

Beckervordersandforth R, Ebert B, Schäffner I, Moss J, Fiebig C, Shin J, Moore DL, Ghosh L, Trinchero MF, Stockburger C, Friedland K, Steib K, von Wittgenstein J, Keiner S, Redecker C, Hölter SM, Xiang W, Wurst W, Jagasia R, Schinder AF, Ming GL, Toni N, Jessberger S, Song H, Lie DC. Role of Mitochondrial Metabolism in the Control of Early Lineage Progression and Aging Phenotypes in Adult Hippocampal Neurogenesis. Neuron. 2017 Feb 8;93(3):560-573.e6. doi: 10.1016/j.neuron.2016.12.017. Epub 2017 Jan 19. Erratum in: Neuron. 2017 Mar 22;93(6):1518. PMID: 28111078; PMCID: PMC5300896.

Belay B, Koivisto JT, Parraga J, Koskela O, Montonen T, Kellomäki M, Figueiras E, Hyttinen J. Optical projection tomography as a quantitative tool for analysis of cell morphology and density in 3D hydrogels. Sci Rep. 2021 Mar 22;11(1):6538. doi: 10.1038/s41598-021-85996-8. PMID: 33753803; PMCID: PMC7985381.

Ben-Ari Y, Spitzer NC. Nature and nurture in brain development. Trends Neurosci. 2004 Jul;27(7):361. doi: 10.1016/j.tins.2004.05.007. PMID: 15219731.

Benito-Kwiecinski S, Lancaster MA. Brain Organoids: Human Neurodevelopment in a Dish. Cold Spring Harb Perspect Biol. 2020 Aug 3;12(8):a035709. doi: 10.1101/cshperspect.a035709. PMID: 31767649; PMCID: PMC7397826.

Bergmann S, Lawler SE, Qu Y, Fadzen CM, Wolfe JM, Regan MS, Pentelute BL, Agar NYR, Cho CF. Blood-brain-barrier organoids for investigating the permeability of CNS therapeutics. Nat Protoc. 2018 Dec;13(12):2827-2843. doi: 10.1038/s41596-018-0066-x. PMID: 30382243; PMCID: PMC6673652.

Bernal J. Action of thyroid hormone in brain. J Endocrinol Invest. 2002 Mar;25(3):268-88. doi: 10.1007/BF03344003. PMID: 11936472.

Bernal J. Thyroid Hormones in Brain Development and Function. 2022 Jan 14. In: Feingold KR, Anawalt B, Boyce A, Chrousos G, de Herder WW, Dhatariya K, Dungan K, Hershman JM, Hofland J, Kalra S, Kaltsas G, Koch C, Kopp P, Korbonits M, Kovacs CS, Kuohung W, Laferrère B, Levy M, McGee EA, McLachlan R, Morley JE, New M, Purnell J, Sahay

R, Singer F, Sperling MA, Stratakis CA, Trence DL, Wilson DP, editors. Endotext [Internet]. South Dartmouth (MA): MDText.com, Inc.; 2000–. PMID: 25905404.

Bershteyn M, Nowakowski TJ, Pollen AA, Di Lullo E, Nene A, Wynshaw-Boris A, Kriegstein AR. Human iPSC-Derived Cerebral Organoids Model Cellular Features of Lissencephaly and Reveal Prolonged Mitosis of Outer Radial Glia. Cell Stem Cell. 2017 Apr 6;20(4):435-449.e4. doi: 10.1016/j.stem.2016.12.007. Epub 2017 Jan 19. PMID: 28111201; PMCID: PMC5667944.

Bifari F, Decimo I, Pino A, Llorens-Bobadilla E, Zhao S, Lange C, Panuccio G, Boeckx B, Thienpont B, Vinckier S, Wyns S, Bouché A, Lambrechts D, Giugliano M, Dewerchin M, Martin-Villalba A, Carmeliet P. Neurogenic Radial Glia-like Cells in Meninges Migrate and Differentiate into Functionally Integrated Neurons in the Neonatal Cortex. Cell Stem Cell. 2017 Mar 2;20(3):360-373.e7. doi: 10.1016/j.stem.2016.10.020. Epub 2016 Nov 23. PMID: 27889318.

Bifari F, Dolci S, Bottani E, Pino A, Di Chio M, Zorzin S, Ragni M, Zamfir RG, Brunetti D, Bardelli D, Delfino P, Cattaneo MG, Bordo R, Tedesco L, Rossi F, Bossolasco P, Corbo V, Fumagalli G, Nisoli E, Valerio A, Decimo I. Complete neural stem cell (NSC) neuronal differentiation requires a branched chain amino acids-induced persistent metabolic shift towards energy metabolism. Pharmacol Res. 2020 Aug;158:104863. doi: 10.1016/j.phrs.2020.104863. Epub 2020 May 12. PMID: 32407957.

Birey F, Andersen J, Makinson CD, Islam S, Wei W, Huber N, Fan HC, Metzler KRC, Panagiotakos G, Thom N, O'Rourke NA, Steinmetz LM, Bernstein JA, Hallmayer J, Huguenard JR, Paşca SP. Assembly of functionally integrated human forebrain spheroids. Nature. 2017 May 4;545(7652):54-59. doi: 10.1038/nature22330. Epub 2017 Apr 26. PMID: 28445465; PMCID: PMC5805137.

Blake AJ, Rodgers FC, Bassuener A, Hippensteel JA, Pearce TM, Pearce TR, Zarnowska ED, Pearce RA, Williams JC. A microfluidic brain slice perfusion chamber for multisite recording using penetrating electrodes. J Neurosci Methods. 2010 May 30;189(1):5-13. doi: 10.1016/j.jneumeth.2010.02.017. Epub 2010 Feb 26. PMID: 20219536; PMCID: PMC3653971.

Blander G, Guarente L. The Sir2 family of protein deacetylases. Annu Rev Biochem. 2004;73:417-35. doi: 10.1146/annurev.biochem.73.011303.073651. PMID: 15189148.

Bogan KL, Brenner C. Nicotinic acid, nicotinamide, and nicotinamide riboside: a molecular evaluation of NAD+ precursor vitamins in human nutrition. Annu Rev Nutr. 2008;28:115-30. doi: 10.1146/annurev.nutr.28.061807.155443. PMID: 18429699.

Boisvert MM, Erikson GA, Shokhirev MN, Allen NJ. The Aging Astrocyte Transcriptome from Multiple Regions of the Mouse Brain. Cell Rep. 2018 Jan 2;22(1):269-285. doi: 10.1016/j.celrep.2017.12.039. PMID: 29298427; PMCID: PMC5783200.

Brand MD, Nicholls DG. Assessing mitochondrial dysfunction in cells. Biochem J. 2011 Apr 15;435(2):297-312. doi: 10.1042/BJ20110162. Erratum in: Biochem J. 2011 Aug 1;437(3):575. PMID: 21726199; PMCID: PMC3076726.

Broguiere N, Isenmann L, Hirt C, Ringel T, Placzek S, Cavalli E, Ringnalda F, Villiger L, Züllig R, Lehmann R, Rogler G, Heim MH, Schüler J, Zenobi-Wong M, Schwank G. Growth of Epithelial Organoids in a Defined Hydrogel. Adv Mater. 2018 Oct;30(43):e1801621. doi: 10.1002/adma.201801621. Epub 2018 Sep 10. PMID: 30203567.

Budday S, Steinmann P, Kuhl E. Physical biology of human brain development. Front Cell Neurosci. 2015 Jul 8;9:257. doi: 10.3389/fncel.2015.00257. PMID: 26217183; PMCID: PMC4495345.

Budday S, Steinmann P, Kuhl E. Physical biology of human brain development. Front Cell Neurosci. 2015 Jul 8;9:257. doi: 10.3389/fncel.2015.00257. PMID: 26217183; PMCID: PMC4495345.

Bugiardini E, Bottani E, Marchet S, Poole OV, Beninca C, Horga A, Woodward C, Lam A, Hargreaves I, Chalasani A, Valerio A, Lamantea E, Venner K, Holton JL, Zeviani M, Houlden H, Quinlivan R, Lamperti C, Hanna MG, Pitceathly RDS. Expanding the molecular and phenotypic spectrum of truncating *MT-ATP6* mutations. Neurol Genet. 2020

Jan 7;6(1):e381. doi: 10.1212/NXG.0000000000000381. PMID: 32042910; PMCID: PMC6984135.

Cahoy JD, Emery B, Kaushal A, Foo LC, Zamanian JL, Christopherson KS, Xing Y, Lubischer JL, Krieg PA, Krupenko SA, Thompson WJ, Barres BA. A transcriptome database for astrocytes, neurons, and oligodendrocytes: a new resource for understanding brain development and function. J Neurosci. 2008 Jan 2;28(1):264-78. doi: 10.1523/JNEUROSCI.4178-07.2008. PMID: 18171944; PMCID: PMC6671143.

Camp JG, Badsha F, Florio M, Kanton S, Gerber T, Wilsch-Bräuninger M, Lewitus E, Sykes A, Hevers W, Lancaster M, Knoblich JA, Lachmann R, Pääbo S, Huttner WB, Treutlein B. Human cerebral organoids recapitulate gene expression programs of fetal neocortex development. Proc Natl Acad Sci U S A. 2015 Dec 22;112(51):15672-7. doi: 10.1073/pnas.1520760112. Epub 2015 Dec 7. PMID: 26644564; PMCID: PMC4697386.

Candelario KM, Shuttleworth CW, Cunningham LA. Neural stem/progenitor cells display a low requirement for oxidative metabolism independent of hypoxia inducible factor-1alpha expression. J Neurochem. 2013 May;125(3):420-9. doi: 10.1111/jnc.12204. Epub 2013 Mar 11. PMID: 23410250; PMCID: PMC4204647.

Cantó C, Menzies KJ, Auwerx J. NAD(+) Metabolism and the Control of Energy Homeostasis: A Balancing Act between Mitochondria and the Nucleus. Cell Metab. 2015 Jul 7;22(1):31-53. doi: 10.1016/j.cmet.2015.05.023. Epub 2015 Jun 25. PMID: 26118927; PMCID: PMC4487780.

Capeling MM, Czerwinski M, Huang S, Tsai YH, Wu A, Nagy MS, Juliar B, Sundaram N, Song Y, Han WM, Takayama S, Alsberg E, Garcia AJ, Helmrath M, Putnam AJ, Spence JR. Nonadhesive Alginate Hydrogels Support Growth of Pluripotent Stem Cell-Derived Intestinal Organoids. Stem Cell Reports. 2019 Feb 12;12(2):381-394. doi: 10.1016/j.stemcr.2018.12.001. Epub 2019 Jan 3. PMID: 30612954; PMCID: PMC6373433.

Cederquist GY, Asciolla JJ, Tchieu J, Walsh RM, Cornacchia D, Resh MD, Studer L. Specification of positional identity in forebrain organoids. Nat Biotechnol. 2019 Apr;37(4):436-444. doi: 10.1038/s41587-019-0085-3. Epub 2019 Apr 1. PMID: 30936566; PMCID: PMC6447454.

Chakrabarty RP, Chandel NS. Mitochondria as Signaling Organelles Control Mammalian Stem Cell Fate. Cell Stem Cell. 2021 Mar 4;28(3):394-408. doi: 10.1016/j.stem.2021.02.011. PMID: 33667360; PMCID: PMC7944920.

Chambers SM, Fasano CA, Papapetrou EP, Tomishima M, Sadelain M, Studer L. Highly efficient neural conversion of human ES and iPS cells by dual inhibition of SMAD signaling. Nat Biotechnol. 2009 Mar;27(3):275-80. doi: 10.1038/nbt.1529. Epub 2009 Mar 1. Erratum in: Nat Biotechnol. 2009 May;27(5):485. PMID: 19252484; PMCID: PMC2756723.

Chen A, Guo Z, Fang L, Bian S. Application of Fused Organoid Models to Study Human Brain Development and Neural Disorders. Front Cell Neurosci. 2020 May 15;14:133. doi: 10.3389/fncel.2020.00133. PMID: 32670022; PMCID: PMC7326106.

Chiarugi A, Dölle C, Felici R, Ziegler M. The NAD metabolome--a key determinant of cancer cell biology. Nat Rev Cancer. 2012 Nov;12(11):741-52. doi: 10.1038/nrc3340. Epub 2012 Sep 28. PMID: 23018234.

Chua CW, Shibata M, Lei M, Toivanen R, Barlow LJ, Bergren SK, Badani KK, McKiernan JM, Benson MC, Hibshoosh H, Shen MM. Single luminal epithelial progenitors can generate prostate organoids in culture. Nat Cell Biol. 2014 Oct;16(10):951-61, 1-4. doi: 10.1038/ncb3047. Epub 2014 Sep 21. PMID: 25241035; PMCID: PMC4183706.

Ciarpella F, Zamfir RG, Campanelli A, Ren E, Pedrotti G, Bottani E, Borioli A, Caron D, Di Chio M, Dolci S, Ahtiainen A, Malpeli G, Malerba G, Bardoni R, Fumagalli G, Hyttinen J, Bifari F, Palazzolo G, Panuccio G, Curia G, Decimo I. Murine cerebral organoids

develop network of functional neurons and hippocampal brain region identity. iScience. 2021 Nov 15;24(12):103438. doi: 10.1016/j.isci.2021.103438. PMID: 34901791; PMCID: PMC8640475.

Cioffi F, Giacco A, Goglia F, Silvestri E. Bioenergetic Aspects of Mitochondrial Actions of Thyroid Hormones. Cells. 2022 Mar 15;11(6):997. doi: 10.3390/cells11060997. PMID: 35326451; PMCID: PMC8947633.

Clarke LE, Barres BA. Emerging roles of astrocytes in neural circuit development. Nat Rev Neurosci. 2013 May;14(5):311-21. doi: 10.1038/nrn3484. Epub 2013 Apr 18. Erratum in: Nat Rev Neurosci. 2013 Jun;14(6):451. PMID: 23595014; PMCID: PMC4431630.

Clevers H. Modeling Development and Disease with Organoids. Cell. 2016 Jun 16;165(7):1586-1597. doi: 10.1016/j.cell.2016.05.082. PMID: 27315476.

Cline H. Synaptogenesis: a balancing act between excitation and inhibition. Curr Biol. 2005 Mar 29;15(6):R203-5. doi: 10.1016/j.cub.2005.03.010. PMID: 15797012.

Corbet C. Stem Cell Metabolism in Cancer and Healthy Tissues: Pyruvate in the Limelight. Front Pharmacol. 2018 Jan 4;8:958. doi: 10.3389/fphar.2017.00958. PMID: 29403375; PMCID: PMC5777397.

Corrò C, Novellasdemunt L, Li VSW. A brief history of organoids. Am J Physiol Cell Physiol. 2020 Jul 1;319(1):C151-C165. doi: 10.1152/ajpcell.00120.2020. Epub 2020 May 27. PMID: 32459504; PMCID: PMC7468890.

Daviaud N, Friedel RH, Zou H. Vascularization and Engraftment of Transplanted Human Cerebral Organoids in Mouse Cortex. eNeuro. 2018 Nov 20;5(6):ENEURO.0219-18.2018. doi: 10.1523/ENEURO.0219-18.2018. PMID: 30460331; PMCID: PMC6243198.

Decimo I, Dolci S, Panuccio G, Riva M, Fumagalli G, Bifari F. Meninges: A Widespread Niche of Neural Progenitors for the Brain. Neuroscientist. 2021 Oct;27(5):506-528. doi:

10.1177/1073858420954826. Epub 2020 Sep 16. PMID: 32935634; PMCID: PMC8442137.

Decimo I, Fumagalli G, Berton V, Krampera M, Bifari F. Meninges: from protective membrane to stem cell niche. Am J Stem Cells. 2012 May 28;1(2):92-105. PMID: 23671802; PMCID: PMC3636743.

Del Dosso A, Urenda JP, Nguyen T, Quadrato G. Upgrading the Physiological Relevance of Human Brain Organoids. Neuron. 2020 Sep 23;107(6):1014-1028. doi: 10.1016/j.neuron.2020.08.029. PMID: 32970996.

Del Río JA, Heimrich B, Borrell V, Förster E, Drakew A, Alcántara S, Nakajima K, Miyata T, Ogawa M, Mikoshiba K, Derer P, Frotscher M, Soriano E. A role for Cajal-Retzius cells and reelin in the development of hippocampal connections. Nature. 1997 Jan 2;385(6611):70-4. doi: 10.1038/385070a0. PMID: 8985248.

Delepine C, Pham VA, Tsang HWS, Sur M. GSK3ß inhibitor CHIR 99021 modulates cerebral organoid development through dose-dependent regulation of apoptosis, proliferation, differentiation and migration. PLoS One. 2021 May 5;16(5):e0251173. doi: 10.1371/journal.pone.0251173. PMID: 33951093; PMCID: PMC8099055.

Dolci S, Pino A, Berton V, Gonzalez P, Braga A, Fumagalli M, Bonfanti E, Malpeli G, Pari F, Zorzin S, Amoroso C, Moscon D, Rodriguez FJ, Fumagalli G, Bifari F, Decimo I. High Yield of Adult Oligodendrocyte Lineage Cells Obtained from Meningeal Biopsy. Front Pharmacol. 2017 Oct 12;8:703. doi: 10.3389/fphar.2017.00703. PMID: 29075188; PMCID: PMC5643910.

Dumitrescu AM, Liao XH, Best TB, Brockmann K, Refetoff S. A novel syndrome combining thyroid and neurological abnormalities is associated with mutations in a monocarboxylate transporter gene. Am J Hum Genet. 2004 Jan;74(1):168-75. doi:

10.1086/380999. Epub 2003 Dec 5. Erratum in: Am J Hum Genet. 2004 Mar;74(3):598. PMID: 14661163; PMCID: PMC1181904.

Dzyubenko E, Rozenberg A, Hermann DM, Faissner A. Colocalization of synapse marker proteins

Edmondson R, Broglie JJ, Adcock AF, Yang L. Three-dimensional cell culture systems and their applications in drug discovery and cell-based biosensors. Assay Drug Dev Technol. 2014 May;12(4):207-18. doi: 10.1089/adt.2014.573. PMID: 24831787; PMCID: PMC4026212.

Eichmüller OL, Knoblich JA. Human cerebral organoids - a new tool for clinical neurology research. Nat Rev Neurol. 2022 Nov;18(11):661-680. doi: 10.1038/s41582-022-00723-9. Epub 2022 Oct 17. PMID: 36253568; PMCID: PMC9576133.

Eiraku M, Sasai Y. Mouse embryonic stem cell culture for generation of three-dimensional retinal and cortical tissues. Nat Protoc. 2011 Dec 15;7(1):69-79. doi: 10.1038/nprot.2011.429. PMID: 22179593.

Eiraku M, Watanabe K, Matsuo-Takasaki M, Kawada M, Yonemura S, Matsumura M, Wataya T, Nishiyama A, Muguruma K, Sasai Y. Self-organized formation of polarized cortical tissues from ESCs and its active manipulation by extrinsic signals. Cell Stem Cell. 2008 Nov 6;3(5):519-32. doi: 10.1016/j.stem.2008.09.002. PMID: 18983967.

Elkabetz Y, Panagiotakos G, Al Shamy G, Socci ND, Tabar V, Studer L. Human ES cell-derived neural rosettes reveal a functionally distinct early neural stem cell stage. Genes Dev. 2008 Jan 15;22(2):152-65. doi: 10.1101/gad.1616208. Erratum in: Genes Dev. 2008 May 1;22(9):1257. PMID: 18198334; PMCID: PMC2192751.

EM, Vogel H, Fan HC, Paşca SP. Generation of Functional Human 3D Cortico-Motor Assembloids. Cell. 2020 Dec 23;183(7):1913-1929.e26. doi: 10.1016/j.cell.2020.11.017. Epub 2020 Dec 16. PMID: 33333020; PMCID: PMC8711252.

Encinas JM, Enikolopov G. Identifying and quantitating neural stem and progenitor cells in the adult brain. Methods Cell Biol. 2008;85:243-72. doi: 10.1016/S0091-679X(08)85011-X. PMID: 18155466.

Espuny-Camacho I, Michelsen KA, Gall D, Linaro D, Hasche A, Bonnefont J, Bali C, Orduz D, Bilheu A, Herpoel A, Lambert N, Gaspard N, Péron S, Schiffmann SN, Giugliano M, Gaillard A, Vanderhaeghen P. Pyramidal neurons derived from human pluripotent stem cells integrate efficiently into mouse brain circuits in vivo. Neuron. 2013 Feb 6;77(3):440-56. doi: 10.1016/j.neuron.2012.12.011. PMID: 23395372.

Evans, A. N. & Rooney, B. F. *Personnel Psychological,* Vol. 62 (eds Craig, S. B. & Clark, A. P.) 633–636, (Wiley, 2009).

Fair SR, Julian D, Hartlaub AM, Pusuluri ST, Malik G, Summerfied TL, Zhao G, Hester AB, Ackerman WE 4th, Hollingsworth EW, Ali M, McElroy CA, Buhimschi IA, Imitola J, Maitre NL, Bedrosian TA, Hester ME. Electrophysiological Maturation of Cerebral Organoids Correlates with Dynamic Morphological and Cellular Development. Stem Cell Reports. 2020 Oct 13;15(4):855-868. doi: 10.1016/j.stemcr.2020.08.017. Epub 2020 Sep 24. PMID: 32976764; PMCID: PMC7562943.

Fang KY, Cao WC, Xie TA, Lv J, Chen JX, Cao XJ, Li ZW, Deng ST, Guo XG. Exploration and validation of related hub gene expression during SARS-CoV-2 infection of human bronchial organoids. Hum Genomics. 2021 Mar 16;15(1):18. doi: 10.1186/s40246-021-00316-5. PMID: 33726831; PMCID: PMC7962432.

Farhy-Tselnicker I, Allen NJ. Astrocytes, neurons, synapses: a tripartite view on cortical circuit development. Neural Dev. 2018 May 1;13(1):7. doi: 10.1186/s13064-018-0104-y. PMID: 29712572; PMCID: PMC5928581.

Farías-Serratos BM, Lazcano I, Villalobos P, Darras VM, Orozco A. Thyroid hormone deficiency during zebrafish development impairs central nervous system myelination. PLoS One. 2021 Aug 17;16(8):e0256207. doi: 10.1371/journal.pone.0256207. PMID: 34403440; PMCID: PMC8370640.

Fatehullah A, Tan SH, Barker N. Organoids as an in vitro model of human development and disease. Nat Cell Biol. 2016 Mar;18(3):246-54. doi: 10.1038/ncb3312. PMID: 26911908.

Fauquier T, Chatonnet F, Picou F, Richard S, Fossat N, Aguilera N, Lamonerie T, Flamant F. Purkinje cells and Bergmann glia are primary targets of the TRα1 thyroid hormone receptor during mouse cerebellum postnatal development. Development. 2014 Jan;141(1):166-75. doi: 10.1242/dev.103226. PMID: 24346699.

Ferraro F, Celso CL, Scadden D. Adult stem cels and their niches. Adv Exp Med Biol. 2010;695:155-68. doi: 10.1007/978-1-4419-7037-4_11. PMID: 21222205; PMCID: PMC4020242.

Figueiras E, Soto AM, Jesus D, Lehti M, Koivisto J, Parraga JE, Silva-Correia J, Oliveira JM, Reis RL, Kellomäki M, Hyttinen J. Optical projection tomography as a tool for 3D imaging of hydrogels. Biomed Opt Express. 2014 Sep 5;5(10):3443-9. doi: 10.1364/BOE.5.003443. PMID: 25360363; PMCID: PMC4206315.

Folmes CD, Nelson TJ, Martinez-Fernandez A, Arrell DK, Lindor JZ, Dzeja PP, Ikeda Y, Perez-Terzic C, Terzic A. Somatic oxidative bioenergetics transitions into pluripotency-dependent glycolysis to facilitate nuclear reprogramming. Cell Metab. 2011 Aug 3;14(2):264-71. doi: 10.1016/j.cmet.2011.06.011. PMID: 21803296; PMCID: PMC3156138.

Formaggio E, Fazzini F, Dalfini AC, Di Chio M, Cantù C, Decimo I, Fiorini Z, Fumagalli G, Chiamulera C. Nicotine increases the expression of neurotrophin receptor tyrosine kinase receptor A in basal forebrain cholinergic neurons. Neuroscience. 2010 Mar 17;166(2):580-9. doi: 10.1016/j.neuroscience.2009.12.073. Epub 2010 Jan 4. PMID: 20056136.

Franze K, Janmey PA, Guck J. Mechanics in neuronal development and repair. Annu Rev Biomed Eng. 2013;15:227-51. doi: 10.1146/annurev-bioeng-071811-150045. Epub 2013 May 3. PMID: 23642242.

Friedlander DR, Mège RM, Cunningham BA, Edelman GM. Cell sorting-out is modulated by both the specificity and amount of different cell adhesion molecules (CAMs) expressed on cell surfaces. Proc Natl Acad Sci U S A. 1989 Sep;86(18):7043-7. doi: 10.1073/pnas.86.18.7043. PMID: 2780560; PMCID: PMC297989.

Fuchs E, Tumbar T, Guasch G. Socializing with the neighbors: stem cells and their niche. Cell. 2004 Mar 19;116(6):769-78. doi: 10.1016/s0092-8674(04)00255-7. PMID: 15035980.

Ganguly K, Schinder AF, Wong ST, Poo M. GABA itself promotes the developmental switch of neuronal GABAergic responses from excitation to inhibition. Cell. 2001 May 18;105(4):521-32. doi: 10.1016/s0092-8674(01)00341-5. PMID: 11371348.

Gao FB, Apperly J, Raff M. Cell-intrinsic timers and thyroid hormone regulate the probability of cell-cycle withdrawal and differentiation of oligodendrocyte precursor cells. Dev Biol. 1998 May 1;197(1):54-66. doi: 10.1006/dbio.1998.8877. PMID: 9578618.

Giandomenico SL, Mierau SB, Gibbons GM, Wenger LMD, Masullo L, Sit T, Sutcliffe M, Boulanger J, Tripodi M, Derivery E, Paulsen O, Lakatos A, Lancaster MA. Cerebral organoids at the air-liquid interface generate diverse nerve tracts with functional output. Nat Neurosci. 2019 Apr;22(4):669-679. doi: 10.1038/s41593-019-0350-2. Epub 2019 Mar 18. PMID: 30886407; PMCID: PMC6436729.

Giannocco G, Kizys MML, Maciel RM, de Souza JS. Thyroid hormone, gene expression, and Central Nervous System: Where we are. Semin Cell Dev Biol. 2021 Jun;114:47-56. doi: 10.1016/j.semcdb.2020.09.007. Epub 2020 Sep 24. PMID: 32980238.

Giynas Ayhan M, Uguz F, Askin R, Gonen MS. The prevalence of depression and anxiety disorders in patients with euthyroid Hashimoto's thyroiditis: a comparative study. Gen Hosp Psychiatry. 2014 Jan-Feb;36(1):95-8. doi: 10.1016/j.genhosppsych.2013.10.002. Epub 2013 Oct 9. PMID: 24211158.

Gomes AR, Fernandes TG, Vaz SH, Silva TP, Bekman EP, Xapelli S, Duarte S, Ghazvini M, Gribnau J, Muotri AR, Trujillo CA, Sebastião AM, Cabral JMS, Diogo MM. Modeling Rett Syndrome With Human Patient-Specific Forebrain Organoids. Front Cell Dev Biol. 2020 Dec 10;8:610427. doi: 10.3389/fcell.2020.610427. PMID: 33363173; PMCID: PMC7758289.

Gordon A, Yoon SJ, Tran SS, Makinson CD, Park JY, Andersen J, Valencia AM, Horvath S, Xiao X, Huguenard JR, Pașca SP, Geschwind DH. Long-term maturation of human cortical organoids matches key early postnatal transitions. Nat Neurosci. 2021 Mar;24(3):331-342. doi: 10.1038/s41593-021-00802-y. Epub 2021 Feb 22. PMID: 33619405; PMCID: PMC8109149.

Gothié JD, Sébillot A, Luongo C, Legendre M, Nguyen Van C, Le Blay K, Perret-Jeanneret M, Remaud S, Demeneix BA. Adult neural stem cell fate is determined by thyroid hormone activation of mitochondrial metabolism. Mol Metab. 2017 Nov;6(11):1551-1561. doi: 10.1016/j.molmet.2017.08.003. Epub 2017 Aug 19. PMID: 29107300; PMCID: PMC5681236.

Gothié JD, Vancamp P, Demeneix B, Remaud S. Thyroid hormone regulation of neural stem cell fate: From development to ageing. Acta Physiol (Oxf). 2020 Jan;228(1):e13316. doi: 10.1111/apha.13316. Epub 2019 Jun 17. PMID: 31121082; PMCID: PMC9286394.

Grijota-Martínez C, Bárez-López S, Gómez-Andrés D, Guadaño-Ferraz A. MCT8 Deficiency: The Road to Therapies for a Rare Disease. Front Neurosci. 2020 Apr 28;14:380. doi: 10.3389/fnins.2020.00380. PMID: 32410949; PMCID: PMC7198743.

Grippo, J. & Menkes, J. H. *Effect of Thyroid on Fatty Acid Biosynthesis in Brain*. *Pediat. Res* vol. 5 466–471 (1971).

Grönholm M, Feodoroff M, Antignani G, Martins B, Hamdan F, Cerullo V. Patient-Derived Organoids for Precision Cancer Immunotherapy. Cancer Res. 2021 Jun 15;81(12):3149-3155. doi: 10.1158/0008-5472.CAN-20-4026. Epub 2021 Mar 9. PMID: 33687948.

Guasch G, Fuchs E. Mice in the world of stem cell biology. Nat Genet. 2005 Nov;37(11):1201-6. doi: 10.1038/ng1667. PMID: 16254567; PMCID: PMC2405927.

Gumbiner BM. Cell adhesion: the molecular basis of tissue architecture and morphogenesis. Cell. 1996 Feb 9;84(3):345-57. doi: 10.1016/s0092-8674(00)81279-9. PMID: 8608588.

Hage MP, Azar ST. The Link between Thyroid Function and Depression. J Thyroid Res. 2012;2012:590648. doi: 10.1155/2012/590648. Epub 2011 Dec 14. PMID: 22220285; PMCID: PMC3246784.

Hayamizu TF, Mangan M, Corradi JP, Kadin JA, Ringwald M. The Adult Mouse Anatomical Dictionary: a tool for annotating and integrating data. Genome Biol. 2005;6(3):R29. doi: 10.1186/gb-2005-6-3-r29. Epub 2005 Feb 15. PMID: 15774030; PMCID: PMC1088948.

He S, Nakada D, Morrison SJ. Mechanisms of stem cell self-renewal. Annu Rev Cell Dev Biol. 2009;25:377-406. doi: 10.1146/annurev.cellbio.042308.113248. PMID: 19575646.

Heo JH, Kang D, Seo SJ, Jin Y. Engineering the Extracellular Matrix for Organoid Culture. Int J Stem Cells. 2022 Feb 28;15(1):60-69. doi: 10.15283/ijsc21190. PMID: 35220292; PMCID: PMC8889330.

Herst PM, Tan AS, Scarlett DJ, Berridge MV. Cell surface oxygen consumption by mitochondrial gene knockout cells. Biochim Biophys Acta. 2004 Jun 7;1656(2-3):79-87. doi: 10.1016/j.bbabio.2004.01.008. PMID: 15178469.

Hofer M, Lutolf MP. Engineering organoids. Nat Rev Mater. 2021;6(5):402-420. doi: 10.1038/s41578-021-00279-y. Epub 2021 Feb 19. PMID: 33623712; PMCID: PMC7893133.

https://mct8.info/treatment: MCT8-AHDS Foundation

Huang Y, Huang Z, Tang Z, Chen Y, Huang M, Liu H, Huang W, Ye Q, Jia B. Research Progress, Challenges, and Breakthroughs of Organoids as Disease Models. Front Cell Dev Biol. 2021 Nov 16;9:740574. doi: 10.3389/fcell.2021.740574. PMID: 34869324; PMCID: PMC8635113.

Inak G, Rybak-Wolf A, Lisowski P, Pentimalli TM, Jüttner R, Glažar P, Uppal K, Bottani E, Brunetti D, Secker C, Zink A, Meierhofer D, Henke MT, Dey M, Ciptasari U, Mlody B, Hahn T, Berruezo-Llacuna M, Karaiskos N, Di Virgilio M, Mayr JA, Wortmann SB, Priller J, Gotthardt M, Jones DP, Mayatepek E, Stenzel W, Diecke S, Kühn R, Wanker EE, Rajewsky N, Schuelke M, Prigione A. Defective metabolic programming impairs early neuronal morphogenesis in neural cultures and an organoid model of Leigh syndrome. Nat Commun. 2021 Mar 26;12(1):1929. doi: 10.1038/s41467-021-22117-z. PMID: 33771987; PMCID: PMC7997884.

Jacob F, Pather SR, Huang WK, Zhang F, Wong SZH, Zhou H, Cubitt B, Fan W, Chen CZ, Xu M, Pradhan M, Zhang DY, Zheng W, Bang AG, Song H, Carlos de la Torre J, Ming GL. Human Pluripotent Stem Cell-Derived Neural Cells and Brain Organoids Reveal SARS-CoV-2 Neurotropism Predominates in Choroid Plexus Epithelium. Cell Stem Cell. 2020 Dec 3;27(6):937-950.e9. doi: 10.1016/j.stem.2020.09.016. Epub 2020 Sep 21. PMID: 33010822; PMCID: PMC7505550.

Ji Y, Pang PT, Feng L, Lu B. Cyclic AMP controls BDNF-induced TrkB phosphorylation and dendritic spine formation in mature hippocampal neurons. Nat Neurosci. 2005 Feb;8(2):164-72. doi: 10.1038/nn1381. Epub 2005 Jan 23. PMID: 15665879.

JM, Boatright JH, Li Y. Systemic Treatment with Nicotinamide Riboside Is Protective in Two Mouse Models of Retinal Ganglion Cell Damage. Pharmaceutics. 2021 Jun 16;13(6):893. doi: 10.3390/pharmaceutics13060893. PMID: 34208613; PMCID: PMC8235058.

Johnson FA, Craig DQ, Mercer AD. Characterization of the block structure and molecular weight of sodium alginates. J Pharm Pharmacol. 1997 Jul;49(7):639-43. doi: 10.1111/j.2042-7158.1997.tb06085.x. PMID: 9255704.

Ju YE, Janmey PA, McCormick ME, Sawyer ES, Flanagan LA. Enhanced neurite growth from mammalian neurons in three-dimensional salmon fibrin gels. Biomaterials. 2007 Apr;28(12):2097-108. doi: 10.1016/j.biomaterials.2007.01.008. Epub 2007 Jan 26. PMID: 17258313; PMCID: PMC1991290.

Kadoshima T, Sakaguchi H, Nakano T, Soen M, Ando S, Eiraku M, Sasai Y. Self-organization of axial polarity, inside-out layer pattern, and species-specific progenitor dynamics in human ES cell-derived neocortex. Proc Natl Acad Sci U S A. 2013 Dec 10;110(50):20284-9. doi: 10.1073/pnas.1315710110. Epub 2013 Nov 25. Erratum in: Proc Natl Acad Sci U S A. 2014 May 20;111(20):7498. PMID: 24277810; PMCID: PMC3864329.

Kadoshima T, Sakaguchi H, Nakano T, Soen M, Ando S, Eiraku M, Sasai Y. Self-organization of axial polarity, inside-out layer pattern, and species-specific progenitor dynamics in human ES cell-derived neocortex. Proc Natl Acad Sci U S A. 2013 Dec 10;110(50):20284-9. doi: 10.1073/pnas.1315710110. Epub 2013 Nov 25. Erratum in: Proc Natl Acad Sci U S A. 2014 May 20;111(20):7498. PMID: 24277810; PMCID: PMC3864329.

Kapałczyńska M, Kolenda T, Przybyła W, Zajączkowska M, Teresiak A, Filas V, Ibbs M, Bliźniak R, Łuczewski Ł, Lamperska K. 2D and 3D cell cultures - a comparison of different

types of cancer cell cultures. Arch Med Sci. 2018 Jun;14(4):910-919. doi: 10.5114/aoms.2016.63743. Epub 2016 Nov 18. PMID: 30002710; PMCID: PMC6040128.

Kellner Y, Gödecke N, Dierkes T, Thieme N, Zagrebelsky M, Korte M. The BDNF effects on dendritic spines of mature hippocampal neurons depend on neuronal activity. Front Synaptic Neurosci. 2014 Mar 20;6:5. doi: 10.3389/fnsyn.2014.00005. PMID: 24688467; PMCID: PMC3960490.

Kelm JM, Timmins NE, Brown CJ, Fussenegger M, Nielsen LK. Method for generation of homogeneous multicellular tumor spheroids applicable to a wide variety of cell types. Biotechnol Bioeng. 2003 Jul 20;83(2):173-80. doi: 10.1002/bit.10655. PMID: 12768623.

Khazipov R, Luhmann HJ. Early patterns of electrical activity in the developing cerebral cortex of humans and rodents. Trends Neurosci. 2006 Jul;29(7):414-418. doi: 10.1016/j.tins.2006.05.007. Epub 2006 May 19. PMID: 16713634.

Kim H, Park HJ, Choi H, Chang Y, Park H, Shin J, Kim J, Lengner CJ, Lee YK, Kim J. Modeling G2019S-LRRK2 Sporadic Parkinson's Disease in 3D Midbrain Organoids. Stem Cell Reports. 2019 Mar 5;12(3):518-531. doi: 10.1016/j.stemcr.2019.01.020. Epub 2019 Feb 21. PMID: 30799274; PMCID: PMC6410341.

Kim H, Xu R, Padmashri R, Dunaevsky A, Liu Y, Dreyfus CF, Jiang P. Pluripotent Stem Cell-Derived Cerebral Organoids Reveal Human Oligodendrogenesis with Dorsal and Ventral Origins. Stem Cell Reports. 2019 May 14;12(5):890-905. doi: 10.1016/j.stemcr.2019.04.011. PMID: 31091434; PMCID: PMC6524754.

Kim J, Koo BK, Knoblich JA. Human organoids: model systems for human biology and medicine. Nat Rev Mol Cell Biol. 2020 Oct;21(10):571-584. doi: 10.1038/s41580-020-0259-3. Epub 2020 Jul 7. PMID: 32636524; PMCID: PMC7339799.

Kim J, Sullivan GJ, Park IH. How well do brain organoids capture your brain? iScience. 2021 Jan 19;24(2):102063. doi: 10.1016/j.isci.2021.102063. PMID: 33554067; PMCID: PMC7856464.

Kim JH, Kim YM, Yum MS, Choi JH, Lee BH, Kim GH, Yoo HW. Clinical and endocrine features of two Allan-Herndon-Dudley syndrome patients with monocarboxylate transporter 8 mutations. Horm Res Paediatr. 2015;83(4):288-92. doi: 10.1159/000371466. Epub 2015 Apr 15. Erratum in: Horm Res Paediatr. 2015;84(4):274. PMID: 25896225.

Kim M, Habiba A, Doherty JM, Mills JC, Mercer RW, Huettner JE. Regulation of mouse embryonic

Kitahara T, Sakaguchi H, Morizane A, Kikuchi T, Miyamoto S, Takahashi J. Axonal Extensions along Corticospinal Tracts from Transplanted Human Cerebral Organoids. Stem Cell Reports. 2020 Aug 11;15(2):467-481. doi: 10.1016/j.stemcr.2020.06.016. Epub 2020 Jul 16. PMID: 32679062; PMCID: PMC7419717.

Knobloch M, Jessberger S. Metabolism and neurogenesis. Curr Opin Neurobiol. 2017 Feb;42:45-52. doi: 10.1016/j.conb.2016.11.006. Epub 2016 Dec 1. PMID: 27915086.

Kothapalli CR, Kamm RD. 3D matrix microenvironment for targeted differentiation of embryonic stem cells into neural and glial lineages. Biomaterials. 2013 Aug;34(25):5995-6007. doi: 10.1016/j.biomaterials.2013.04.042. Epub 2013 May 18. PMID: 23694902.

Krieger TG, Moran CM, Frangini A, Visser WE, Schoenmakers E, Muntoni F, Clark CA, Gadian D, Chong WK, Kuczynski A, Dattani M, Lyons G, Efthymiadou A, Varga-Khadem F, Simons BD, Chatterjee K, Livesey FJ. Mutations in thyroid hormone receptor α1 cause premature neurogenesis and progenitor cell depletion in human cortical development. Proc Natl Acad Sci U S A. 2019 Nov 5;116(45):22754-22763. doi: 10.1073/pnas.1908762116. Epub 2019 Oct 18. Erratum in: Proc Natl Acad Sci U S A. 2020 Mar 31;117(13):7537-7538. PMID: 31628250; PMCID: PMC6842615.

Kuegler PB, Zimmer B, Waldmann T, Baudis B, Ilmjärv S, Hescheler J, Gaughwin P, Brundin P, Mundy W, Bal-Price AK, Schrattenholz A, Krause KH, van Thriel C, Rao MS, Kadereit S, Leist M. Markers of murine embryonic and neural stem cells, neurons and astrocytes: reference points for developmental neurotoxicity testing. ALTEX. 2010;27(1):17-42. PMID: 20390237.

Kwon HB, Sabatini BL. Glutamate induces de novo growth of functional spines in developing cortex.

Lancaster MA, Knoblich JA. Generation of cerebral organoids from human pluripotent stem cells. Nat Protoc. 2014 Oct;9(10):2329-40. doi: 10.1038/nprot.2014.158. Epub 2014 Sep 4. PMID: 25188634; PMCID: PMC4160653.

Lancaster MA, Knoblich JA. Organogenesis in a dish: modeling development and disease using organoid technologies. Science. 2014 Jul 18;345(6194):1247125. doi: 10.1126/science.1247125. Epub 2014 Jul 17. PMID: 25035496.

Lancaster MA, Renner M, Martin CA, Wenzel D, Bicknell LS, Hurles ME, Homfray T, Penninger JM, Jackson AP, Knoblich JA. Cerebral organoids model human brain development and microcephaly. Nature. 2013 Sep 19;501(7467):373-9. doi: 10.1038/nature12517. Epub 2013 Aug 28. PMID: 23995685; PMCID: PMC3817409.

Lange C, Turrero Garcia M, Decimo I, Bifari F, Eelen G, Quaegebeur A, Boon R, Zhao H, Boeckx B, Chang J, Wu C, Le Noble F, Lambrechts D, Dewerchin M, Kuo CJ, Huttner WB, Carmeliet P. Relief of hypoxia by angiogenesis promotes neural stem cell differentiation by targeting glycolysis. EMBO J. 2016 May 2;35(9):924-41. doi: 10.15252/embj.201592372. Epub 2016 Feb 8. PMID: 26856890; PMCID: PMC5207321.

Lanni A, Moreno M, Goglia F. Mitochondrial Actions of Thyroid Hormone. Compr Physiol. 2016 Sep 15;6(4):1591-1607. doi: 10.1002/cphy.c150019. PMID: 27783852.

Lazutkin A, Podgorny O, Enikolopov G. Modes of division and differentiation of neural stem cells. Behav Brain Res. 2019 Nov 18;374:112118. doi: 10.1016/j.bbr.2019.112118. Epub 2019 Jul 29. PMID: 31369774; PMCID: PMC6892343.

Lee J, Sutani A, Kaneko R, Takeuchi J, Sasano T, Kohda T, Ihara K, Takahashi K, Yamazoe M, Morio T, Furukawa T, Ishino F. In vitro generation of functional murine heart organoids via FGF4 and extracellular matrix. Nat Commun. 2020 Sep 3;11(1):4283. doi: 10.1038/s41467-020-18031-5. PMID: 32883967; PMCID: PMC7471119.

Lee JH, Shin H, Shaker MR, Kim HJ, Park SH, Kim JH, Lee N, Kang M, Cho S, Kwak TH, Kim JW, Song MR, Kwon SH, Han DW, Lee S, Choi SY, Rhyu IJ, Kim H, Geum D, Cho IJ, Sun W. Production of human spinal-cord organoids recapitulating neural-tube morphogenesis. Nat Biomed Eng. 2022 Apr;6(4):435-448. doi: 10.1038/s41551-022-00868-4. Epub 2022 Mar 28. PMID: 35347276.

Lehmann R, Lee CM, Shugart EC, Benedetti M, Charo RA, Gartner Z, Hogan B, Knoblich J, Nelson CM, Wilson KM. Human organoids: a new dimension in cell biology. Mol Biol Cell. 2019 May 1;30(10):1129-1137. doi: 10.1091/mbc.E19-03-0135. PMID: 31034354; PMCID: PMC6724519.

Levinson JN, El-Husseini A. Building excitatory and inhibitory synapses: balancing neuroligin partnerships. Neuron. 2005 Oct 20;48(2):171-4. doi: 10.1016/j.neuron.2005.09.017. PMID: 16242398.

Li X, Liu T, Song K, Yao L, Ge D, Bao C, Ma X, Cui Z. Culture of neural stem cells in calcium alginate beads. Biotechnol Prog. 2006 Nov-Dec;22(6):1683-9. doi: 10.1021/bp060185z. PMID: 17137318.

Li Y, Muffat J, Omer A, Bosch I, Lancaster MA, Sur M, Gehrke L, Knoblich JA, Jaenisch R. Induction of Expansion and Folding in Human Cerebral Organoids. Cell Stem Cell. 2017 Mar 2;20(3):385-396.e3. doi: 10.1016/j.stem.2016.11.017. Epub 2016 Dec 29. PMID: 28041895; PMCID: PMC6461394.

Lima FR, Gervais A, Colin C, Izembart M, Neto VM, Mallat M. Regulation of microglial development: a novel role for thyroid hormone. J Neurosci. 2001 Mar 15;21(6):2028-38. doi: 10.1523/JNEUROSCI.21-06-02028.2001. PMID: 11245686; PMCID: PMC6762591.

Lima FR, Gonçalves N, Gomes FC, de Freitas MS, Moura Neto V. Thyroid hormone action on astroglial cells from distinct brain regions during development. Int J Dev Neurosci. 1998 Feb;16(1):19-27. doi: 10.1016/s0736-5748(98)00002-1. PMID: 9664219.

Liour SS, Yu RK. Differentiation of radial glia-like cells from embryonic stem cells. Glia. 2003 Apr 15;42(2):109-17. doi: 10.1002/glia.10202. PMID: 12655595.

Liu G, David BT, Trawczynski M, Fessler RG. Advances in Pluripotent Stem Cells: History, Mechanisms, Technologies, and Applications. Stem Cell Rev Rep. 2020 Feb;16(1):3-32. doi: 10.1007/s12015-019-09935-x. PMID: 31760627; PMCID: PMC6987053.

Liu H, Zhang Y, Zhang YY, Li YP, Hua ZQ, Zhang CJ, Wu KC, Yu F, Zhang Y, Su J, Jin ZB. Human embryonic stem cell-derived organoid retinoblastoma reveals a cancerous origin. Proc Natl Acad Sci U S A. 2020 Dec 29;117(52):33628-33638. doi: 10.1073/pnas.2011780117. Epub 2020 Dec 14. PMID: 33318192; PMCID: PMC7776986.

Liu R, Wang J, Liang S, Zhang G, Yang X. Role of NKCC1 and KCC2 in Epilepsy: From Expression to Function. Front Neurol. 2020 Jan 17;10:1407. doi: 10.3389/fneur.2019.01407. PMID: 32010056; PMCID: PMC6978738.

Logan S, Arzua T, Canfield SG, Seminary ER, Sison SL, Ebert AD, Bai X. Studying Human Neurological Disorders Using Induced Pluripotent Stem Cells: From 2D Monolayer to 3D Organoid and Blood Brain Barrier Models. Compr Physiol. 2019 Mar 14;9(2):565-611. doi: 10.1002/cphy.c180025. PMID: 30873582; PMCID: PMC6705133.

López-Espíndola D, Morales-Bastos C, Grijota-Martínez C, Liao XH, Lev D, Sugo E, Verge CF, Refetoff S, Bernal J, Guadaño-Ferraz A. Mutations of the thyroid hormone

transporter MCT8 cause prenatal brain damage and persistent hypomyelination. J Clin Endocrinol Metab. 2014 Dec;99(12):E2799-804. doi: 10.1210/jc.2014-2162. PMID: 25222753; PMCID: PMC4255116.

Lou YR, Leung AW. Next generation organoids for biomedical research and applications. Biotechnol Adv. 2018 Jan-Feb;36(1):132-149. doi: 10.1016/j.biotechadv.2017.10.005. Epub 2017 Oct 19. Erratum in: Biotechnol Adv. 2019 May - Jun;37(3):505. PMID: 29056474.

Ludikhuize MC, Meerlo M, Burgering BMT, Rodríguez Colman MJ. Protocol to profile the bioenergetics of organoids using Seahorse. STAR Protoc. 2021 Mar 18;2(1):100386. doi: 10.1016/j.xpro.2021.100386. PMID: 33778780; PMCID: PMC7982773.

Luo C, Lancaster MA, Castanon R, Nery JR, Knoblich JA, Ecker JR. Cerebral Organoids Recapitulate Epigenomic Signatures of the Human Fetal Brain. Cell Rep. 2016 Dec 20;17(12):3369-3384. doi: 10.1016/j.celrep.2016.12.001. PMID: 28009303; PMCID: PMC5495578.

Ma T, Li J, Xu Y, Yu C, Xu T, Wang H, Liu K, Cao N, Nie BM, Zhu SY, Xu S, Li K, Wei WG, Wu Y, Guan KL, Ding S. Atg5-independent autophagy regulates mitochondrial clearance and is essential for iPSC reprogramming. Nat Cell Biol. 2015 Nov;17(11):1379-87. doi: 10.1038/ncb3256. Epub 2015 Oct 26. PMID: 26502054.

Mall EM, Herrmann D, Niemann H. Murine pluripotent stem cells with a homozygous knockout of Foxg1 show reduced differentiation towards cortical progenitors in vitro. Stem Cell Res. 2017 Dec;25:50-60. doi: 10.1016/j.scr.2017.10.012. Epub 2017 Oct 19. PMID: 29080444.

Mariani J, Coppola G, Zhang P, Abyzov A, Provini L, Tomasini L, Amenduni M, Szekely A, Palejev D, Wilson M, Gerstein M, Grigorenko EL, Chawarska K, Pelphrey KA, Howe JR, Vaccarino FM. FOXG1-Dependent Dysregulation of GABA/Glutamate Neuron

Differentiation in Autism Spectrum Disorders. Cell. 2015 Jul 16;162(2):375-390. doi: 10.1016/j.cell.2015.06.034. PMID: 26186191; PMCID: PMC4519016.

Marshall JJ, Mason JO. Mouse vs man: Organoid models of brain development & disease. Brain Res. 2019 Dec 1;1724:146427. doi: 10.1016/j.brainres.2019.146427. Epub 2019 Aug 29. PMID: 31473222.

Martin I, Wendt D, Heberer M. The role of bioreactors in tissue engineering. Trends Biotechnol. 2004 Feb;22(2):80-6. doi: 10.1016/j.tibtech.2003.12.001. PMID: 14757042.

Mayerl S, Müller J, Bauer R, Richert S, Kassmann CM, Darras VM, Buder K, Boelen A, Visser TJ, Heuer H. Transporters MCT8 and OATP1C1 maintain murine brain thyroid hormone homeostasis. J Clin Invest. 2014 May;124(5):1987-99. doi: 10.1172/JCI70324. Epub 2014 Apr 1. PMID: 24691440; PMCID: PMC4001533.

McCauley HA, Wells JM. Pluripotent stem cell-derived organoids: using principles of developmental biology to grow human tissues in a dish. Development. 2017 Mar 15;144(6):958-962. doi: 10.1242/dev.140731. PMID: 28292841; PMCID: PMC5358106.

Mehmel M, Jovanović N, Spitz U. Nicotinamide Riboside-The Current State of Research and Therapeutic Uses. Nutrients. 2020 May 31;12(6):1616. doi: 10.3390/nu12061616. PMID: 32486488; PMCID: PMC7352172.

Menacho C, Prigione A. Tackling mitochondrial diversity in brain function: from animal models to human brain organoids. Int J Biochem Cell Biol. 2020 Jun;123:105760. doi: 10.1016/j.biocel.2020.105760. Epub 2020 Apr 25. PMID: 32339638.

Mendoza A, Hollenberg AN. New insights into thyroid hormone action. Pharmacol Ther. 2017 May;173:135-145. doi: 10.1016/j.pharmthera.2017.02.012. Epub 2017 Feb 4. PMID: 28174093; PMCID: PMC5407910.

Miura Y, Li MY, Birey F, Ikeda K, Revah O, Thete MV, Park JY, Puno A, Lee SH, Porteus MH, Pașca SP. Generation of human striatal organoids and cortico-striatal assembloids from human pluripotent stem cells. Nat Biotechnol. 2020 Dec;38(12):1421-1430. doi: 10.1038/s41587-020-00763-w. Epub 2020 Dec 3. PMID: 33273741; PMCID: PMC9042317.

Mohan V, Sinha RA, Pathak A, Rastogi L, Kumar P, Pal A, Godbole MM. Maternal thyroid hormone deficiency affects the fetal neocorticogenesis by reducing the proliferating pool, rate of neurogenesis and indirect neurogenesis. Exp Neurol. 2012 Oct;237(2):477-88. doi: 10.1016/j.expneurol.2012.07.019. Epub 2012 Aug 7. PMID: 22892247.

Morita M, Ikeshima-Kataoka H, Kreft M, Vardjan N, Zorec R, Noda M. Metabolic Plasticity of Astrocytes and Aging of the Brain. Int J Mol Sci. 2019 Feb 21;20(4):941. doi: 10.3390/ijms20040941. PMID: 30795555; PMCID: PMC6413111.

Morte B, Díez D, Ausó E, Belinchón MM, Gil-Ibáñez P, Grijota-Martínez C, Navarro D, de Escobar GM, Berbel P, Bernal J. Thyroid hormone regulation of gene expression in the developing rat fetal cerebral cortex: prominent role of the Ca2+/calmodulin-dependent protein kinase IV pathway. Endocrinology. 2010 Feb;151(2):810-20. doi: 10.1210/en.2009-0958. Epub 2010 Jan 7. PMID: 20056827.

Morte B, Gil-Ibañez P, Heuer H, Bernal J. Brain Gene Expression in Systemic Hypothyroidism and Mouse Models of MCT8 Deficiency: The Mct8-Oatp1c1-Dio2 Triad. Thyroid. 2021 Jun;31(6):985-993. doi: 10.1089/thy.2020.0649. Epub 2021 Mar 18. PMID: 33307956.

Murrow LM, Weber RJ, Gartner ZJ. Dissecting the stem cell niche with organoid models: an engineering-based approach. Development. 2017 Mar 15;144(6):998-1007. doi: 10.1242/dev.140905. PMID: 28292846; PMCID: PMC5358107.

Nasu M, Takata N, Danjo T, Sakaguchi H, Kadoshima T, Futaki S, Sekiguchi K, Eiraku M, Sasai Y. Robust formation and maintenance of continuous stratified cortical

neuroepithelium by laminin-containing matrix in mouse ES cell culture. PLoS One. 2012;7(12):e53024. doi: 10.1371/journal.pone.0053024. Epub 2012 Dec 31. PMID: 23300850; PMCID: PMC3534089.

Nature. 2011 Jun 2;474(7349):100-4. doi: 10.1038/nature09986. Epub 2011 May 8. PMID: 21552280; PMCID: PMC3107907.

Navarro D, Alvarado M, Morte B, Berbel D, Sesma J, Pacheco P, Morreale de Escobar G, Bernal J, Berbel P. Late maternal hypothyroidism alters the expression of Camk4 in neocortical subplate neurons: a comparison with Nurr1 labeling. Cereb Cortex. 2014 Oct;24(10):2694-706. doi: 10.1093/cercor/bht129. Epub 2013 May 16. PMID: 23680840.

Negraes PD, Trujillo CA, Yu NK, Wu W, Yao H, Liang N, Lautz JD, Kwok E, McClatchy D, Diedrich J, de Bartolome SM, Truong J, Szeto R, Tran T, Herai RH, Smith SEP, Haddad GG, Yates JR 3rd, Muotri AR. Altered network and rescue of human neurons derived from individuals with early-onset genetic epilepsy. Mol Psychiatry. 2021 Nov;26(11):7047-7068. doi: 10.1038/s41380-021-01104-2. Epub 2021 Apr 22. PMID: 33888873; PMCID: PMC8531162.

Neniskyte U, Gross CT. Errant gardeners: glial-cell-dependent synaptic pruning and neurodevelopmental disorders. Nat Rev Neurosci. 2017 Nov;18(11):658-670. doi: 10.1038/nrn.2017.110. Epub 2017 Sep 21. PMID: 28931944.

Noguchi TK, Kurisaki A. Formation of Stomach Tissue by Organoid Culture Using Mouse Embryonic Stem Cells. Methods Mol Biol. 2017;1597:217-228. doi: 10.1007/978-1-4939-6949-4_16. PMID: 28361321.

O'Brien LC, Keeney PM, Bennett JP Jr. Differentiation of Human Neural Stem Cells into Motor Neurons Stimulates Mitochondrial Biogenesis and Decreases Glycolytic Flux. Stem Cells Dev. 2015 Sep 1;24(17):1984-94. doi: 10.1089/scd.2015.0076. Epub 2015 May 20. PMID: 25892363; PMCID: PMC4545371.

O'Leary DD, Chou SJ, Sahara S. Area patterning of the mammalian cortex. Neuron. 2007 Oct 25;56(2):252-69. doi: 10.1016/j.neuron.2007.10.010. PMID: 17964244.

Osakada F, Mori T, Cetin AH, Marshel JH, Virgen B, Callaway EM. New rabies virus variants for monitoring and manipulating activity and gene expression in defined neural circuits. Neuron. 2011 Aug 25;71(4):617-31. doi: 10.1016/j.neuron.2011.07.005. Erratum in: Neuron. 2012 Apr 12;74(1):206. PMID: 21867879; PMCID: PMC3189471.

Palazzolo G, Broguiere N, Cenciarelli O, Dermutz H, Zenobi-Wong M. Ultrasoft Alginate Hydrogels Support Long-Term Three-Dimensional Functional Neuronal Networks. Tissue Eng Part A. 2015 Aug;21(15-16):2177-85. doi: 10.1089/ten.TEA.2014.0518. Epub 2015 May 29. PMID: 25915796.

Palazzolo G, Moroni M, Soloperto A, Aletti G, Naldi G, Vassalli M, Nieus T, Difato F. Fast wide-volume functional imaging of engineered in vitro brain tissues. Sci Rep. 2017 Aug 17;7(1):8499. doi: 10.1038/s41598-017-08979-8. PMID: 28819205; PMCID: PMC5561227.

Palmqvist L, Glover CH, Hsu L, Lu M, Bossen B, Piret JM, Humphries RK, Helgason CD. Correlation of murine embryonic stem cell gene expression profiles with functional measures of pluripotency. Stem Cells. 2005 May;23(5):663-80. doi: 10.1634/stemcells.2004-0157. PMID: 15849174.

Pampaloni F, Reynaud EG, Stelzer EH. The third dimension bridges the gap between cell culture and live tissue. Nat Rev Mol Cell Biol. 2007 Oct;8(10):839-45. doi: 10.1038/nrm2236. PMID: 17684528.

Paridaen JT, Huttner WB. Neurogenesis during development of the vertebrate central nervous system. EMBO Rep. 2014 Apr;15(4):351-64. doi: 10.1002/embr.201438447. Epub 2014 Mar 17. PMID: 24639559; PMCID: PMC3989667.

Park JC, Jang SY, Lee D, Lee J, Kang U, Chang H, Kim HJ, Han SH, Seo J, Choi M, Lee DY, Byun MS, Yi D, Cho KH, Mook-Jung I. A logical network-based drug-screening

platform for Alzheimer's disease representing pathological features of human brain organoids. Nat Commun. 2021 Jan 12;12(1):280. doi: 10.1038/s41467-020-20440-5. PMID: 33436582; PMCID: PMC7804132.

Park Y, Franz CK, Ryu H, Luan H, Cotton KY, Kim JU, Chung TS, Zhao S, Vazquez-Guardado A, Yang DS, Li K, Avila R, Phillips JK, Quezada MJ, Jang H, Kwak SS, Won SM, Kwon K, Jeong H, Bandodkar AJ, Han M, Zhao H, Osher GR, Wang H, Lee K, Zhang Y, Huang Y, Finan JD, Rogers JA. Three-dimensional, multifunctional neural interfaces for cortical spheroids and engineered assembloids. Sci Adv. 2021 Mar 17;7(12):eabf9153. doi: 10.1126/sciadv.abf9153. PMID: 33731359; PMCID: PMC7968849.

Paşca AM, Sloan SA, Clarke LE, Tian Y, Makinson CD, Huber N, Kim CH, Park JY, O'Rourke NA, Nguyen KD, Smith SJ, Huguenard JR, Geschwind DH, Barres BA, Paşca SP. Functional cortical neurons and astrocytes from human pluripotent stem cells in 3D culture. Nat Methods. 2015 Jul;12(7):671-8. doi: 10.1038/nmeth.3415. Epub 2015 May 25. PMID: 26005811; PMCID: PMC4489980.

Paşca SP. Assembling human brain organoids. Science. 2019 Jan 11;363(6423):126-127. doi: 10.1126/science.aau5729. PMID: 30630918.

Paşca SP. Personalized Human Cortical Spheroids. Am J Psychiatry. 2016 Apr 1;173(4):332-3. doi: 10.1176/appi.ajp.2016.16020133. PMID: 27035533.

Pekny M, Nilsson M. Astrocyte activation and reactive gliosis. Glia. 2005 Jun;50(4):427-434. doi: 10.1002/glia.20207. PMID: 15846805.

Pekny M, Pekna M. Reactive gliosis in the pathogenesis of CNS diseases. Biochim Biophys Acta. 2016 Mar;1862(3):483-91. doi: 10.1016/j.bbadis.2015.11.014. Epub 2015 Dec 2. PMID: 26655603.

Pellegrini L, Albecka A, Mallery DL, Kellner MJ, Paul D, Carter AP, James LC, Lancaster MA. SARS-CoV-2 Infects the Brain Choroid Plexus and Disrupts the Blood-CSF Barrier in Human Brain Organoids. Cell Stem Cell. 2020 Dec 3;27(6):951-961.e5. doi:

10.1016/j.stem.2020.10.001. Epub 2020 Oct 13. PMID: 33113348; PMCID: PMC7553118.

Pellegrini L, Albecka A, Mallery DL, Kellner MJ, Paul D, Carter AP, James LC, Lancaster MA. SARS-CoV-2 Infects the Brain Choroid Plexus and Disrupts the Blood-CSF Barrier in Human Brain Organoids. Cell Stem Cell. 2020 Dec 3;27(6):951-961.e5. doi: 10.1016/j.stem.2020.10.001. Epub 2020 Oct 13. PMID: 33113348; PMCID: PMC7553118.

Pham MT, Pollock KM, Rose MD, Cary WA, Stewart HR, Zhou P, Nolta JA, Waldau B. Generation of human vascularized brain organoids. Neuroreport. 2018 May 2;29(7):588-593. doi: 10.1097/WNR.0000000000001014. PMID: 29570159; PMCID: PMC6476536.

Pino A, Fumagalli G, Bifari F, Decimo I. New neurons in adult brain: distribution, molecular mechanisms and therapies. Biochem Pharmacol. 2017 Oct 1;141:4-22. doi: 10.1016/j.bcp.2017.07.003. Epub 2017 Jul 8. PMID: 28690140.

Pollen AA, Bhaduri A, Andrews MG, Nowakowski TJ, Meyerson OS, Mostajo-Radji MA, Di Lullo E, Alvarado B, Bedolli M, Dougherty ML, Fiddes IT, Kronenberg ZN, Shuga J, Leyrat AA, West JA, Bershteyn M, Lowe CB, Pavlovic BJ, Salama SR, Haussler D, Eichler EE, Kriegstein AR. Establishing Cerebral Organoids as Models of Human-Specific Brain Evolution. Cell. 2019 Feb 7;176(4):743-756.e17. doi: 10.1016/j.cell.2019.01.017. PMID: 30735633; PMCID: PMC6544371.

Prezioso G, Giannini C, Chiarelli F. Effect of Thyroid Hormones on Neurons and Neurodevelopment. Horm Res Paediatr. 2018;90(2):73-81. doi: 10.1159/000492129. Epub 2018 Aug 29. PMID: 30157487.

Prezioso G, Giannini C, Chiarelli F. Effect of Thyroid Hormones on Neurons and Neurodevelopment. Horm Res Paediatr. 2018;90(2):73-81. doi: 10.1159/000492129. Epub 2018 Aug 29. PMID: 30157487.

Qian X, Nguyen HN, Jacob F, Song H, Ming GL. Using brain organoids to understand Zika virus-induced microcephaly. Development. 2017 Mar 15;144(6):952-957. doi: 10.1242/dev.140707. PMID: 28292840; PMCID: PMC5358105.

Qian X, Nguyen HN, Song MM, Hadiono C, Ogden SC, Hammack C, Yao B, Hamersky GR, Jacob F, Zhong C, Yoon KJ, Jeang W, Lin L, Li Y, Thakor J, Berg DA, Zhang C, Kang E, Chickering M, Nauen D, Ho CY, Wen Z, Christian KM, Shi PY, Maher BJ, Wu H, Jin P, Tang H, Song H, Ming GL. Brain-Region-Specific Organoids Using Mini-bioreactors for Modeling ZIKV Exposure. Cell. 2016 May 19;165(5):1238-1254. doi: 10.1016/j.cell.2016.04.032. Epub 2016 Apr 22. PMID: 27118425; PMCID: PMC4900885.

Qian X, Song H, Ming GL. Brain organoids: advances, applications and challenges. Development. 2019 Apr 16;146(8):dev166074. doi: 10.1242/dev.166074. PMID: 30992274; PMCID: PMC6503989.

Quadrato G, Nguyen T, Macosko EZ, Sherwood JL, Min Yang S, Berger DR, Maria N, Scholvin J, Goldman M, Kinney JP, Boyden ES, Lichtman JW, Williams ZM, McCarroll SA, Arlotta P. Cell diversity and network dynamics in photosensitive human brain organoids. Nature. 2017 May 4;545(7652):48-53. doi: 10.1038/nature22047. Epub 2017 Apr 26. PMID: 28445462; PMCID: PMC5659341.

Quiros PM, Goyal A, Jha P, Auwerx J. Analysis of mtDNA/nDNA Ratio in Mice. Curr Protoc Mouse Biol. 2017 Mar 2;7(1):47-54. doi: 10.1002/cpmo.21. PMID: 28252199; PMCID: PMC5335900.

Raja WK, Mungenast AE, Lin YT, Ko T, Abdurrob F, Seo J, Tsai LH. Self-Organizing 3D Human Neural Tissue Derived from Induced Pluripotent Stem Cells Recapitulate Alzheimer's Disease Phenotypes. PLoS One. 2016 Sep 13;11(9):e0161969. doi: 10.1371/journal.pone.0161969. PMID: 27622770; PMCID: PMC5021368.

Rash BG, Grove EA. Area and layer patterning in the developing cerebral cortex. Curr Opin Neurobiol. 2006 Feb;16(1):25-34. doi: 10.1016/j.conb.2006.01.004. Epub 2006 Jan 19. PMID: 16426837.

Rauth S, Karmakar S, Batra SK, Ponnusamy MP. Recent advances in organoid development and applications in disease modeling. Biochim Biophys Acta Rev Cancer. 2021 Apr;1875(2):188527. doi: 10.1016/j.bbcan.2021.188527. Epub 2021 Feb 26. PMID: 33640383; PMCID: PMC8068668.

Renner H, Grabos M, Becker KJ, Kagermeier TE, Wu J, Otto M, Peischard S, Zeuschner D, TsyTsyura Y, Disse P, Klingauf J, Leidel SA, Seebohm G, Schöler HR, Bruder JM. A fully automated high-throughput workflow for 3D-based chemical screening in human midbrain organoids. Elife. 2020 Nov 3;9:e52904. doi: 10.7554/eLife.52904. PMID: 33138918; PMCID: PMC7609049.

Renner M, Lancaster MA, Bian S, Choi H, Ku T, Peer A, Chung K, Knoblich JA. Self-organized developmental patterning and differentiation in cerebral organoids. EMBO J. 2017 May 15;36(10):1316-1329. doi: 10.15252/embj.201694700. Epub 2017 Mar 10. PMID: 28283582; PMCID: PMC5430225.

Richiardone, E., Van den Bossche, V. & Corbet, C. Metabolic Studies in Organoids: Current Applications, Opportunities and Challenges. *Organoids* **1**, 85–105 (2022).

Rivera C, Voipio J, Kaila K. Two developmental switches in GABAergic signalling: the K+-Cl- cotransporter KCC2 and carbonic anhydrase CAVII. J Physiol. 2005 Jan 1;562(Pt 1):27-36. doi: 10.1113/jphysiol.2004.077495. Epub 2004 Nov 4. Erratum in: J Physiol. 2005 May 1;564(Pt 3):953. PMID: 15528236; PMCID: PMC1665491.

Rodríguez-Peña A. Oligodendrocyte development and thyroid hormone. J Neurobiol. 1999 Sep 15;40(4):497-512. doi: 10.1002/(sici)1097-4695(19990915)40:4<497::aid-neu7>3.0.co;2-#. PMID: 10453052.

Romito A, Cobellis G. Pluripotent Stem Cells: Current Understanding and Future Directions. Stem Cells Int. 2016;2016:9451492. doi: 10.1155/2016/9451492. Epub 2015 Dec 20. PMID: 26798367; PMCID: PMC4699068.

Rosenberg SS, Spitzer NC. Calcium signaling in neuronal development. Cold Spring Harb Perspect Biol. 2011 Oct 1;3(10):a004259. doi: 10.1101/cshperspect.a004259. PMID: 21730044; PMCID: PMC3179332.

Rossi G, Manfrin A, Lutolf MP. Progress and potential in organoid research. Nat Rev Genet. 2018 Nov;19(11):671-687. doi: 10.1038/s41576-018-0051-9. PMID: 30228295.

Sakaguchi H, Kadoshima T, Soen M, Narii N, Ishida Y, Ohgushi M, Takahashi J, Eiraku M, Sasai Y. Generation of functional hippocampal neurons from self-organizing human embryonic stem cell-derived dorsomedial telencephalic tissue. Nat Commun. 2015 Nov 17;6:8896. doi: 10.1038/ncomms9896. PMID: 26573335; PMCID: PMC4660208.

Sakaguchi H, Kadoshima T, Soen M, Narii N, Ishida Y, Ohgushi M, Takahashi J, Eiraku M, Sasai Y. Generation of functional hippocampal neurons from self-organizing human embryonic stem cell-derived dorsomedial telencephalic tissue. Nat Commun. 2015 Nov 17;6:8896. doi: 10.1038/ncomms9896. PMID: 26573335; PMCID: PMC4660208.

Sarret C, Oliver Petit I, Tonduti D. Allan-Herndon-Dudley Syndrome. 2010 Mar 9 [updated 2020 Jan 16]. In: Adam MP, Everman DB, Mirzaa GM, Pagon RA, Wallace SE, Bean LJH, Gripp KW, Amemiya A, editors. GeneReviews® [Internet]. Seattle (WA): University of Washington, Seattle; 1993–2022. PMID: 20301789.

Sato T, Vries RG, Snippert HJ, van de Wetering M, Barker N, Stange DE, van Es JH, Abo A, Kujala P, Peters PJ, Clevers H. Single Lgr5 stem cells build crypt-villus structures in vitro without a mesenchymal niche. Nature. 2009 May 14;459(7244):262-5. doi: 10.1038/nature07935. Epub 2009 Mar 29. PMID: 19329995.

Sawano E, Takahashi M, Negishi T, Tashiro T. Thyroid hormone-dependent development of the GABAergic pre- and post-synaptic components in the rat hippocampus. Int J Dev Neurosci. 2013 Dec;31(8):751-61. doi: 10.1016/j.ijdevneu.2013.09.007. Epub 2013 Sep 26. PMID: 24076339.

Saxena K, Blutt SE, Ettayebi K, Zeng XL, Broughman JR, Crawford SE, Karandikar UC, Sastri NP, Conner ME, Opekun AR, Graham DY, Qureshi W, Sherman V, Foulke-Abel J, In J, Kovbasnjuk O, Zachos NC, Donowitz M, Estes MK. Human Intestinal Enteroids: a New Model To Study Human Rotavirus Infection, Host Restriction, and Pathophysiology. J Virol. 2015 Oct 7;90(1):43-56. doi: 10.1128/JVI.01930-15. PMID: 26446608; PMCID: PMC4702582.

Sayre NL, Sifuentes M, Holstein D, Cheng SY, Zhu X, Lechleiter JD. Stimulation of astrocyte fatty acid oxidation by thyroid hormone is protective against ischemic stroke-induced damage. J Cereb Blood Flow Metab. 2017 Feb;37(2):514-527. doi: 10.1177/0271678X16629153. Epub 2016 Jul 20. PMID: 26873887; PMCID: PMC5381439.

Schroeder AC, Privalsky ML. Thyroid hormones, T3 and T4, in the brain. Front Endocrinol (Lausanne). 2014 Mar 31;5:40. doi: 10.3389/fendo.2014.00040. PMID: 24744751; PMCID: PMC3978256.

Schutgens F, Clevers H. Human Organoids: Tools for Understanding Biology and Treating Diseases. Annu Rev Pathol. 2020 Jan 24;15:211-234. doi: 10.1146/annurev-pathmechdis-012419-032611. Epub 2019 Sep 24. PMID: 31550983.

Schwank G, Koo BK, Sasselli V, Dekkers JF, Heo I, Demircan T, Sasaki N, Boymans S, Cuppen E, van der Ent CK, Nieuwenhuis EE, Beekman JM, Clevers H. Functional repair of CFTR by CRISPR/Cas9 in intestinal stem cell organoids of cystic fibrosis patients. Cell Stem Cell. 2013 Dec 5;13(6):653-8. doi: 10.1016/j.stem.2013.11.002. PMID: 24315439.

Seto Y, Eiraku M. Human brain development and its in vitro recapitulation. Neurosci Res. 2019 Jan;138:33-42. doi: 10.1016/j.neures.2018.09.011. Epub 2018 Oct 13. PMID: 30326251.

Sharma TP, Wiley LA, Whitmore SS, Anfinson KR, Cranston CM, Oppedal DJ, Daggett HT, Mullins RF, Tucker BA, Stone EM. Patient-specific induced pluripotent stem cells to evaluate the pathophysiology of TRNT1-associated Retinitis pigmentosa. Stem Cell Res. 2017 May;21:58-70. doi: 10.1016/j.scr.2017.03.005. Epub 2017 Mar 18. PMID: 28390992.

Shevde NK, Mael AA. Techniques in embryoid body formation from human pluripotent stem cells. Methods Mol Biol. 2013;946:535-46. doi: 10.1007/978-1-62703-128-8_33. PMID: 23179854.

Shi Y, Kirwan P, Livesey FJ. Directed differentiation of human pluripotent stem cells to cerebral cortex neurons and neural networks. Nat Protoc. 2012 Oct;7(10):1836-46. doi: 10.1038/nprot.2012.116. Epub 2012 Sep 13. PMID: 22976355.

Shi Y, Sun L, Wang M, Liu J, Zhong S, Li R, Li P, Guo L, Fang A, Chen R, Ge WP, Wu Q, Wang X. Vascularized human cortical organoids (vOrganoids) model cortical development in vivo. PLoS Biol. 2020 May 13;18(5):e3000705. doi: 10.1371/journal.pbio.3000705. PMID: 32401820; PMCID: PMC7250475.

Shiraishi A, Muguruma K, Sasai Y. Generation of thalamic neurons from mouse embryonic stem cells. Development. 2017 Apr 1;144(7):1211-1220. doi: 10.1242/dev.144071. Epub 2017 Feb 20. PMID: 28219951.

Silva A, Pereira J, Oliveira CR, Relvas JB, Rego AC. BDNF and extracellular matrix regulate differentiation of mice neurosphere-derived cells into a GABAergic neuronal phenotype. J Neurosci Res. 2009 Jul;87(9):1986-96. doi: 10.1002/jnr.22041. PMID: 19267421.

Silva JE, Rudas P. Effects of congenital hypothyroidism on microtubule-associated protein-2 expression in the cerebellum of the rat. Endocrinology. 1990 Feb;126(2):1276-82. doi: 10.1210/endo-126-2-1276. PMID: 2298164.

Silva TP, Cotovio JP, Bekman E, Carmo-Fonseca M, Cabral JMS, Fernandes TG. Design Principles for Pluripotent Stem Cell-Derived Organoid Engineering. Stem Cells Int. 2019 Apr 18;2019:4508470. doi: 10.1155/2019/4508470. PMID: 31149014; PMCID: PMC6501244.

Simian M, Bissell MJ. Organoids: A historical perspective of thinking in three dimensions. J Cell Biol. 2017 Jan 2;216(1):31-40. doi: 10.1083/jcb.201610056. Epub 2016 Dec 28. PMID: 28031422; PMCID: PMC5223613.

Siracusa R, Fusco R, Cuzzocrea S. Astrocytes: Role and Functions in Brain Pathologies. Front Pharmacol. 2019 Sep 27;10:1114. doi: 10.3389/fphar.2019.01114. PMID: 31611796; PMCID: PMC6777416.

Smith AG. Embryo-derived stem cells: of mice and men. Annu Rev Cell Dev Biol. 2001;17:435-62. doi: 10.1146/annurev.cellbio.17.1.435. PMID: 11687496.

Smits LM, Reinhardt L, Reinhardt P, Glatza M, Monzel AS, Stanslowsky N, Rosato-Siri MD, Zanon A, Antony PM, Bellmann J, Nicklas SM, Hemmer K, Qing X, Berger E, Kalmbach N, Ehrlich M, Bolognin S, Hicks AA, Wegner F, Sterneckert JL, Schwamborn JC. Modeling Parkinson's disease in midbrain-like organoids. NPJ Parkinsons Dis. 2019 Apr 5;5:5. doi: 10.1038/s41531-019-0078-4. PMID: 30963107; PMCID: PMC6450999.

Sofroniew MV. Molecular dissection of reactive astrogliosis and glial scar formation. Trends Neurosci. 2009 Dec;32(12):638-47. doi: 10.1016/j.tins.2009.08.002. Epub 2009 Sep 24. PMID: 19782411; PMCID: PMC2787735.

Son G, Han J. Roles of mitochondria in neuronal development. BMB Rep. 2018 Nov;51(11):549-556. doi: 10.5483/BMBRep.2018.51.11.226. PMID: 30269744; PMCID: PMC6283025.

Son H, Kim S, Jung DH, Baek JH, Lee DH, Roh GS, Kang SS, Cho GJ, Choi WS, Lee DK, Kim HJ. Insufficient glutamine synthetase activity during synaptogenesis causes spatial memory impairment in adult mice. Sci Rep. 2019 Jan 22;9(1):252. doi: 10.1038/s41598-018-36619-2. PMID: 30670758; PMCID: PMC6342969.

Spence JR, Mayhew CN, Rankin SA, Kuhar MF, Vallance JE, Tolle K, Hoskins EE, Kalinichenko VV, Wells SI, Zorn AM, Shroyer NF, Wells JM. Directed differentiation of human pluripotent stem cells into intestinal tissue in vitro. Nature. 2011 Feb 3;470(7332):105-9. doi: 10.1038/nature09691. Epub 2010 Dec 12. PMID: 21151107; PMCID: PMC3033971.

Srikanth P, Lagomarsino VN, Muratore CR, Ryu SC, He A, Taylor WM, Zhou C, Arellano M, Young-Pearse TL. Shared effects of DISC1 disruption and elevated WNT signaling in human cerebral organoids. Transl Psychiatry. 2018 Apr 12;8(1):77. doi: 10.1038/s41398-018-0122-x. PMID: 29643329; PMCID: PMC5895714.

Stoppini L, Buchs PA, Muller D. A simple method for organotypic cultures of nervous tissue. J Neurosci Methods. 1991 Apr;37(2):173-82. doi: 10.1016/0165-0270(91)90128-m. PMID: 1715499.

Takahashi K, Tanabe K, Ohnuki M, Narita M, Ichisaka T, Tomoda K, Yamanaka S. Induction of pluripotent stem cells from adult human fibroblasts by defined factors. Cell. 2007 Nov 30;131(5):861-72. doi: 10.1016/j.cell.2007.11.019. PMID: 18035408.

Takahashi K, Yamanaka S. Induction of pluripotent stem cells from mouse embryonic and adult fibroblast cultures by defined factors. Cell. 2006 Aug 25;126(4):663-76. doi: 10.1016/j.cell.2006.07.024. Epub 2006 Aug 10. PMID: 16904174.

Takata N, Sakakura E, Eiraku M, Kasukawa T, Sasai Y. Self-patterning of rostral-caudal neuroectoderm requires dual role of Fgf signaling for localized Wnt antagonism. Nat Commun. 2017 Nov 7;8(1):1339. doi: 10.1038/s41467-017-01105-2. PMID: 29109536; PMCID: PMC5673904.

Takebe T, Enomura M, Yoshizawa E, Kimura M, Koike H, Ueno Y, Matsuzaki T, Yamazaki T, Toyohara T, Osafune K, Nakauchi H, Yoshikawa HY, Taniguchi H. Vascularized and Complex Organ Buds from Diverse Tissues via Mesenchymal Cell-Driven Condensation. Cell Stem Cell. 2015 May 7;16(5):556-65. doi: 10.1016/j.stem.2015.03.004. Epub 2015 Apr 16. PMID: 25891906.

Takebe T, Sekine K, Suzuki Y, Enomura M, Tanaka S, Ueno Y, Zheng YW, Taniguchi H. Self-organization of human hepatic organoid by recapitulating organogenesis in vitro. Transplant Proc. 2012 May;44(4):1018-20. doi: 10.1016/j.transproceed.2012.02.007. PMID: 22564614.

Tan X, Shi SH. Neocortical neurogenesis and neuronal migration. Wiley Interdiscip Rev Dev Biol. 2013 Jul;2(4):443-59. doi: 10.1002/wdev.88. Epub 2012 Sep 18. PMID: 24014417; PMCID: PMC3767922.

Taverna E, Götz M, Huttner WB. The cell biology of neurogenesis: toward an understanding of the development and evolution of the neocortex. Annu Rev Cell Dev Biol. 2014;30:465-502. doi: 10.1146/annurev-cellbio-101011-155801. Epub 2014 Jun 27. PMID: 25000993.

TeSlaa T, Chaikovsky AC, Lipchina I, Escobar SL, Hochedlinger K, Huang J, Graeber TG, Braas D, Teitell MA. α-Ketoglutarate Accelerates the Initial Differentiation of Primed Human Pluripotent Stem Cells. Cell Metab. 2016 Sep 13;24(3):485-493. doi: 10.1016/j.cmet.2016.07.002. Epub 2016 Jul 28. PMID: 27476976; PMCID: PMC5023506.

Tewary M, Shakiba N, Zandstra PW. Stem cell bioengineering: building from stem cell biology. Nat Rev Genet. 2018 Oct;19(10):595-614. doi: 10.1038/s41576-018-0040-z. PMID: 30089805.

Thompson CK, Cline HT. Thyroid Hormone Acts Locally to Increase Neurogenesis, Neuronal Differentiation, and Dendritic Arbor Elaboration in the Tadpole Visual System. J Neurosci. 2016 Oct 5;36(40):10356-10375. doi: 10.1523/JNEUROSCI.4147-15.2016. PMID: 27707971; PMCID: PMC5050329.

Thomson JA, Itskovitz-Eldor J, Shapiro SS, Waknitz MA, Swiergiel JJ, Marshall VS, Jones JM. Embryonic stem cell lines derived from human blastocysts. Science. 1998 Nov 6;282(5391):1145-7. doi: 10.1126/science.282.5391.1145. Erratum in: Science 1998 Dec 4;282(5395):1827. PMID: 9804556.

Trujillo CA, Gao R, Negraes PD, Gu J, Buchanan J, Preissl S, Wang A, Wu W, Haddad GG, Chaim IA, Domissy A, Vandenberghe M, Devor A, Yeo GW, Voytek B, Muotri AR. Complex Oscillatory Waves Emerging from Cortical Organoids Model Early Human Brain Network Development. Cell Stem Cell. 2019 Oct 3;25(4):558-569.e7. doi: 10.1016/j.stem.2019.08.002. Epub 2019 Aug 29. PMID: 31474560; PMCID: PMC6778040.

Ubink I, Bolhaqueiro ACF, Elias SG, Raats DAE, Constantinides A, Peters NA, Wassenaar ECE, de Hingh IHJT, Rovers KP, van Grevenstein WMU, Laclé MM, Kops GJPL, Borel Rinkes IHM, Kranenburg O. Organoids from colorectal peritoneal metastases as a platform for improving hyperthermic intraperitoneal chemotherapy. Br J Surg. 2019 Sep;106(10):1404-1414. doi: 10.1002/bjs.11206. Epub 2019 Jun 14. PMID: 31197820; PMCID: PMC6771632.

Ugolini G. Rabies virus as a transneuronal tracer of neuronal connections. Adv Virus Res. 2011;79:165-202. doi: 10.1016/B978-0-12-387040-7.00010-X. PMID: 21601048.

Underwood E, Redell JB, Zhao J, Moore AN, Dash PK. A method for assessing tissue respiration in anatomically defined brain regions. Sci Rep. 2020 Aug 6;10(1):13179. doi: 10.1038/s41598-020-69867-2. PMID: 32764697; PMCID: PMC7413397.

Urresti J, Zhang P, Moran-Losada P, Yu NK, Negraes PD, Trujillo CA, Antaki D, Amar M, Chau K, Pramod AB, Diedrich J, Tejwani L, Romero S, Sebat J, Yates Iii JR, Muotri AR, Iakoucheva LM. Cortical organoids model early brain development disrupted by 16p11.2 copy number variants in autism. Mol Psychiatry. 2021 Dec;26(12):7560-7580. doi: 10.1038/s41380-021-01243-6. Epub 2021 Aug 26. Erratum in: Mol Psychiatry. 2021 Sep 21;: PMID: 34433918; PMCID: PMC8873019.

Vancamp P, Deprez MA, Remmerie M, Darras VM. Deficiency of the Thyroid Hormone Transporter Monocarboxylate Transporter 8 in Neural Progenitors Impairs Cellular Processes Crucial for Early Corticogenesis. J Neurosci. 2017 Nov 29;37(48):11616-11631. doi: 10.1523/JNEUROSCI.1917-17.2017. Epub 2017 Nov 6. PMID: 29109240; PMCID: PMC6705747.

Vatine GD, Al-Ahmad A, Barriga BK, Svendsen S, Salim A, Garcia L, Garcia VJ, Ho R, Yucer N, Qian T, Lim RG, Wu J, Thompson LM, Spivia WR, Chen Z, Van Eyk J, Palecek SP, Refetoff S, Shusta EV, Svendsen CN. Modeling Psychomotor Retardation using iPSCs from MCT8-Deficient Patients Indicates a Prominent Role for the Blood-Brain Barrier. Cell Stem Cell. 2017 Jun 1;20(6):831-843.e5. doi: 10.1016/j.stem.2017.04.002. Epub 2017 May 16. PMID: 28526555; PMCID: PMC6659720.

Vazin T, Freed WJ. Human embryonic stem cells: derivation, culture, and differentiation: a review. Restor Neurol Neurosci. 2010;28(4):589-603. doi: 10.3233/RNN-2010-0543. PMID: 20714081; PMCID: PMC2973558.

Velasco S, Kedaigle AJ, Simmons SK, Nash A, Rocha M, Quadrato G, Paulsen B, Nguyen L, Adiconis X, Regev A, Levin JZ, Arlotta P. Individual brain organoids reproducibly form cell diversity of the human cerebral cortex. Nature. 2019 Jun;570(7762):523-527. doi: 10.1038/s41586-019-1289-x. Epub 2019 Jun 5. PMID: 31168097; PMCID: PMC6906116.

Verge CF, Konrad D, Cohen M, Di Cosmo C, Dumitrescu AM, Marcinkowski T, Hameed S, Hamilton J, Weiss RE, Refetoff S. Diiodothyropropionic acid (DITPA) in the treatment of MCT8 deficiency. J Clin Endocrinol Metab. 2012 Dec;97(12):4515-23. doi: 10.1210/jc.2012-2556. Epub 2012 Sep 19. PMID: 22993035; PMCID: PMC3513545.

Viscomi C, Bottani E, Zeviani M. Emerging concepts in the therapy of mitochondrial disease. Biochim Biophys Acta. 2015 Jun-Jul;1847(6-7):544-57. doi: 10.1016/j.bbabio.2015.03.001. Epub 2015 Mar 10. PMID: 25766847.

Vrinda M, Arun S, Srikumar BN, Kutty BM, Shankaranarayana Rao BS. Temporal lobe epilepsy-induced neurodegeneration and cognitive deficits: Implications for aging. J Chem Neuroanat. 2019 Jan;95:146-153. doi: 10.1016/j.jchemneu.2018.02.005. Epub 2018 Feb 19. PMID: 29471022.

Wang L, Ye X, Zhao Q, Zhou Z, Dan J, Zhu Y, Chen Q, Liu L. Drp1 is dispensable for mitochondria biogenesis in induction to pluripotency but required for differentiation of embryonic stem cells. Stem Cells Dev. 2014 Oct 15;23(20):2422-34. doi: 10.1089/scd.2014.0059. Epub 2014 Aug 4. PMID: 24937776.

Wang P, Mokhtari R, Pedrosa E, Kirschenbaum M, Bayrak C, Zheng D, Lachman HM. CRISPR/Cas9-mediated heterozygous knockout of the autism gene CHD8 and characterization of its transcriptional networks in cerebral organoids derived from iPS cells. Mol Autism. 2017 Mar 20;8:11. doi: 10.1186/s13229-017-0124-1. PMID: 28321286; PMCID: PMC5357816.

Watanabe K, Kamiya D, Nishiyama A, Katayama T, Nozaki S, Kawasaki H, Watanabe Y, Mizuseki K, Sasai Y. Directed differentiation of telencephalic precursors from embryonic stem cells. Nat Neurosci. 2005 Mar;8(3):288-96. doi: 10.1038/nn1402. Epub 2005 Feb 6. PMID: 15696161.

Watanabe M, Buth JE, Vishlaghi N, de la Torre-Ubieta L, Taxidis J, Khakh BS, Coppola G, Pearson CA, Yamauchi K, Gong D, Dai X, Damoiseaux R, Aliyari R, Liebscher S,

Schenke-Layland K, Caneda C, Huang EJ, Zhang Y, Cheng G, Geschwind DH, Golshani P, Sun R, Novitch BG. Self-Organized Cerebral Organoids with Human-Specific Features Predict Effective Drugs to Combat Zika Virus Infection. Cell Rep. 2017 Oct 10;21(2):517-532. doi: 10.1016/j.celrep.2017.09.047. PMID: 29020636; PMCID: PMC5637483.

Watanabe N, Santostefano KE, Yachnis AT, Terada N. A pathologist's perspective on induced pluripotent stem cells. Lab Invest. 2017 Oct;97(10):1126-1132. doi: 10.1038/labinvest.2017.81. Epub 2017 Jul 31. PMID: 28759008; PMCID: PMC5918271.

Weitzel JM, Iwen KA, Seitz HJ. Regulation of mitochondrial biogenesis by thyroid hormone. Exp Physiol. 2003 Jan;88(1):121-8. doi: 10.1113/eph8802506. PMID: 12552316.

Wémeau JL, Pigeyre M, Proust-Lemoine E, d'Herbomez M, Gottrand F, Jansen J, Visser TJ, Ladsous M. Beneficial effects of propylthiouracil plus L-thyroxine treatment in a patient with a mutation in MCT8. J Clin Endocrinol Metab. 2008 Jun;93(6):2084-8. doi: 10.1210/jc.2007-2719. Epub 2008 Mar 11. PMID: 18334584.

Wen Wang, Xiao Zhang, Ning Zhao, Ze-Hua Xu, Kangxin Jin, Zi-Bing Jin. Profiling of chimeric RNAs in human retinal development with retinal organoids. bioRxiv 2022.11.10.515982; doi: https://doi.org/10.1101/2022.11.10.515982, preprint

Wennekamp S, Mesecke S, Nédélec F, Hiiragi T. A self-organization framework for symmetry breaking in the mammalian embryo. Nat Rev Mol Cell Biol. 2013 Jul;14(7):452-9. doi: 10.1038/nrm3602. Epub 2013 Jun 19. PMID: 23778971.

Wickersham IR, Finke S, Conzelmann KK, Callaway EM. Retrograde neuronal tracing with a deletion-mutant rabies virus. Nat Methods. 2007 Jan;4(1):47-9. doi: 10.1038/nmeth999. Epub 2006 Dec 10. PMID: 17179932; PMCID: PMC2755236.

Winanto, Khong ZJ, Hor JH, Ng SY. Spinal cord organoids add an extra dimension to traditional motor neuron cultures. Neural Regen Res. 2019 Sep;14(9):1515-1516. doi: 10.4103/1673-5374.255966. PMID: 31089045; PMCID: PMC6557099.

Wulf A, Harneit A, Weitzel JM. T3-mediated gene expression is independent of PGC-1alpha. Mol Cell Endocrinol. 2007 May 30;270(1-2):57-63. doi: 10.1016/j.mce.2007.02.008. Epub 2007 Feb 24. PMID: 17382463.

Xiang Y, Tanaka Y, Cakir B, Patterson B, Kim KY, Sun P, Kang YJ, Zhong M, Liu X, Patra P, Lee SH, Weissman SM, Park IH. hESC-Derived Thalamic Organoids Form Reciprocal Projections When Fused with Cortical Organoids. Cell Stem Cell. 2019 Mar 7;24(3):487-497.e7. doi: 10.1016/j.stem.2018.12.015. Epub 2019 Feb 21. PMID: 30799279; PMCID: PMC6853597.

Xiang Y, Tanaka Y, Patterson B, Kang YJ, Govindaiah G, Roselaar N, Cakir B, Kim KY, Lombroso AP, Hwang SM, Zhong M, Stanley EG, Elefanty AG, Naegele JR, Lee SH, Weissman SM, Park IH. Fusion of Regionally Specified hPSC-Derived Organoids Models Human Brain Development and Interneuron Migration. Cell Stem Cell. 2017 Sep 7;21(3):383-398.e7. doi: 10.1016/j.stem.2017.07.007. Epub 2017 Jul 27. PMID: 28757360; PMCID: PMC5720381.

Xie AW, Binder BYK, Khalil AS, Schmitt SK, Johnson HJ, Zacharias NA, Murphy WL. Controlled Self-assembly of Stem Cell Aggregates Instructs Pluripotency and Lineage Bias. Sci Rep. 2017 Oct 25;7(1):14070. doi: 10.1038/s41598-017-14325-9. PMID: 29070799; PMCID: PMC5656593.

Yakoub AM, Sadek M. Development and Characterization of Human Cerebral Organoids: An Optimized Protocol. Cell Transplant. 2018 Mar;27(3):393-406. doi: 10.1177/0963689717752946. Epub 2018 May 11. PMID: 29749250; PMCID: PMC6038047.

Yang Y, Wang QQ, Bozinov O, Xu RX, Sun YL, Wang SS. GSK-3 inhibitor CHIR99021 enriches glioma stem-like cells. Oncol Rep. 2020 May;43(5):1479-1490. doi: 10.3892/or.2020.7525. Epub 2020 Feb 28. PMID: 32323804; PMCID: PMC7108089.

Yang Z, Ming GL, Song H. Postnatal neurogenesis in the human forebrain: from two migratory streams to dribbles. Cell Stem Cell. 2011 Nov 4;9(5):385-6. doi: 10.1016/j.stem.2011.10.007. PMID: 22056132; PMCID: PMC3218098.

Yao H, Wu W, Cerf I, Zhao HW, Wang J, Negraes PD, Muotri AR, Haddad GG. Methadone interrupts neural growth and function in human cortical organoids. Stem Cell Res. 2020 Dec;49:102065. doi: 10.1016/j.scr.2020.102065. Epub 2020 Oct 27. PMID: 33137567.

Yin X, Mead BE, Safaee H, Langer R, Karp JM, Levy O. Engineering Stem Cell Organoids. Cell Stem Cell. 2016 Jan 7;18(1):25-38. doi: 10.1016/j.stem.2015.12.005. PMID: 26748754; PMCID: PMC4728053.

Zafeiriou MP, Bao G, Hudson J, Halder R, Blenkle A, Schreiber MK, Fischer A, Schild D, Zimmermann WH. Developmental GABA polarity switch and neuronal plasticity in Bioengineered Neuronal Organoids. Nat Commun. 2020 Jul 29;11(1):3791. doi: 10.1038/s41467-020-17521-w. PMID: 32728089; PMCID: PMC7391775.

Zakrzewski W, Dobrzyński M, Szymonowicz M, Rybak Z. Stem cells: past, present, and future. Stem Cell Res Ther. 2019 Feb 26;10(1):68. doi: 10.1186/s13287-019-1165-5. PMID: 30808416; PMCID: PMC6390367.

Zhang H, Ryu D, Wu Y, Gariani K, Wang X, Luan P, D'Amico D, Ropelle ER, Lutolf MP, Aebersold R, Schoonjans K, Menzies KJ, Auwerx J. NAD^+ repletion improves mitochondrial and stem cell function and enhances life span in mice. Science. 2016 Jun 17;352(6292):1436-43. doi: 10.1126/science.aaf2693. Epub 2016 Apr 28. PMID: 27127236.

Zhang J, Khvorostov I, Hong JS, Oktay Y, Vergnes L, Nuebel E, Wahjudi PN, Setoguchi K, Wang G, Do A, Jung HJ, McCaffery JM, Kurland IJ, Reue K, Lee WN, Koehler CM, Teitell MA. UCP2 regulates energy metabolism and differentiation potential of human pluripotent stem cells. EMBO J. 2016 Apr 15;35(8):899. doi: 10.15252/embj.201694054. Erratum for: EMBO J. 2011 Dec 14;30(24):4860-73. PMID: 27084758; PMCID: PMC4972131.

Zhang X, Zhang N, Chrenek MA, Girardot PE, Wang J, Sellers JT, Geisert EE, Brenner C, Nickerson

Zhang Y, Chen K, Sloan SA, Bennett ML, Scholze AR, O'Keeffe S, Phatnani HP, Guarnieri P, Caneda C, Ruderisch N, Deng S, Liddelow SA, Zhang C, Daneman R, Maniatis T, Barres BA, Wu JQ. An RNA-sequencing transcriptome and splicing database of glia, neurons, and vascular cells of the cerebral cortex. J Neurosci. 2014 Sep 3;34(36):11929-47. doi: 10.1523/JNEUROSCI.1860-14.2014. Erratum in: J Neurosci. 2015 Jan 14;35(2):846-6. PMID: 25186741; PMCID: PMC4152602.

Zhao, Z., Chen, X., Dowbaj, A.M. *et al.* Organoids. *Nat Rev Methods Primers* **2**, 94 (2022).

https://doi.org/10.1038/s43586-022-00174-y

Zheng X, Boyer L, Jin M, Mertens J, Kim Y, Ma L, Ma L, Hamm M, Gage FH, Hunter T. Metabolic reprogramming during neuronal differentiation from aerobic glycolysis to neuronal oxidative phosphorylation. Elife. 2016 Jun 10;5:e13374. doi: 10.7554/eLife.13374. PMID: 27282387; PMCID: PMC4963198.